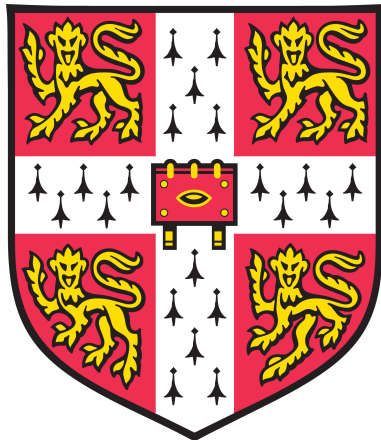


Mathematical modelling of noise generation in turbofan aeroengines using Green's functions



James Richard Mathews

Department of Applied Mathematics and Theoretical Physics
University of Cambridge

July 2016

This dissertation is submitted for the degree of
Doctor of Philosophy

Abstract

With demand for aircraft travel set to double in the next twenty years, targets are in place to reduce noise levels and emissions. For example, one target is that the effective perceived noise from aircraft in 2020 should be half of the 2000 level. One of the key noise components is the aeroengine. Building and designing an aeroengine costs millions of pounds and furthermore, to prove the aeroengine is safe, it has to be tested to destruction. Engineers and mathematicians are employed to design aeroengines that will not only be quieter but more fuel efficient and produce fewer harmful emissions while maintaining or improving performance.

The main topic of this thesis is investigating rotor-stator interaction which occurs when the turbulent, swirling air produced by the rotor hits the stator and generates noise. We do this in two distinct ways, firstly we calculate the Green's function for pressure in a turbofan duct with swirling mean flow and secondly we investigate the effect of turbulence hitting an isolated aerofoil.

The Green's function allows engineers to calculate the noise from rotor-stator interaction in simple cases and can be used in beamforming to analyse noise sources in the aeroengine. We consider an infinite duct, and use the Euler equations to derive a sixth order partial differential equation for pressure in the duct. We then find a Green's function of this equation, which can be done numerically or analytically using high-frequency asymptotics. Our main interest is the analytic Green's function, which we compare to numerical results. We begin by assuming the base flow has shear and swirling components in a constantly lined duct, and our analytic Green's function is a new result. We then calculate the Green's function for a base flow with variable entropy and a lining that varies with circumferential position.

To consider flow-blade interaction we simulate the turbulent wake of the rotor hitting a single stator blade. Tests in wind tunnels have shown that, depending on the parameters, introducing a serration on the leading edge of the aerofoil can reduce the noise significantly. We build an analytical model to investigate the effect of the serrated edge, which again involves solving a differential equation by using a Green's function. It also requires modelling the turbulence, which we do by using either deterministic eddies or stochastic eddies. We show it is possible to reduce the noise by using a serrated leading edge, but it is hard to predict the correct choice of serration to minimise the noise.

Preface

This dissertation is the result of my own work and includes nothing which is the outcome of work done in collaboration except as declared in the text below. The majority of [Chapter 6](#) was presented at the 21st AIAA/CEAS Aeroacoustics Conference in Dallas ([Mathews and Peake, 2015](#)). Some of the key results from [Chapter 3](#) and results with real data were presented at the 22nd AIAA/CEAS Aeroacoustics Conference in Lyon ([Mathews et al., 2016](#)).

It is not substantially the same as any that I have submitted, or, is being concurrently submitted for a degree or diploma or other qualification at the University of Cambridge or any other University or similar institution except as declared in the Preface and specified in the text. I further state that no part of my dissertation has already been submitted, or, is being concurrently submitted for any such degree, diploma or other qualification at the University of Cambridge or any other University or similar institution except as declared in the Preface and specified in the text.

Acknowledgements

This thesis couldn't have happened without a lot of people. Firstly, thanks to Professor Nigel Peake for being a wonderful supervisor and guiding me throughout the four years at Cambridge. Thank you to the CCA directors for admitting me into the doctoral training centre four years ago, and to EPSRC for funding me for the four years. Darwin College also contributed towards the cost of a conference in Dallas. Thank you to the numerous waves group people for having many interesting discussions (mainly in the pub); in particular Doran Khamis, Ed Brambley and Lorna Ayton.

Thank you to Hélène Posson for allowing use of the Fortran program she created in Cambridge to calculate the Green's function in swirling flow, which allowed me to validate the results from my MATLAB program. Hélène also allowed me to visit her at Airbus in Toulouse for two days to discuss future work and collaboration. Thank you to Chris Heaton for providing his MATLAB code for calculating the hydrodynamic modes, which was used in [Chapter 4](#). Thank you to Stefano Bianchi from Rolls-Royce for providing CFD data, which Examples 7-10 use in [Chapter 3](#), and it was also used in [Mathews et al. \(2016\)](#). This data was provided under the University Gas Turbine Partnership between University of Cambridge and Rolls-Royce.

Thank you to the team at Chebfun¹ who have developed such useful, open source software and also answering my many questions about it. Thank you also to Nico Schlömer for creating matlab2tikz², which I have used to great effect to produce nice looking figures from MATLAB.

Thank you to the rest of the CCA cohort for making lunchtimes fun, in particular Alex Bastounis, Karen Habermann, Kim Moore, Henry Jackson, Rob Hocking, Tom Begley and Vittoria Silvestri. Thank you to my office mate Marcus Webb for answering my many questions and introducing me to Chebfun. Thank you to everyone who read a chapter of my thesis, providing very useful feedback.

Thank you to my wonderful girlfriend, Rachael Holt, for supporting me though the four years and helping me express myself more clearly. Thank you to my parents, Annie and David, for encouraging me and enthusiastically reading some of my thesis, despite not understanding much of the mathematics. Finally, thank you to Miss Pritchard, my maths teacher from Imberhorne School, for convincing me to study mathematics at university.

¹<http://www.chebfun.org/>

²<https://github.com/matlab2tikz/matlab2tikz>

Contents

1	Introduction	1
1.1	Background	1
1.2	Mathematically modelling turbofan aeroengines and aerofoils	6
1.2.1	Modelling a turbofan aeroengine	6
1.2.2	Modelling stators as aerofoils	9
1.3	Literature review	10
1.4	Mathematical techniques	16
1.4.1	Generalised functions	16
1.4.2	Euler equations	18
1.4.3	Eigenmodes	21
2	A new acoustic analogy	25
2.1	The base flow	25
2.1.1	Simple forms of entropy in the base flow	27
2.2	A new acoustic analogy with entropy	28
2.2.1	Euler equations for generalised functions	28
2.2.2	Derivation of acoustic analogy	29
2.2.3	Using the acoustic analogy	32
2.2.4	Reducing to a form similar to Posson and Peake, 2013b	34
3	The Green's function	39
3.1	High-frequency Green's function	39
3.1.1	Boundary conditions	41
3.1.2	High-frequency limit	42
3.1.3	Applicability of high-frequency limit	43
3.1.4	Consequences of using high-frequency limit everywhere	43
3.2	Using WKB analysis to calculate the Green's function G_n as κ varies.	43
3.2.1	Zero turning point solution	45
3.2.2	One turning point solution	47
3.2.3	Regions for WKB analysis	50
3.3	Calculating the acoustic eigenmodes	52
3.3.1	Asymptotic method	52

3.3.2	Numerical method	53
3.4	Comparison of asymptotic and numerical eigenmodes	56
3.4.1	Test cases	57
3.4.2	Semi-realistic shear and swirl	63
3.4.3	Effect of entropy on the eigenmodes	65
3.5	Calculating the Green's function G_ω	70
3.5.1	Contribution from acoustic eigenmodes	72
3.5.2	Contribution from critical layer integral	75
3.5.3	Significance of the critical layer	77
3.6	Comparison of asymptotic and numerical Green's function	78
3.6.1	Test cases	79
3.6.2	Semi-realistic shear and swirl	82
3.6.3	Effect of entropy on the Green's function	84
3.7	Limitations of the method for calculating the asymptotic Green's function	87
3.7.1	Critical layer contribution	87
3.7.2	Multiple zeros of $q_n(r, \kappa)$	87
3.7.3	A more accurate dispersion relation	88
3.7.4	A single azimuthal mode	91
4	Hydrodynamic modes	95
4.1	Results from Heaton and Peake, 2006	95
4.1.1	Deriving Heaton and Peake's result in the simplest case	97
4.1.2	Summary of Heaton and Peake's results	98
4.1.3	Failure of Heaton and Peake's method for simplest case	99
4.1.4	Showing that the exponential accumulation rate is correct	100
4.1.5	Heaton and Peake's method in the other cases	102
4.2	Effect of entropy	103
4.2.1	Summary of asymptotic results	104
4.2.2	Numerical results	105
4.3	Failure to calculate the exponential constant of proportionality asymptotically	107
4.3.1	Showing the constant of proportionality is not a local property . . .	107
4.3.2	Showing that the constant of proportionality is a global property .	109
4.4	Bifurcating hydrodynamic modes	111
5	Green's function with acoustic lining varying circumferentially	115
5.1	Examples of lining varying circumferentially	115
5.2	Green's function with new boundary conditions	117
5.2.1	Green's function	117
5.2.2	Boundary conditions	118
5.3	High-frequency limit	120
5.3.1	Green's function differential equation	120

5.3.2	WKB solution	121
5.3.3	Boundary conditions	122
5.4	Calculating the eigenmodes asymptotically	124
5.4.1	Wroński and dispersion relation	124
5.4.2	Reducing to a finite system	125
5.4.3	Boundary condition at $r = h$ (calculating \mathbf{B}^h)	126
5.4.4	Boundary condition at $r = 1$ (calculating \mathbf{B}^1)	127
5.4.5	Simplifications with no swirl	128
5.4.6	Solving the dispersion relation	128
5.5	Calculating the eigenmodes numerically	128
5.5.1	Numerical dispersion relation	129
5.5.2	Eigenmode problem	129
5.6	Calculating the Green's function	131
5.6.1	Asymptotic method	132
5.6.2	Numerical method	132
5.7	Results	132
5.7.1	$n = 16$	133
5.7.2	$n = -25$	136
6	Turbulence hitting an aerofoil with a serrated leading edge	141
6.1	Howe's approach	141
6.2	Green's function for the Helmholtz equation tailored to an aerofoil with a serrated leading edge	143
6.2.1	Infinite half plane	143
6.2.2	Far-field Green's function	145
6.2.3	Serrated aerofoil	146
6.2.4	Summary of approximations made	147
6.3	Synthetic turbulence	147
6.4	Turbulence from a single eddy	148
6.4.1	Calculation of scattered pressure	149
6.4.2	Effect of the parameters	152
6.5	Turbulence from multiple eddies	155
6.5.1	Two eddies	155
6.5.2	Multiple eddies	157
6.6	Angle of attack	159
6.6.1	Green's function at angle of attack	160
6.6.2	Synthetic turbulence	160
6.6.3	Calculating the scattered pressure	160
6.6.4	Results	162

7 Conclusions	165
7.1 Future work	168
A Further mathematical techniques	173
A.1 The WKB method	173
A.2 Chebfun	177
B Hydrodynamic modes intermediate solution	181
B.1 Heuristic argument for intermediate solution for modes accumulating exponentially	181
C Calculations for an aerofoil with serrated leading edge	184
C.1 Analytic calculation of pressure for two eddies with different sources	184
C.2 Parameters for stochastic eddies in Section 6.5	185
C.3 Analytic calculation of integrals $I_\gamma^{\alpha,1/2}$ and $I_\gamma^{\alpha,3/2}$	187

List of Figures

1.1	Old and modern open-rotor engine designs.	2
1.2	Open-rotor blade.	2
1.3	Schematic of a modern General Electric GEnx-1B turbofan.	3
1.4	EPN from early and modern turbofans.	4
1.5	Frequency spectrum for tonal and broadband noise.	4
1.6	Rotor self-noise at subsonic and supersonic blade speeds.	5
1.7	Models of turbofan aeroengines.	6
1.8	Geometry of the duct, rotor and stator.	7
1.9	Geometry of serrated aerofoils.	9
1.10	A whale fin and a whale inspired blade.	15
1.11	Schematic view of eigenmodes in the complex k plane.	23
3.1	Branch cut for 2/3 root.	47
3.2	Effect of using the correct dispersion relation, parameters given by Example 3 in Section 3.4.1.	50
3.3	(a) Region \mathcal{R} when $\omega = 25$, $h = 0.6$; (b) to (d) three different regimes for the region \mathcal{K} when $h = 0.6$, $\omega = 25$, $U_x = 0.5$ and $U_\theta(r) = 0.1r + 0.1/r$. Blue line: exact critical points; shaded region: close to a critical point.	51
3.4	Shear and swirl profiles with $U_x(r) = 0.5 + 0.4r - 0.2r^2$ and $U_\theta(r) = 0.1r + 0.1/r$	57
3.5	Eigenmodes for Examples 1 & 2.	58
3.6	Eigenmodes for Examples 3 & 4.	60
3.7	Eigenmodes for Examples 5 & 6.	62
3.8	Semi-realistic mean flow profiles from a typical Rolls-Royce civil aeroengine.	63
3.9	Eigenmodes for Examples 7 & 8.	64
3.10	Eigenmodes for Examples 9 & 10.	66
3.11	Comparison between numerical and asymptotic eigenmodes as the entropy $s_0(r) = -\log(r^\beta)$ varies. The parameters are $\omega = 25$, $\eta = 0.6$, $U_x = 0.5$, $U_\theta = 0$ and lined walls of impedance $Z_j = 1 - 2i$	67
3.12	Comparison between numerical and asymptotic eigenmodes as the entropy $s_0(r) = -\log(r^\beta)$ varies. The parameters are $\omega = 25$, $\eta = 0.48$, $U_x(r) = 0.3 + 0.2r^2$, $U_\theta(r) = 0.2r + 0.1/r$ and lined walls of impedance $Z_j = 1 - 2i$	67

3.13 Comparison between numerical and asymptotic eigenmodes, for $\beta = -1.5$ (circles) and $\beta = 1$ (crosses). The parameters are $\omega = 25$, $\eta = 0.6$, $U_x = 0.5$, $U_\theta = 0$ and lined walls of different impedances.	68
3.14 Comparison between numerical and asymptotic eigenmodes, for $\beta = -1$ (circles) and $\beta = 1$ (crosses). The parameters are $\omega = 25$, $\eta = 0.48$, $U_x(r) = 0.3 + 0.2r^2$, $U_\theta(r) = 0.2r + 0.1/r$ and lined walls of different impedances.	68
3.15 Real part of numerical pressure eigenfunction for different eigenmodes for the parameters in Figure 3.11 when $\beta = -1.5$. Red: “surface-entropy” mode $k = -7.62 + 55.25i$, green: “surface-entropy” mode $k = 25.49 - 94.02i$, blue: other cut-off modes.	69
3.16 Plot of $q_n(r, \kappa)$ for $r \in [0.6, 1]$ for the parameters in Example 4 with $\omega\kappa = -4.29 + 1.11i$. Branch cut of square root in black.	73
3.17 Schematic of contour Γ_{CLH}	75
3.18 Comparison of the effect of the acoustic modes and critical layer on the pressure.	77
3.19 Comparison of the asymptotic and numerical Green’s function \hat{p}_n^m for Example 2. The source is at $r_0 = 0.8$ and $x - x_0 = 0.5$	79
3.20 Colour plot of the asymptotic Green’s function \hat{p}_n^A for Example 2, with a source at $(x_0, r_0) = (0, 0.8)$ as x and r vary.	79
3.21 Comparison of the asymptotic and numerical Green’s function \hat{p}_n^m for Example 3. The source is at $r_0 = 0.8$ and $x - x_0 = 0.5$	80
3.22 Comparison of the asymptotic and numerical Green’s function \hat{p}_n^m for Example 4. The source is at $r_0 = 0.8$ and $x - x_0 = 0.5$	81
3.23 Colour plot of the asymptotic Green’s function \hat{p}_n^A with a source at $(x_0, r_0) = (0, 0.8)$ as x and r vary. Top: Example 3 (hard-walled duct), bottom: Example 4 (lined walls).	82
3.24 Comparison of the asymptotic and numerical Green’s function \hat{p}_n^m for Example 7. The source is at $r_0 = 0.8$ and $x - x_0 = 0.5$	83
3.25 Comparison of the asymptotic and numerical Green’s function \hat{p}_n^m for Example 8. The source is at $r_0 = 0.8$ and $x - x_0 = 0.5$	83
3.26 Colour plot of the asymptotic Green’s function \hat{p}_n^A with a source at $(x_0, r_0) = (0, 0.8)$ as x and r vary. Top: Example 7 (hard-walled duct), bottom: Example 8 (lined walls).	84
3.27 Real and imaginary parts of asymptotic and numerical Green’s function as entropy varies for a source at $x - x_0 = 0.5$ and $r_0 = 0.8$	85
3.28 Colour plot of real part of asymptotic Green’s function \hat{p}_n^A with a source at $(x_0, r_0) = (0, 0.8)$ as x and r vary. We vary the entropy and impedance, and the rest of the parameters are the same as Figure 3.27.	86
3.29 Effect of new dispersion relation on asymptotic Green’s functions from the numerical eigenmode at $k = -10.880 + 14.499i$. in Example 4.	91

3.30	Colour plot of the numerical acoustic Green's function \hat{p}_ω^A with a source at $(r_0, \theta_0) = (0.8, 0)$ and $x - x_0 = 0.5$ as r and θ vary. The other flow parameters are $U_x = 0.5$, hard walls, $\omega = 25$ and $h = 0.6$.	92
3.31	Plot of $\max_{r \in [h, 1]} \hat{p}_n^A(r r_0) $ for each azimuthal number n for both hard and lined walls (of impedance $Z_j = 1 - 2i$) with the other parameters $U_x = 0.5$, $U_\theta(r) = 0.1r + 0.1/r$, $\omega = 25$, $h = 0.6$, $x - x_0 = 0.5$ and $r_0 = 0.8$.	92
4.1	Plot of the pressure eigenfunction for a hydrodynamic mode at $k = 44.0081$. The parameters are $U_x(r) = 0.5 + 0.2(r - 1)^2$, $U_\theta = 0.2$, $n = 15$, $\omega = 25$ and $h = 0.6$.	100
4.2	Right-hand side of critical layer (solid line) showing first five hydrodynamic modes (crosses). The parameters are $U_x = 0.5$, $U_\theta(r) = 0.1r + 0.1/r$, $\omega = 25$, $n = 15$ and $h = 0.6$.	105
4.3	Plot of the hydrodynamic modes as we vary entropy for different flow parameters.	106
4.4	Graph of shear flow $U_x(r)$ (left) and $k_c(r)$ (right) for the flows \mathbf{X}_l .	108
4.5	Plot of $(k - 44) \exp(0.7629m)$ against m for each of the ten flows \mathbf{X}_l to determine constant of proportionality numerically.	109
4.6	Graph of shear flow $U_x(r)$ (left) and $k_c(r)$ (right) for the flows ζ_a .	110
4.7	Graph of $k_c(r)$ for the flows in Table 4.7.	112
4.8	Plot of hydrodynamic modes as we consider shear flows of the form $U_x(r) = 0.5 - y(r - 1)^2$, with $0.241 \leq y \leq 0.284$. The vertical scale is different values of y in increments of 0.005. The other parameters are $n = 15$, $\omega = 25$, $U_\theta = 0.2$ and $h = 0.6$.	112
4.9	Plot of the pressure eigenfunctions P for the hydrodynamic modes from flows \mathbf{Y}_1 , \mathbf{Y}_2 and \mathbf{Y}_a to \mathbf{Y}_d .	113
5.1	Real and imaginary part of the truncated Fourier series of $1/Z^b(\theta)$ when $M = 8$ (red) and $1/Z^b(\theta)$ (blue).	116
5.2	Plot of truncated Fourier series of $1/Z^c(\theta)$ (black) for $M = 10$ (blue), $M = 30$ (red), $M = 100$ (green).	117
5.3	Plot of regions $\omega \mathcal{K}_n$ as n varies from $n = -100$ (blue) to $n = 100$ (red). We only plot intervals of $n = 10$. The other parameters of the flow are $\omega = 25$, $h = 0.6$, $U_x(r) = 0.2 + 0.4r^2$ and $U_\theta(r) = 0.1r + 0.2/r$.	122
5.4	Plot of shear flow $U_x(r) = 0.2 + 0.4r^2$ and swirl $U_\theta(r) = 0.1r + 0.2/r$.	133
5.5	Eigenmodes as lining varies circumferentially, $n = 16$.	134
5.6	Close up of trajectories of eigenmodes from Figure 5.5 as we vary the impedance function Z^c .	135
5.7	Asymptotic Green's function for each mode as the impedance function varies when $n = 16$ with $x - x_0 = 0.5$ and $r_0 = 0.8$. The other parameters are given in Figure 5.5.	136

5.8	Eigenmodes as lining varies circumferentially, $n = -25$	137
5.9	Close up of trajectories of downstream eigenmodes from Figure 5.8 as we vary the impedance function Z^s	138
5.10	Asymptotic Green's function for each mode as the impedance function varies when $n = -25$ with $x - x_0 = 0.5$ and $r_0 = 0.8$. The other parameters are given in Figure 5.5.	139
6.1	Plot of $\Re(P_s^{\mathcal{F}}(\mathbf{x}, \omega))$ for a straight and serrated edge at fixed $z = -5$. The parameters are $\omega = 1$, $u_0 = 0.25$ with eddy $\mathbf{A} = (1, 2, 1)$, $\mathbf{B} = (1, 1, 2)$ and $\mathbf{x}_e = (0, 0, 0)$	150
6.2	Plot of $\Re(P_s^{\mathcal{F}}(\mathbf{x}, \omega))$ for straight and serrated edges at fixed $\theta^* = \pi$. The parameters are $\omega = 1$, $u_0 = 0.25$ with eddy $\mathbf{A} = (1, 2, 1)$, $\mathbf{B} = (1, 1, 2)$ and $\mathbf{x}_e = (0, 0, 0)$	151
6.3	Plot of p_{diff} for serrations $\mathcal{F}_\mu(z) = a \sin(\mu z)$ as μ and a vary. The parameters are $\omega = 1$, $u_0 = 0.25$, $\mathbf{A} = (-1, 1, -2)$, $\mathbf{B} = (3, 1, 2)$ and $\mathbf{x}_e = (-3, 0, 1)$	153
6.4	Plot of $\Re(P_s^{\mathcal{F}}(\mathbf{x}, \omega))$ for a straight and serrated edge at fixed $z = -5$. The parameters are $\omega = 0.2$, $u_0 = 0.25$ with eddy $\mathbf{A} = (1, 2, 1)$, $\mathbf{B} = (1, 1, 2)$ and $\mathbf{x}_e = (0, 0, 0)$	153
6.5	Effect of serrations of the form $\mathcal{F}_\mu(z) = 0.5 \sin(\mu z)$ on $\Re(P_s^{\mathcal{F}}(\mathbf{x}, \omega))$. The parameters are given by $\omega = 1$, $u_0 = 0.25$, $\mathbf{A} = (1, 2, 1)$, $\mathbf{B} = (1, 1, 2)$ and $\mathbf{x}_e = (0, 0, 0)$. The colour scale is the same on each plot.	154
6.6	Plot of p_{diff} against serration angle $\angle \mathcal{F}_\mu$ for $\mathcal{F}_\mu(z) = 0.5 \sin(\mu z)$. The eddy parameters are $\mathbf{A} = (1, 2, 1)$, $\mathbf{B} = (1, 1, 2)$ and $\mathbf{x}_e = (0, 0, 0)$. The other parameters are $u_0 = 0.25$ and $\omega = 1$ (blue), $\omega = 0.2$ (red).	154
6.7	Plot of p_{diff} against serrations $\mathcal{F}_\mu(z) = 0.5 \sin(\mu z)$ as μ varies, for six randomly generated turbulence fields. The eddy parameters are given in Appendix C.2. The other paramaters are $\omega = 1$ and $u_0 = 0.25$	159
6.8	Plot of $\Re(P_s^{\mathcal{F}, \alpha}(\mathbf{x}, \omega))$ for a straight edge and serrated edge at angle of attack $\alpha = 6^\circ$ and $\theta^* = \pi + \alpha$. The parameters are $\omega = 0.5$, $u_0 = 0.25$ with eddy $\mathbf{A} = (1, 1, 1)$, $\mathbf{B} = (1, 1, 1)$ and $\mathbf{x}_e = (-1, -0.1, 0)$	162
6.9	Plot of p_{diff} for serrations $\mathcal{F}_\mu(z) = 0.5 \sin(\mu z)$ as μ varies, for aerofoils at different angle of attacks. The parameters are $\omega = 0.5$, $u_0 = 0.25$ with eddy $\mathbf{A} = (1, 2, 1)$, $\mathbf{B} = (1, 1, 2)$ and $\mathbf{x}_e = (-1, 0.1, 0)$	163
A.1	Plot of a chebfun of the Airy function $\text{Ai}(x)$	178
A.2	Plot of a chebfun of the Airy function $\text{Ai}'(x)$	179
A.3	Plot of Chebfun solution $g(x)$ of the differential equation $0.1g''(x) + g'(x) = -1$ with boundary conditions $g(-5) = 0$ and $g(5) = 0$	179
A.4	Chebfun eigenvalues for the eigenvalue problem (A.2.2) with associated boundary conditions (A.2.3).	180

List of Tables

3.1	Legend for eigenmode figures.	56
3.2	Parameters for Examples 1 to 6.	57
3.3	Improved accuracy of asymptotic (cut-on) eigenmodes by using the new asymptotic dispersion relation.	90
4.1	Analytic accumulation rate $\lambda^*(1)$ and numerical constant of proportionality of the hydrodynamic modes for the flows given in Figure 4.2.	106
4.2	Different shear flows with $U_x(1) = 0.5$ and $U'_x(1) = 0$	107
4.3	More shear flows with $U_x(1) = 0.5$ and $U'_x(1) = 0$	108
4.4	First nine hydrodynamic modes for the flows \mathbf{X}_l	108
4.5	Constant of proportionality for each of the ten flows \mathbf{X}_l	109
4.6	First five hydrodynamics modes for the flows ζ_a	110
4.7	Shear flows as $k_c(r)$ goes from being monotonic to non-monotonic.	111
4.8	Hydrodynamic modes for flows \mathbf{Y}_1 and \mathbf{Y}_2 . Numerical constant of proportionality for exponential accumulation given in brackets.	111
C.1	Parameters for stochastic eddies with seed 34.	185
C.2	Parameters for stochastic eddies with seed 73.	185
C.3	Parameters for stochastic eddies with seed 93.	186
C.4	Parameters for stochastic eddies with seed 345.	186
C.5	Parameters for stochastic eddies with seed 874.	186
C.6	Parameters for stochastic eddies with seed 1240.	186

Nomenclature

Latin Characters

A	Amplitudes of eddy Φ
A^j, B^j	Constants in solution v_j after using WKB method
B	Gaussian strengths of eddy Φ
B_∞^j	Infinite vector of constants we solve for in asymptotic eigenmode problem when lining varies circumferentially
$B^j = (B_m^j)$	Finite vector of constants we solve for in asymptotic eigenmode problem when lining varies circumferentially
B	Function in differential equation for unsteady potential φ
B_R	Number of rotor blades
C	Amplitudes of eddy Ψ
c	Total speed of sound of the flow
c_0	Base flow speed of sound
c_m, d_m	Fourier series coefficients of $1/Z(\theta)$
c_p, c_v	Specific heat capacities at constant pressure and volume respectively
D	Gaussian strengths of eddy Ψ
D	Function in differential equation for unsteady potential φ
D_0/Dt	Base flow convective derivative
d^e	Displacement between source positions of two eddies
e_j	Unit vector in j -th direction
e	Internal energy per unit mass of total flow
f_j	Function used in boundary condition for v_j

$f_S(t)$	The rotor-stator space \mathcal{S}_f is defined by $f_S(\mathbf{x}, t) = 0$
G	Green's function
$G^{\mathcal{F}}$	Green's function for serrated half plane defined by $x > \mathcal{F}(z)$
$[G^{\mathcal{F}}]$	Jump in Green's function $G^{\mathcal{F}}$ over serrated aerofoil
$_m G^{\mathcal{F}}$	The m -th component in the series of $G^{\mathcal{F}}$
G_n	Axial Fourier transform of the n -th azimuthal Fourier series coefficient of G_{ω}
G_n^{CL}	Contribution to G_n from the integral enclosing the critical layer and hydrodynamic modes
G_{ω}	Reduced Green's function at a particular frequency in the duct
g_1, g_2	Solutions to the homogeneous equation that G_n solves with certain boundary conditions
H	Heaviside function
\hat{H}	A smooth but non-analytic approximation of the Heaviside function
$H_{\nu_m}^{(1)}, H_{\nu_m}^{(2)}$	Hankel functions of the first and second kind, order ν_m
h	Non-dimensionalised inner radius of the duct
$I_{\gamma}^{\alpha, l}, J_{\gamma}^{\alpha}$	Integrals needed to calculate the scattered pressure P_s for an aerofoil at non-zero angle of attack
i	Imaginary unit
J	Jump in first order derivative when finding the Green's function G_n
J_{ν_m}	Bessel function of the first kind, order ν_m
j	Used for indexing, $j \in \{1, 2\}$, $j \in \{h, 1\}$, $j \in \{1, 2, 3\}$ or $j \in \{x, y, z\}$
K	Isentropic bulk modulus of a fluid
K_l	Modified Bessel function of the second kind, of order l
k	Axial wavenumber and eigenmode
k_A, k_B, k_C	Specific hydrodynamic eigenmodes
$k_c(r)$	Function that defines the critical layer

k_n^m	A specific acoustic eigenmode indexed by m at a specific azimuthal number n
k_m^\pm	A specific hydrodynamic eigenmode indexed by m (at a particular azimuthal number)
l	Used for indexing
M	Number of terms taken in truncated Fourier series of $1/Z(\theta)$
$M(r)$	Mach number of flow
m	Used for indexing, generally $m \in \mathbb{Z}$ or $m \in \mathbb{N}$
N, N_1	Number of non-zero terms in finite eigenmode system when lining varies circumferentially, with $N_1 = 2N + 1$
N_e	Number of eddies
\mathbf{n}	Unit normal
n	Azimuthal number
P	Fourier transform of pressure perturbation
P_I, P_O	Inner and outer solutions for the pressure P
P_i	Fourier transform of incident pressure
ΔP_l	Pressure jump over the l -th blade of the rotor
$P_s, P_s^{\mathcal{F}}, P_s^{\mathcal{F},\alpha}$	Fourier transform of scattered pressure for an aerofoil with serration \mathcal{F} at angle of attack α
\hat{P}	Used in numerical eigenvalue problem, $\hat{P} = kP$
\underline{p}	Total pressure of the flow
p	Pressure perturbation
\tilde{p}	Pressure perturbation multiplied by $H(f_S)$
p_0	Base flow pressure
p_{diff}	Proxy for measuring noise reduction for serrated aerofoils, $p_{\text{diff}} = \log(\mathcal{P}^{\mathcal{F}}/\mathcal{P}^0)$
p_{diff}^\dagger	Actual noise reduction in Decibels for serrated aerofoils
p_i	Incident pressure

\hat{p}_n	Axial Fourier transform of the n -th azimuthal Fourier series coefficient of \hat{p}_ω
\hat{p}_n^A	Contribution towards \hat{p}_n from all the acoustic modes
\hat{p}_n^{CL}	Contribution to \hat{p}_n from the integral enclosing the critical layer and hydrodynamic modes
\hat{p}_n^m	Contribution to \hat{p}_n from the acoustic eigenmode k_n^m
p_s	Scattered pressure
\hat{p}_ω	Reduced Green's function at a particular frequency to match Posson and Peake (2013b)
\hat{p}_ω^A	Contribution towards \hat{p}_ω from all the acoustic modes
Q_1	Term in integrand to calculate the scattered pressure P_s for a single eddy
Q_1^α	Term in integrand to calculate the scattered pressure P_s for a single eddy at angle of attack α
Q_2^S, Q_2^D	Term in integrand to calculate the scattered pressure P_s for two eddies, with the same or different sources
$Q_{N_e}^D$	Term in integrand to calculate the scattered pressure P_s for N_e eddies, with different sources
q_n	Function in WKB differential equation. The number of zeros of q_n determines the form of the solution
R	Ideal gas constant, $R = c_p - c_v$
$R(r)$	Fourier transform of density
R_e	Eddy radius, dependent on source position \mathbf{x}_e of the eddy
r	Non-dimensionalised radial coordinate
$\mathbf{r} = (r^*, \theta^*, z^*)$	Modified cylindrical coordinates in x - y plane, centred at $(\mathcal{F}(z), 0)$
$\mathbf{r}_0 = (r_0^*, \theta_0^*, z_0^*)$	Source position in modified cylindrical coordinates
r_c (r_n^c)	Zero of q_n
$r_{c,j}$	Zeros of q_n when we have multiple zeros
r_{cl}	Zero of Ω
r_{cl}^*	Critical point of k_c , $k'_c(r_{cl}^*) = 0$

r_D	Zero of D
S	Fourier transform of entropy perturbation
\underline{s}	Total entropy of the flow
s	Entropy perturbation
s_0	Base flow entropy
s^\pm (s_n^\pm)	Function used to find \mathcal{K} , $\mathcal{K} = s^+(\mathcal{R}) \cup s^-(\mathcal{R})$
\underline{T}	Temperature of total flow
T_{jl}	Lighthill stress tensor
t	Time
U, V, W	Fourier transform of velocity perturbations
$U_\theta(r)$	Swirl profile for base flow
$U_x(r)$	Shear profile for base flow
$(\underline{u}, \underline{v}, \underline{w})$	Total velocities of the flow (in x , r and θ directions respectively)
(u, v, w)	Velocity perturbations
$(\tilde{u}, \tilde{v}, \tilde{w})$	Velocity perturbations multiplied by $H(fs)$
(u_0, v_0, w_0)	Base flow velocities
v_1, v_2	Scaled versions of g_1 and g_2 used in WKB solution
\mathbf{v}^s	Surface speed of rotor-stator space \mathcal{S}_f
$\mathbf{X}_l, \mathbf{Y}_l$	Base flow regimes when calculating hydrodynamic modes
x	Non-dimensionalised axial coordinate
$\mathbf{x} = (x, r, \theta)$	Cylindrical coordinates in the duct
$\mathbf{x}_0 = (x_0, r_0, \theta_0)$	Source position in the duct
\mathbf{x}_e	Source position of the eddy, $\mathbf{x}_e = (x_e, y_e, z_e)$
Z_p	Non-isentropic factor, $Z_p = p/c_0^2 - \rho$
Z_j (Z)	Complex impedance of acoustic lining at duct walls
Z^a, Z^b, Z^c, Z^s	Complex impedances of acoustic lining at duct walls which varies circumferentially

\mathbf{z}_s Centre of modified cylindrical coordinates, $\mathbf{z}_s = (\mathcal{F}(z_0), 0, z_0)$, so that $|\mathbf{x} - \mathbf{z}_s|^2 = r^{\star 2} + (z - z_0)$

z Non-dimensionalised height above aerofoil

Greek Characters

α Angle of attack of aerofoil

β Varying parameter in base flow entropy $s_0(r) = -\log(r^\beta)$

β_{jl} Product of amplitudes and Gaussian strengths in j and l direction, for a single eddy $\beta_{jl} = A_j B_j A_l B_l$

Γ Contour for calculating the inverse Fourier transform of the Green's function, using the Briggs-Bers method

Γ_{CLH} Contour enclosing the critical layer and hydrodynamic modes

γ Ratio of specific heat capacities

$\gamma(k_z)$ Function used in Green's function for serrated aerofoil, $\gamma(k_z) = \sqrt{\omega^2 - k_z^2}$

γ_{jl} Sum of Gaussian strengths in j and l direction, for a single eddy $\gamma_{jl} = B_j + B_l$

$\delta(f)$ Dirac delta

δ_{jl} Kronecker delta

ε Small parameter

ϵ_r Similar to Levi-Civita symbol, $\epsilon_h = 1$ and $\epsilon_1 = -1$

ζ Compressibility factor, used in the numerical eigenvalue problem

ζ_l Base flow regime when calculating hydrodynamic modes

η Scaled azimuthal number, $\eta = n/\omega$

θ Circumferential coordinate

ι (ι^\star) Angle between r (r^\star) and $z - z_0$, used to calculate Green's function of a serrated aerofoil in the far field

κ Scaled axial wavenumber, $\kappa = k/\omega$

κ_n^m A specific scaled acoustic eigenmode indexed by m at a specific azimuthal number n

Λ^j	Finite matrix in asymptotic eigenmode problem when lining varies circumferentially
Λ_∞^j	Infinite matrix in asymptotic eigenmode problem when lining varies circumferentially
λ, λ^*	Defines accumulation rate for hydrodynamic modes, λ^* is same as λ but with additional entropy factor related to \mathcal{E}
μ	Free parameter, different in each chapter
μ^j	Finite vector in asymptotic eigenmode problem when lining varies circumferentially
μ_∞^j	Infinite vector in asymptotic eigenmode problem when lining varies circumferentially
$\nu (\nu^*)$	Related to $\lambda (\lambda^*)$ with $2\lambda = \sqrt{4\nu - 1}$ ($2\lambda^* = \sqrt{4\nu^* - 1}$)
ν_m	$\nu_m = m/2$
$\underline{\rho}$	Density of the total flow
ρ	Density perturbation
$\tilde{\rho}$	Density perturbation multiplied by $H(f_s)$
ρ_0	Base flow density
Σ_h, Σ_1	Functions relating to the impedance at the duct walls
σ_h, σ_1	Functions relating to the impedance at the duct walls, zero for hard walls
ς	Free parameter, different in each chapter
$\tau, \hat{\tau} (\tau_n, \hat{\tau}_n)$	Variables that the Airy functions act on in the WKB solution
τ_{jl}	Viscous stress tensor
$\Upsilon (\Upsilon_n)$	Function in differential equation for G_n
$\Upsilon^* (\Upsilon_n^*)$	Scaled version of Υ , $\Upsilon = \omega \Upsilon^*$
Φ, Ψ	Eddies
$\Phi (\Phi_n)$	Scaled version of Ω , $\Omega = \omega \Phi$
$\Phi_{j,l}$	Shape function of the l -th eddy, with either a Gaussian or Mexican hat profile
φ	Unsteady potential

ϕ	Fourier transform of unsteady potential φ
χ	Function relating to the Fourier transform of unsteady potential, ϕ
χ_I, χ_O	Inner and outer solutions of χ
Ψ_n	Integral of $\sqrt{q_n}$ between r_c and 1, used in WKB method for one turning point solution
Ψ_n^j	Extension of Ψ_n when we have two zeros of q_n
ψ_n	Integral of $\sqrt{q_n}$ in the duct, used in WKB method for zero turning point solution
Ω (Ω_n)	Function in differential equation for G_n , $\Omega = 0$ defines critical layer
$\hat{\Omega}, (\hat{\Omega}_n)$	Related function to Ω , used in the numerical eigenvalue problem
Ω_R	Angular speed of the rotor
ω	Non-dimensionalised frequency

Other Characters

\mathcal{A}	Coefficient of highest derivative in differential equation for pressure P
\mathcal{A}_m	Coefficient of constant A_m in $v_m(r)$
\mathbb{A}_m	Coefficient of constant A_m in $v'_m(r)$
$\mathcal{B}, \hat{\mathcal{B}}$	Coefficient of first order derivative in differential equation for pressure P , $\hat{\mathcal{B}} = \mathcal{B}/\mathcal{A}$
\mathcal{B}_m	Coefficient of constant B_m in $v_m(r)$
\mathbb{B}_m	Coefficient of constant B_m in $v'_m(r)$
$\mathcal{C}, \hat{\mathcal{C}}$	Coefficient in differential equation for pressure, P , $\hat{\mathcal{C}} = \mathcal{C}/\mathcal{A}$
$\mathcal{D}, \mathcal{D}_{\text{mass}}, \mathcal{D}_e$	Surface source terms from momentum, mass and energy equations
$\mathcal{E}(r)$	Extra entropy term in ν^* for accumulation rate of hydrodynamic modes
$\mathbb{E}, \mathbb{E}^{AOA}$	Exponential terms needed to calculate the scattered pressure P_s , \mathbb{E}^{AOA} reduces to \mathbb{E} at zero angle of attack
$\mathcal{F}^{PP}, \mathcal{F}^M$	Sixth order differential operators acting on pressure perturbation p in acoustic analogy
\mathcal{F}	Serration function for leading edge of aerofoil

$\angle \mathcal{F}$	Angle of serration \mathcal{F} at $z = 0$
\mathcal{H}	Function in volume source terms in acoustic analogy
\mathcal{K}_n^+	Set of all acoustic downstream eigenmodes for a specific azimuthal number n
\mathcal{K}_n^-	Set of all acoustic upstream eigenmodes for a specific azimuthal number n
\mathcal{K}^{CL}	Critical layer
\mathcal{K} (\mathcal{K}_n)	Region of κ space when we should use the one turning point solution in the WKB method
$\mathcal{P}^{\mathcal{F}}, \mathcal{P}^{\mathcal{F},\alpha}$	Power of scattered pressure for an aerofoil with serratation \mathcal{F} at angle of attack α
\mathcal{Q}	If $\mathcal{Q} > 0$ then $\Re(q_n) > 0$ at $r = 1$ and $\Re(q_n) < 0$ at $r = h$
\mathcal{Q}_j	Extension of \mathcal{Q} to when we have two zeros of q_n
\mathcal{R}, \mathcal{T}	Differential operators in the acoustic analogy
\mathcal{R}	Region of r space when we should use the one turning point solution in the WKB method
$\mathcal{S}_f(\mathbf{x}, t)$	Space occupied by the rotor and stator in the duct
$\mathcal{S}, \mathcal{S}_{\text{mass}}, \mathcal{S}_e$	Volume source terms from momentum, mass and energy equations
$\mathbb{S}^M, \mathbb{S}_V^M, \mathbb{S}_S^M$	Source terms in Mathews' acoustic analogy
$\mathbb{S}^{PP}, \mathbb{S}_{FWH}^{PP}$	Source terms in Posson and Peake's acoustic analogy
\mathcal{U}_0	Function in differential equation for unsteady potential φ , dependent on mean flow
\mathcal{U}_θ	Function in differential equation for G_n which depends only on swirl U_θ
\mathbb{U}_θ	Function in acoustic analogy which depends only on swirl U_θ
$\mathcal{V} (\mathcal{V}_n)$	Wrońskián of v_1 and v_2
$\mathcal{W} (\mathcal{W}_n)$	Wrońskián of g_1 and g_2
$\mathcal{X}_{n,m}, \mathcal{X}_{n,m}^*$	Coefficients in boundary condition for v_n when lining varies circumferentially
$\mathcal{Z}_{n,m}, \mathcal{Z}_{n,m}^*$	Coefficients in boundary condition for g_n when lining varies circumferentially

Function spaces

$C_c^\infty(\mathbb{R})$	Space of test functions, which are smooth and have compact support
$L^1_{\text{loc}}(\mathbb{R})$	Space of locally integrable functions, $f \in L^1_{\text{loc}}(\mathbb{R})$ if $\int_K f dx < \infty$ for all compact sets K

Other notation

$\mathbb{1}_K$	Indicator function for a set K ; $\mathbb{1}_K = \begin{cases} 1 & x \in K \\ 0 & x \in K^C \end{cases}$
Bar derivatives	Generalised derivatives
Complement	The complement of a set K is $K^C = \mathbb{C} \setminus K$
Double dagger \ddagger	Quantities with dimension
Subscript $_0$	Base flow functions
Tilde	Function multiplied by Heaviside function to make generalised function
Underlined	Total function, sum of perturbation and base flow

Abbreviations

ACARE	Advisory Council for Aeronautics Research in Europe
BPF	Blade passing frequency
CAA	Computational aeroacoustics
CFD	Computational fluid dynamics
EPN	Effective perceived noise
SPL	Sound pressure level
WKB	Wentzel-Kramers-Brillouin method (Bender and Orszag, 1978) for solving a differential equation with a small parameter

Chapter 1

Introduction

1.1 Background

Environmental concerns such as noise pollution, emission of greenhouse gases and fuel efficiency mean that designing a modern aeroengine is a challenge. In 2002 the Advisory Council for Aeronautics Research in Europe (ACARE) set targets for 2020 such as a 50% cut in carbon dioxide (CO_2) emissions, an 80% cut in nitrous oxides (NO_x) emissions and a 50% reduction of effective perceived noise (EPN) from their 2000 levels (ACARE, 2002). In 2011 the High Level Group on Aviation Research (Flightpath, 2011) proposed stricter targets by 2050, codenamed Flightpath 2050. They aim to achieve a 75% cut in CO_2 emissions, a 90% cut in NO_x emissions and a 65% reduction of effective perceived noise, all in relation to 2000 levels. According to The Clean Sky Joint Technology Initiative¹ (Clean Sky), air transport contributes to 2% of all human CO_2 emissions and produces 628,000,000 tonnes of CO_2 a year. In 2008 the UK introduced the Climate Change Act (Climate Change Act, 2008) which contains legally binding targets. However, it does not cover international aviation emissions because of a lack of agreement over allocation of flights.

Despite these environmental concerns, demand for air travel is booming, and the worldwide aircraft fleet is expected to double in 20 – 25 years. This growth would require the equivalent of 1300 new international airports, leading to additional environmental concerns. Passengers will also be expecting better service. Flightpath 2050 also expects 90% of travellers on European flights to complete their journey door to door in under four hours and flights to arrive within one minute of the planned time.

The emission targets have led to a number of European funded collaborative projects, such as Clean Sky and ENOVAL. Clean Sky's partners include major industrial bodies such as Rolls-Royce and Airbus, universities, research institutions and many other small to medium enterprises. There is limited numerical evidence to show the progress towards the 2020 targets. Of the 50% reduction in CO_2 emissions, around 15% to 20% was attributed to the aeroengine, and most of the rest to the airframe. The Clean Sky and ENOVAL

¹<http://www.cleansky.eu/content/homepage/aviation-environment>

projects have generally surpassed the target for the aeroengine, with ENOVAL claiming a 26% reduction on their webpage². However, the overall target for CO₂ emissions looks likely to be missed, according to [Clean Sky \(2014\)](#), and will instead be around 30% to 40%. Published data suggests that noise reduction will be very close to the target, but probably fall short. ENOVAL² suggest that there will be a 9.3dB decrease in EPN, corresponding to a 48% reduction, while [Clean Sky \(2014\)](#) suggest the noise reduction will be between 30% and 50%. It appears that the NO_x emission target will be missed by a significant margin, with prediction of around a 20% to 40% reduction by [Clean Sky \(2014\)](#).



(a) General Electric GE36 open-rotor engine.³ (b) Safran open-rotor engine from Clean Sky.⁴

Figure 1.1: Old and modern open-rotor engine designs.

One of the main outcomes of these targets is the re-emergence of open-rotor engines (or propfans) which usually consist of a number of contra-rotating propellers. These were originally popular between the 1970s and the 1990s, with designs including the General Electric GE36 ([Figure 1.1a](#)). The Clean Sky project has seen the development of new, cutting edge open-rotor designs, for example the design from Safran in [Figure 1.1b](#). Many other manufacturers are developing open-rotor technology and these could be in commercial aircraft before 2030, with a concept from Rolls-Royce shown in [Peake and Parry \(2012\)](#).

Despite being more fuel efficient than the current turbofans, research of open-rotor engines was almost universally dropped in the 1990s. This was due to major concerns around noise, safety and performance whilst plummeting fuel prices meant that the design's major advantage, its efficiency, was becoming less important. At typical cruising speeds the flow around the rotating open-rotor blades in old designs could become supersonic, causing shocks to form around the blades which significantly reduced performance. However, modern open-rotor designs use more blades and these blades are highly swept to prevent shocks and hence improve performance. In [Figure 1.2](#) we see a blade from the Safran open-rotor. The



Figure 1.2:
Open-rotor blade.⁵

²<http://www.enoval.eu/page/about-enoval/objectives.php>

³http://www.b-domke.de/AviationImages/Propfan/Images/MD-81_N980DC_GE36_UDF_810.jpg

⁴http://cleansky.eu/sites/default/files/photos/1._open_rotor.jpg

⁵http://cleansky.eu/sites/default/files/photos/2._open_rotor_blade.jpg

two main concerns that new open-rotor designs need to overcome are related to noise and safety. The lack of casing around the open-rotor means there is no containment of debris in case of events such as a bird strike. Additionally, the lack of casing compared to a turbofan means we have very limited control of the noise. The casing from a turbofan is often fitted with an acoustic liner to dampen and absorb noise.

In contrast to the open-rotor technologies being developed in Clean Sky, ENOVAL is solely focussed on the conventional turbofan. Today, turbofans are used on nearly all modern commercial aircraft. The major manufacturers of turbofans are General Electric, Rolls-Royce and Pratt & Whitney, and we show a typical, modern turbofan from General Electric in [Figure 1.3](#). The first turbofan to be developed was the Rolls-Royce Conway, around fifty years ago, when Sir Frank Whittle conceived the idea of the by-pass aeroengine⁶. This technology replaced turbojet engines, which produced all of their thrust from the turbine and were very inefficient.

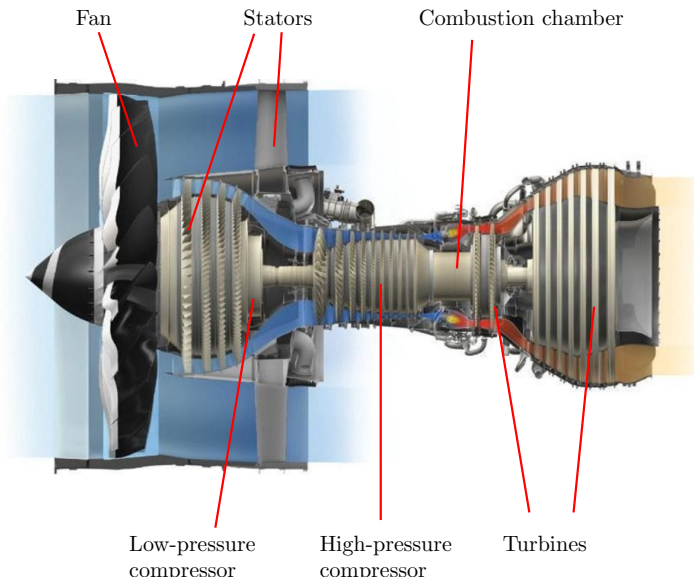


Figure 1.3: Schematic of a modern General Electric GEnx-1B turbofan.⁷

The turbofan is designed so that incoming air is split into two channels, as seen in the schematic in [Figure 1.3](#). Some of the air enters the compressor, turbine and combustor, which provides most of the thrust. The rest bypasses the turbine, but is still sped up by the fan, so it provides additional thrust. The mixing of the hot core flow of air coming out of the nozzle and the cooler bypass flow of air creates what is called jet noise. The ratio between these flows of air is called the bypass ratio. A higher bypass ratio means that more of the air bypasses the turbine and core of the aeroengine. Since the early turbofans, manufacturers have been increasing the bypass ratio, which has led to changes in the overall noise from the turbofan, although many other factors are also responsible. [Figure 1.4](#) shows how the different components of the turbofan contribute to the noise from a modern design and an early turbofan.

⁶<https://www.flightglobal.com/pdfarchive/view/1960/1960-0077.html>

⁷https://c2.staticflickr.com/8/7271/7677149070_0f7ffc9ff1_b.jpg

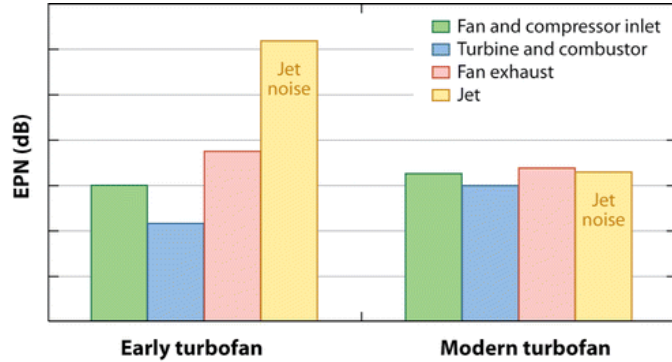


Figure 1.4: Effective perceived noise from early and modern turbofans, taken from Peake and Parry (2012).

We see that the jet noise has significantly decreased and the fan noise is now the dominant source for modern turbofans. The ENOVAL project is looking to reduce noise by further increasing the bypass ratio and using a number of new developments to the turbofan including new blade technologies, lightweight casing, new acoustic lining technologies and a shorter design⁸.

We split the noise into tonal and broadband components. The frequency spectrum for a noise source is a plot of sound pressure level (SPL), measured in Decibels, versus frequency, measured in Hertz. Broadband noise has a frequency spectrum where the amplitude is insensitive to frequency and there are no dominant frequencies. We see an example of broadband noise in Figure 1.5a. Tonal noise is where there are dominant discrete frequencies in a spectrum. In Figures 1.5b and 1.5c there is tonal noise at 1000 Hz and integer multiples of it. Tonal noise can be pure, where the SPL is close to zero away from the tones, and we give an example in Figure 1.5b. However, most tonal noise sources in an aeroengine have underlying broadband noise, so away from the tones the SPL is non-zero, and we give an example in Figure 1.5c.

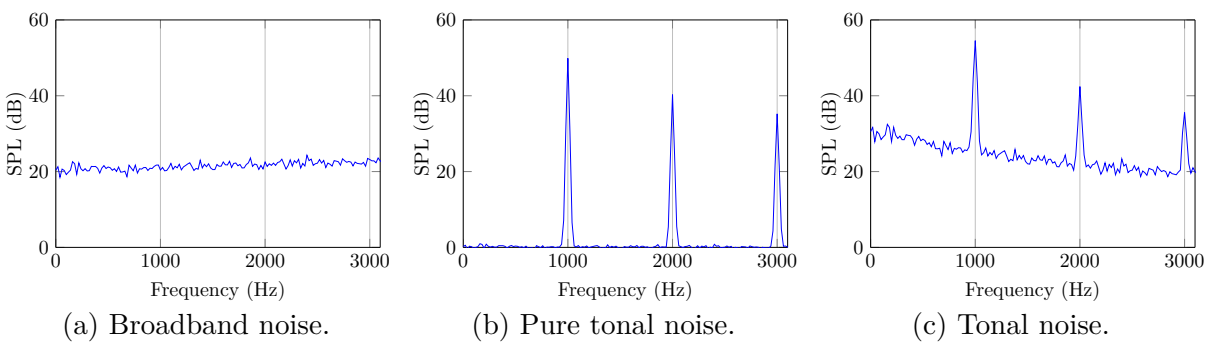
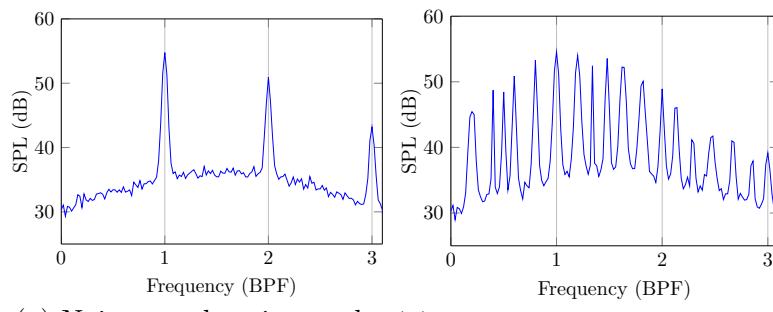


Figure 1.5: Frequency spectrum for tonal and broadband noise.

For a turbofan, the main sources of fan noise identified by Peake and Parry (2012) are the rotor (or fan) self-noise, rotor-stator (or fan-vane) interaction, rotor casing boundary-layer interaction and droop-fan interaction. In addition, there are sources unique to open-rotors, with the latter two sources for turbofans not present. For a complete overview of all sources of noise from an aircraft, see Smith (2004).

⁸<http://www.enoval.eu/page/technologies.php>

Rotor self-noise has both tonal and broadband components. It occurs because of the forces exerted on the fluid (air) from the rotating blades. A subsonic rotor with B_R blades produces tonal noise at harmonics of the blade passing frequency (BPF). The BPF is $B_R\Omega_R$, where Ω_R is the angular speed of the rotor. The tip blade speed can become supersonic, for example at take-off. This causes shocks in the flow around the rotor blade, which then produces tonal noise at non-integer multiples of the BPF due to blade-to-blade differences between the shocks. This is generally referred to as multiple pure tone noise or “buzz saw” noise. However, this is largely controlled through the use of acoustic liners and changing the geometry of the rotor blades. We show the comparison between the subsonic and supersonic frequency spectra in [Figure 1.6](#). We also see that the underlying broadband component of rotor self-noise is significant.



(a) Noise at subsonic speed. (b) Noise at supersonic speed.

Figure 1.6: Rotor self-noise at subsonic and supersonic blade speeds.

Rotor-stator interaction noise also has both broadband and tonal elements, and is the dominant broadband and tonal source of noise. The purpose of the stators (or outlet guide vanes) is to straighten the swirling flow, but they do so at the expense of creating noise. In [Figure 1.3](#) we see there are usually a number of stators, with each stator generally having more blades than the rotor. The rotor wake is the sum of a uniform rotating flow plus a turbulent wake from each rotor blade, with a typical wake evolution shown in [Cooper and Peake \(2005, Figure 2\)](#). The turbulent wake from the rotor then interacts with the stators that block the wake, producing broadband noise. There is also tonal noise produced at harmonics of the BPF. The rotor-stator interaction can be controlled by using the theory of [Tyler and Sofrin \(1962\)](#). By tuning the turbofan with different combinations of rotor and stator blades we can control the tonal noise ([Rienstra and Hirschberg, 2003](#)). In an open-rotor there is a similar effect due to the wake of the first rotor interacting with the contra-rotating second rotor (rotor-rotor interaction), and the interaction is louder than the rotor-stator interaction due to the increased speed difference.

The rotor casing boundary-layer interaction is a broadband source of noise, and arises because there is only a very small clearance between the casing and the tips of the rotor blades. The presence of a turbulent boundary layer at the casing outer wall produces the noise, but a careful design of the casing all but alleviates this noise source ([Peake and Parry, 2012](#)). A final source of tonal noise for turbofans is droop-fan interaction ([Peake and Parry, 2012](#)). Geometric considerations such as ground clearance dictate that in some designs, the engine intake is not axisymmetric and is squashed at the top or bottom. This lack of

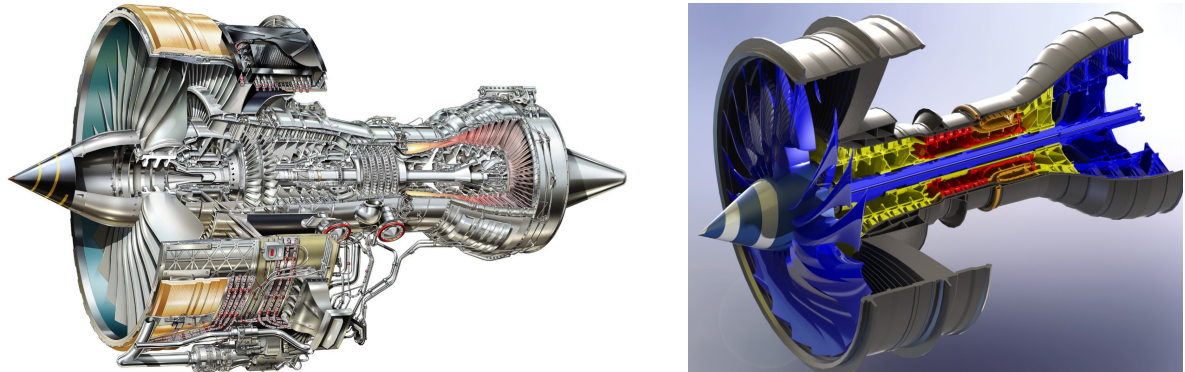
symmetry causes the tonal noise.

In an open-rotor there are new sources to deal with in addition to rotor self-noise and rotor-rotor interaction. The main new source is due to installation effects from the lack of engine casing. Broadband noise is produced from the rotor wake interacting with the wings, fuselage or pylons (structural supports such as in Figure 1.1b). New technologies such as trailing-edge blowing reduce pylon noise. The graph in Peake and Parry (2012, Section 7.2) shows that with blowing technology implemented, the pylon effects are minimal. In addition to rotor-rotor interaction there is a similar source of tip-vortex-interaction which is described in Peake and Parry (2012).

1.2 Mathematically modelling turbofan aeroengines and aerofoils

1.2.1 Modelling a turbofan aeroengine

Next, we consider how to mathematically model a turbofan aeroengine, such as the Rolls-Royce Trent 700 in Figure 1.7a. Figure 1.7b shows a model of a Rolls-Royce Trent 1000 that can be used in computational fluid dynamics (CFD) to model the airflow through the aeroengine.



(a) Rolls-Royce Trent 700.⁹

(b) Rolls-Royce Trent 1000.¹⁰

Figure 1.7: Models of turbofan aeroengines.

Our aeroengine model is considerably simpler, and is an infinite duct, with the air flowing between two cylinders. This is a suitable approximation for considering rotor self-interaction and rotor-stator interaction. In Figure 1.8a we see the cylindrical coordinate system, with x the axial coordinate, r the radial coordinate and θ the azimuthal coordinate.

We let \underline{u} , \underline{v} , and \underline{w} be the velocities in the x , r and θ directions respectively. We refer to the velocity in the x direction, \underline{u} , as the **shear**, and the velocity in the θ direction, \underline{w} , as the **swirl**. We split the inviscid total flow (underlined) of air into a base flow (subscript 0)

⁹<http://tinyurl.com/RRTrent700>

¹⁰<https://grabcad.com/library/trent-1000-high-bypass-turbofan>

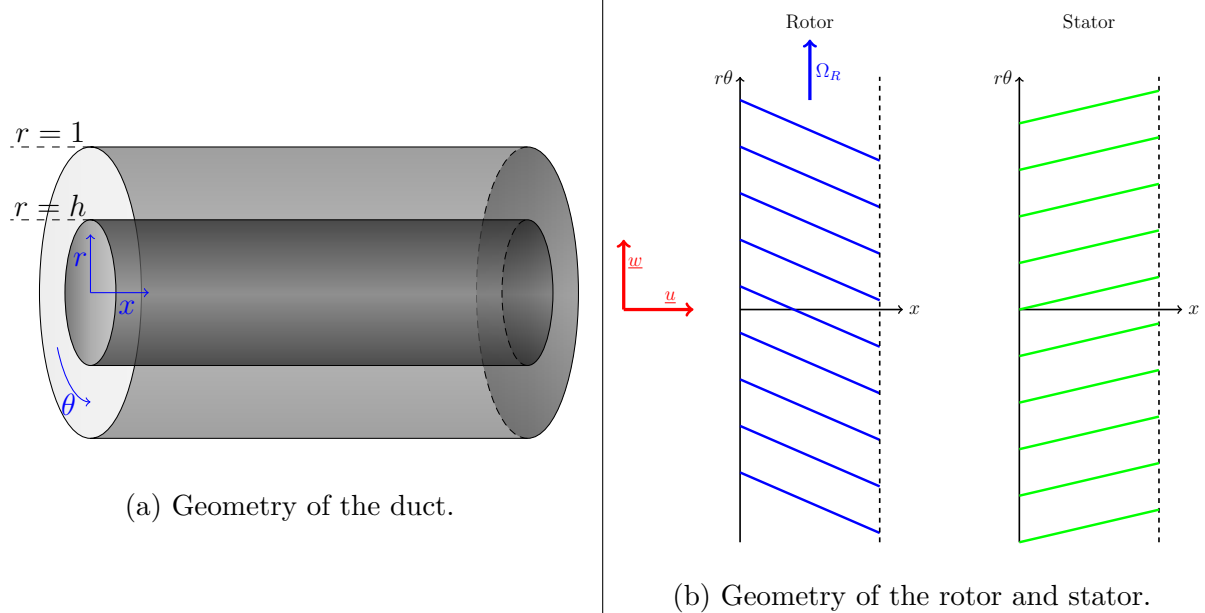


Figure 1.8: Geometry of the duct, rotor and stator.

plus some small perturbations, so we have

$$(\underline{u}, \underline{v}, \underline{w}, \underline{\rho}, \underline{p}) = (u_0, v_0, w_0, \rho_0, p_0) + (u, v, w, \rho, p), \quad (1.2.1)$$

where $\underline{u} = (\underline{u}, \underline{v}, \underline{w})$ is the total velocity of the air, $\underline{\rho}$ is the total density and \underline{p} the total pressure.

Non-dimensionalisation

We use \ddagger to denote quantities with dimension. Let the inner and outer duct walls be given by $r^\ddagger = h^\ddagger$ and $r^\ddagger = d^\ddagger$ respectively. We non-dimensionalise all distances by d^\ddagger , so that the inner wall lies at $r = h := h^\ddagger/d^\ddagger$ and the outer wall at $r = 1$. We non-dimensionalise all velocities by the speed of sound at $r = 1$, $c_0^\ddagger(1)$. Finally, we non-dimensionalise times by $d^\ddagger/c_0^\ddagger(1)$. Thus we have

$$r = \frac{r^\ddagger}{d^\ddagger}, \quad x = \frac{x^\ddagger}{d^\ddagger}, \quad \mathbf{u} = \frac{\mathbf{u}^\ddagger}{c_0^\ddagger(1)}, \quad \mathbf{u}_0 = \frac{\mathbf{u}_0^\ddagger}{c_0^\ddagger(1)}, \quad t = \frac{t^\ddagger c_0^\ddagger(1)}{d^\ddagger}, \quad \omega = \frac{\omega^\ddagger d^\ddagger}{c_0^\ddagger(1)}, \quad (1.2.2)$$

where ω is the frequency. We could also non-dimensionalise the pressures and densities by $p_0^\ddagger(1)$ and $\rho_0^\ddagger(1)$.

Rotor and stator in the duct

To model the rotor blades and the stator we can use simple cascade models such as from [Posson et al. \(2009\)](#). We show a simple geometric model in [Figure 1.8b](#), where we have unwrapped the θ coordinate. The rotor is rotating at an angular speed of Ω_R , while the stator blades are fixed. We consider the blades to be infinitely thin planes, with zero lean or sweep. The blade stagger angle (angle between the blade and x axis) is positive for the

rotor and negative for the stator, which allows the stator to straighten the swirling flow from the rotor.

Acoustic lining in the aeroengine

In the duct, we either consider the walls to be hard or have an acoustic lining. If we consider a duct with hard walls then the boundary condition for the flow is very simple and becomes the no-penetration boundary condition. Thus, the normal velocity must be zero at the walls, or

$$v_0(h) = v_0(1) = v(h) = v(1) = 0, \quad (1.2.3)$$

with the conditions on v_0 coming from the inviscid nature of the flow. Now suppose the duct walls are treated with an acoustic lining to absorb some of the sound energy. To mathematically model the acoustic lining we introduce the impedances $Z_h, Z_1 \in \mathbb{C}$ of the liner at the duct walls. We non-dimensionalise the impedances by $Z_j = Z_j^\ddagger c_0^\ddagger(1)/p_0^\ddagger(1)$. We further assume that the lining is locally reacting, so these impedances are functions of frequency only, and in fact we assume that these impedances are constant. The real part of the impedance corresponds to damping and the imaginary part to reactance. The boundary conditions for the unsteady flow are the standard Ingard-Myers boundary conditions (([Ingard, 1959](#)), ([Myers, 1980](#))), which due to the geometry of the duct are given by

$$\begin{aligned} i\omega v &= \left(-i\omega + u_0 \frac{\partial}{\partial x} + v_0 \frac{\partial}{\partial r} + \frac{w_0}{r} \frac{\partial}{\partial \theta} \right) \left(\frac{p}{Z_h} \right) \text{ on } r = h, \\ -i\omega v &= \left(-i\omega + u_0 \frac{\partial}{\partial x} + v_0 \frac{\partial}{\partial r} + \frac{w_0}{r} \frac{\partial}{\partial \theta} \right) \left(\frac{p}{Z_1} \right) \text{ on } r = 1. \end{aligned} \quad (1.2.4)$$

In the Ingard-Myers boundary condition we assume the time dependence of the flow is of the form $\exp(-i\omega t)$. The impedances we choose are of the form $Z_j = 1 - Z_{\text{imag}}i$, where Z_{imag} is positive, as suggested in [Posson and Peake \(2013a\)](#). A typical choice we use is $Z_j = 1 - 2i$. We always take the imaginary part of the impedance negative because of how we later define our Fourier transforms, so that the lining absorbs energy. We consider $\Re(Z_j) = 1$ a realistic value ([Posson and Peake, 2013a](#)) of impedance after non-dimensionalisation. The case of hard walls corresponds to an impedance of $Z_j = \infty$, for which the boundary conditions in (1.2.4) reduce to (1.2.3).

When using the Ingard-Myers boundary conditions we can (and will) consider a base flow which does not satisfy the no-penetration boundary condition ($v_0 = 0$) or the no-slip boundary conditions ($u_0 = w_0 = 0$). This is because in the derivation of the Ingard-Myers boundary conditions a boundary layer is added to the base flow so that both the no-slip and no-penetration boundary conditions are satisfied.

1.2.2 Modelling stators as aerofoils

To investigate the effect of turbulence hitting a stator, we model a single aerofoil blade as an infinitely thin half plane. To study the effect of serrations we consider a serratation function $\mathcal{F}(z)$ (such as a sinusoidal wave or sawtooth) on the leading edge of the aerofoil. We see this in [Figure 1.9](#). Mathematically, the aerofoil is defined by

$$\{(x, y, z) \in \mathbb{R}^3 \mid z \in \mathbb{R}, \quad \mathcal{F}(z) \cos \alpha < x < \infty, \quad y = x \tan \alpha\}, \quad (1.2.5)$$

where α is the angle of attack of the aerofoil. We introduce serrated cylindrical coordinates

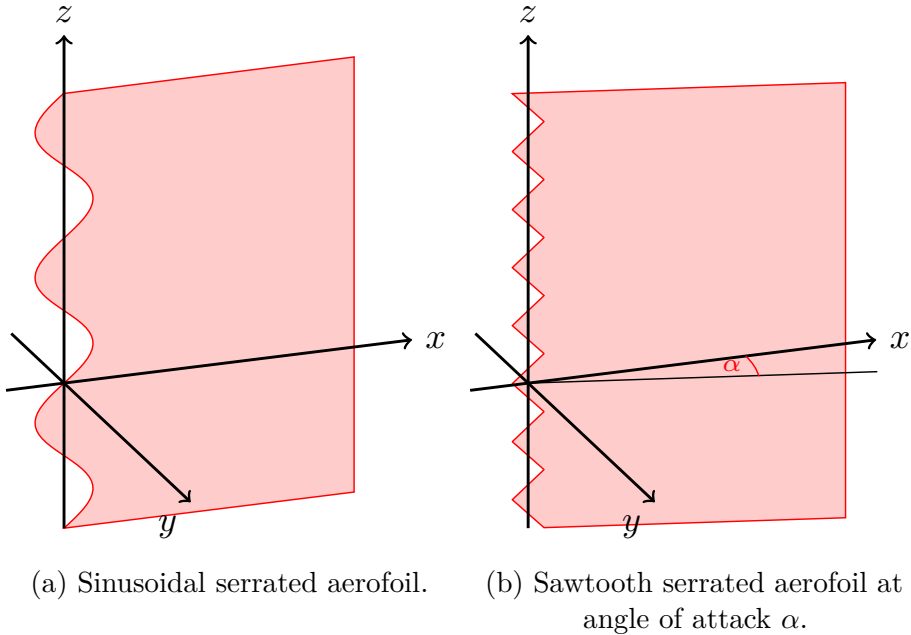


Figure 1.9: Geometry of serrated aerofoils.

of (r^*, θ^*, z^*) , defined by

$$(x, y, z) = (\cos \alpha \mathcal{F}(z^*) - r^* \cos \theta^*, -\sin \alpha \mathcal{F}(z^*) - r^* \sin \theta^*, z^*). \quad (1.2.6)$$

In these modified cylindrical coordinates r^* is the distance to the leading edge of the aerofoil, θ^* is the angle in the x - y plane, and z^* the height. We define θ^* such that the two sides of the aerofoil correspond to $\theta^* = \pm\pi + \alpha$.

When there is no angle of attack we calculate that

$$(x, y, z) = (\mathcal{F}(z^*) - r^* \cos \theta^*, -r^* \sin \theta^*, z^*), \quad (1.2.7)$$

and hence the new coordinates are just cylindrical coordinates in the x - y plane, centred at $(\mathcal{F}(z^*), 0)$. When we consider the flow around the aerofoil, the flow in the x direction is the shear u and the flow in the y direction is the swirl w .

Non-dimensionalisation

We non-dimensionalise all velocities by the (assumed constant) speed of sound c_0^\ddagger , so the non-dimensionalised speed of sound is given by $c_0 = 1$. Since we want to vary the amplitude and wavelength of serrations, and also the distance parameters in the eddy, we are not able to use any of these to non-dimensionalise distances by. Instead, we use the frequency to get a quantity d^\ddagger , where

$$\omega = \frac{\omega^\ddagger d^\ddagger}{c_0^\ddagger}. \quad (1.2.8)$$

We then use d^\ddagger to non-dimensionalise all distances.

1.3 Literature review

The main topic of this thesis is investigating rotor-stator interaction. We do this in two distinct ways. First, we calculate the Green's function for pressure in a turbofan duct with swirling mean flow. Second, we investigate the effect of turbulence hitting an isolated stator blade in [Chapter 6](#).

The Green's function does not directly give us the noise from rotor-stator interaction. There are two possible ways of using the Green's function we derive in the thesis. The first is to use an acoustic analogy, which is derived in [Chapter 2](#). On the left-hand side of the acoustic analogy is a differential operator acting on pressure, and we find the Green's function of this operator. The right-hand side of the acoustic analogy gives us the source terms from a rotor and stator. These source terms can be calculated analytically if we assume a very simple geometry of the rotor and stator (such as in [Figure 1.8b](#)), as detailed in [Posson and Peake \(2013b\)](#). Once we calculate the sound source terms, we can calculate the pressure and hence the noise analytically by calculating the convolution of the source terms and Green's function.

Alternatively, the Green's function can be used in beamforming to analyse noise sources in the aeroengine. This has applications to both rotor-stator interaction and rotor self-interaction. Significant recent progress has been made, such as by [Sijtsma \(2006\)](#), and beamforming is now one of the major processing tools used to analyse microphone array data in aeroengine noise tests. However, until now the Green's function used in the technique has been relatively simple so far, with the most complicated Green's function only assuming radial, piecewise constant shear flow in the duct ([Sijtsma, 2012](#)). In realistic industrial problems, we need to consider swirling flow, and not using an appropriate Green's function can lead to spurious and inaccurate results from beamforming.

In [Chapter 6](#) we directly compute the pressure (and hence noise) from turbulence hitting an isolated stator blade. This enables us to see the effect of serrations on a single blade, and we show that it is always possible to reduce the noise by choosing a serrated aerofoil, but the optimum choice depends on the turbulence. Although we only consider a very idealised blade such as those in [Figure 1.9](#), we could use cascade models such as those in

[Posson et al. \(2009\)](#) to calculate the effect of turbulence hitting a whole stator instead of a single blade. Also, we could apply the results of [Chapter 6](#) to other aerofoils, such as the aircraft wings to understand and reduce the noise from the airframe.

Chapter 2

[Lighthill \(1952\)](#) famously derived the first acoustic analogy by rearranging the Navier–Stokes equations into a single equation for the density perturbation ρ . The analogy was derived for a medium at rest, with the left-hand side the wave operator acting on the density perturbation and the right-hand side the other terms such as pressure and velocity. The exact rearrangement is given by

$$\frac{\partial^2 \rho}{\partial t^2} - c_0^2 \Delta \rho = \frac{\partial^2 T_{jl}}{\partial x_j \partial x_l}, \quad (1.3.1)$$

where

$$T_{jl} = \underline{\rho} \underline{u}_j \underline{u}_l + (p - c_0^2 \rho) \delta_{jl} - \tau_{jl}, \quad (1.3.2)$$

with τ_{jl} the viscous stress tensor, δ_{jl} the Kronecker delta and c_0 the speed of sound of the base flow. The right-hand side is commonly referred to as the (double) divergence of the Lighthill stress tensor T_{jl} and is interpreted as a sound source. For this analogy, the free space Green's function of the wave operator is easily found (see for example [Duffy \(2001\)](#)) and approximations exist to calculate the source terms on the right-hand side such as those in [Colonius and Lele \(2004\)](#).

Lighthill's analogy has been extended in a number of ways. These include considering moving surfaces in the flow, considering moving media and looking at different variables on the left-hand side.

[Curle \(1955\)](#) and [Ffowcs Williams and Hawkings \(1969\)](#) addressed this first extension. Curle considered solid static surfaces, while Ffowcs Williams and Hawkings generalised this further to account for arbitrary, moving impermeable or permeable surfaces. The approach by [Ffowcs Williams and Hawkings \(1969\)](#) uses the theory of what is now known as generalised functions (see [Section 1.4.1](#)), which allows clear identification of the source terms as monopole, dipole or quadrupole sources.

By considering non-zero base flows, we can extend the acoustic analogy to moving media. [Lilley \(1974\)](#) extended Lighthill's analogy to account for shear flow. On the left-hand side of Lilley's analogy is a third order, non-linear operator acting on the logarithm of the pressure. This non-linear operator is often approximated by the linear Pridmore-Brown operator ([Goldstein, 2001](#)), although this makes the source terms on the right-hand side very complicated. Additionally, Goldstein showed that for small fluctuations we can replace the logarithm of pressure by just pressure. The exact source terms on the right-hand side of Lilley's analogy with the Pridmore-Brown operator are given in [Colonius et al. \(1997\)](#), which also gives a simpler approximate form of the source terms, based on the work in

Goldstein (1984).

Other extensions consider the acoustic analogy acting on different variables. For example, Goldstein (2001) considered the variable $(p/p_0)^{(1/\gamma)} - 1$, where $\gamma = 1.4$ for air. Morfey and Wright (2007) also considered several different pressure related variables. Each different formulation of their analogy is suited to a particular type of flow, for example the acoustic analogy acting on the pressure related variable from Morfey and Wright (2007) is useful when the flow is being heated. The analogy by Morfey and Wright also deals with moving surfaces and a moving medium.

In Posson and Peake (2013b) an acoustic analogy is developed with a moving medium (with shear and swirl) and moving surfaces in an infinite duct. The acoustic analogy is a sixth order linear operator acting on the pressure perturbation, which is obtained from rearranging the Euler equations. In their own words, they define it as a “generalisation of Ffowcs Williams-Hawkings’s acoustic analogy to swirling mean flow with duct walls”.

In Chapter 2 we extend the acoustic analogy from Posson and Peake (2013b) to a swirling, non-isentropic base flow, so the base flow entropy varies. This necessitates including the energy equation in the derivation of the acoustic analogy.

Chapter 3

In Chapter 3 we find the Green’s function for the acoustic analogy derived in Chapter 2. We do this both numerically and analytically using high-frequency asymptotics and the WKB method (see Appendix A.1). Our main interest is the analytic Green’s function, which we compare to numerical results. The Green’s function we calculate applies for flow with arbitrary shear and swirl in a lined, infinite duct. The method we use to calculate the Green’s function requires us to first calculate the eigenmodes of the flow (see Section 1.4.3), which we do by finding an asymptotic dispersion relation which these eigenmodes satisfy.

There are two compelling reasons for calculating the Green’s function analytically. First, it allows us to better understand the behaviour of the Green’s function by writing it in terms of elementary functions. Second, the asymptotic method offers us some speed advantages compared to computing the numerical Green function. However, both of these advantages are tarnished somewhat by the fact that we have to currently solve the asymptotic dispersion relation for the eigenmodes numerically, and often need to use the numerical eigenmodes as a starting guess to find the asymptotic eigenmodes.

When calculating the Green’s function from the acoustic analogy we should choose a Green’s function tailored for the geometry. For example, for flow in a duct, cylinder or between two walls our Green’s function should have appropriate no-penetration and no-slip boundary conditions. Wundrow and Khavaran (2004) consider a high-frequency, free-field asymptotic Green’s function in the case of no swirl, but since the Green’s function is not tailored to the duct, it is not very relevant. In Cooper and Peake (2005) and Heaton and Peake (2005) the eigenmodes and eigenfunctions for swirling flow in a hard-walled infinite duct were calculated asymptotically, using the WKB method. In both papers they show we

can get turning points in the WKB method, corresponding physically to caustics ([Cooper and Peake, 2005](#), Figure 10). [Heaton and Peake \(2005\)](#) use the uniformly-valid Langer solution for the eigenfunctions, which we will also use.

In [Vilenski and Rienstra \(2007a,b\)](#) a lined infinite duct is considered, but for no swirl. They only seek the eigenmodes and eigenfunctions of the resulting Pridmore–Brown ([Pridmore-Brown, 1958](#)) differential equation, and not the Green’s function. They compare numerical and asymptotic results for only a couple of simple cases, and do not elaborate too much on their actual method for calculating the asymptotic eigenmodes. Instead, they focus on the trajectories of the asymptotic eigenmodes as they vary the impedance of the lining. In [Posson and Peake \(2012\)](#) and [Posson and Peake \(2013b\)](#) the sixth order acoustic analogy was derived and the eigenmodes and Green’s functions were calculated numerically. A base flow with swirl flow and constant entropy was considered in a hard-walled infinite duct. In [Posson and Peake \(2013a\)](#) the results were extended to an infinite duct with acoustic lining.

There has also been research into the correct boundary conditions to use in a lined duct. Although the Ingard-Myers boundary conditions are often used, recent work by [Brambley \(2011\)](#) and [Khamis and Brambley \(2016\)](#) showed the Ingard-Myers boundary condition is not well-posed and does not always model the physics correctly, leading to an inaccurate boundary condition. However, the new proposed boundary condition involves integral terms and is harder to work with, so we only consider the Ingard-Myers boundary condition.

We also consider the Green’s function in the case of variable entropy, which requires the new acoustic analogy from [Chapter 2](#). Relatively little work has been carried out on the effect of entropy on the eigenmodes and Green’s function, although [Tam and Auriault \(1998\)](#) considered it. They calculate eigenmodes and a Green’s function in the case of simple swirling flow in an infinite hard-walled duct, and their choice of base flow density ensured the entropy of the base flow varied. We instead specify the base flow entropy, and calculate the density from this, which is the method used in [Cooper \(2006\)](#). We use the base flow entropy from [Cooper \(2006\)](#), although it is easy to consider different forms.

Chapter 4

In [Chapter 3](#) we calculate the eigenmodes of the flow, but we are unable to calculate some of them (the hydrodynamic modes - see [Section 1.4.3](#)) using our high-frequency asymptotics. In [Chapter 4](#) we predict the hydrodynamic modes asymptotically by using a different method. We numerically calculate these modes for a variety of different base flows, some of which have varying entropy, and compare to the asymptotic results. We conclude that to accurately calculate all of the hydrodynamic modes for a particular base flow we need to numerically calculate at least some of them.

The hydrodynamic modes were first shown to exist by [Kerrebrock \(1977\)](#), and were not just numerical errors. It was shown that there are infinitely many of them when we consider swirling mean flow by [Golubev and Atassi \(1998\)](#), who were among the first to study the asymptotic behaviour of these modes. A further numerical study of the modes

was performed by [Nijboer \(2001\)](#). The first full asymptotic treatment of the hydrodynamic modes was done by [Heaton and Peake \(2006\)](#), who showed three possible asymptotic regimes of the hydrodynamic modes, depending on the flow parameters. It was shown that the modes could accumulate either exponentially or algebraically, with the latter splitting into two cases, on the real line and in the complex plane. Heaton and Peake's work corrected several issues with earlier work such as the use of a thin duct assumption in [Golubev and Atassi \(1998\)](#).

We extend the work from [Heaton and Peake \(2006\)](#) to include a base flow with varying entropy, and correct a small mistake in [Heaton and Peake \(2006\)](#), although the main results are unaffected. We also show that for some base flows, the hydrodynamic modes bifurcate.

Chapter 5

In [Chapter 5](#) we consider the effect of the acoustic lining varying circumferentially. We derive an asymptotic dispersion relation for the eigenmodes in the high-frequency limit and then numerically solve it. We then use [Chapter 3](#) to calculate the asymptotic Green's function in swirling flow as the impedance of the acoustic lining varies circumferentially.

By considering the impedance to be a discontinuous function, we can model splices in the lining. Splices are needed because the acoustic liner in the aeroengine duct is often made in two (or more) semicircular pieces and then joined together, and this join is not lined. Although both Airbus¹¹ and Rolls-Royce¹² have recently developed zero-splice liners, these are only applicable in the aeroengine inlet and not in the interstage between the rotor and stator. Thus, when studying rotor-stator interaction we need to consider the effect of splices. We can also consider lining when the impedance is a continuous function. For example, liners can be damaged during service, creating harder patches in the lining, so the impedance varies circumferentially. Or, we could deliberately choose the acoustic lining such that the impedance smoothly varies circumferentially to dampen some of the azimuthal modes. We will only consider the case of a smooth impedance function.

The eigenmode problem for splices has previously only been considered analytically for very simple cases of flow in the duct. The case of no flow was first considered by [Fuller \(1984\)](#), while [Campos and Oliveira \(2004\)](#) extended this to uniform shear. However, their boundary condition was incorrect ([Brambley et al., 2012b](#)). In [Brambley et al. \(2012b\)](#) the eigenmodes and Green's function were found for the case of uniform shear flow, exploiting the thinness of the splice to use asymptotic methods. It was shown that the splice only affected eigenmodes with small imaginary parts, while upstream modes are more affected than downstream modes.

A numerical method to calculate the eigenmodes in the spliced duct was given in [Wright](#)

¹¹<http://www.technology-licensing.com/etl/int/en/What-we-offer/Technologies-for-licensing/Green-Technologies/Zero-splice-air-inlet-for-jet-engines.html>

¹²<http://www.rolls-royce.com/sustainability/performance/case-studies/noise-technology.aspx>

(2006), but only considers the case of no flow in the duct. Other numerical methods to consider the effect of splices include the multimodal method, which was developed in Pagneux et al. (1996) and then considered in the case of no flow in Bi et al. (2006) and uniform shear flow in Bi (2008). The effect of damaged splices was studied numerically by Mustafi et al. (2014).

Chapter 6

In Chapter 6 we consider flow-blade interaction in the context of the turbulent wake of the rotor hitting a single aerofoil, a stator blade. Several analytical models have been developed for the interaction of turbulence with an aerofoil, such as the theories of Amiet (1976) and Howe (1978). Both theories involve considering only the trailing edge noise from a semi-infinite aerofoil and using a Green's function of the half plane. Howe's model assumed that the flow was at a low Mach number and the turbulence was frozen and didn't interact with the trailing edge. Amiet's model is valid for all subsonic flows, and differs from Howe's in how the turbulence interacts with the aerofoil. Howe extended his theory to both sinusoidal (Howe, 1991a) and sawtooth (Howe, 1991b) serrations, and showed that serrations reduce the noise. According to his theory, reducing the wavelength of the serrations (and hence making them less shallow) reduced the noise. However, his Green's function was only valid for shallow serrations. Howe also extended his theory to aerofoils with a finite chord (Howe, 2001). Roger and Moreau (2005) extended Amiet's model in two ways. Firstly, they considered three dimensions and secondly they included the effect of back-scattering.

One inspiration for looking at serrations comes from nature, more precisely, a whale's fin. In Figure 1.10a we see a whale fin has both a leading and a trailing edge serration, and also they are different. However, the whale's fin is shaped like this for hydrodynamic and



Figure 1.10: A whale fin and a whale inspired blade.

efficiency reasons, rather than to reduce the noise. A company called Whalepower¹⁴ has already begun to use leading edge serrations (or as they call it, the “tubercle effect”) to develop quieter wind turbines and improve the efficiency of fans. We see an example of an early prototype they made in Figure 1.10b.

There have been a number of recent experimental and numerical studies on the effect of the serrations. A recent CFD study from Haeri et al. (2014) showed numerically that leading

¹³<http://www.asknature.org/strategy/3f2fb504a0cd000eae85d5dcc4915dd4#.VMu3TK1tPUY>

¹⁴<http://www.whalepowercorporation.com/>

edge serrations reduce aerofoil noise. Additionally, experimental work by Gruber (2012), Gruber et al. (2013) and Narayanan et al. (2014) further validated the theory that leading edge serrations can reduce aerofoil noise by a significant amount. In particular, Gruber (2012) showed that Howe's model over-predicted the sound reduction from serrations, due to the assumption of frozen turbulence. However, the Green's function from Howe's method is only valid for shallow serrations, which is not the case for the serrations in Gruber (2012, Figure 4.4).

We use the Green's function from Howe's analytical model and the model of turbulence from Haeri et al. (2014) to investigate the effect of turbulent flow interacting with an aerofoil with a sinusoidal serrated leading edge. We show it is possible to reduce the noise by using a serrated leading edge, but it is hard to predict the correct choice of serration to minimise the noise.

1.4 Mathematical techniques

In this section we review some of the mathematical techniques that are commonly used throughout this thesis. We give some additional techniques in Appendix A. Many of these techniques are covered by undergraduate courses or first year graduate level courses.

1.4.1 Generalised functions

First, we consider the theory of generalised functions or distributions. This is because we want to differentiate functions which are not differentiable in the classical sense. Most of the content in this section is based on Crighton et al. (1992) and Farassat (1996). Given a locally integrable function $f \in L^1_{\text{loc}}(\mathbb{R})$ and a test function $\phi_c \in C_c^\infty(\mathbb{R})$, we define the generalised function F as

$$F[\phi_c] = \int_{-\infty}^{\infty} f(x)\phi_c(x)dx. \quad (1.4.1)$$

We introduce the notions of the Dirac delta function $\delta(x)$ and Heaviside function $H(x)$ through the definitions

$$\delta[\phi_c] = \int_{-\infty}^{\infty} \delta(x)\phi_c(x)dx = \phi_c(0) \text{ and } H[\phi_c] = \int_{-\infty}^{\infty} H(x)\phi_c(x)dx = \int_0^{\infty} \phi_c(x)dx. \quad (1.4.2)$$

We define the derivative of F to be the generalised function F' that satisfies

$$F'[\phi_c] = -F[\phi'_c] \quad (1.4.3)$$

for all test function $\phi_c \in C_c^\infty(\mathbb{R})$. We justify this formula heuristically by using integration by parts. If there is a locally integrable function g such that $F'[\phi_c] = \int_{-\infty}^{\infty} g(x)\phi_c(x)dx$ for all test functions $\phi_c \in C_c^\infty$, then we say that f has generalised derivative g , which we write as $\overline{f}'(x) = g(x)$. In this sense, $\overline{H}'(x) = \delta(x)$.

We now consider a function $\varphi_1 \in L^1_{\text{loc}}(\mathbb{R})$, which is piecewise smooth apart from a discontinuity at x_0 . If we let $[\varphi_1]_{x_0-}^{x_0+} := \varphi_1(x_0+) - \varphi_1(x_0-)$ be the jump that φ_1 makes at the discontinuity, then it is simple to show that

$$\overline{\varphi'_1}(x) = \varphi'_1(x) + [\varphi_1]_{x_0-}^{x_0+} \delta(x - x_0). \quad (1.4.4)$$

We extend this result to three dimensions, where the discontinuity is at a surface described by $f_s(x) = 0$, which gives

$$\frac{\partial \varphi_1}{\partial x_j} = \frac{\partial \varphi_1}{\partial x_j} + [\varphi_1]_{f_s=0-}^{f_s=0+} \frac{\partial f_s}{\partial x_j} \delta(f_s). \quad (1.4.5)$$

We could calculate the generalised gradient $\overline{\nabla}\varphi_1$, generalised divergence $\overline{\nabla} \cdot \boldsymbol{\varphi}_1$ and generalised curl $\overline{\nabla} \times \boldsymbol{\varphi}_1$ in a similar manner (Farassat, 1996).

Next, consider a surface defined by $f_s(\mathbf{x}, t) = 0$, and define

$$\nabla f_s(\mathbf{x}, t) = \mathbf{n} \text{ and } \frac{\partial f_s}{\partial t} = -\mathbf{v}^s \cdot \mathbf{n}, \quad (1.4.6)$$

where \mathbf{v}^s is the surface speed. Given functions $\varphi_1(\mathbf{x}, t)$ and $\boldsymbol{\varphi}_1(\mathbf{x}, t)$, we define the generalised functions

$$\widetilde{\varphi}_1(\mathbf{x}, t) := H(f_s)\varphi_1(\mathbf{x}, t) \text{ and } \widetilde{\boldsymbol{\varphi}}_1(\mathbf{x}, t) := H(f_s)\boldsymbol{\varphi}_1(\mathbf{x}, t), \quad (1.4.7)$$

and then the following relations hold (Farassat, 1996):

$$\frac{\partial \widetilde{\varphi}_1}{\partial t} = H(f_s) \frac{\partial \varphi_1}{\partial t} - [(\mathbf{v}^s \cdot \mathbf{n})\varphi_1] \delta(f_s), \quad (1.4.8)$$

$$\frac{\partial \widetilde{\varphi}_1}{\partial x_j} = H(f_s) \frac{\partial \varphi_1}{\partial x_j} + n_j \varphi_1 \delta(f_s), \quad (1.4.9)$$

$$\overline{\nabla} \cdot \widetilde{\boldsymbol{\varphi}}_1 = H(f_s)(\overline{\nabla} \cdot \boldsymbol{\varphi}_1) + [\boldsymbol{\varphi}_1 \cdot \mathbf{n}] \delta(f_s), \quad (1.4.10)$$

and

$$\overline{\nabla} \widetilde{\varphi}_1 = H(f_s) \overline{\nabla} \varphi_1 + [\varphi_1 \mathbf{n}] \delta(f_s). \quad (1.4.11)$$

From these definitions we see that

$$\frac{\partial}{\partial x_j} (\widetilde{\varphi}_1 + \widetilde{\psi}_1) = \frac{\partial \widetilde{\varphi}_1}{\partial x_j} + \frac{\partial \widetilde{\psi}_1}{\partial x_j}. \quad (1.4.12)$$

Additionally,

$$\frac{\partial}{\partial x_j} (\widetilde{\varphi}_1 \widetilde{\psi}_1) = \widetilde{\varphi}_1 \frac{\partial \widetilde{\psi}_1}{\partial x_j} + \widetilde{\psi}_1 \frac{\partial \widetilde{\varphi}_1}{\partial x_j} \quad (1.4.13)$$

if ψ_1 is independent of x_j . There is also a general product rule for differentiating the product of a smooth function f and a generalised function φ_1 (Grubb, 2009), which is given by

$$\frac{\bar{\partial}}{\partial x_j}(f\varphi_1) = f \frac{\bar{\partial}\varphi_1}{\partial x_j} + \varphi_1 \frac{\partial f}{\partial x_j}, \quad (1.4.14)$$

while it is clear from (1.4.8) that

$$\frac{\bar{\partial}}{\partial x_j}(\widetilde{\psi_1\varphi_1}) = \psi_1 \frac{\bar{\partial}}{\partial x_j}\widetilde{\varphi_1} + \varphi_1 \frac{\bar{\partial}}{\partial x_j}\widetilde{\psi_1} - \psi_1\varphi_1 n_j \delta(f_s). \quad (1.4.15)$$

We can also exchange the order of derivatives, which follows at once from (1.4.3) and the smoothness of test functions, so

$$\frac{\bar{\partial}}{\partial x_l} \left[\frac{\bar{\partial}}{\partial x_j} \widetilde{\varphi_1} \right] = \frac{\bar{\partial}}{\partial x_j} \left[\frac{\bar{\partial}}{\partial x_l} \widetilde{\varphi_1} \right]. \quad (1.4.16)$$

1.4.2 Euler equations

Let us next consider the motion of an inviscid fluid, which is described by the Euler equations. The Euler equations are a particular case of the Navier–Stokes equations when the viscosity is zero. Let \underline{u} be the total velocity of the fluid, $\underline{\rho}$ the total density of the fluid, \underline{p} the total pressure of the fluid and \underline{e} the total internal energy per unit mass of the fluid. The Euler equations are given by

$$\frac{\partial \underline{\rho}}{\partial t} + \nabla \cdot (\underline{\rho}\underline{u}) = 0, \quad (1.4.17)$$

$$\frac{\partial}{\partial t}(\underline{\rho}\underline{u}) + (\nabla(\underline{u} \otimes \underline{\rho}\underline{u})) + \nabla\underline{p} = 0, \quad (1.4.18)$$

$$\frac{\partial}{\partial t}(\underline{\rho}\underline{e}) + \nabla \cdot (\underline{\rho}\underline{e}\underline{u}) + \underline{p}(\nabla \cdot \underline{u}) = 0. \quad (1.4.19)$$

The first equation comes from conservation of mass, and the second from conservation of momentum. The third equation is conservation of energy. They are derived from first principles in [Chapman \(2000\)](#). In the conservation of momentum equation \otimes is the tensor product, and we write the equation in a more convenient way as

$$\underline{\rho} \left(\frac{\partial \underline{u}}{\partial t} + \underline{u} \cdot \nabla \underline{u} \right) + \nabla \underline{p} = 0, \quad (1.4.20)$$

after using the conservation of mass equation. We can write the energy equation in many different ways. For example, if \underline{s} is the total entropy of the fluid then the energy equation becomes

$$\frac{\partial \underline{s}}{\partial t} + \underline{u} \cdot \nabla \underline{s} = 0. \quad (1.4.21)$$

Whatever form of the energy equation we choose, there are only five equations but six variables. To close the system we need extra constitutive equations. This means we need to make some more assumptions about our fluid. We assume that the fluid is a perfect gas to make the constitutive equations relatively simple. We introduce two equations of state

from Chapman (2000). One equation of state is the ideal gas law, which is given by

$$\underline{p} = R\underline{\rho}\underline{T}, \quad (1.4.22)$$

where \underline{T} is the absolute temperature, c_p is the specific heat capacity at constant pressure, c_v is the specific heat capacity at constant volume and $R = c_p - c_v$. We also define the ratio of specific heat capacities as $\gamma = c_p/c_v$. We have introduced another variable, the temperature \underline{T} , so we now have seven variables but only six equations. To rectify this, we need another equation of state, the perfect gas law. This is given by

$$\underline{e} = c_v\underline{T}. \quad (1.4.23)$$

The perfect gas law also assumes c_p and c_v are constants. Typical values¹⁵ for air at room temperature are $c_p = 1.005$ and $c_v = 0.718$, giving $\gamma = 1.4$. From the two equations of state we calculate that

$$\underline{\rho}\underline{e} = \frac{\underline{p}c_v}{R}, \quad (1.4.24)$$

which we substitute into the energy equation (1.4.19) to simplify it to

$$\frac{\partial \underline{p}}{\partial t} + \underline{\mathbf{u}} \cdot \nabla \underline{p} + \gamma \underline{p}(\nabla \cdot \underline{\mathbf{u}}) = 0. \quad (1.4.25)$$

Different equation of state

Instead of using the perfect gas law in (1.4.23), we could use the equation of state

$$\underline{s} = c_v \log \left(\frac{\gamma \underline{p}}{\underline{\rho}^\gamma} \right), \quad (1.4.26)$$

which is given in Lilley (1974); Chapman (2000); Goldstein (2001). There are many different forms of the relation (1.4.26), for example we could define

$$\underline{s}^* = c_p \log \left(\frac{\underline{p}^{1/\gamma}}{\underline{\rho}} \right) \quad (1.4.27)$$

and then \underline{s} and \underline{s}^* differ by a constant, with $\underline{s} = c_v \log \gamma + \underline{s}^*$. From (1.4.26) and (1.4.21) we derive a relationship between pressure and density, which is given by

$$\frac{\partial \underline{p}}{\partial t} + \underline{\mathbf{u}} \cdot \nabla \underline{p} = \frac{\gamma \underline{p}}{\underline{\rho}} \left(\frac{\partial \underline{\rho}}{\partial t} + \underline{\mathbf{u}} \cdot \nabla \underline{\rho} \right). \quad (1.4.28)$$

Using the conservation of mass equation, it is easy to see that we can derive (1.4.25) from (1.4.28).

¹⁵https://www.ohio.edu/mechanical/thermo/property_tables/gas/idealGas.html

Speed of sound

We calculate the speed of sound, \underline{c} , by using the Newton-Laplace equation

$$\underline{c} = \sqrt{\frac{K}{\rho}}, \quad (1.4.29)$$

where K is the isentropic bulk modulus of the material and ρ the density. For an ideal gas the bulk modulus is related to the pressure, with $K = \gamma p$, and thus we get the equation

$$\underline{c}^2 = \frac{\gamma p}{\rho}. \quad (1.4.30)$$

We find that it is more convenient to use the speed of sound than the density in the Euler equations in the rest of this thesis.

Cylindrical coordinates

When we consider cylindrical coordinates and use the geometry in [Figure 1.8a](#), equations [\(1.4.17\)](#), [\(1.4.20\)](#) and [\(1.4.25\)](#) become

$$\frac{\partial \rho}{\partial t} + \frac{1}{r} \frac{\partial}{\partial r}(r \rho v) + \frac{1}{r} \frac{\partial}{\partial \theta}(\rho w) + \frac{\partial}{\partial x}(\rho u) = 0, \quad (1.4.31)$$

$$\rho \left(\frac{\partial u}{\partial t} + v \frac{\partial u}{\partial r} + \frac{w}{r} \frac{\partial u}{\partial \theta} + u \frac{\partial u}{\partial x} \right) = - \frac{\partial p}{\partial x}, \quad (1.4.32)$$

$$\rho \left(\frac{\partial v}{\partial t} + v \frac{\partial v}{\partial r} + \frac{w}{r} \frac{\partial v}{\partial \theta} + u \frac{\partial v}{\partial x} - \frac{w^2}{r} \right) = - \frac{\partial p}{\partial r}, \quad (1.4.33)$$

$$\rho \left(\frac{\partial w}{\partial t} + v \frac{\partial w}{\partial r} + \frac{w}{r} \frac{\partial w}{\partial \theta} + u \frac{\partial w}{\partial x} + \frac{vw}{r} \right) = - \frac{1}{r} \frac{\partial p}{\partial \theta}, \quad (1.4.34)$$

$$\frac{\partial p}{\partial t} + v \frac{\partial p}{\partial r} + \frac{w}{r} \frac{\partial p}{\partial \theta} + u \frac{\partial p}{\partial x} + \gamma p \left(\frac{1}{r} \frac{\partial}{\partial r}(rv) + \frac{1}{r} \frac{\partial w}{\partial \theta} + \frac{\partial u}{\partial x} \right) = 0. \quad (1.4.35)$$

The total flow is the sum of a base or mean flow and small perturbations, so

$$(\underline{u}, \underline{v}, \underline{w}, \underline{\rho}, \underline{p}) = (u_0, v_0, w_0, \rho_0, p_0) + (u, v, w, \rho, p). \quad (1.4.36)$$

We linearise the Euler equations about a base flow with $v_0 = 0$ and where u_0 and w_0 only depend on the radial position. Once we specify u_0 and w_0 we can calculate p_0 and ρ_0 since the base flow must satisfy the Euler equations.

We then consider an exact rearrangement of the system of equations [\(1.4.31\)](#) to [\(1.4.35\)](#) such that the left-hand side is a linear operator acting on perturbations and the right-hand side consists of all the non-linear effects. The rearrangement is given by

$$\frac{D_0 \rho}{Dt} + v \frac{d\rho_0}{dr} + \rho_0 (\nabla \cdot \mathbf{u}) = - \nabla \cdot (\rho \mathbf{u}), \quad (1.4.37)$$

$$\rho_0 \left(\frac{D_0 u}{Dt} + v \frac{du_0}{dr} \right) + \frac{\partial p}{\partial x} = -\underline{\rho} \mathbf{u} \cdot \nabla u - \rho \frac{D_0 u}{Dt} - \rho v \frac{du_0}{dr}, \quad (1.4.38)$$

$$\rho_0 \left(\frac{D_0 v}{Dt} - \frac{2w_0 w}{r} \right) - \rho \frac{w_0^2}{r} + \frac{\partial p}{\partial r} = -\underline{\rho} \mathbf{u} \cdot \nabla v - \rho \frac{D_0 v}{Dt} + \frac{2\rho w_0 w}{r} + \underline{\rho} \frac{w^2}{r}, \quad (1.4.39)$$

$$\rho_0 \left(\frac{D_0 w}{Dt} + \frac{v}{r} \frac{d}{dr}(rw_0) \right) + \frac{1}{r} \frac{\partial p}{\partial \theta} = -\underline{\rho} \mathbf{u} \cdot \nabla w - \rho \frac{D_0 w}{Dt} - \rho \frac{v}{r} \frac{d}{dr}(rw_0) - \underline{\rho} \frac{v}{r} \frac{\partial}{\partial r}(rw), \quad (1.4.40)$$

$$\frac{D_0 p}{Dt} + v \frac{\rho_0 w_0^2}{r} + \gamma p_0 (\nabla \cdot \mathbf{u}) = -\mathbf{u} \cdot \nabla p - \gamma p \nabla \cdot \mathbf{u}, \quad (1.4.41)$$

where we use the notation

$$\mathbf{u} = (u, v, w), \quad \nabla = \left(\frac{\partial}{\partial x}, \frac{\partial}{\partial r}, \frac{1}{r} \frac{\partial}{\partial \theta} \right), \quad \nabla \cdot \mathbf{u} = \frac{\partial u}{\partial x} + \frac{1}{r} \frac{\partial}{\partial r}(rv) + \frac{1}{r} \frac{\partial w}{\partial \theta}, \quad (1.4.42)$$

with the material derivative given by

$$\frac{D_0}{Dt} = \frac{\partial}{\partial t} + u_0 \frac{\partial}{\partial x} + \frac{w_0}{r} \frac{\partial}{\partial \theta}. \quad (1.4.43)$$

By setting all non-linear terms to be zero we obtain the linearised Euler equations:

$$\frac{D_0 \rho}{Dt} + v \frac{d\rho_0}{dr} + \rho_0 (\nabla \cdot \mathbf{u}) = 0, \quad (1.4.44)$$

$$\rho_0 \left(\frac{D_0 u}{Dt} + v \frac{du_0}{dr} \right) + \frac{\partial p}{\partial x} = 0, \quad (1.4.45)$$

$$\rho_0 \left(\frac{D_0 v}{Dt} - \frac{2w_0 w}{r} \right) - \rho \frac{w_0^2}{r} + \frac{\partial p}{\partial r} = 0, \quad (1.4.46)$$

$$\rho_0 \left(\frac{D_0 w}{Dt} + \frac{v}{r} \frac{d}{dr}(rw_0) \right) + \frac{1}{r} \frac{\partial p}{\partial \theta} = 0, \quad (1.4.47)$$

$$\frac{D_0 p}{Dt} + v \frac{\rho_0 w_0^2}{r} + \gamma p_0 (\nabla \cdot \mathbf{u}) = 0. \quad (1.4.48)$$

1.4.3 Eigenmodes

Finally, we find the eigenmodes of the linearised Euler equations, where we linearise about a base flow depending only on radial position and where $v_0 = 0$. To do this we Fourier transform equations (1.4.44) to (1.4.48), by introducing the Fourier transform of the variables

$$\{u, v, w, p, \rho\}(r, x, \theta, t) = \int \sum_n \int \{U(r), V(r), W(r), P(r), R(r)\} e^{ikx} dk e^{in\theta} e^{-i\omega t} d\omega. \quad (1.4.49)$$

Alternatively, we could just assume the perturbations are of the form

$$\{u, v, w, p, \rho\}(r, x, \theta, t) = \{U(r), V(r), W(r), P(r), R(r)\} e^{ikx} e^{in\theta} e^{-i\omega t}. \quad (1.4.50)$$

We then combine the Fourier transformed linearised Euler equations into a single, linear second order differential equation for P , which is of the form

$$\mathcal{A}_{n,k,\omega}(r)P''(r) + \mathcal{B}_{n,k,\omega}(r)P'(r) - \mathcal{C}_{n,k,\omega}(r)P(r) = 0. \quad (1.4.51)$$

We show later the exact form of the coefficients. In the case of no swirl ($w_0 = 0$), the equation becomes the well-known Pridmore–Brown equation (Pridmore-Brown, 1958)

$$(\omega - ku_0)P'' + \left[(\omega - ku_0) \left(\frac{1}{r} - \frac{\rho'_0}{\rho_0} \right) + 2ku'_0 \right] P' + (\omega - ku_0) \left(\frac{(\omega - ku_0)^2}{c_0^2} - k^2 - \frac{n^2}{r^2} \right) P = 0. \quad (1.4.52)$$

We also have two homogeneous boundary conditions at the duct walls, which are of the form

$$a_h P(h) + b_h P'(h) = 0 \text{ and } a_1 P(1) + b_1 P'(1), \quad (1.4.53)$$

where we can calculate a_j and b_j from the Ingard-Myers boundary conditions in (1.2.4). We thus have a boundary value problem to solve, and so we can find the eigenmodes and eigenfunctions. We fix ω and n and look for eigenmodes of the axial wavenumber k . These are values of k where we can solve (1.4.51) with both boundary conditions in (1.4.53).

Eigenmodes from the Green's function

Let us suppose we are finding the Green's function of the operator in (1.4.51), so we wish to find G_P which solves

$$\mathcal{A}_{n,k,\omega}(r)G_P''(r, r_0) + \mathcal{B}_{n,k,\omega}(r)G_P'(r, r_0) - \mathcal{C}_{n,k,\omega}(r)G_P(r, r_0) = \delta(r - r_0). \quad (1.4.54)$$

Using Duffy (2001) we write the Green's function as

$$G_P(r, r_0; k) = \frac{1}{J(r_0, k)\mathcal{W}(r, k)} \begin{cases} g_1(r; k)g_2(r_0; k) & r \leq r_0 \\ g_1(r_0; k)g_2(r; k) & r > r_0 \end{cases}, \quad (1.4.55)$$

where $g_1(r; k)$ and $g_2(r; k)$ solve the homogeneous equation and one boundary condition each. We can easily calculate the jump function J , and the Wrońskiian $\mathcal{W}(r, k)$ is given by

$$\mathcal{W}(r, k) = g_1(r; k)g'_2(r; k) - g'_1(r; k)g_2(r; k). \quad (1.4.56)$$

Clearly, the Green's function is no longer valid at values of k such that $\mathcal{W}(r, k) = 0$. At these values of k , $g_1(r; k)$ and $g_2(r; k)$ are linearly dependent, and satisfy (1.4.51) with both boundary conditions in (1.4.53), and hence are eigenmodes of the flow. There is a one-to-one correspondence between finding the eigenmodes of the system (1.4.51) and (1.4.53), and solving $\mathcal{W}(r, k) = 0$ for the differential equation (1.4.54).

Classifying the eigenmodes

Before we classify the eigenmodes we define the critical layer. This is the range of values of k for which the coefficient of the largest derivative in (1.4.51) vanishes at one or more

values of $r \in [h, 1]$, with at least one of the other coefficients non-zero. When the swirl is zero, this corresponds to

$$\inf_{h < r < 1} \frac{\omega}{u_0(r)} \leq k \leq \sup_{h < r < 1} \frac{\omega}{u_0(r)}. \quad (1.4.57)$$

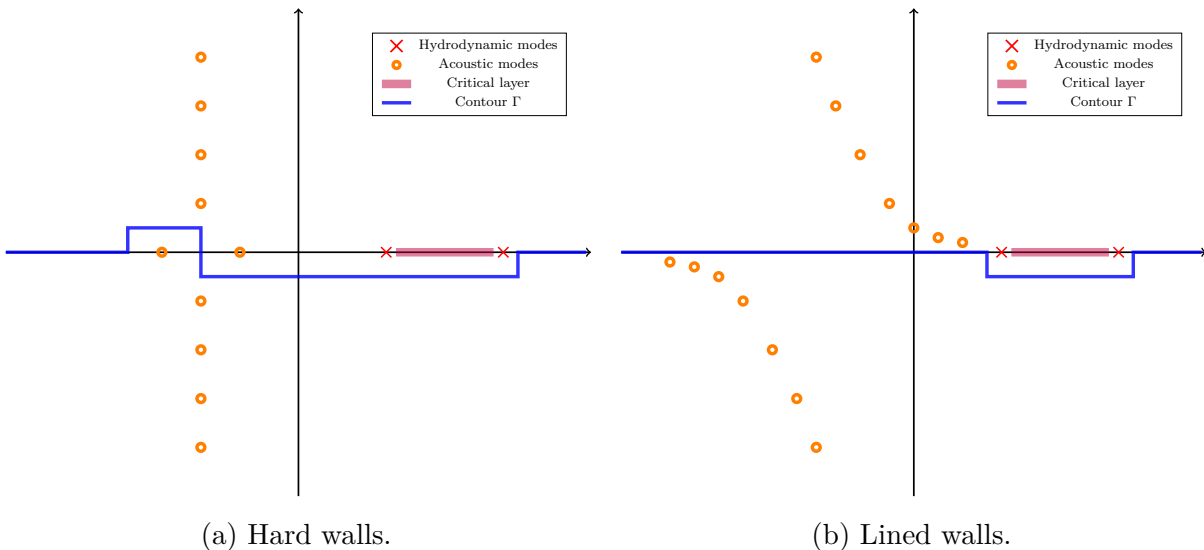
When the swirl is non-zero, the critical layer is instead given by

$$\inf_{h < r < 1} \frac{1}{u_0(r)} \left(\omega - \frac{n w_0(r)}{r} \right) \leq k \leq \sup_{h < r < 1} \frac{1}{u_0(r)} \left(\omega - \frac{n w_0(r)}{r} \right). \quad (1.4.58)$$

The critical layer corresponds to a mathematical singularity caused by our inviscid assumption (Brambley et al., 2011). It can be removed by adding in non-linear terms or viscous terms to the linearised Euler equations.

Eigenmodes are classified as either acoustic or hydrodynamic modes, which form two distinct families. The schematic in Figure 1.11 shows the two families of eigenmodes, for both hard-walled and acoustically lined ducts.

Figure 1.11: Schematic view of eigenmodes in the complex k plane.



Acoustic modes are also commonly referred to as sonic or pressure dominated modes. The acoustic modes are all discrete and lie away from the critical layer. Acoustic modes are further split into upstream or downstream modes and cut-on or cut-off modes. For a hard-walled duct, cut-on modes have zero imaginary part while cut-off modes have non-zero imaginary part. In a lined duct, there are no modes with zero imaginary part, but some modes lie close to the real line and decay less than the other modes. We refer to these modes that are close to the real line as the equivalent of the hard wall cut-on modes.

Upstream and downstream modes for lined walls are easy to classify in most cases, with downstream modes lying in the upper half plane and upstream modes lying in the lower half plane. Upstream and downstream modes are classified for hard walls in two equivalent ways. The traditional way is to introduce a small, positive imaginary part to the frequency ω . This shifts all the eigenmodes by a small amount. The downstream modes now all lie in the upper half plane and the upstream modes lie in the lower half plane. Alternatively, we

could introduce an acoustic lining with a large impedance. The eigenmodes all shift a small amount and then the downstream modes lie in the upper half plane. We note that there is a possible mode instability when we have an acoustically lined duct, which was shown in Brambley and Peake (2006b). If this instability is present then we would have to be more careful when classifying the upstream and downstream modes.

Hydrodynamic modes are also commonly referred to as nearly-convected modes or rotational modes, and they contain most of the unsteady vorticity of the flow. The existence of these modes has often been debated, and Kerrebrock (1977) was one of the first to show that they exist. The modes are all discrete and cluster around the ends of the critical layer, and there are infinitely many of them when we consider swirling flow.

Contour of integration

Once we calculate G_P , the Green's function of the Fourier transform of pressure P , we can find g_p , the Green's function of pressure p . We do this by inverse Fourier transforming G_P . It is clear from the schematic of modes that if we perform the inversion on the real line we run into problems at the critical layer, the hydrodynamic modes and any acoustic modes on the real line, since at these modes $\mathcal{W} = 0$. Furthermore, along the critical layer is a branch cut which we must integrate around and not through. To calculate the inverse Fourier transform of G_P we modify the contour of integration by using the Briggs-Bers procedure, described in Brambley (2009). We again add a small, positive imaginary part to the frequency which shifts all the cut-on downstream modes above the real line and below for the upstream cut-on modes. The hydrodynamic modes and critical layer also shift above the real line. Thus, integrating along the real line now encounters no problems since the Wroński is now non-zero on the real line. As we let the small imaginary part of frequency tend to 0, it is clear that the integration contour Γ must be of the specified form in Figures 1.11a and 1.11b.

Chapter 2

A new acoustic analogy

In this chapter, we derive a new acoustic analogy, based on the work from [Posson and Peake \(2013b\)](#). In [Posson and Peake \(2013b\)](#) the base flow used in the acoustic analogy is homentropic, while we allow the entropy to vary radially in the base flow.

We begin by calculating the base flow for a non-homentropic fluid, which solves the Euler equations. We then derive the acoustic analogy before showing it is very similar to the analogy from [Posson and Peake \(2013b\)](#) when the entropy is constant. The differences arise because we consider the full energy equation, resulting in different source terms. However, when we estimate the source terms to calculate the pressure we only use the loading noise source terms, which are the same for both analogies when the entropy is constant.

2.1 The base flow

The base flow is a solution to equations [\(1.4.17\)](#), [\(1.4.20\)](#) and [\(1.4.25\)](#), which for convenience we restate here:

$$\frac{\partial \rho_0}{\partial t} + \nabla \cdot (\rho_0 \mathbf{u}_0) = 0, \quad (2.1.1)$$

$$\rho_0 \left(\frac{\partial \mathbf{u}_0}{\partial t} + \mathbf{u}_0 \cdot \nabla \mathbf{u}_0 \right) + \nabla p_0 = 0, \quad (2.1.2)$$

$$\frac{\partial p_0}{\partial t} + \mathbf{u}_0 \cdot \nabla p_0 + \gamma p_0 (\nabla \cdot \mathbf{u}_0) = 0. \quad (2.1.3)$$

The base flow entropy s_0 satisfies the constitutive relation

$$s_0 = c_v \log \left(\frac{\gamma p_0}{\rho_0^\gamma} \right), \quad (2.1.4)$$

while the speed of sound c_0 is defined from the Newton-Laplace equation, giving

$$c_0^2 = \frac{\gamma p_0}{\rho_0}. \quad (2.1.5)$$

This gives us seven base flow variables to calculate. Rather than finding the general solution of the Euler equations, we specify the velocity and entropy, and calculate the other variables from (2.1.1) to (2.1.5). We specify that the base flow velocity is of the form

$$(u_0, v_0, w_0) = (U_x(r), 0, U_\theta(r)), \quad (2.1.6)$$

where we have a free choice of $U_x(r)$ and $U_\theta(r)$. CFD calculations¹ suggest that for a swirling flow between the rotor and stator, the amplitude of u_0 and w_0 are similar, while the amplitude of v_0 is around 10–15% of u_0 and w_0 . Thus, setting $v_0 = 0$ should still give realistic results. We assume that the base flow velocity only depends on r to simplify our calculations, but in CFD results the dependence on θ and x is considerably weaker than the dependence on r . We also specify that the base flow entropy only depends on the radial position.

It remains to calculate the pressure, density and speed of sound for the base flow. We choose the pressure so that the Euler equations are satisfied, which essentially comes down to conservation of angular momentum, with

$$p'_0(r) = \frac{\rho_0(r)U_\theta^2(r)}{r} \text{ or } p_0(r) = p_0(1) + \int_1^r \frac{\rho_0(s)U_\theta^2(s)}{s} ds. \quad (2.1.7)$$

To determine c_0 and ρ_0 we first differentiate the two relations in (2.1.4) and (2.1.5), which gives (after using (2.1.7))

$$s'_0(r) = c_p \left[\frac{U_\theta^2(r)}{rc_0^2(r)} - \frac{1}{\rho_0(r)} \frac{d\rho_0}{dr}(r) \right] \quad (2.1.8)$$

and

$$\frac{c_0^{2'}(r)}{c_0^2(r)} = \frac{p'_0(r)}{p_0(r)} - \frac{\rho'_0(r)}{\rho_0(r)}. \quad (2.1.9)$$

Thus we find that

$$\frac{c_0^{2'}(r)}{c_0^2(r)} = \frac{(\gamma-1)U_\theta^2(r)}{rc_0^2(r)} + \frac{1}{c_p} s'_0(r). \quad (2.1.10)$$

We solve this differential equation by using an integrating factor (of $\exp[-s_0(r)/c_p]$), which gives

$$c_0^2(r) = c_0^2(1) \exp \left(\frac{s_0(r) - s_0(1)}{c_p} \right) + (\gamma-1) \exp \left(\frac{s_0(r)}{c_p} \right) \int_1^r \exp \left(-\frac{s_0(s)}{c_p} \right) \frac{U_\theta^2(s)}{s} ds. \quad (2.1.11)$$

From rearranging (2.1.4) we get

$$p_0(r) = \frac{\rho_0^\gamma(r)}{\gamma} \exp \left(\frac{s_0(r)}{c_v} \right), \quad (2.1.12)$$

and substituting this, (2.1.7) and (2.1.10) into (2.1.9) gives a first order differential equation

¹Private communication with Stefano Bianchi, Rolls-Royce

for density:

$$\frac{d}{dr} \left(\rho_0^{\gamma-1}(r) \right) + \rho_0^{\gamma-1}(r) \frac{\gamma-1}{c_p} s'_0(r) = \frac{U_\theta^2(r)}{r} \exp \left(-\frac{s_0(r)}{c_v} \right). \quad (2.1.13)$$

We solve this by again using an integrating factor, this time $\exp((\gamma-1)s_0(r)/c_p)$, and hence we find that

$$\begin{aligned} \rho_0^{\gamma-1}(r) &= \rho_0^{\gamma-1}(1) \exp \left(\frac{\gamma-1}{c_p} [s_0(1) - s_0(r)] \right) \\ &\quad + (\gamma-1) \exp \left(\frac{1-\gamma}{c_p} s_0(r) \right) \int_1^r \exp \left(-\frac{s_0(s)}{c_p} \right) \frac{U_\theta^2(s)}{s} ds. \end{aligned} \quad (2.1.14)$$

Hence, we conclude that

$$\rho_0^{\gamma-1}(r) = c_0^2(r) \exp \left(-\frac{s_0(r)}{c_v} \right) \text{ or } \rho_0(r) = \left[c_0^2(r) \exp \left(-\frac{s_0(r)}{c_v} \right) \right]^{1/(\gamma-1)}. \quad (2.1.15)$$

2.1.1 Simple forms of entropy in the base flow

We consider two different choices of base flow entropy, one from [Cooper \(2006\)](#) and the other is $s_0(r)$ constant.

Logarithmic entropy

[Cooper \(2006\)](#) suggests the base flow has entropy of the form

$$s_0(r) = -\log(r^\beta), \quad (2.1.16)$$

where β is a constant. Using the previous section, we see that the speed of sound satisfies

$$c_0^2(r) = c_0^2(1)r^{-\beta/c_p} + (\gamma-1)r^{-\beta/c_p} \int_1^r s^{\beta/c_p} \frac{U_\theta^2(s)}{s} ds, \quad (2.1.17)$$

and the density satisfies

$$\rho_0^{\gamma-1}(r) = r^{\beta/c_v} c_0^2(r). \quad (2.1.18)$$

Constant entropy

For the homentropic case of [Posson and Peake \(2013b\)](#), $\beta = 0$, and we calculate the speed of sound as

$$c_0^2(r) = c_0^2(1) + (\gamma-1) \int_1^r \frac{U_\theta^2(s)}{s} ds, \quad (2.1.19)$$

while the density satisfies

$$\rho_0^{\gamma-1}(r) = c_0^2(r). \quad (2.1.20)$$

2.2 A new acoustic analogy with entropy

Next, we consider a time-dependent surface $\mathcal{S}_f(t)$, defined by $f_{\mathcal{S}}(\mathbf{x}, t) = 0$ which separates a fluid into a region where the fluid is moving and a region where it is at rest. The surface \mathcal{S}_f represents the blades of a rotor and/or stator, with $f_{\mathcal{S}}(\mathbf{x}, t) = 0$ corresponding to the blade tips and edges. The fluid is at rest inside this surface, and moving outside the surface. Using the convention from [Posson and Peake \(2013b\)](#), we choose $f_{\mathcal{S}}$ such that $f_{\mathcal{S}} < 0$ when the fluid is at rest, $f_{\mathcal{S}} > 0$ when the fluid is moving and $|\nabla f_{\mathcal{S}}| = 1$. We define the normal \mathbf{n} and surface speed $\mathbf{v}^{\mathcal{S}}$ through

$$\nabla f(\mathbf{x}, t) = \mathbf{n} \text{ and } \frac{\partial f}{\partial t} = -\mathbf{v}^{\mathcal{S}} \cdot \mathbf{n}. \quad (2.2.1)$$

2.2.1 Euler equations for generalised functions

Multiplying equations [\(1.4.37\)](#) to [\(1.4.41\)](#) by the Heaviside function $H(f_{\mathcal{S}})$ and using the relations in [Section 1.4.1](#) gives a system of differential equations which act on the distributions $(\tilde{u}, \tilde{v}, \tilde{w}, \tilde{\rho}, \tilde{p})$ with various source terms. These are given by:

$$\frac{\overline{D_0}\tilde{\rho}}{Dt} + \tilde{v} \frac{d\rho_0}{dr} + \rho_0 (\bar{\nabla} \cdot \tilde{\mathbf{u}}) = \mathcal{S}_{\text{mass}} + \mathcal{D}_{\text{mass}}, \quad (2.2.2)$$

$$\rho_0 \left(\frac{\overline{D_0}\tilde{u}}{Dt} + \tilde{v} \frac{dU_x}{dr} \right) + \frac{\bar{\partial}\tilde{p}}{\partial x} = \mathcal{S}_x + \mathcal{D}_x, \quad (2.2.3)$$

$$\rho_0 \left(\frac{\overline{D_0}\tilde{v}}{Dt} - \frac{2U_{\theta}\tilde{w}}{r} \right) - \tilde{\rho} \frac{U_{\theta}^2}{r} + \frac{\bar{\partial}\tilde{p}}{\partial r} = \mathcal{S}_r + \mathcal{D}_r, \quad (2.2.4)$$

$$\rho_0 \left(\frac{\overline{D_0}\tilde{w}}{Dt} + \frac{\tilde{v}}{r} \frac{d}{dr}(rU_{\theta}) \right) + \frac{1}{r} \frac{\bar{\partial}\tilde{p}}{\partial \theta} = \mathcal{S}_{\theta} + \mathcal{D}_{\theta}, \quad (2.2.5)$$

$$\frac{\overline{D_0}\tilde{\rho}}{Dt} + \tilde{v} \frac{\rho_0 U_{\theta}^2}{r} + \gamma p_0 (\bar{\nabla} \cdot \tilde{\mathbf{u}}) = \mathcal{S}_e + \mathcal{D}_e. \quad (2.2.6)$$

The volume sources terms are defined by

$$\mathcal{S}_{\text{mass}} = -\bar{\nabla} \cdot (\tilde{\rho}\tilde{\mathbf{u}}), \quad (2.2.7)$$

$$\mathcal{S} = (\mathcal{S}_x, \mathcal{S}_r, \mathcal{S}_{\theta}) = -(\rho_0 + \tilde{\rho})\tilde{\mathbf{u}} \cdot \bar{\nabla} \tilde{\mathbf{u}} - \tilde{\rho} \frac{\overline{D_0}\tilde{\mathbf{u}}}{Dt} - \tilde{\rho} \mathcal{H}, \quad (2.2.8)$$

and

$$\mathcal{S}_e = -\tilde{\mathbf{u}} \cdot \bar{\nabla} \tilde{p} - \gamma \tilde{p} \bar{\nabla} \cdot \tilde{\mathbf{u}}, \quad (2.2.9)$$

where

$$\mathcal{H} = \left(\tilde{v} \frac{dU_x}{dr}, -\frac{2U_{\theta}\tilde{w}}{r}, \frac{\tilde{v}}{r} \frac{d}{dr}(rU_{\theta}) \right). \quad (2.2.10)$$

The surface source terms are defined by

$$\mathcal{D}_{\text{mass}} = \delta(f_{\mathcal{S}}) \left[\rho (\underline{\mathbf{u}} - \mathbf{v}^{\mathcal{S}}) \cdot \mathbf{n} + \rho_0 (\mathbf{u} \cdot \mathbf{n}) \right], \quad (2.2.11)$$

$$\mathcal{D} = (\mathcal{D}_x, \mathcal{D}_r, \mathcal{D}_\theta) = \delta(f_S)[\underline{\rho} \mathbf{u} (\underline{\mathbf{u}} - \mathbf{v}^S) \cdot \mathbf{n} + p \mathbf{n}], \quad (2.2.12)$$

and

$$\mathcal{D}_e = \delta(f_S) [p (\underline{\mathbf{u}} - \mathbf{v}^S) \cdot \mathbf{n} + \gamma p_0 (\mathbf{u} \cdot \mathbf{n}) + \gamma p (\mathbf{u} \cdot \mathbf{n})], \quad (2.2.13)$$

where $\delta(f_S)$ is the Dirac delta function. To derive these source terms, we assume that the distribution of the product of two smooth functions is equal to the product of the two distributions, for example $\widetilde{\rho u} = \widetilde{\rho} \times \widetilde{u}$. Technically, we cannot multiply distributions together, but the reason for doing so here is that we are only using the distributions to extract the source terms in the analogy.

When the surface $S(t)$ is rigid (impermeable and non-vibrating), then $(\mathbf{u}_0 + \mathbf{u}) \cdot \mathbf{n} = \mathbf{v}^S \cdot \mathbf{n}$ and hence we have

$$(\underline{\mathbf{u}} - \mathbf{v}^S) \cdot \mathbf{n} = 0, \quad (2.2.14)$$

so the surface source terms simplify significantly. For most designs of rotor and stator blades, we can assume that the surface is rigid. In addition, if we have no angle of attack on the blades then we also have

$$(\mathbf{u}_0 - \mathbf{v}^S) \cdot \mathbf{n} = 0, \quad (2.2.15)$$

which further simplifies the source terms. The surface source term \mathcal{D} is related to the loading noise and $\mathcal{D}_{\text{mass}}$ is related to thickness noise from the surfaces (Posson and Peake, 2013b).

2.2.2 Derivation of acoustic analogy

Next, we combine equations (2.2.2) to (2.2.6) into a single equation for the pressure field. We first note that the three relations

$$\frac{\bar{\partial}}{\partial x} \left(\overline{\frac{D_0}{Dt}} \right) = \overline{\frac{D_0}{Dt}} \left(\frac{\bar{\partial}}{\partial x} \right), \quad (2.2.16)$$

$$\frac{\bar{\partial}}{\partial r} \left(\overline{\frac{D_0}{Dt}} \right) = \overline{\frac{D_0}{Dt}} \frac{\bar{\partial}}{\partial r} + U'_x(r) \frac{\bar{\partial}}{\partial x} + \left(\frac{U_\theta(r)}{r} \right)' \frac{\bar{\partial}}{\partial \theta}, \quad (2.2.17)$$

$$\frac{1}{r} \frac{\bar{\partial}}{\partial \theta} \left(\overline{\frac{D_0}{Dt}} \right) = \overline{\frac{D_0}{Dt}} \left(\frac{1}{r} \frac{\bar{\partial}}{\partial \theta} \right), \quad (2.2.18)$$

hold. Thus, the material derivative commutes with circumferential and axial derivatives but not radial derivatives. Using (2.2.5) we express the material derivative of the swirl \tilde{w} in terms of \tilde{v} , \tilde{p} and source terms:

$$\rho_0 \frac{\overline{D_0 \tilde{w}}}{Dt} = \mathcal{D}_\theta + \mathcal{S}_\theta - \frac{1}{r} \frac{\bar{\partial} \tilde{p}}{\partial \theta} - \tilde{v} \frac{\rho_0}{r} \frac{d}{dr} (r U_\theta). \quad (2.2.19)$$

Combining the mass (2.2.2) and energy (2.2.6) equations allows us to express the material derivative of the density $\tilde{\rho}$ similarly:

$$\frac{\overline{D}_0 \tilde{\rho}}{Dt} = \mathcal{D}_{\text{mass}} + \mathcal{S}_{\text{mass}} - \frac{\mathcal{D}_e + \mathcal{S}_e}{c_0^2} + \frac{1}{c_0^2} \frac{\overline{D}_0 \tilde{p}}{Dt} + \frac{\rho_0 U_\theta^2}{rc_0^2} \tilde{v} - \rho'_0 \tilde{v}. \quad (2.2.20)$$

Next, we take the material derivative of the radial momentum equation (2.2.4), which gives

$$\rho_0 \frac{\overline{D}_0^2 \tilde{v}}{Dt^2} - \frac{2\rho_0 U_\theta}{r} \frac{\overline{D}_0 \tilde{w}}{Dt} - \frac{U_\theta^2}{r} \frac{\overline{D}_0 \tilde{\rho}}{Dt} + \frac{\overline{D}_0}{Dt} \frac{\overline{\partial} \tilde{p}}{\partial r} = \frac{\overline{D}_0}{Dt} (\mathcal{D}_r + \mathcal{S}_r). \quad (2.2.21)$$

Upon substituting (2.2.19) and (2.2.20) into the above equation we find

$$\rho_0 \mathcal{R}(\tilde{v}) = \mathcal{T}(\tilde{p}) + \mathbb{S}_1^M, \quad (2.2.22)$$

where the differential operators \mathcal{R} and \mathcal{T} are defined by

$$\mathcal{R} = \frac{\overline{D}_0^2}{Dt^2} + \mathcal{U}_\theta \quad \text{and} \quad \mathcal{T} = -\frac{\overline{D}_0}{Dt} \frac{\overline{\partial}}{\partial r} - \frac{2U_\theta}{r^2} \frac{\overline{\partial}}{\partial \theta} + \frac{U_\theta^2}{rc_0^2} \frac{\overline{D}_0}{Dt}, \quad (2.2.23)$$

where

$$\mathcal{U}_\theta = \frac{2U_\theta(r)}{r^2} \frac{d}{dr}(rU_\theta) + \frac{U_\theta^2}{r} \left(\frac{\rho'_0}{\rho_0} - \frac{U_\theta^2}{rc_0^2} \right), \quad (2.2.24)$$

and the source term \mathbb{S}_1^M is given by

$$\mathbb{S}_1^M = \frac{\overline{D}_0}{Dt} (\mathcal{D}_r + \mathcal{S}_r) + \frac{U_\theta^2}{r} \left(\mathcal{D}_{\text{mass}} + \mathcal{S}_{\text{mass}} - \frac{\mathcal{D}_e + \mathcal{S}_e}{c_0^2} \right) + \frac{2U_\theta}{r} (\mathcal{D}_\theta + \mathcal{S}_\theta). \quad (2.2.25)$$

Compared to the notation in [Posson and Peake \(2013b\)](#) we have $\mathcal{R} = -\mathcal{D}$ and $\mathcal{T} = -\mathcal{M}$. To simplify matters in what follows we introduce the notation

$$\mathbb{U}_\theta(r) = \frac{1}{r^2} \frac{d}{dr}(rU_\theta). \quad (2.2.26)$$

The next step is to differentiate the axial momentum equation (2.2.3) with respect to x , and take $\frac{1}{r} \frac{\overline{\partial}}{\partial \theta}$ of the circumferential momentum equation (2.2.5), which gives

$$\rho_0 \frac{\overline{D}_0}{Dt} \frac{\overline{\partial} \tilde{u}}{\partial x} = -\rho_0 U'_x \frac{\overline{\partial} \tilde{v}}{\partial x} - \frac{\overline{\partial}^2 \tilde{p}}{\partial x^2} + \frac{\overline{\partial}}{\partial x} (\mathcal{D}_x + \mathcal{S}_x), \quad (2.2.27)$$

and

$$\rho_0 \frac{\overline{D}_0}{Dt} \left(\frac{1}{r} \frac{\overline{\partial} \tilde{w}}{\partial \theta} \right) = -\rho_0 \mathbb{U}_\theta \frac{\overline{\partial} \tilde{v}}{\partial \theta} - \frac{1}{r^2} \frac{\overline{\partial}^2 \tilde{p}}{\partial \theta^2} + \frac{1}{r} \frac{\overline{\partial}}{\partial \theta} (\mathcal{D}_\theta + \mathcal{S}_\theta). \quad (2.2.28)$$

We then divide the energy equation (2.2.6) by $c_0^2(r)$ and then take the material derivative of it, which gives

$$\frac{1}{c_0^2} \frac{\overline{D}_0^2 \tilde{p}}{Dt^2} + \rho_0 \frac{\overline{D}_0}{Dt} \frac{\overline{\partial} \tilde{u}}{\partial x} + \rho_0 \frac{\overline{D}_0}{Dt} \left(\frac{\overline{\partial} \tilde{v}}{\partial r} + \frac{\tilde{v}}{r} \right) + \rho_0 \frac{\overline{D}_0}{Dt} \left(\frac{1}{r} \frac{\overline{\partial} \tilde{w}}{\partial \theta} \right) + \frac{\rho_0 U_\theta^2}{rc_0^2} \frac{\overline{D}_0 \tilde{v}}{Dt} = \frac{\overline{D}_0}{Dt} \left(\frac{\mathcal{D}_e + \mathcal{S}_e}{c_0^2} \right). \quad (2.2.29)$$

Substituting (2.2.27) and (2.2.28) into (2.2.29) then gives

$$\frac{1}{c_0^2} \frac{\overline{D}_0^2 \tilde{p}}{Dt^2} - \frac{\overline{\partial}^2 \tilde{p}}{\partial x^2} - \frac{1}{r^2} \frac{\overline{\partial}^2 \tilde{p}}{\partial \theta^2} + \rho_0 \frac{\overline{D}_0}{Dt} \left(\frac{\overline{\partial} \tilde{v}}{\partial r} + \frac{\tilde{v}}{r} \right) - \rho_0 U'_x \frac{\overline{\partial} \tilde{v}}{\partial x} - \rho_0 \mathbb{U}_\theta \frac{\overline{\partial} \tilde{v}}{\partial \theta} + \frac{\rho_0 U_\theta^2}{rc_0^2} \frac{\overline{D}_0 \tilde{v}}{Dt} = \mathbb{S}_2^M, \quad (2.2.30)$$

where the source term \mathbb{S}_2^M is given by

$$\mathbb{S}_2^M = \frac{\overline{D}_0}{Dt} \left(\frac{\mathcal{D}_e + \mathcal{S}_e}{c_0^2} \right) - \frac{\overline{\partial}}{\partial x} (\mathcal{S}_x + \mathcal{D}_x) - \frac{1}{r} \frac{\overline{\partial}}{\partial \theta} (\mathcal{S}_\theta + \mathcal{D}_\theta). \quad (2.2.31)$$

In (2.2.30) we have eliminated the axial and circumferential velocities \tilde{u} and \tilde{w} from the left-hand side, as well as the density $\tilde{\rho}$.

The final step in the derivation of the acoustic analogy is to eliminate the radial velocity \tilde{v} from the left-hand side of (2.2.30). To do this we insert equation (2.2.22) into (2.2.30), but first we need to ensure all the terms involving \tilde{v} in (2.2.30) are of the form $\rho_0 \mathcal{R}(\tilde{v})$. The operator \mathcal{R} commutes with derivatives with respect to θ and x , as well as the material derivative, but not derivatives with respect to r . Using

$$\frac{\overline{D}_0^2}{Dt^2} \frac{\overline{\partial}}{\partial r} = \frac{\overline{\partial}}{\partial r} \frac{\overline{D}_0^2}{Dt^2} - 2U'_x \frac{\overline{\partial}}{\partial x} \frac{\overline{D}_0}{Dt} - 2 \left(\frac{U_\theta}{r} \right)' \frac{\overline{\partial}}{\partial \theta} \frac{\overline{D}_0}{Dt}, \quad (2.2.32)$$

which follows from (2.2.17), we calculate that

$$\begin{aligned} \mathcal{R} \left(\frac{\overline{D}_0}{Dt} \frac{\overline{\partial} \tilde{v}}{\partial r} \right) &= \frac{\overline{D}_0^3}{Dt^3} \frac{\overline{\partial} \tilde{v}}{\partial r} + \mathcal{U}_\theta \frac{\overline{D}_0}{Dt} \frac{\overline{\partial} \tilde{v}}{\partial r}, \\ &= \frac{\overline{D}_0}{Dt} \left(\frac{\overline{\partial}}{\partial r} \frac{\overline{D}_0^2}{Dt^2} - 2U'_x \frac{\overline{\partial}}{\partial x} \frac{\overline{D}_0}{Dt} - 2 \left(\frac{U_\theta}{r} \right)' \frac{\overline{\partial}}{\partial \theta} \frac{\overline{D}_0}{Dt} \right) \tilde{v} + \frac{\overline{D}_0}{Dt} \left(\mathcal{U}_\theta \frac{\overline{\partial} \tilde{v}}{\partial r} \right), \\ &= \frac{\overline{D}_0}{Dt} \frac{\overline{\partial}}{\partial r} \mathcal{R}(v) - 2U'_x \frac{\overline{\partial}}{\partial x} \frac{\overline{D}_0^2 \tilde{v}}{Dt^2} - 2 \left(\frac{U_\theta}{r} \right)' \frac{\overline{\partial}}{\partial \theta} \frac{\overline{D}_0^2 \tilde{v}}{Dt^2} - \mathcal{U}'_\theta \frac{\overline{D}_0 \tilde{v}}{Dt}. \end{aligned} \quad (2.2.33)$$

If we apply the differential operator \mathcal{R} to (2.2.30) then we get

$$\begin{aligned} \left(\frac{1}{c_0^2} \frac{\overline{D}_0^2}{Dt^2} - \frac{\overline{\partial}^2}{\partial x^2} - \frac{1}{r^2} \frac{\overline{\partial}^2}{\partial \theta^2} \right) \mathcal{R}(\tilde{p}) + \rho_0 \mathcal{R} \left(\frac{\overline{D}_0}{Dt} \frac{\overline{\partial} \tilde{v}}{\partial r} \right) + \\ \rho_0 \left(\frac{1}{r} \frac{\overline{D}_0}{Dt} - U'_x \frac{\overline{\partial}}{\partial x} - \mathbb{U}_\theta \frac{\overline{\partial}}{\partial \theta} + \frac{U_\theta^2}{rc_0^2} \frac{\overline{D}_0}{Dt} \right) \mathcal{R}(\tilde{v}) = \mathcal{R}(\mathbb{S}_2^M), \end{aligned} \quad (2.2.34)$$

and hence inserting (2.2.33) into (2.2.34) gives

$$\begin{aligned} \left(\frac{1}{c_0^2} \frac{\overline{D}_0^2}{Dt^2} - \frac{\overline{\partial}^2}{\partial x^2} - \frac{1}{r^2} \frac{\overline{\partial}^2}{\partial \theta^2} \right) \mathcal{R}(\tilde{p}) + \rho_0 \left(\left[\frac{1}{r} + \frac{U_\theta^2}{rc_0^2} \right] \frac{\overline{D}_0}{Dt} - U'_x \frac{\overline{\partial}}{\partial x} - \mathbb{U}_\theta \frac{\overline{\partial}}{\partial \theta} \right) \mathcal{R}(\tilde{v}) \\ + \rho_0 \frac{\overline{D}_0}{Dt} \frac{\overline{\partial}}{\partial r} \mathcal{R}(v) - \rho_0 \left[2U'_x \frac{\overline{\partial}}{\partial x} \frac{\overline{D}_0^2 \tilde{v}}{Dt^2} + 2 \left(\frac{U_\theta}{r} \right)' \frac{\overline{\partial}}{\partial \theta} \frac{\overline{D}_0^2 \tilde{v}}{Dt^2} + \mathcal{U}'_\theta \frac{\overline{D}_0 \tilde{v}}{Dt} \right] = \mathcal{R}(\mathbb{S}_2^M), \end{aligned} \quad (2.2.35)$$

which we rewrite as

$$\begin{aligned} & \left(\frac{1}{c_0^2} \frac{\overline{D}_0^2}{Dt^2} - \frac{\bar{\partial}^2}{\partial x^2} - \frac{1}{r^2} \frac{\bar{\partial}^2}{\partial \theta^2} \right) \mathcal{R}(\tilde{p}) + \rho_0 \left(\frac{1}{r} \frac{\overline{D}_0}{Dt} - U'_x \frac{\bar{\partial}}{\partial x} - \mathbb{U}_\theta \frac{\bar{\partial}}{\partial \theta} + \left(\frac{U_\theta^2}{rc_0^2} - \frac{\rho'_0}{\rho_0} \right) \frac{\overline{D}_0}{Dt} \right) \mathcal{R}(\tilde{v}) + \\ & \frac{\overline{D}_0}{Dt} \frac{\bar{\partial}}{\partial r} (\rho_0 \mathcal{R}(v)) - \rho_0 \left[2U'_x \frac{\bar{\partial}}{\partial x} \frac{\overline{D}_0^2 \tilde{v}}{Dt^2} + 2 \left(\frac{U_\theta}{r} \right)' \frac{\bar{\partial}}{\partial \theta} \frac{\overline{D}_0^2 \tilde{v}}{Dt^2} + \mathcal{U}'_\theta \frac{\overline{D}_0 \tilde{v}}{Dt} \right] = \mathcal{R}(\mathbb{S}_2^M). \end{aligned} \quad (2.2.36)$$

Despite applying \mathcal{R} to (2.2.30) once, we still have some \tilde{v} terms which are not of the form $\rho_0 \mathcal{R}(\tilde{v})$. However, these terms now only involve material derivatives and derivatives with respect to θ and x , so we just apply the differential operator \mathcal{R} to (2.2.36) once more. This gives

$$\begin{aligned} & \left(\frac{1}{c_0^2} \frac{\overline{D}_0^2}{Dt^2} - \frac{\bar{\partial}^2}{\partial x^2} - \frac{1}{r^2} \frac{\bar{\partial}^2}{\partial \theta^2} \right) \mathcal{R}^2(\tilde{p}) + \rho_0 \left(\frac{1}{r} \frac{\overline{D}_0}{Dt} - U'_x \frac{\bar{\partial}}{\partial x} - \mathbb{U}_\theta \frac{\bar{\partial}}{\partial \theta} + \left(\frac{U_\theta^2}{rc_0^2} - \frac{\rho'_0}{\rho_0} \right) \frac{\overline{D}_0}{Dt} \right) \mathcal{R}^2(\tilde{v}) + \\ & \mathcal{R} \left[\frac{\overline{D}_0}{Dt} \frac{\bar{\partial}}{\partial r} (\rho_0 \mathcal{R}(\tilde{v})) \right] - \rho_0 \frac{\overline{D}_0}{Dt} \left[2U'_x \frac{\bar{\partial}}{\partial x} \frac{\overline{D}_0}{Dt} + 2 \left(\frac{U_\theta}{r} \right)' \frac{\bar{\partial}}{\partial \theta} \frac{\overline{D}_0}{Dt} + \mathcal{U}'_\theta \frac{\overline{D}_0}{Dt} \right] \mathcal{R}(\tilde{v}) = \mathcal{R}^2(\mathbb{S}_2^M). \end{aligned} \quad (2.2.37)$$

Finally, we insert equation (2.2.22) into (2.2.37) which gives

$$\mathcal{F}^M(\tilde{p}) = \mathbb{S}^M.$$

(2.2.38)

The operator \mathcal{F}^M is defined by

$$\begin{aligned} \mathcal{F}^M := & \left(\frac{1}{c_0^2} \frac{\overline{D}_0^2}{Dt^2} - \frac{\bar{\partial}^2}{\partial x^2} - \frac{1}{r^2} \frac{\bar{\partial}^2}{\partial \theta^2} \right) \mathcal{R}^2 + \left(\frac{1}{r} \frac{\overline{D}_0}{Dt} - U'_x \frac{\bar{\partial}}{\partial x} - \mathbb{U}_\theta \frac{\bar{\partial}}{\partial \theta} + \left(\frac{U_\theta^2}{rc_0^2} - \frac{\rho'_0}{\rho_0} \right) \frac{\overline{D}_0}{Dt} \right) \mathcal{R} \mathcal{T} \\ & + \mathcal{R} \frac{\overline{D}_0}{Dt} \frac{\bar{\partial}}{\partial r} \mathcal{T} - \frac{\overline{D}_0}{Dt} \left[2U'_x \frac{\bar{\partial}}{\partial x} \frac{\overline{D}_0}{Dt} + 2 \left(\frac{U_\theta}{r} \right)' \frac{\bar{\partial}}{\partial \theta} \frac{\overline{D}_0}{Dt} + \mathcal{U}'_\theta \frac{\overline{D}_0}{Dt} \right] \mathcal{T}, \end{aligned} \quad (2.2.39)$$

and the source term is

$$\begin{aligned} \mathbb{S}^M = & \mathcal{R}^2(\mathbb{S}_2^M) - \mathcal{R} \left(\frac{\overline{D}_0}{Dt} \left(\frac{1}{r} + \frac{\bar{\partial}}{\partial r} \right) - U'_x \frac{\bar{\partial}}{\partial x} - \mathbb{U}_\theta \frac{\bar{\partial}}{\partial \theta} + \left(\frac{U_\theta^2}{rc_0^2} - \frac{\rho'_0}{\rho_0} \right) \frac{\overline{D}_0}{Dt} \right) \mathbb{S}_1^M \\ & + \frac{\overline{D}_0}{Dt} \left[2U'_x \frac{\bar{\partial}}{\partial x} \frac{\overline{D}_0}{Dt} + 2 \left(\frac{U_\theta}{r} \right)' \frac{\bar{\partial}}{\partial \theta} \frac{\overline{D}_0}{Dt} + \mathcal{U}'_\theta \frac{\overline{D}_0}{Dt} \right] \mathbb{S}_1^M. \end{aligned} \quad (2.2.40)$$

2.2.3 Using the acoustic analogy

Once we find the Green's function of the operator \mathcal{F}^M , by solving

$$\mathcal{F}^M(G(\mathbf{x}, t | \mathbf{x}_0, t_0)) = \delta(\mathbf{x} - \mathbf{x}_0) \delta(t - t_0), \quad (2.2.41)$$

then we can calculate the pressure by using

$$p(\mathbf{x}, t) = \int G(\mathbf{x}, t | \mathbf{x}_0, t_0) \mathbb{S}^M(\mathbf{x}_0, t) d\mathbf{x}_0 dt_0. \quad (2.2.42)$$

The Green's function was calculated numerically in [Posson and Peake \(2013b\)](#) and we calculate it analytically in [Chapter 3](#). It remains to estimate the source terms. By only considering some of the surface source terms, an analytical result is possible and the full derivation was shown in [Posson and Peake \(2013b\)](#). We outline the main steps below, which would allow us to calculate the pressure for a rotor, such as in [Posson and Peake \(2012, Figures 4 and 5\)](#).

- Use integration by parts to move all the derivatives from the source terms to the Green's function. Then use the definition of the Dirac delta and the Heaviside function to get integrals over the duct walls and blade surfaces (surface source terms) and over the whole space (volume source terms) ([Posson and Peake, 2013b](#), Section 5).
- Decide which source terms are important and feasible to calculate. In [Posson and Peake \(2013b, Section 6.1\)](#) all the volume source terms are ignored, and only the surface source terms involving loading noise were considered. Additionally, the integrals over the duct walls were shown to be zero in [Posson and Peake \(2013b\)](#).
- Define the rotor geometry ([Posson and Peake, 2013b](#), Figure 3), and assume the blades have zero lean and sweep, like in [Figure 1.8b](#). Then, perform a coordinate transformation so that the blades don't move in time.
- Introduce the pressure jump ΔP_l over the l -th blade. This is an input to the model, and depends on the blade geometry. In [Posson et al. \(2010\)](#) the pressure jump is calculated analytically for the blades in a rotor. This was based on earlier work by [Glegg \(1999\)](#).
- Fourier transform and Fourier series the differential operator acting on the Green's function ([Posson and Peake, 2013b](#), Equation 6.5). We already know the Fourier transform and Fourier series of the Green's function from how we calculate it.
- Split the pressure field into contributions from the acoustic modes and the critical layer integral ([Posson and Peake, 2012](#), Equation 34).
- Calculate each separately, the acoustic contribution is given in [Posson and Peake \(2012, Equation 35\)](#) and the contribution from the critical layer is given in [Posson and Peake \(2012, Equation 37\)](#). The integration is performed over the blade surface. At this point we could instead consider a serrated aerofoil and then integrate over a different region, although this would require a different pressure jump response ΔP_l .

2.2.4 Reducing to a form similar to Posson and Peake (2013b)

When the entropy is constant, from (2.1.8) we see that

$$\frac{\rho'_0(r)}{\rho_0(r)} = \frac{U_\theta^2(r)}{rc_0^2(r)}. \quad (2.2.43)$$

Thus, we find for constant entropy

$$\mathcal{F}^M = \mathcal{F}^{PP}, \quad (2.2.44)$$

where \mathcal{F}^{PP} is the sixth order differential operator from Posson and Peake (2013b). Let \mathbb{S}_V^M denote the volume source terms (with a Heaviside function) and let the surface source terms (involving Dirac deltas) be denoted as \mathbb{S}_S^M . We will show that

$$\mathbb{S}_V^M = \mathbb{S}_{FWH}^{PP}, \quad (2.2.45)$$

but

$$\mathbb{S}_S^M \neq \mathbb{S}_{FWH}^{PP}, \quad (2.2.46)$$

where the PP superscript denotes the source terms from Posson and Peake (2013b). These are defined by $\mathbb{S}^{PP} = \mathbb{S}_1^{PP} + \mathbb{S}_2^{PP}$, with \mathbb{S}_j^{PP} given in (2.2.49) and (2.2.50), and $\mathbb{S}_{FWH}^{PP} = \mathbb{S}_{FWH,1}^{PP} + \mathbb{S}_{FWH,2}^{PP}$, with $\mathbb{S}_{FWH,j}^{PP}$ given in (2.2.62) and (2.2.63). Thus, the two analogies are equivalent when there are no surfaces present and the entropy is constant, but differ as soon as we have surfaces present. The difference in source terms arises since the full energy equation is not included in the derivation by Posson and Peake (2013b), which produces terms not picked up by their acoustic analogy. However, the formulation of the analogy in Posson and Peake (2013b) is correct for their choice of combined mass and energy equation (Posson and Peake, 2013b, Equation 2.4).

We could reduce our analogy to Lilley's analogy (Lilley, 1974) in the same way as in Posson and Peake (2013b) when we have no swirl and no surfaces present.

Volume source terms

Let us define

$$\mathbb{S}_{V,1}^M := \frac{\overline{D}_0}{Dt}(\mathcal{S}_r) + \frac{U_\theta^2}{r} \left(\mathcal{S}_{\text{mass}} - \frac{\mathcal{S}_e}{c_0^2} \right) + \frac{2U_\theta}{r} \mathcal{S}_\theta \quad (2.2.47)$$

and

$$\mathbb{S}_{V,2}^M := \frac{\overline{D}_0}{Dt} \left(\frac{\mathcal{S}_e}{c_0^2} \right) - \frac{\bar{\partial}}{\partial x}(\mathcal{S}_x) - \frac{1}{r} \frac{\bar{\partial}}{\partial \theta} \mathcal{S}_\theta, \quad (2.2.48)$$

which are the volume source terms from \mathbb{S}_1^M and \mathbb{S}_2^M . We compare the volume source term $\mathbb{S}_{V,1}^M$ to \mathbb{S}_1^{PP} , and the volume source term $\mathbb{S}_{V,2}^M$ to \mathbb{S}_2^{PP} , where \mathbb{S}_j^{PP} are defined in Posson and

Peake (2013b, Equation 3.17) as

$$\mathbb{S}_1^{PP} = \frac{\overline{D}_0}{Dt}(\mathcal{S}_r^{PP}) + \frac{2U_\theta}{r}\mathcal{S}_\theta^{PP} \quad (2.2.49)$$

and

$$\mathbb{S}_2^{PP} = \frac{\overline{D}_0}{Dt}(\mathcal{S}_\rho^{PP}) - \frac{\bar{\partial}}{\partial x}(\mathcal{S}_x^{PP}) - \frac{1}{r} \frac{\bar{\partial}}{\partial \theta} \mathcal{S}_\theta^{PP}. \quad (2.2.50)$$

The following relations between the source terms hold:

$$\mathcal{S}_{\text{mass}} = \mathcal{S}_\rho^{PP} - \frac{\overline{D}_0 \widetilde{Z}_p}{Dt} = -\bar{\nabla} \cdot (\tilde{\rho} \tilde{\mathbf{u}}), \quad (2.2.51)$$

$$\mathcal{S}_x = \mathcal{S}_x^{PP}, \quad (2.2.52)$$

$$\mathcal{S}_r = \mathcal{S}_r^{PP} + \frac{U_\theta^2}{r_0} \widetilde{Z}_p, \quad (2.2.53)$$

$$\mathcal{S}_\theta = \mathcal{S}_\theta^{PP}, \quad (2.2.54)$$

$$\mathcal{S}_e = -\tilde{\mathbf{u}} \cdot \bar{\nabla} \tilde{p} - \gamma \tilde{p} \bar{\nabla} \cdot \tilde{\mathbf{u}}, \quad (2.2.55)$$

where we have used the definitions in (2.2.7) to (2.2.9) and the definitions of \mathcal{S}_j^{PP} in Posson and Peake (2013b). The quantity Z_p is the non-isentropic factor, and is defined by

$$Z_p = \frac{p}{c_0^2} - \rho. \quad (2.2.56)$$

We can calculate the material derivative of Z_p by using the mass and momentum equations, or the relation between density and pressure in (1.4.28). We find that when the entropy is constant

$$\frac{D_0 Z_p}{Dt} = \bar{\nabla} \cdot (\rho \mathbf{u}) - \frac{1}{c_0^2} (\mathbf{u} \cdot \bar{\nabla} p + \gamma p (\bar{\nabla} \cdot \mathbf{u})). \quad (2.2.57)$$

Hence, we see that (up to surface source terms involving Dirac deltas)

$$\mathcal{S}_\rho^{PP} = \bar{\nabla} \cdot (\tilde{\rho} \tilde{\mathbf{u}}) + \frac{\overline{D}_0 \widetilde{Z}_p}{Dt} = -\frac{1}{c_0^2} (\tilde{\mathbf{u}} \cdot \bar{\nabla} \tilde{p} - \gamma \tilde{p} \bar{\nabla} \cdot \tilde{\mathbf{u}}) = \frac{\mathcal{S}_e}{c_0^2}, \quad (2.2.58)$$

so the volume surface terms in (2.2.48) and (2.2.50) are equal. We then find

$$\frac{\overline{D}_0}{Dt}(\mathcal{S}_r) + \frac{U_\theta^2}{r} \left(\mathcal{S}_{\text{mass}} - \frac{\mathcal{S}_e}{c_0^2} \right) = \frac{\overline{D}_0}{Dt}(\mathcal{S}_r) - \frac{U_\theta^2}{r} \frac{\overline{D}_0 \widetilde{Z}_p}{Dt} = \frac{\overline{D}_0}{Dt}(\mathcal{S}_r^{PP}), \quad (2.2.59)$$

and hence the volume surface terms in (2.2.47) and (2.2.49) are equal, so we see that the volume source terms in the two acoustic analogies are equivalent.

Surface source terms

We now define

$$\mathbb{S}_{S,1}^M := \frac{\overline{D}_0}{Dt}(\mathcal{D}_r) + \frac{U_\theta^2}{r} \left(\mathcal{D}_{\text{mass}} - \frac{\mathcal{D}_e}{c_0^2} \right) + \frac{2U_\theta}{r} \mathcal{D}_\theta \quad (2.2.60)$$

and

$$\mathbb{S}_{S,2}^M := \frac{\overline{D}_0}{Dt} \left(\frac{\mathcal{D}_e}{c_0^2} \right) - \frac{\overline{\partial}}{\partial x} (\mathcal{D}_x) - \frac{1}{r} \frac{\overline{\partial}}{\partial \theta} \mathcal{D}_\theta, \quad (2.2.61)$$

which are the surface source terms in \mathbb{S}_1^M and \mathbb{S}_2^M . We compare $\mathbb{S}_{S,1}^M$ to $\mathbb{S}_{FWH,1}^{PP}$ and $\mathbb{S}_{S,2}^M$ to $\mathbb{S}_{FWH,2}^{PP}$, with the surface source terms from [Posson and Peake \(2013b, Equation 3.18\)](#) given by

$$\mathbb{S}_{FWH,1}^{PP} = \frac{\overline{D}_0}{Dt} (\mathcal{D}_r^{PP}) + \frac{2U_\theta}{r} \mathcal{D}_\theta^{PP}, \quad (2.2.62)$$

and

$$\mathbb{S}_{FWH,2}^{PP} = \frac{\overline{D}_0}{Dt} (\mathcal{D}_\rho^{PP}) - \frac{\overline{\partial}}{\partial x} (\mathcal{D}_x^{PP}) - \frac{1}{r} \frac{\overline{\partial}}{\partial \theta} \mathcal{D}_\theta^{PP}. \quad (2.2.63)$$

We find that

$$\mathcal{D}_{\text{mass}} = \mathcal{D}_\rho^{PP} = \delta(f_S) [\rho (\underline{\mathbf{u}} - \mathbf{v}^S) \cdot \mathbf{n} + \rho_0 (\mathbf{u} \cdot \mathbf{n})], \quad (2.2.64)$$

$$\mathcal{D} = \mathcal{D}^{PP}, \quad (2.2.65)$$

$$\mathcal{D}_e = \delta(f_S) [p (\underline{\mathbf{u}} - \mathbf{v}^S) \cdot \mathbf{n} + \gamma p_0 (\mathbf{u} \cdot \mathbf{n}) + \gamma p (\mathbf{u} \cdot \mathbf{n})], \quad (2.2.66)$$

where we use the definitions in [\(2.2.11\)](#) to [\(2.2.13\)](#) and the definitions of \mathcal{D}_j^{PP} in [Posson and Peake \(2013b\)](#). We calculate that

$$\frac{\mathcal{D}_e}{c_0^2} = \mathcal{D}_{\text{mass}} + \delta(f_S) [Z_p (\underline{\mathbf{u}} - \mathbf{v}^S) \cdot \mathbf{n} + \gamma p (\mathbf{u} \cdot \mathbf{n})], \quad (2.2.67)$$

which follows from the above equations or rearranging the mass and energy equations. Thus, we find that

$$\mathbb{S}_{S,1}^M + \frac{U_\theta^2}{r} \delta(f_S) [Z_p (\underline{\mathbf{u}} - \mathbf{v}^S) \cdot \mathbf{n} + \gamma p (\mathbf{u} \cdot \mathbf{n})] = \mathbb{S}_{FWH,1}^{PP} \quad (2.2.68)$$

and

$$\mathbb{S}_{S,2}^M = \mathbb{S}_{FWH,2}^{PP} + \frac{\overline{D}_0}{Dt} (\delta(f_S) [Z_p (\underline{\mathbf{u}} - \mathbf{v}^S) \cdot \mathbf{n} + \gamma p (\mathbf{u} \cdot \mathbf{n})]). \quad (2.2.69)$$

The differences in these surface source terms is attributed to the relation [\(2.2.57\)](#). Although it holds for normal functions, when we replace the functions by generalised functions it does not hold exactly. Instead, we get linear surface source terms on the left-hand side of [\(2.2.57\)](#) and quadratic source terms on the right-hand side. Since we end up with the terms on the right-hand side of [\(2.2.57\)](#) in our mass/energy equation, while [Posson and Peake \(2013b\)](#) use the left-hand side of [\(2.2.57\)](#), the surface source terms in the two analogies do not cancel out, and it is precisely these terms that appear in [\(2.2.68\)](#) and [\(2.2.69\)](#). However, when we calculate the pressure using the method in [Section 2.2.3](#) we only use the loading noise surface source term. Since $\mathcal{D} = \mathcal{D}^{PP}$ the loading noise term is the same for both analogies when we have constant entropy.

When the base flow has varying entropy we cannot use the approach by [Posson and Peake \(2013b\)](#), since

$$\frac{D_0 Z_p}{Dt} = \nabla \cdot (\rho \mathbf{u}) - \frac{1}{c_0^2} (\mathbf{u} \cdot \nabla p + \gamma p (\nabla \cdot \mathbf{u})) + \rho_0 \left(\frac{U_\theta^2}{rc_0^2} - \frac{\rho'_0}{\rho_0} \right) v, \quad (2.2.70)$$

and hence the material derivative of Z_p contains linear terms. Thus, using it on the right-hand side of the acoustic analogy (where it appears in [Posson and Peake \(2013b\)](#)) as a source would not give the correct result. So the formulation in [Posson and Peake \(2013b\)](#) is valid in the case of no entropy (with their combined mass and energy equation), but to extend the result we need to use our formulation with the full energy equation rather than the non-isentropic factor Z_p .

Chapter 3

The Green's function

In this chapter, we develop a high-frequency asymptotic approximation for calculating the eigenmodes and the Green's function for swirling flow in an acoustically lined duct. We find an asymptotic Green's function of the operator \mathcal{F}^M from [Chapter 2](#) in the high-frequency limit using the WKB method. To do this, we first need to calculate an asymptotic dispersion relation that the eigenmodes satisfy, and we find there are several different forms of it, depending on the parameters of the flow. We present a number of comparisons between the asymptotic eigenmodes and numerical eigenmodes. We develop our own numerical eigenmode and Green's function solver, which reproduces the results from [Posson and Peake \(2013b\)](#). This allows us to compare the numerical and asymptotic Green's function for some simple mean flows, and then we consider semi-realistic swirling flow and flows with variable entropy. We conclude the chapter by considering the limitations of the high-frequency asymptotic approximation.

It is the first time an asymptotic Green's function has been calculated for swirling mean flow in a duct with acoustically lined walls, and it agrees extremely favourably with the numerical results. Additionally, it is the first study on the effect of entropy on the eigenmodes and Green's function in swirling flow, both numerically and asymptotically. When we investigate the effect of entropy on the eigenmodes in a lined duct, we discover surface modes which appear as we vary entropy and we term “surface-entropy” modes. Some of the results from this chapter were presented at the 22nd AIAA/CEAS Aeroacoustics Conference in Lyon ([Mathews et al., 2016](#)).

3.1 High-frequency Green's function

We find the reduced Green's function $G_\omega(\mathbf{x}|\mathbf{x}_0)$ of the operator \mathcal{F}^M in [\(2.2.39\)](#), which satisfies

$$\mathcal{F}^M \left(G_\omega(\mathbf{x}|\mathbf{x}_0) e^{-i\omega t} \right) = \delta(\mathbf{x} - \mathbf{x}_0) e^{-i\omega t} = \delta(x - x_0) \frac{\delta(r - r_0)}{r} \delta(\theta - \theta_0) e^{-i\omega t}. \quad (3.1.1)$$

We look for a reduced Green's function of the form

$$G_\omega(\mathbf{x}|\mathbf{x}_0) = \frac{1}{4\pi^2} \sum_{n=-\infty}^{\infty} e^{in(\theta-\theta_0)} \int_{\mathbb{R}} G_n(r|r_0; \omega, k) e^{ik(x-x_0)} dk, \quad (3.1.2)$$

where we choose a circumferential Fourier series to ensure it is 2π periodic in θ . The Dirac delta function satisfies the identities (Duffy, 2001)

$$\frac{1}{2\pi} \sum_{n=-\infty}^{\infty} e^{in(\theta-\theta_0)} = \delta(\theta-\theta_0) \text{ and } \frac{1}{2\pi} \int_{\mathbb{R}} e^{ik(x-x_0)} dk = \delta(x-x_0), \quad (3.1.3)$$

while we also have the relations

$$\frac{D_0^m}{Dt^m} (G_\omega(\mathbf{x}|\mathbf{x}_0) e^{-i\omega t}) = \frac{e^{-i\omega t}}{4\pi^2} \sum_{n=-\infty}^{\infty} e^{in(\theta-\theta_0)} \int_{\mathbb{R}} (-i)^m \Omega^m(r) G_n(r|r_0; \omega, k) e^{ik(x-x_0)} dk, \quad (3.1.4)$$

$$\mathcal{R}(G_\omega(\mathbf{x}|\mathbf{x}_0) e^{-i\omega t}) = \frac{e^{-i\omega t}}{4\pi^2} \sum_{n=-\infty}^{\infty} e^{in(\theta-\theta_0)} \int_{\mathbb{R}} [\mathcal{U}_\theta(r) - \Omega^2(r)] G_n(r|r_0; \omega, k) e^{ik(x-x_0)} dk, \quad (3.1.5)$$

and

$$\mathcal{T}(G_\omega(\mathbf{x}|\mathbf{x}_0) e^{-i\omega t}) = \frac{e^{-i\omega t}}{4\pi^2} \sum_{n=-\infty}^{\infty} e^{in(\theta-\theta_0)} \int_{\mathbb{R}} i \left[\Omega(r) \frac{dG_n}{dr}(r) - \Upsilon(r) G_n(r) \right] e^{ik(x-x_0)} dk, \quad (3.1.6)$$

where

$$\Omega(r) = \omega - k U_x(r) - \frac{n U_\theta(r)}{r} \text{ and } \Upsilon(r) = \frac{U_\theta^2(r)}{r c_0^2(r)} \Omega(r) + \frac{2 n U_\theta(r)}{r^2}, \quad (3.1.7)$$

with \mathcal{U}_θ defined in (2.2.26). Inserting (3.1.2) into (3.1.1), using the definition of \mathcal{F}^M and the relations (3.1.3) to (3.1.6) then gives (after some considerable algebra)

$$\begin{aligned} & (\mathcal{U}_\theta - \Omega^2) \Omega^2 \frac{d^2 G_n}{dr^2} + \Omega^2 \left[(\mathcal{U}_\theta - \Omega^2) \left(\frac{1}{r} - \frac{\rho'_0}{\rho_0} \right) + (\Omega^2 - \mathcal{U}_\theta)' \right] \frac{dG_n}{dr} + \left[(\mathcal{U}_\theta - \Omega^2)^2 \left(k^2 + \frac{n^2}{r^2} - \frac{\Omega^2}{c_0^2} \right) \right. \\ & \left. + \Upsilon(\Omega^2 - \mathcal{U}_\theta) \left[\Upsilon + \Omega \left(\frac{1}{r} - \frac{\rho'_0}{\rho_0} \right) \right] + \Upsilon' \Omega (\Omega^2 - \mathcal{U}_\theta) - \Upsilon [\Omega(\Omega^2 - \mathcal{U}_\theta)]' \right] G_n = \frac{\delta(r-r_0)}{r}. \end{aligned} \quad (3.1.8)$$

For calculating the Green's function, it is convenient to write the differential equation in self-adjoint form. This is given below:

$$\begin{aligned} & \frac{p_0}{c_0^2 r} (\mathcal{U}_\theta - \Omega^2)^2 \Omega^2 \frac{d}{dr} \left(\frac{rc_0^2}{p_0(\Omega^2 - \mathcal{U}_\theta)} \frac{dG_n}{dr} \right) + \left[(\mathcal{U}_\theta - \Omega^2)^2 \left(\frac{\Omega^2}{c_0^2} - k^2 - \frac{n^2}{r^2} \right) \right. \\ & \left. + \Upsilon(\mathcal{U}_\theta - \Omega^2) \left[\Upsilon + \Omega \left(\frac{1}{r} - \frac{\rho'_0}{\rho_0} \right) \right] - \Upsilon' \Omega (\Omega^2 - \mathcal{U}_\theta) + \Upsilon [\Omega(\Omega^2 - \mathcal{U}_\theta)]' \right] G_n = -\frac{\delta(r-r_0)}{r}. \end{aligned} \quad (3.1.9)$$

Using Duffy (2001) the Green's function is given by

$$G_n(r|r_0; \omega, k, n) = \frac{1}{r_0 \mathcal{W}(r_0) J(r_0, k)} \begin{cases} g_1(r_0; \omega, k, n) g_2(r; \omega, k, n) & r \leq r_0 \\ g_2(r_0; \omega, k, n) g_1(r; \omega, k, n) & r > r_0 \end{cases}, \quad (3.1.10)$$

where

$$J(r_0, k) = [\Omega^2(r_0, k) - \mathcal{U}_\theta(r_0)] \Omega^2(r_0, k), \quad (3.1.11)$$

and

$$\mathcal{W}(r_0, \omega, k, n) = g_1(r_0; \omega, k, n) \frac{dg_2}{dr}(r_0; \omega, k, n) - \frac{dg_1}{dr}(r_0; \omega, k, n) g_2(r_0; \omega, k, n) \quad (3.1.12)$$

is the Wrońskiian. In (3.1.10), $g_1(r; \omega, k, n)$ and $g_2(r; \omega, k, n)$ solve (3.1.9) with zero right-hand side, with $g_2(r; \omega, k, n)$ satisfying the boundary condition at $r = h$ and $g_1(r; \omega, k, n)$ satisfying the boundary condition at $r = 1$.

3.1.1 Boundary conditions

We use the Ingard-Myers boundary conditions from Section 1.2.1. From the derivation of the acoustic analogy we have

$$\rho_0 \mathcal{R}(v) = \mathcal{T}(p), \quad (3.1.13)$$

when we ignore source terms in (2.2.22). The Ingard-Myers boundary conditions in (1.2.4) then become

$$\begin{aligned} \frac{i\omega \mathcal{T}(p)}{\rho_0} &= \frac{1}{Z_h} \left(-i\omega + U_x \frac{\partial}{\partial x} + \frac{U_\theta}{r} \frac{\partial}{\partial \theta} \right) \mathcal{R}(p) \text{ on } r = h, \\ -\frac{i\omega \mathcal{T}(p)}{\rho_0} &= \frac{1}{Z_1} \left(-i\omega + U_x \frac{\partial}{\partial x} + \frac{U_\theta}{r} \frac{\partial}{\partial \theta} \right) \mathcal{R}(p) \text{ on } r = 1. \end{aligned} \quad (3.1.14)$$

Fourier transforming these gives the boundary condition at $r = h$ for $g_2(r)$ as

$$\frac{dg_2}{dr}(h) - \left[\frac{2nU_\theta(h)}{h^2\Omega(h)} + \frac{U_\theta^2(h)}{hc_0^2(h)} \right] g_2(h) + \frac{i\rho_0(h)}{\omega Z_h} [\Omega^2(h) - \mathcal{U}_\theta(h)] g_2(h) = 0, \quad (3.1.15)$$

while the boundary condition at $r = 1$ for $g_1(r)$ is given by

$$\frac{dg_1}{dr}(1) - \left[\frac{2nU_\theta(1)}{\Omega(1)} + \frac{U_\theta^2(1)}{c_0^2(1)} \right] g_1(1) - \frac{i\rho_0(1)}{\omega Z_1} [\Omega^2(1) - \mathcal{U}_\theta(1)] g_1(1) = 0. \quad (3.1.16)$$

If we let $Z_j \rightarrow \infty$ then we recover the hard wall boundary conditions from [Posson and Peake \(2013b\)](#), which are

$$\frac{dg_j}{dr}(r) - \left[\frac{2nU_\theta(r)}{r^2\Omega(r)} + \frac{U_\theta^2(r)}{rc_0^2(r)} \right] g_j(r) = 0, \quad (3.1.17)$$

for $j = 1, r = 1$ and $j = 2, r = h$.

3.1.2 High-frequency limit

The differential equation in (3.1.9) is much too complicated to find an exact analytical solution. Instead, we consider the equation in the high-frequency limit, which allows us to use the WKB method in [Appendix A.1](#) to find an approximate solution. We introduce a scaling of the axial wavenumber and azimuthal number with frequency;

$$\kappa = \frac{k}{\omega} \text{ and } \eta = \frac{n}{\omega}, \quad (3.1.18)$$

and assume that both $\kappa, \eta = \mathcal{O}(1)$. We treat η as a constant since we look at each azimuthal number individually. However, we treat κ as a variable, since once we calculate G_n we integrate it over κ to find G_ω . We also introduce the scaled functions

$$\Phi(r) = 1 - \kappa U_x(r) - \frac{\eta U_\theta(r)}{r}, \text{ and } \Upsilon^*(r) = \frac{U_\theta^2(r)}{rc_0^2(r)} \Phi(r) + \frac{2\eta U_\theta(r)}{r^2}, \quad (3.1.19)$$

so that $\Omega = \omega \Phi$ and $\Upsilon = \omega \Upsilon^*$.

The homogeneous differential equation for $g_j(r)$, (3.1.9) with zero right-hand side, becomes

$$(\mathcal{U}_\theta - \omega^2 \Phi^2) \omega^2 \Phi^2 \frac{d^2 g_j}{dr^2} + \omega^2 \Phi^2 \left[(\mathcal{U}_\theta - \omega^2 \Phi^2) \left(\frac{1}{r} - \frac{\rho'_0}{\rho_0} \right) + (\omega^2 \Phi^2 - \mathcal{U}_\theta)' \right] \frac{dg_j}{dr} - \mathcal{C}(r) g_j = 0, \quad (3.1.20)$$

where

$$\begin{aligned} \frac{\mathcal{C}(r)}{\omega^2} &= (\mathcal{U}_\theta - \omega^2 \Phi^2)^2 \left(\frac{\Phi^2}{c_0^2} - \kappa^2 - \frac{\eta^2}{r^2} \right) + \Upsilon^* (\mathcal{U}_\theta - \omega^2 \Phi^2) \left[\Upsilon^* + \Phi \left(\frac{1}{r} - \frac{\rho'_0}{\rho_0} \right) \right] \\ &\quad + \Upsilon^* [\Phi(\omega^2 \Phi^2 - \mathcal{U}_\theta)]' - \Phi(\omega^2 \Phi^2 - \mathcal{U}_\theta^*) \Upsilon^{*\prime}. \end{aligned} \quad (3.1.21)$$

The boundary conditions for $g_j(r)$ become

$$\frac{dg_2}{dr}(h) - \left[\frac{2\eta U_\theta(h)}{h^2 \Phi(h)} + \frac{U_\theta^2(h)}{hc_0^2(h)} \right] g_2(h) + \frac{i\rho_0(h)}{Z_h} \left[\omega \Phi^2(h) - \frac{\mathcal{U}_\theta(h)}{\omega} \right] g_2(h) = 0, \quad (3.1.22)$$

and

$$\frac{dg_1}{dr}(1) - \left[\frac{2\eta U_\theta(1)}{\Phi(1)} + \frac{U_\theta^2(1)}{c_0^2(1)} \right] g_1(1) - \frac{i\rho_0(1)}{Z_1} \left[\omega \Phi^2(1) - \frac{\mathcal{U}_\theta(1)}{\omega} \right] g_1(1) = 0. \quad (3.1.23)$$

When ω is large, some of the terms in (3.1.20) can be discarded. Assuming that $\Phi = \mathcal{O}(1)$, then to leading order the differential equation becomes

$$\frac{d^2 g_j}{dr^2}(r; \kappa) + \left(\frac{1}{r} - \frac{\rho'_0(r)}{\rho_0(r)} - 2 \frac{\partial_r \Phi(r, \kappa)}{\Phi(r)} \right) \frac{dg_j}{dr}(r; \kappa) + \omega^2 q_n(r, \kappa) g_j(r; \kappa) = 0, \quad (3.1.24)$$

where

$$q_n(r, \kappa) = \left(\frac{\Phi^2(r, \kappa)}{c_0^2(r)} - \kappa^2 - \frac{\eta^2}{r^2} \right). \quad (3.1.25)$$

We refer to (3.1.24) as the high-frequency limit of (3.1.20).

3.1.3 Applicability of high-frequency limit

The high-frequency limit in (3.1.24) is only valid when $\Phi = \mathcal{O}(1)$. Thus, if $\Phi(r, \kappa)$ is close to zero then the limit is not valid, since the coefficient of the second derivative in (3.1.20) approaches zero. Recall from Section 1.4.3 that the critical layer contains all values of κ where the coefficient of the largest derivative vanishes in (3.1.20) for some value of r in the duct. In this case, the critical layer is given by κ such that $\Phi(r, \kappa) = 0$ for some $r \in [h, 1]$, so

$$\mathcal{K}^{CL} = \left\{ \kappa \in \mathbb{C} \mid \inf_{h < r < 1} \frac{1}{U_x(r)} \left[1 - \frac{\eta U_\theta(r)}{r} \right] \leq \kappa \leq \sup_{h < r < 1} \frac{1}{U_x(r)} \left[1 - \frac{\eta U_\theta(r)}{r} \right] \right\}. \quad (3.1.26)$$

Although there is another zero at $\mathcal{U}_\theta - \omega^2 \Phi^2 = 0$, Heaton and Peake (2006) showed that it is removable. When we are close to \mathcal{K}^{CL} the high-frequency differential equation (3.1.24) is not valid, but when we are sufficiently far enough away from \mathcal{K}^{CL} then we use (3.1.24).

3.1.4 Consequences of using high-frequency limit everywhere

There are several consequences if we only consider the differential equation (3.1.20) and its Wrońskiian \mathcal{W} in the high-frequency limit (3.1.24). First, we are only able to find acoustic eigenmodes by solving the asymptotic dispersion relation $\mathcal{W} = 0$. The hydrodynamic eigenmodes lie close to the critical layer and do not solve $\mathcal{W} = 0$ for the Wrońskiian of (3.1.24). We consider a different method for asymptotically calculating the hydrodynamic modes in Chapter 4. Second, the Green's function will not be accurate around the critical layer.

3.2 Using WKB analysis to calculate the Green's function G_n as κ varies.

We now calculate the Green's function $G_n(r|r_0)$ in the high-frequency limit. To do this we solve (3.1.24) with the boundary conditions (3.1.22) and (3.1.23) to find $g_j(r)$, and then we calculate $G_n(r|r_0)$ from (3.1.10). It is clear from the canonical equations

$$(i) \ g''(r) + g(r) = 0, \quad (ii) \ g''(r) - g(r) = 0 \text{ and } (iii) \ g''(r) + rg(r) = 0, \quad (3.2.1)$$

that the behaviour of $q_n(r, \kappa)$ is going to be very important in determining the solutions $g_j(r; \kappa)$ of (3.1.24). The solutions to the equations in (3.2.1) are given by (i) a linear

combination of sines and cosines, (ii) a linear combination of exponentials and (iii) a linear combination of Airy functions.

When we use the WKB method to solve the differential equation in (3.1.24), we distinguish between the cases when $q_n(r, \kappa)$ has no zeros for $r \in [h, 1]$ and when it has a single zero or multiple zeros. Furthermore, when considering the solutions of (3.1.24) we allow κ to take values in the complex plane, so we are able to find the cut-off acoustic modes. Before we proceed any further we introduce the change of variables

$$g_j(r; \kappa) = \frac{\rho_0^{1/2}(r)\Phi(r, \kappa)v_j(r; \kappa)}{r^{1/2}}, \quad (3.2.2)$$

and then G_n is given by

$$G_n(r|r_0; \kappa) = \left(\frac{\rho_0(r)r_0}{\rho_0(r_0)r} \right)^{1/2} \frac{\Phi(r, \kappa)}{r_0 \mathcal{V}(r_0, \kappa) J(r_0, \kappa) \Phi(r_0, \kappa)} \begin{cases} v_1(r_0; \kappa)v_2(r; \kappa) & r \leq r_0 \\ v_2(r_0; \kappa)v_1(r; \kappa) & r > r_0 \end{cases}. \quad (3.2.3)$$

After substituting (3.2.2) into (3.1.24), we see that $v_j(r; \kappa)$ solves the differential equation

$$v_j''(r; \kappa) + (\omega^2 q_n(r, \kappa) + q_n^*(r, \kappa))v_j(r; \kappa) = 0, \quad (3.2.4)$$

where $q_n^*(r, \kappa)$ is some $\mathcal{O}(1)$ function. By Abel's theorem (Boyce et al., 1992) the Wrońskiian

$$\mathcal{V}(r_0, \kappa) = v_1(r_0; \kappa)v_2'(r_0; \kappa) - v_1'(r_0; \kappa)v_2(r_0; \kappa) \quad (3.2.5)$$

is now independent of r_0 . The boundary conditions are given by

$$\frac{dv_2}{dr}(h; \kappa) + f_2(h, \kappa)v_2(h; \kappa) = 0 \text{ and } \frac{dv_1}{dr}(1; \kappa) + f_1(1, \kappa)v_1(1; \kappa) = 0, \quad (3.2.6)$$

where

$$f_2(h, \kappa) = \frac{i\rho_0(h)\Phi^2(h, \kappa)}{Z_h}\omega + \frac{1}{2} \left(2 \frac{\partial}{\partial r} \Phi(h, \kappa) + \frac{\rho'_0(h)}{\rho_0(h)} - \frac{1}{h} \right) - \frac{\Upsilon^*(h)}{\Phi(h, \kappa)} - \frac{i\rho_0(h)\mathcal{U}_\theta(h)}{\omega Z_h}, \quad (3.2.7)$$

and

$$f_1(1, \kappa) = -\frac{i\rho_0(1)\Phi^2(1, \kappa)}{Z_1}\omega + \frac{1}{2} \left(2 \frac{\partial}{\partial r} \Phi(1, \kappa) + \frac{\rho'_0(1)}{\rho_0(1)} - 1 \right) - \frac{\Upsilon^*(1)}{\Phi(1, \kappa)} + \frac{i\rho_0(1)\mathcal{U}_\theta(1)}{\omega Z_1}. \quad (3.2.8)$$

The following proposition links the solutions of the various approximations of the differential equation (3.1.20), including the high-frequency limit in (3.1.24).

Proposition 3.2.1. *Let us assume that $\Phi = \mathcal{O}(1)$, so we are away from the critical layer. Then the physical optics WKB approximation (first two terms) of equations (3.1.20), (3.1.24), (3.2.4) and*

$$v_j''(r; \kappa) + \omega^2 q_n(r, \kappa)v_j(r; \kappa) = 0, \quad (3.2.9)$$

are exactly the same, where $v_j(r; \kappa)$ and $g_j(r; \kappa)$ are related by (3.2.2).

Proof. The solutions to (3.1.24) and (3.2.4) are the same due to the change of variables in (3.2.2). To show the rest of the solutions are equivalent we simply use the methods of Appendix A.1 and Bender and Orszag (1978) to calculate the WKB solution when $q_n(r, \kappa)$ has no zeros or a single zero. When we have no zeros of $q_n(r, \kappa)$ we make the substitution in (A.1.1), find $\delta = 1/\omega$ and then determine the S_m terms. The terms we neglect in the differential equation (3.1.20) compared to (3.1.24) and in (3.2.4) compared to (3.2.9) appear in S_2 and higher order terms, so the physical optics approximation is the same. When we have a single zero at $r = r_c$ we first make a change of variables $\tau = \omega^{2/3}\alpha^{1/3}(r_c - r)$, where $\alpha = q'_n(r_c)$, which gives an approximate Airy equation. The solution to this equation is then an Airy function plus a correction term. The terms we neglected from the differential equations (3.1.20) and (3.2.4) only affect the correction to the Airy function. We then match the solution of the approximate Airy equation to the two term zero turning point solution by equating powers of ω , as in Appendix A.1, and we find that we can ignore the correction term entirely. We thus get a solution of the form (A.1.19), and find the physical optics approximation is the same for each differential equation. \square

Our next step is to construct the zero and one turning point solutions of (3.2.9) using the WKB method.

3.2.1 Zero turning point solution

When there are no zeros of $q_n(r, \kappa)$ we easily find $v_1(r; \kappa)$ and $v_2(r; \kappa)$ using the method in Appendix A.1 with $1/\varepsilon = \omega$. We have that

$$v_j(r; \kappa) = |q_n(r, \kappa)|^{-1/4} \left(A^j(\kappa) e^{i\omega\psi_n(r, \kappa)} + B^j(\kappa) e^{-i\omega\psi_n(r, \kappa)} \right) \text{ with } \psi_n(r, \kappa) = \int_h^r \sqrt{q_n(s, \kappa)} ds, \quad (3.2.10)$$

where A^j and B^j are determined from the boundary conditions and depend on κ . After calculating

$$\frac{dv_j}{dr}(r; \kappa) = -\frac{\frac{\partial}{\partial r}q_n(r, \kappa)}{4q_n(r, \kappa)} v_j(r; \kappa) + i\omega |q_n(r, \kappa)|^{-1/4} \sqrt{q_n(r, \kappa)} \left(A^j(\kappa) e^{i\omega\psi_n(r, \kappa)} - B^j(\kappa) e^{-i\omega\psi_n(r, \kappa)} \right), \quad (3.2.11)$$

we find that the Wrońskiian is given by

$$\mathcal{V}(\kappa) = 2i\omega \left[B^1(\kappa)A^2(\kappa) - A^1(\kappa)B^2(\kappa) \right], \quad (3.2.12)$$

when $q_n(r, \kappa) > 0$ and

$$\mathcal{V}(\kappa) = 2\omega \left[B^1(\kappa)A^2(\kappa) - A^1(\kappa)B^2(\kappa) \right], \quad (3.2.13)$$

when $q_n(r, \kappa) < 0$. In either case we see that the Wrońskián is independent of r_0 , and zero for values of κ such that $B^1 A^2 - A^1 B^2 = 0$, and these values of κ are the eigenmodes of the flow.

From the boundary conditions in (3.2.6) we calculate that

$$A^1(\kappa) = \frac{B^1(\kappa)}{e^{2i\omega\psi_n(1,\kappa)}} \frac{i\omega\sqrt{q_n(1,\kappa)} + \frac{q'_n(1,\kappa)}{4q_n(1,\kappa)} - f_1(1,\kappa)}{i\omega\sqrt{q_n(1,\kappa)} - \frac{q'_n(1,\kappa)}{4q_n(1,\kappa)} + f_1(1,\kappa)} \quad (3.2.14)$$

and

$$A^2(\kappa) = \frac{B^2(\kappa)}{e^{2i\omega\psi_n(h,\kappa)}} \frac{i\omega\sqrt{q_n(h,\kappa)} + \frac{q'_n(h,\kappa)}{4q_n(h,\kappa)} - f_2(h,\kappa)}{i\omega\sqrt{q_n(h,\kappa)} - \frac{q'_n(h,\kappa)}{4q_n(h,\kappa)} + f_2(h,\kappa)}. \quad (3.2.15)$$

Inserting the definition of $f_j(r, \kappa)$ from (3.2.7) and (3.2.8) into (3.2.14) and (3.2.15) and expanding in inverse powers of frequency gives

$$A^1(\kappa) = \frac{B^1(\kappa)}{e^{2i\omega\psi_n(1,\kappa)}} \left[\frac{1 + \sigma_1(\kappa)}{1 - \sigma_1(\kappa)} + \mathcal{O}\left(\frac{1}{\omega}\right) \right] \quad (3.2.16)$$

and

$$A^2(\kappa) = B^2(\kappa) \left[\frac{1 - \sigma_h(\kappa)}{1 + \sigma_h(\kappa)} + \mathcal{O}\left(\frac{1}{\omega}\right) \right], \quad (3.2.17)$$

where

$$\sigma_h(\kappa) = \frac{\rho_0(h)\Phi^2(h, \kappa)}{Z_h\sqrt{q_n(h, \kappa)}} \text{ and } \sigma_1(\kappa) = \frac{\rho_0(1)\Phi^2(1, \kappa)}{Z_1\sqrt{q_n(1, \kappa)}}. \quad (3.2.18)$$

Thus, up to order $\mathcal{O}(1/\omega)$ we find

$$v_1(r; \kappa) = A^1(\kappa)|q_n(r, \kappa)|^{-1/4} \left(e^{i\omega\psi_n(r, \kappa)} + e^{2i\omega\psi_n(1, \kappa)} \frac{1 - \sigma_1(\kappa)}{1 + \sigma_1(\kappa)} e^{-i\omega\psi_n(r, \kappa)} \right), \quad (3.2.19)$$

$$v_2(r; \kappa) = A^2(\kappa)|q_n(r, \kappa)|^{-1/4} \left(e^{i\omega\psi_n(r, \kappa)} + \frac{1 + \sigma_h(\kappa)}{1 - \sigma_h(\kappa)} e^{-i\omega\psi_n(r, \kappa)} \right), \quad (3.2.20)$$

and (when $q_n(r, \kappa) > 0$)

$$\mathcal{V}(\kappa) = 2i\omega A^1(\kappa) A^2(\kappa) \frac{1 - \sigma_1(\kappa)}{1 + \sigma_1(\kappa)} \left[e^{2i\omega\psi_n(1, \kappa)} - \frac{(1 + \sigma_1(\kappa))(1 + \sigma_h(\kappa))}{(1 - \sigma_1(\kappa))(1 - \sigma_h(\kappa))} \right]. \quad (3.2.21)$$

Hence, we get the dispersion relation

$$e^{2i\omega\psi_n(1, \kappa)} = \frac{(1 + \sigma_1(\kappa))(1 + \sigma_h(\kappa))}{(1 - \sigma_1(\kappa))(1 - \sigma_h(\kappa))}, \quad (3.2.22)$$

which corresponds to $\mathcal{V} = 0$, and solving it gives the acoustic eigenmodes when $q_n(r, \kappa)$ has no zeros in the duct. Our dispersion relation agrees with [Vilenski and Rienstra \(2007a\)](#) when we set $U_\theta = 0$.

3.2.2 One turning point solution

When there is a single zero of $q_n(r, \kappa)$, at $r = r_c(\kappa)$, the uniformly valid (Langer) WKB solution is given by

$$v_j(r; \kappa) = \sqrt{\pi} \left(\frac{\tau(r, \kappa)}{q_n(r, \kappa)} \right)^{1/4} [A^j(\kappa) \text{Ai}(-\tau(r, \kappa)) + B^j(\kappa) \text{Bi}(-\tau(r, \kappa))], \quad (3.2.23)$$

where

$$\tau(r, \kappa) = \left(\frac{3\omega\Psi_n(r, \kappa)}{2} \right)^{2/3} \text{ and } \Psi_n(r, \kappa) = \int_{r_c}^r \sqrt{q_n(s, \kappa)} ds. \quad (3.2.24)$$

We then apply the boundary conditions at the duct walls to determine the constants $A^j(\kappa)$ and $B^j(\kappa)$. Since $\kappa \in \mathbb{C}$ we need to choose appropriate branch cuts so that we take the correct $1/2$ and $2/3$ roots. We choose the branch cut of the square root to be on the negative imaginary axis, so that

$$\lim_{\varepsilon_1 \rightarrow 0, \varepsilon_2 \rightarrow 0} \sqrt{-1 + \varepsilon_1 + i\varepsilon_2} = i \text{ and } \lim_{\varepsilon_1 \rightarrow 0, \varepsilon_2 \rightarrow 0} \sqrt{1 + \varepsilon_1 + i\varepsilon_2} = 1. \quad (3.2.25)$$

In [Figure 3.1](#) we see the chosen branch cut of the $2/3$ root, a line from 0 to ∞ between $-i$ and 1 . By choosing this branch cut we ensure

$$\lim_{\varepsilon_1 \rightarrow 0, \varepsilon_2 \rightarrow 0} (-i + \varepsilon_1 + i\varepsilon_2)^{2/3} = e^{i\pi} = -1 \text{ and } \lim_{\varepsilon_1 \rightarrow 0, \varepsilon_2 \rightarrow 0} (1 + \varepsilon_1 + i\varepsilon_2)^{2/3} = 1. \quad (3.2.26)$$

Given κ , let

$$\mathcal{Q}(\kappa) = \frac{\partial q_n}{\partial r}(r_c(\kappa), \kappa). \quad (3.2.27)$$

There are two different cases for the boundary conditions, depending on whether $\Re(\mathcal{Q}) > 0$ or $\Re(\mathcal{Q}) < 0$. The case $\Re(\mathcal{Q}) > 0$ corresponds to $\Re(q_n(1, \kappa)) > 0$ and $\Re(q_n(h, \kappa)) < 0$, and the signs are swapped for $\Re(\mathcal{Q}) < 0$. We differentiate between these two cases since the exponential and sinusoidal behaviour of $v_j(r; \kappa)$ at the duct walls depends on the sign of $\Re(\mathcal{Q})$.

We assume that r_c is far enough away from h and 1 such that we can use the asymptotic formulae for the Airy functions in [\(A.1.13\)](#) and [\(A.1.14\)](#), which we extend to the complex plane. The formulae in [\(A.1.13\)](#) apply for $|t| \rightarrow \infty$ with $\pi/3 < \arg(t) < 5\pi/3$, and the formulae in [\(A.1.14\)](#) apply for $|t| \rightarrow \infty$ with $|\arg(t)| < \pi/3$. We consider the situation when r_c is close to one of the duct walls in [Section 3.7.3](#).

The case when $\Re(\mathcal{Q}) > 0$

When $\Re(\mathcal{Q}) > 0$, $\Re(q_n(1, \kappa)) > 0$ and hence $\Psi_n(1, \kappa)$ is close to the positive real axis with our choice of branch cuts. Similarly, $\Psi_n(h, \kappa)$ is close to the negative imaginary axis. To apply the boundary conditions we first use the branch cut in [Figure 3.1](#) for calculating the

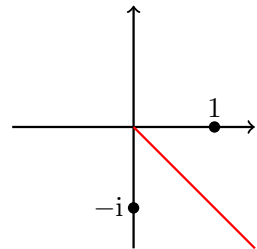


Figure 3.1: Branch cut for $2/3$ root.

$2/3$ root of $\tau(r, \kappa)$. We then use the asymptotic formulae for the Airy functions. For r close to 1 we use (A.1.13) and hence

$$\begin{aligned} v_j(r; \kappa) &\sim (q_n(r, \kappa))^{-1/4} \left[A^j(\kappa) \sin(\omega \Psi_n(r, \kappa) + \pi/4) + B^j(\kappa) \cos(\omega \Psi_n(r, \kappa) + \pi/4) \right], \\ &\sim (q_n(r, \kappa))^{-1/4} \left[\overline{A^j}(\kappa) e^{i\omega \Psi_n(r, \kappa)} + \overline{B^j}(\kappa) e^{-i\omega \Psi_n(r, \kappa)} \right], \end{aligned} \quad (3.2.28)$$

when $r \sim 1$, where

$$2\overline{A^j} = A^j e^{-i\pi/4} + B^j e^{i\pi/4} \text{ and } 2\overline{B^j} = A^j e^{i\pi/4} + B^j e^{-i\pi/4}. \quad (3.2.29)$$

For r close to h we use (A.1.14) and hence

$$v_j(r; \kappa) \sim (-q_n(r, \kappa))^{-1/4} \left[\frac{A^j(\kappa)}{2} e^{-i\omega \Psi_n(r, \kappa)} + B^j(\kappa) e^{i\omega \Psi_n(r, \kappa)} \right], \quad (3.2.30)$$

when $r \sim h$. We then apply the Ingard-Myers boundary conditions in the same way as Section 3.2.1, which gives

$$\frac{A^2(\kappa)}{2} = \Sigma_h(\kappa) B^2(\kappa), \text{ where } \Sigma_h(\kappa) = e^{2i\omega \Psi_n(h, \kappa)} \frac{1 + \sigma_h(\kappa)}{1 - \sigma_h(\kappa)} \quad (3.2.31)$$

and

$$\overline{B^1}(\kappa) = \Sigma_1(\kappa) \overline{A^1}(\kappa), \text{ where } \Sigma_1(\kappa) = e^{2i\omega \Psi_n(1, \kappa)} \frac{1 - \sigma_1(\kappa)}{1 + \sigma_1(\kappa)}. \quad (3.2.32)$$

We evaluate the Wrońskiian $\mathcal{V} = v_1 v'_2 - v'_1 v_2$ at $r = h$ to get

$$\mathcal{V}(\kappa) = i\omega \overline{A^1}(\kappa) B^2(\kappa) e^{-i\pi/4} [\Sigma_1(\kappa)(2\Sigma_h(\kappa) + i) - (2i\Sigma_h(\kappa) + 1)]. \quad (3.2.33)$$

Using (3.2.31) and (3.2.32) we find that

$$\begin{aligned} v_1(r; \kappa) &= \sqrt{\pi} \overline{A^1}(\kappa) \left(\frac{\tau(r, \kappa)}{q_n(r, \kappa)} \right)^{1/4} \times \\ &\quad \left[e^{i\pi/4} (1 - i\Sigma_1(\kappa)) \operatorname{Ai}(-\tau(r, \kappa)) + e^{-i\pi/4} (1 + i\Sigma_1(\kappa)) \operatorname{Bi}(-\tau(r, \kappa)) \right], \end{aligned} \quad (3.2.34)$$

and

$$v_2(r; \kappa) = \sqrt{\pi} B^2(\kappa) \left(\frac{\tau(r, \kappa)}{q_n(r, \kappa)} \right)^{1/4} [2\Sigma_h(\kappa) \operatorname{Ai}(-\tau(r, \kappa)) + \operatorname{Bi}(-\tau(r, \kappa))]. \quad (3.2.35)$$

The case when $\Re(\mathcal{Q}) < 0$

When $\Re(\mathcal{Q}) < 0$, $\Psi_n(1, \kappa)$ is close to the positive imaginary axis and $\Psi_n(h, \kappa)$ is close to the negative real axis. Thus, $-\Psi_n(1, \kappa)$ is close to the negative imaginary axis and $-\Psi_n(h, \kappa)$ is close to the positive real line. We define

$$\hat{\tau}(r, \kappa) = \left(-\frac{3\omega\Psi_n(r, \kappa)}{2} \right)^{2/3}, \quad (3.2.36)$$

and then replace τ by $\hat{\tau}$ in (3.2.23). We then perform the same analysis as when $\Re(\mathcal{Q}) > 0$, but switching h and 1. We find the Wrońskiian is given by

$$\mathcal{V}(\kappa) = \frac{\omega e^{i\pi/4} \overline{B^2}(\kappa) A^1(\kappa)}{2} [(2 + i\Sigma_1(\kappa)) - \Sigma_h(\kappa)(\Sigma_1(\kappa) + 2i)], \quad (3.2.37)$$

and the solutions $v_1(r; \kappa)$ and $v_2(r; \kappa)$ are given by

$$v_1(r; \kappa) = \sqrt{\pi} \frac{A^1(\kappa)}{2} \left(\frac{\hat{\tau}(r, \kappa)}{-q_n(r, \kappa)} \right)^{1/4} [2 \operatorname{Ai}(-\hat{\tau}(r, \kappa)) + \Sigma_1(\kappa) \operatorname{Bi}(-\hat{\tau}(r, \kappa))], \quad (3.2.38)$$

and

$$v_2(r; \kappa) = \sqrt{\pi} \overline{B^2}(\kappa) \left(\frac{\hat{\tau}(r, \kappa)}{-q_n(r, \kappa)} \right)^{1/4} \times \\ \left[e^{i\pi/4} (\Sigma_h(\kappa) - i) \operatorname{Ai}(-\hat{\tau}(r, \kappa)) + e^{-i\pi/4} (\Sigma_h(\kappa) + i) \operatorname{Bi}(-\hat{\tau}(r, \kappa)) \right]. \quad (3.2.39)$$

Limit for (very) large frequency

The dispersion relation when $\Re(\mathcal{Q}) > 0$ is given by

$$\Sigma_1(\kappa)(2\Sigma_h(\kappa) + i) - (2i\Sigma_h(\kappa) + 1) = 0. \quad (3.2.40)$$

Using the definition of $\Sigma_h(\kappa)$ and $\Sigma_1(\kappa)$, for large ω we expect Σ_h to be exponentially large compared to Σ_1 , since $\Psi_n(1, \kappa)$ is close to the positive real axis and $\Psi_n(h, \kappa)$ is close to the negative imaginary axis. Thus, we could simplify the dispersion relation to

$$\Sigma_1(\kappa) - i = e^{2i\omega\Psi_n(1, \kappa)} \frac{1 - \sigma_1(\kappa)}{1 + \sigma_1(\kappa)} - i = 0. \quad (3.2.41)$$

However, we show below this is a bad idea, even for large frequencies such as $\omega = 25$. In [Vilenski and Rienstra \(2007a\)](#) this dispersion relation was used in the case of no swirl. They also suggested that (in the case of no swirl) the lining of the wall where $q_n(r, \kappa)$ is negative (in this case $r = h$) should not have a significant effect on the dispersion relation. If we use the dispersion relation (3.2.41) instead of (3.2.40) then the dispersion relation does not depend on the duct wall $r = h$.

Let us set $U_x = 0.5$, $U_\theta(r) = 0.1r + 0.1/r$, $\omega = 25$, $\eta = 0.6$ and $h = 0.6$ in a hard-walled duct. We later refer to these parameters as Example 3 in [Section 3.4.1](#). Using [Section 3.3.2](#) we find a numerical eigenmode at $\omega\kappa = -13.83 + 10.67i$ which has a critical point at $r_c = 0.613 - 0.004i$.

In [Figure 3.2](#) we see the corresponding asymptotic eigenmodes which solve the two different dispersion relations (3.2.40) and (3.2.41). We see that the asymptotic mode that

solves (3.2.40) is significantly closer to the numerical mode and more accurate. We also plot

$$v_{DR}(r, \kappa) = \begin{cases} Av_1(0.8, \kappa)v_2(r, \kappa) & r \leq 0.8 \\ Av_2(0.8, \kappa)v_1(r, \kappa) & r > 0.8 \end{cases}, \quad (3.2.42)$$

for some constant A and κ being the asymptotic eigenmode in Figure 3.2. We will see later that v_{DR} is the Green's function associated to this eigenmode. When κ is an eigenmode, the function v_{DR} should be smooth since $v_1(r; \kappa)$ and $v_2(r; \kappa)$ are linearly dependent. We

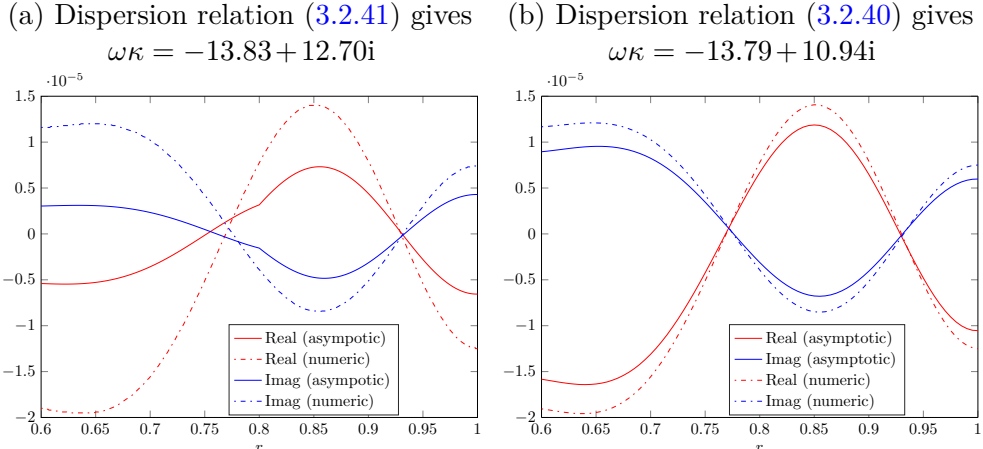


Figure 3.2: Effect of using the correct dispersion relation, parameters given by Example 3 in Section 3.4.1.

see this is not the case when we use the dispersion relation (3.2.41) in Figure 3.2a. However, in Figure 3.2b we see that v_{DR} is smooth and does not have a kink when we use the correct asymptotic dispersion relation. In Figure 3.2 we also numerically calculate $v_1(r; \kappa)$ and $v_2(r; \kappa)$ from the differential equation (3.1.20) at the numerical eigenmode, and we see the numerical results are more accurately approximated by using the dispersion relation (3.2.40). The reason for the dispersion relation (3.2.41) performing so poorly is that the critical point is close to the duct walls. We will use the full dispersion relations in (3.2.21), (3.2.33) and (3.2.37) for the rest of this work.

3.2.3 Regions for WKB analysis

Having calculated the WKB solutions of the differential equation (3.2.9), we next identify the regions of κ space when we should use the zero turning point solution and the one turning point solution.

The r region

Suppose we define the region to use the one turning point solution to be precisely κ such that $r_c(\kappa) \in [h, 1]$, where $q_n(r_c(\kappa), \kappa) = 0$, and we use the zero turning point solution everywhere else. What happens when $r_c(\kappa) = h - \varepsilon$? Then we would use the zero turning point solution, consisting of linear combinations of sines and cosines or exponentials, since $q_n(r, \kappa)$ has no zeros for $r \in [h, 1]$. However, it would not be accurate, since for r close to h

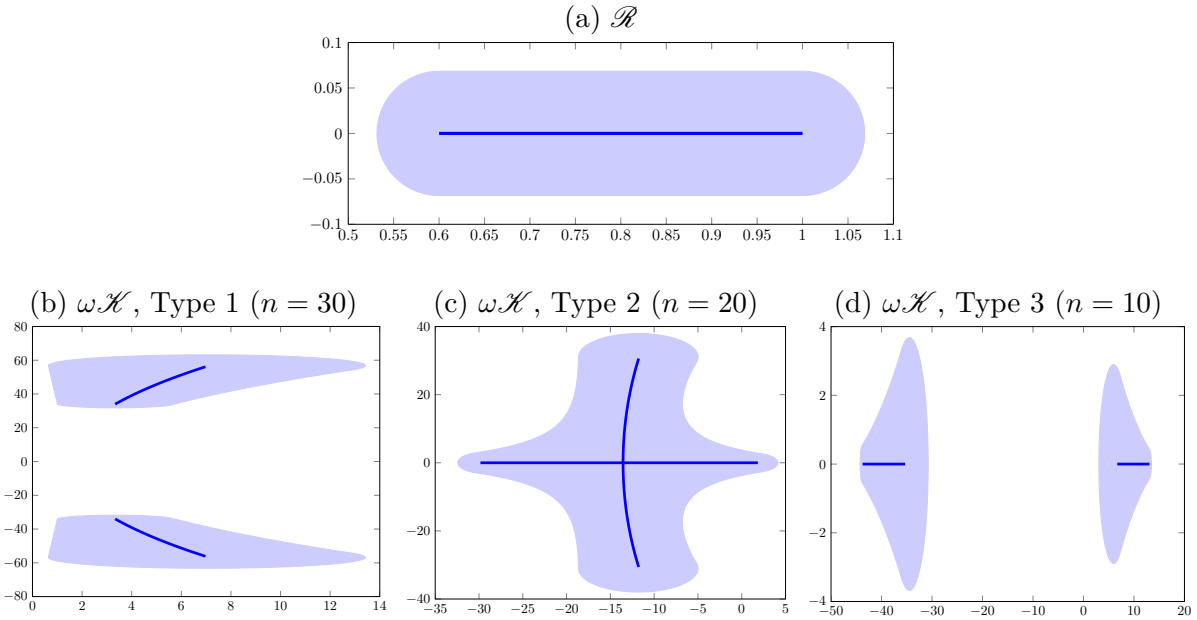


Figure 3.3: (a) Region \mathcal{R} when $\omega = 25$, $h = 0.6$; (b) to (d) three different regimes for the region \mathcal{K} when $h = 0.6$, $\omega = 25$, $U_x = 0.5$ and $U_\theta(r) = 0.1r + 0.1/r$. Blue line: exact critical points; shaded region: close to a critical point.

(and hence the critical point) the true solution would a linear combination of Airy functions such as (3.2.34) or (3.2.35).

Thus, for any r_c outside but close to the duct walls, we use the one turning point solution, so that near r_c the solution behaves like the Airy function. We use the one turning point solution when $\omega^{-2/3} \ll h - r_c \ll \omega^{-1}$ and $\omega^{-2/3} \ll r_c - 1 \ll \omega^{-1}$, which follows from (A.1.19). To be precise, we choose the one turning point solution region to be r_c such that $h - \omega^{-5/6} < r_c < 1 + \omega^{-5/6}$, although we could choose any exponent between $-2/3$ and -1 .

Since κ is complex, we consider the situation when $r_c(\kappa)$ is complex. We define the one turning point solution region to consist of r_c which lie within a distance of $\omega^{-5/6}$ from the duct $[h, 1]$. We denote this region \mathcal{R} , with

$$\mathcal{R} = \left\{ r_c \in \mathbb{C} \mid |r_c - r| < \omega^{-5/6} \text{ for } r \in [h, 1] \right\}, \quad (3.2.43)$$

and we see an example in Figure 3.3a. We use the one turning point solution in \mathcal{R} , and the zero turning point solution in $\mathbb{C} \setminus \mathcal{R}$. We could also use the one turning point solution in $\mathbb{C} \setminus \mathcal{R}$, but using the asymptotic behaviour of the Airy functions from Appendix A.1 reduces the solution to the same form as the zero turning point solution.

The κ region

We could define the one turning point region in κ space as κ such that $r_c(\kappa) \in \mathcal{R}$, but it is much more useful to determine an exact formula. To do this we find $\kappa(r_c)$, which are zeros of $q_n(r, \kappa)$. We use the definition of $q_n(r, \kappa)$ in (3.1.25), and then the zeros satisfy

$$\kappa^2 \left(\frac{U_x^2(r_c)}{c_0^2(r_c)} - 1 \right) + 2 \frac{U_x(r_c)}{c_0^2(r_c)} \left(\frac{\eta U_\theta(r_c)}{r_c} - 1 \right) \kappa + \frac{1}{c_0^2(r_c)} \left(1 - \frac{\eta U_\theta(r_c)}{r_c} \right)^2 - \frac{\eta^2}{r_c^2} = 0, \quad (3.2.44)$$

which is just a quadratic in κ . Thus, we find that $\kappa = s^\pm(r_c)$, where

$$s^\pm(r_c) = \frac{U_x(r_c) \left(1 - \frac{\eta U_\theta(r_c)}{r_c}\right) \pm c_0(r_c) \sqrt{\left(1 - \frac{\eta U_\theta(r_c)}{r_c}\right)^2 + \frac{\eta^2}{r_c^2} [U_x^2(r_c) - c_0^2(r_c)]}}{U_x^2(r_c) - c_0^2(r_c)}. \quad (3.2.45)$$

We denote the region of κ space where we use the one turning point solution as \mathcal{K} , and it is given by

$$\mathcal{K} = s^+(\mathcal{R}) \cup s^-(\mathcal{R}) = \{s^+(r) | r \in \mathcal{R}\} \cup \{s^-(r) | r \in \mathcal{R}\}. \quad (3.2.46)$$

In this region there is either a critical point r_c in the duct, or a critical point close enough to the duct that we should use the one turning point solution.

Three distinct regions

We find that there are three distinct shapes that the region \mathcal{K} takes. Type 1 corresponds to $q_n(r, \kappa)$ having no solutions $\kappa \in \mathbb{R}$ for $r \in [h, 1]$. Type 2 corresponds to $q_n(r, \kappa)$ having solutions $\kappa \in \mathbb{R}$ for some values of $r \in [h, 1]$, while Type 3 corresponds to $q_n(r, \kappa)$ having solutions $\kappa \in \mathbb{R}$ for all values of $r \in [h, 1]$. Each type gives a distinct shape for \mathcal{K} , which we see in [Figure 3.3](#). To determine which regime \mathcal{K} is in, we look at the discriminant in [\(3.2.45\)](#). The region \mathcal{K} is Type 1 if the discriminant is negative for all values of $r \in [h, 1]$, Type 3 if the discriminant is positive for all values of $r \in [h, 1]$ and Type 2 if the discriminant changes sign in the duct.

In [Figure 3.3](#) we see the three different regimes for the flow $U_x = 0.5$, $U_\theta(r) = 0.1r + 0.1/r$, which is the flow we consider in Examples 3 and 4 in [Section 3.4.1](#). If we have non-zero swirl then the \mathcal{K} region does not have left-right symmetry, although it is still symmetric about the real line. The lining has no effect on the region \mathcal{K} . The different regimes for \mathcal{K} have no effect on the method for determining the Green's function or eigenmodes. However, the regime generally changes the number of cut-on eigenmodes, since we find most (but not all) of the cut-on modes in the region \mathcal{K} .

3.3 Calculating the acoustic eigenmodes

3.3.1 Asymptotic method

To find the eigenmodes asymptotically we numerically solve the dispersion relations from [Section 3.2](#). Thus, we solve

$$e^{2i\omega\psi_n(1, \kappa)} - \frac{(1 + \sigma_1(\kappa))(1 + \sigma_h(\kappa))}{(1 - \sigma_1(\kappa))(1 - \sigma_h(\kappa))} = 0 \text{ for } \kappa \in \mathbb{C} \setminus \mathcal{K}, \quad (3.3.1)$$

$$\Sigma_1(\kappa)(2\Sigma_h(\kappa) + i) - (2i\Sigma_h(\kappa) + 1) = 0 \text{ for } \kappa \in \mathcal{K} \text{ and } \Re(\mathcal{Q}(\kappa)) > 0, \quad (3.3.2)$$

$$(2 + i\Sigma_1(\kappa)) - \Sigma_h(\kappa)(\Sigma_1(\kappa) + 2i) = 0 \text{ for } \kappa \in \mathcal{K} \text{ and } \Re(\mathcal{Q}(\kappa)) < 0. \quad (3.3.3)$$

Implementation

To solve the dispersion relations (3.3.1), (3.3.2) and (3.3.3) we employ numerical methods. Our main philosophy for solving them is to use the numerical eigenmodes as a starting guess and then use a numerical non-linear equation solver, for example “fsolve” in MATLAB.

There are other approaches too, for example, it is well known that we can calculate the numerical eigenmodes exactly in the case of constant shear, zero swirl and hard walls. The differential equation in (3.1.24) reduces to the Pridmore-Brown equation, whose solutions are a linear combination of Bessel functions. We could use these eigenmodes as an initial guess for our numerical solver rather than the numerical eigenmodes. However, as soon as we start varying the shear, swirl or lining the initial guess will be poor and we may not be able to find all the eigenmodes asymptotically.

Another possible approach is to apply asymptotic methods to solve the dispersion relations. To leading order, the eigenmodes are given by ([Heaton and Peake, 2005](#))

$$\kappa_n = an + b + \mathcal{O}(n^{-1}), \quad (3.3.4)$$

where the coefficients are given by

$$a = \frac{i\pi}{\omega} \left(\int_h^1 \sqrt{1 - \frac{U_x^2(r)}{c_0^2(r)}} dr \right)^{-1} \quad \text{and} \quad b = a \left(\frac{\omega}{i\pi} \int_h^1 \frac{U_x(r) \left(\frac{\eta U_\theta(r)}{r} - 1 \right)}{c_0^2(r) \sqrt{1 - \frac{U_x^2(r)}{c_0^2(r)}}} dr \right), \quad (3.3.5)$$

and the effect of the lining is restricted to lower order terms. However, this leading order approximation is only accurate for far away cut-off modes. The modes we will be most interested in are the cut-on modes and nearest cut-off modes, for which this approximation is not sufficiently accurate. In [Vilenski and Rienstra \(2007a\)](#), more terms were calculated in the asymptotic expansion. However, their results do not include swirl and rely on the impedances Z_j being large, so are not very applicable. In addition, their results only apply when there are no zeros of $q_n(r, \kappa)$, so for $\kappa \in \mathbb{C} \setminus \mathcal{K}$.

3.3.2 Numerical method

To calculate the eigenmodes numerically, we begin with the linearised Euler equations from [Section 1.4.2](#), but using the energy equation in (1.4.21). After using the combined mass and energy equation in (1.4.25), the system of linearised equations is given by

$$\frac{1}{c_0^2} \frac{D_0 p}{Dt} + \frac{\rho_0 U_\theta^2}{rc_0^2} v + \rho_0 (\nabla \cdot \mathbf{u}) = 0, \quad (3.3.6)$$

$$\rho_0 \left(\frac{D_0 u}{Dt} + v \frac{dU_x}{dr} \right) + \frac{\partial p}{\partial x} = 0, \quad (3.3.7)$$

$$\rho_0 \left(\frac{D_0 v}{Dt} - \frac{2U_\theta w}{r} \right) - \frac{U_\theta^2}{r} \rho + \frac{\partial p}{\partial r} = 0, \quad (3.3.8)$$

$$\rho_0 \left(\frac{D_0 w}{Dt} + \frac{v}{r} \frac{d}{dr} (r U_\theta) \right) + \frac{1}{r} \frac{\partial p}{\partial \theta} = 0, \quad (3.3.9)$$

$$\frac{D_0 s}{Dt} + \frac{ds_0}{dr} v = 0. \quad (3.3.10)$$

This is a system of five equations involving six variables, so we use the constitutive equations for the total flow to eliminate ρ . We first define s to be the entropy perturbation and \underline{s} to be the total entropy of the flow. Rearranging (2.1.4) for the total flow gives

$$\underline{\rho} = \gamma^{1/\gamma} \underline{p}^{1/\gamma} e^{-\underline{s}/\gamma}, \quad (3.3.11)$$

and hence expanding this about the base flow gives

$$\begin{aligned} \rho_0 + \rho &= \gamma^{1/\gamma} (p_0 + p)^{1/\gamma} \exp \left(-\frac{s_0 + s}{c_p} \right) \\ &= \gamma^{1/\gamma} \left(p_0^{1/\gamma} + p \frac{p_0^{(1/\gamma)-1}}{\gamma} + \dots \right) \left(e^{-s_0/c_p} - s \frac{e^{-s_0/c_p}}{c_p} + \dots \right). \end{aligned} \quad (3.3.12)$$

Equating $\mathcal{O}(1)$ terms gives precisely (2.1.4). Equating first order perturbations then gives

$$\rho = p \gamma^{1/\gamma} \frac{p_0^{(1/\gamma)-1} e^{-s_0/c_p}}{\gamma} - s \frac{\gamma^{1/\gamma} p_0^{1/\gamma} e^{-s_0/c_p}}{c_p} = \frac{1}{c_0^2} p - \frac{\rho_0}{c_p} s. \quad (3.3.13)$$

We thus eliminate the density perturbation ρ from the system of equations by using (3.3.13), which gives a system of five equation acting on five variables. We then Fourier transform the five variables using

$$\{u, v, w, p, s\}(r, x, \theta, t) = \int \sum_n \int \{U(r), V(r), W(r), P(r), S(r)\} e^{ikx} dk e^{in\theta} e^{-i\omega t} d\omega. \quad (3.3.14)$$

After Fourier transforming we find

$$-\frac{i\Omega P}{c_0^2} + V \frac{\rho_0 U_\theta^2}{rc_0^2} + \rho_0 \left[\frac{inW}{r} + ikU + \frac{V}{r} + \frac{dV}{dr} \right] = 0, \quad (3.3.15)$$

$$\rho_0 \left[-i\Omega U + V \frac{dU_x}{dr} \right] + ikP = 0, \quad (3.3.16)$$

$$\rho_0 \left[-i\Omega V - \frac{2U_\theta}{r} W \right] + \frac{dP}{dr} - \frac{U_\theta^2}{rc_0^2} P + \frac{\rho_0 U_\theta^2}{rc_p} S = 0, \quad (3.3.17)$$

$$\rho_0 \left[-i\Omega W + \frac{V}{r} \frac{d}{dr} (r U_\theta) \right] + \frac{inP}{r} = 0, \quad (3.3.18)$$

$$-i\Omega S + \frac{ds_0}{dr} V = 0. \quad (3.3.19)$$

We then let

$$\hat{\Omega} = \omega - \frac{nU_\theta}{r} \text{ and } \zeta = 1 - \frac{U_x^2}{c_0^2}, \quad (3.3.20)$$

and after some rearranging we have the final eigenvalue problem to be solved:

$$-\frac{U_x \hat{\Omega}}{c_0^2 \zeta} iU + \left[\frac{U_x}{c_0^2 \zeta} \frac{dU_x}{dr} - \frac{1}{r\zeta} - \frac{U_\theta^2}{\zeta r c_0^2} \right] V - \frac{1}{\zeta} \frac{dV}{dr} - \frac{n}{r\zeta} iW + \frac{i\hat{\Omega}}{c_0^2 \rho_0 \zeta} P = kiU, \quad (3.3.21)$$

$$\frac{\hat{\Omega}}{U_x} V - \frac{2U_\theta}{rU_x} iW + \frac{i}{\rho_0 U_x} \frac{dP}{dr} - \frac{iU_\theta^2}{\rho_0 U_x r c_0^2} P + i \frac{U_\theta^2}{rc_p U_x} S = kV, \quad (3.3.22)$$

$$-\frac{1}{U_x} \left[\frac{U_\theta}{r} + \frac{dU_\theta}{dr} \right] V + \frac{\hat{\Omega}}{U_x} iW - \frac{in}{r\rho_0 U_x} P = kiW, \quad (3.3.23)$$

$$-\frac{i\rho_0 \hat{\Omega}}{\zeta} iU + i \frac{\rho_0}{\zeta} \left[\frac{dU_x}{dr} - \left(\frac{U_\theta^2}{c_0^2} + 1 \right) \frac{U_x}{r} \right] V - \frac{i\rho_0 U_x}{\zeta} \frac{dV}{dr} - \frac{in\rho_0 U_x}{r\zeta} iW - \frac{U_x \hat{\Omega}}{c_0^2 \zeta} P = kP, \quad (3.3.24)$$

$$i \frac{1}{U_x} \frac{ds_0}{dr} V + \frac{\hat{\Omega}}{U_x} S = kS. \quad (3.3.25)$$

The boundary conditions for the eigenvalue problem are given by the Ingard-Myers boundary conditions in (1.2.4). Fourier transforming these gives

$$i\omega V(h) = -i \frac{\Omega(h)}{Z_h} P(h) \text{ and } i\omega V(1) = i \frac{\Omega(1)}{Z_1} P(1), \quad (3.3.26)$$

which we rearrange to give

$$Z_h \frac{\omega V(h)}{U_x(h)} + \frac{\hat{\Omega}(h)P(h)}{U_x(h)} - kP(h) = 0, \quad (3.3.27)$$

and

$$Z_1 \frac{\omega V(1)}{U_x(1)} - \frac{\hat{\Omega}(1)P(1)}{U_x(1)} + kP(1) = 0. \quad (3.3.28)$$

Homentropic case

A homentropic fluid has constant entropy, so s_0 is constant. As a result, the only possible non-zero solution S to (3.3.25) is when k is in the critical layer, which is defined by

$$\mathcal{K}^{CL} = \inf_{h < r < 1} \frac{\hat{\Omega}}{U_x} \leq k \leq \sup_{h < r < 1} \frac{\hat{\Omega}}{U_x}. \quad (3.3.29)$$

So, away from the critical layer (and hence for all acoustic eigenmodes), $S = 0$ and we only need to solve a system of four differential equations. These are the four equations that are solved in [Posson and Peake \(2013b\)](#).

Implementation

We implement the numerical scheme using Chebfun. We solve the system directly using Chebfun's capabilities without discretising the system of equation, as in [Appendix A.2](#). There are two ways to deal with the eigenmode k appearing in the boundary condition. The first is to use (3.3.24) to eliminate kP , although this makes our boundary condition more complicated and unwieldy. The alternative is to introduce a sixth variable, \hat{P} , and a

sixth equation, $\hat{P} = kP$. Our boundary conditions then stay relatively simple. In practice, we find both approaches work equally well and give the same eigenmodes.

We validate our numerical solution by comparing to code written by Hélène Posson and used in [Posson and Peake \(2012, 2013a,b\)](#). However, there was a mistake in Posson's code for swirling mean flow in a duct with acoustically lined walls. This affects some figures and results in [Posson and Peake \(2013a\)](#), although not significantly. The approach used by Posson involved discretising the equations using a staggered Chebyshev grid, based on [Khorrami \(1991\)](#), with the full details given in [Posson and Peake \(2013b\)](#). Other approaches to solving the numerical eigenvalue problem involve using finite differences, such as in [Maldonado et al. \(2015\)](#).

We find that both our numerical scheme and Posson's are able to calculate as many acoustic modes as we want, with results agreeing to at least five decimal places except for swirling mean flow in an acoustically lined duct. We note that our solver has an advantage compared to Posson's in that we can input any shear or swirl profile and not just a Laurent series.

Posson's solver also found a significant number of hydrodynamic modes. Using our Chebfun implementation we find just a few hydrodynamic modes, but only when we choose the start point for finding modes to be close to one end of the critical layer. We discuss a different numerical solver for finding the hydrodynamic modes in [Chapter 4](#).

3.4 Comparison of asymptotic and numerical eigenmodes

In this section, we compare the numerical and asymptotic eigenmodes for a variety of mean flow profiles. We begin with some simple examples, before moving onto semi-realistic swirling flow. We show the effects of swirl, lining and entropy on the eigenmodes. For each example, we plot the acoustic asymptotic and numeric eigenmodes, and give a table of the most cut-on eigenmodes, with all results to two decimal places. [Table 3.1](#) provides a legend for the eigenmode figures such as [Figure 3.5](#). We label the cut-off modes outwards from the real axis, and number them independently for the upstream and downstream modes.

Table 3.1: Legend for eigenmode figures.

Symbol	Meaning
	The region $\omega\mathcal{H}$.
	κ corresponding to $r_c(\kappa) \in [h, 1]$.
	Numerical eigenmode.
	Asymptotic eigenmode solving the zero turning point dispersion relation (3.3.1).
	Asymptotic eigenmode solving the one turning point dispersion relations (3.3.2) or (3.3.3).
Bold eigenmode	Eigenmode in \mathcal{H} but we solve the zero turning point dispersion relation.

In some cases we get more accurate results from solving the zero turning point dispersion relation in the region \mathcal{K} , when we should be using the one turning point dispersion relation. These asymptotic modes are in bold, and there are two reasons for using the “wrong” dispersion relation. First, the region \mathcal{K} is only asymptotically defined. By choosing the region \mathcal{R} to be within ω^{-1} of the duct we make \mathcal{K} smaller, while choosing the region \mathcal{R} to be within $\omega^{-2/3}$ of the duct we make \mathcal{K} larger. Second, we assumed in [Section 3.2](#) that $v_1(r; \kappa)$ and $v_2(r; \kappa)$ are exponential or sinusoidal at the duct walls to calculate the constants A^j and B^j . This is only true if the critical point r_c is not close to the duct walls. If r_c is close to the duct walls we should use explicit Airy functions and we consider this further in [Section 3.7.3](#).

3.4.1 Test cases

We first consider some simple polynomial mean flows with constant entropy. This allows us to see the effect of both swirl and lining on the eigenmodes. [Table 3.2](#) shows the different parameters for each example. Additionally, for each example we assume the inner duct wall is at $h = 0.6$. We plot some of the more complicated mean flow profiles in [Figure 3.4](#).

Table 3.2: Parameters for Examples 1 to 6.

Example	Shear $U_x(r)$	Swirl $U_\theta(r)$	ω	η	Lining	\mathcal{K} region
1	0.5	0	25	0.6	Hard walls	Type 3
2	0.5	0	25	0.6	$Z_j = 1 - 2i$	Type 3
3	0.5	$0.1r + 0.1/r$	25	0.6	Hard walls	Type 2
4	0.5	$0.1r + 0.1/r$	25	0.6	$Z_j = 1 - 2i$	Type 2
5	$0.5 + 0.4r - 0.2r^2$	0	25	0.6	Hard walls	Type 3
6	$0.5 + 0.4r - 0.2r^2$	0	25	0.6	$Z_j = 1 - 2i$	Type 3

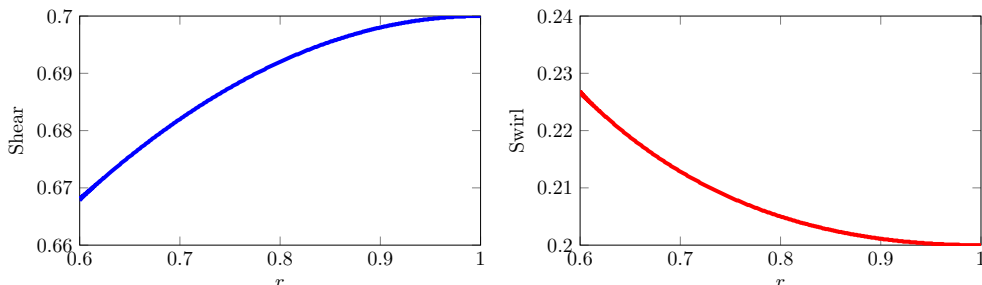


Figure 3.4: Shear and swirl profiles with $U_x(r) = 0.5 + 0.4r - 0.2r^2$ and $U_\theta(r) = 0.1r + 0.1/r$.

Example 1

For Example 1 we first plot the region $\omega\mathcal{K}$ in [Figure 3.5](#) and we see that it is of the third type from [Section 3.2.3](#). We choose these flow parameters because they were given in [Vilenski and Rienstra \(2007a\)](#). In [Figure 3.5](#) we find every asymptotic eigenmode (green or blue), and the asymptotic eigenmodes agree very favourably with the numerical eigenmodes (red). For the cut-off modes, we find the real part of the asymptotic eigenmode agrees exactly with the numerical mode. The imaginary part of the asymptotic mode differs

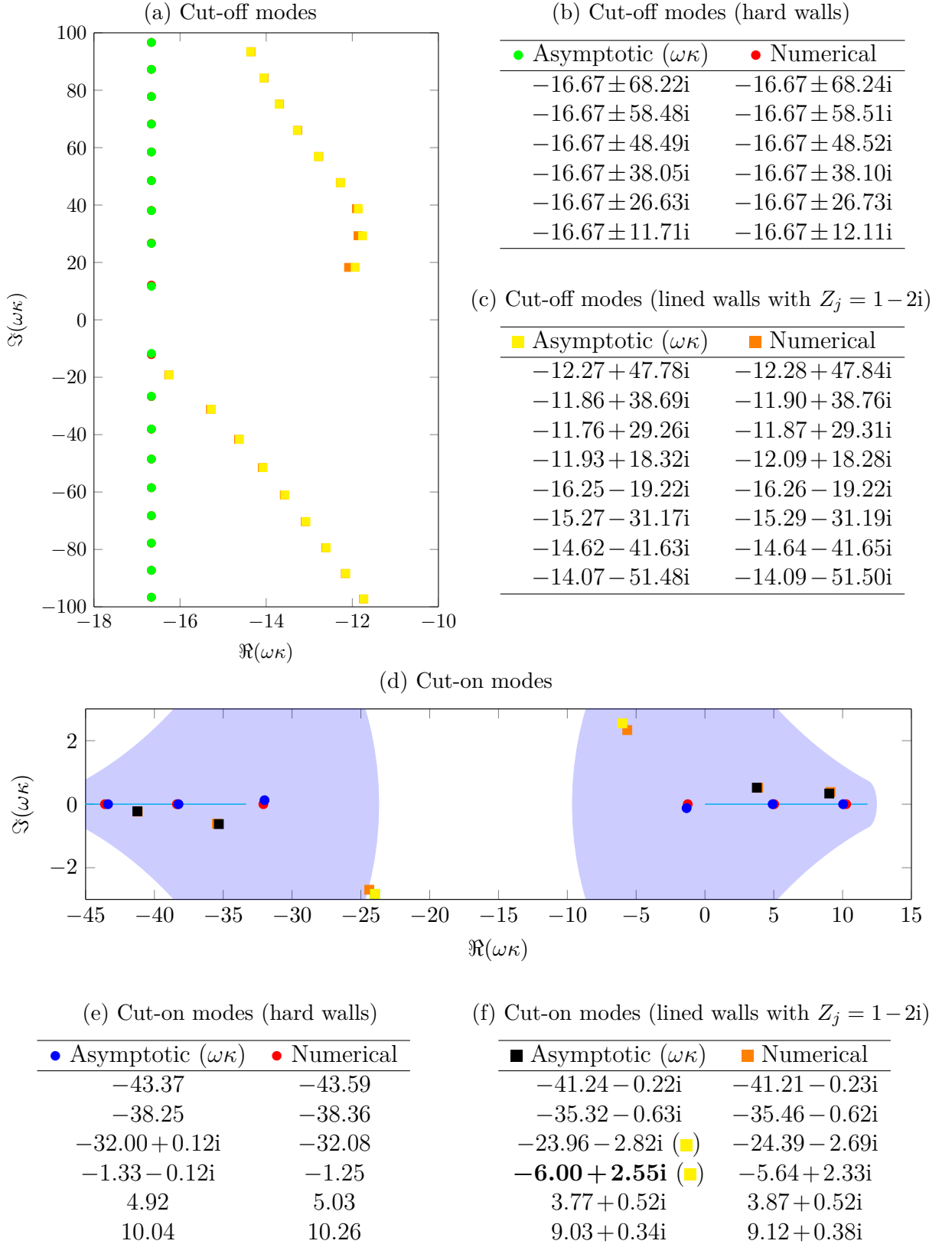


Figure 3.5: Examples 1 & 2: constant shear with zero swirl.

Plot of the asymptotic and numerical eigenmodes. The parameters are $\omega = 25$, $\eta = 0.6$, $U_x = 0.5$, $U_\theta = 0$, $h = 0.6$ with both hard walls (green, blue; red) and lined walls of impedance $Z_j = 1 - 2i$ (yellow, black; orange).

slightly, although it is still very close and we see that by the fifth and sixth modes there is almost no difference. The relative error for the first cut-off mode is 1.13%, while for the sixth cut-off mode it is 0.02%.

In Figure 3.5 we find there are six cut-on asymptotic modes, three either side of the line of cut-off modes. They were all found by solving the one turning point dispersion relation. Of these six modes, four have a critical point in the duct, and these asymptotic eigenmodes approximate the numerical eigenmodes reasonably well, although the asymptotic modes are not as accurate as the cut-off modes. The other two cut-on modes (given numerically by $k = -32.08$ and $k = -1.25$) have a critical point r_c outside of the duct walls, and we find the corresponding asymptotic eigenmodes have a small non-zero imaginary part. This is a quirk of the asymptotic method, but despite this, we still asymptotically approximate these two eigenmodes very accurately. This non-zero imaginary part originates because we assume that $v_1(r; \kappa)$ and $v_2(r; \kappa)$ are either exponential or sinusoidal at the duct walls to calculate A^j and B^j .

We note that our asymptotic results differ from those in Vilenski and Rienstra (2007a), since we use the more accurate dispersion relation (3.2.40) and not (3.2.41). Additionally, our $q_n(r, \kappa)$ term differs to their q term by $\mathcal{O}(1/\omega^2)$ factors.

Example 2

In Example 2 the parameters are the same as Example 1, but now the duct walls have acoustic lining of impedance $Z_j = 1 - 2i$. In Figure 3.5 we plot the asymptotic eigenmodes (yellow, black) and the numerical eigenmodes (orange), and see very good agreement between them. The lining shifts all the cut-on modes off the real line, with the downstream modes now having a positive imaginary part and the upstream modes now having a negative imaginary part. In Figure 3.5 we see that we asymptotically approximate four of the six cut-on numerical eigenmodes very accurately. These four modes correspond to the four cut-on modes in a hard-walled duct with a critical point r_c in the duct. For the other two cut-on modes, we solve the zero turning point dispersion relation to obtain the most accurate asymptotic modes. The numerical eigenmode $k = -24.39 - 2.69i$ lies outside of the region $\omega\mathcal{K}$, so we solve the zero turning point dispersion relation to find the asymptotic mode. The numerical eigenmode $k = -5.64 + 2.33i$ lies inside the region $\omega\mathcal{K}$, so we should solve the one turning point dispersion relation to find the asymptotic mode. This would give us an asymptotic eigenmode of $k = -5.33 + 0.17i$, which is a terrible approximation, whereas solving the zero turning point dispersion relation gives an asymptotic eigenmode at $k = -6.00 + 2.55i$.

In Figure 3.5 we see that the lining causes all of the cut-off modes to shift right, and they no longer lie in a straight line. Additionally, they are no longer symmetric about the real line. We approximate the cut-off modes very accurately with the asymptotic method, with the first downstream mode having a relative error of 0.25% and the fourth downstream mode having a relative error of 0.12%. In Figure 3.5 we also see that both the first upstream

and downstream cut-off modes are significantly further from the real line than when we had hard walls.

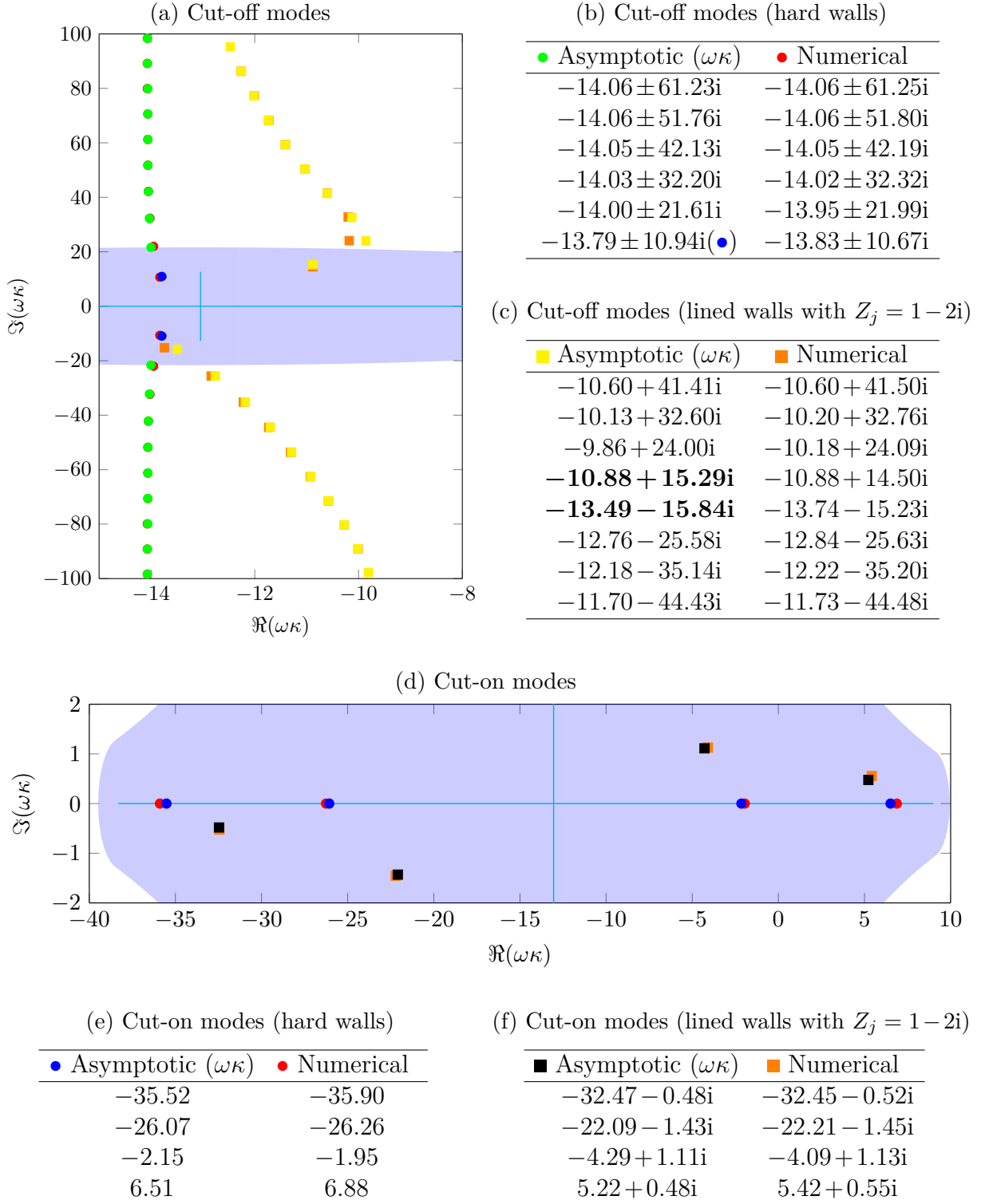


Figure 3.6: **Examples 3 & 4: constant shear with polynomial swirl.**

Plot of the asymptotic and numerical eigenmodes. The parameters are $\omega = 25$, $\eta = 0.6$, $U_x = 0.5$, $U_\theta(r) = 0.1r + 0.1/r$, $h = 0.6$ with both hard walls (green, blue; red) and lined walls of impedance $Z_j = 1 - 2i$ (yellow, black; orange).

Example 3

Example 3 allows us to see the effect of swirl, since all the parameters are the same as Example 1 except the swirl profile. In [Figure 3.6](#) we plot the asymptotic eigenmodes (green, blue), the numeric eigenmodes (red) and the region $\omega\mathcal{K}$. The first thing we notice in [Figure 3.6](#) is that the \mathcal{K} region has changed type and is now of the second type. We also now only have four cut-on modes, compared to six when we had no swirl. The four cut-on modes all have a critical radius within the duct and we approximate these modes accurately by solving the asymptotic one turning point dispersion relation.

The cut-off modes shift right in Example 3 compared to Example 1, but are still symmetric since we have no lining in the duct. The first cut-off asymptotic mode is in the $\omega\mathcal{K}$ region so to find it we solve the one turning point dispersion relation and see that it is a good approximation to the numerical mode. To calculate subsequent cut-off asymptotic modes we solve the zero turning point dispersion relation. The relative error for the first cut-off mode is 0.77%, while the second one is less accurate with a relative error of 1.22%, since it lies close to the edge of the $\omega\mathcal{K}$ region. Subsequent cut-off modes become more and more accurate, with the sixth cut-off mode having a relative error of 0.03%.

Example 4

In Example 4 the parameters are the same as in Example 2 except for the swirl, so we see the effect of swirl in a lined duct on the eigenmodes in [Figure 3.6](#). The main differences between the eigenmodes for Examples 2 and 4 are that we only have four cut-on modes in Example 4 compared to six in Example 2, while the cut-off modes shift right in Example 4. In comparison with Example 3, the cut-on modes move off the real line. Additionally, the symmetry of the cut-off modes has been broken by the lining and they shift right and further from the real line.

In [Figure 3.6](#) we see the cut-on asymptotic eigenmodes are as accurate as when we had no lining, and more accurate than when we had no swirl. The cut-off modes are slightly less accurate than when we had no lining or no swirl, in particular the first and second cut-off modes. The first cut-off modes (upstream and downstream) lie in the region $\omega\mathcal{K}$, but we get more accurate asymptotic eigenmodes if we solve the zero turning point dispersion relation instead. For the numerical eigenmode $k = -10.88 + 14.50i$, solving the one turning point dispersion relation gives an asymptotic eigenmode at $k = -12.63 + 14.91i$, while solving the zero turning point dispersion relation gives an asymptotic eigenmode at $k = -10.88 + 15.29i$, which is significantly closer. The second cut-off mode is not that accurate since it is close to the edge of the $\omega\mathcal{K}$ region. To calculate the asymptotic eigenmodes more accurately we could use the improved dispersion relation in [Section 3.7.3](#), and we will show the improvement later on.

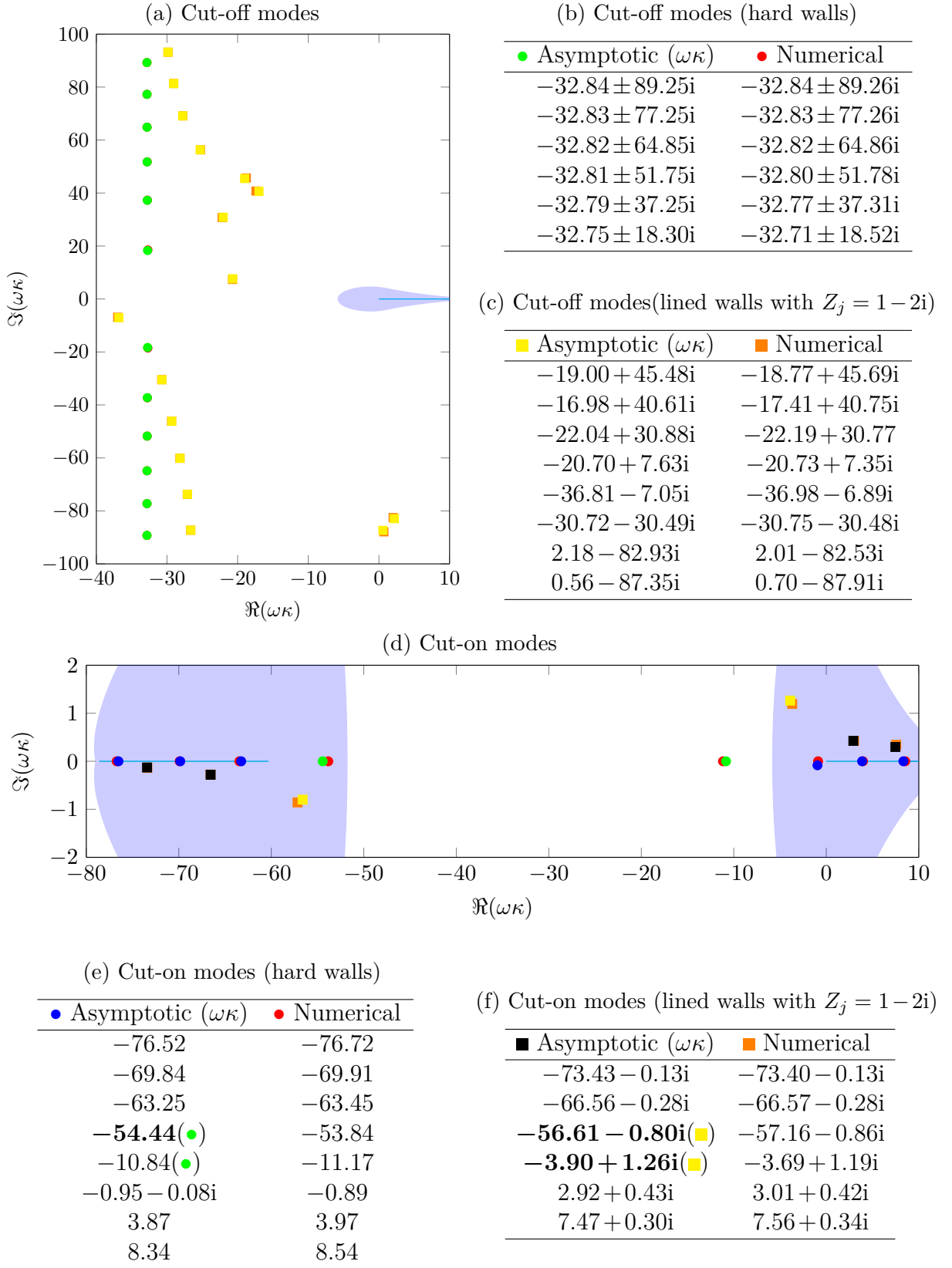


Figure 3.7: Examples 5 & 6: polynomial shear with zero swirl.

Plot of the asymptotic and numerical eigenmodes. The parameters are $\omega = 25$, $\eta = 0.6$, $U_x(r) = 0.5 + 0.4r - 0.2r^2$, $U_\theta = 0$, $h = 0.6$ with both hard walls (green, blue; red) and lined walls of impedance $Z_j = 1 - 2i$ (yellow, black; orange).

Examples 5 and 6

In [Figure 3.7](#) we plot the asymptotic eigenmodes (green, blue; yellow, black) and numerical eigenmodes (red; orange) for Examples 5 and 6, and see very good agreement between the modes. We choose Examples 5 and 6 to illustrate two things. First, lining can make cut-on modes cut-off. The two numerical eigenmodes at $k = -53.84$ and $k = -11.17$ in Example 5 move to $k = -36.81 - 7.05i$ and $k = -20.70 + 7.63i$ in a lined duct, making them cut-off. Second, Example 6 illustrates how well we approximate the eigenmodes asymptotically, even when the numerical eigenmodes do bizarre things. For example, there are two upstream cut-off modes at $k = 2.01 - 82.53i$ and $k = 0.70 - 87.91i$, which are a long way from the main line of cut-off modes, but we still approximate these very well asymptotically.

3.4.2 Semi-realistic shear and swirl

We now consider a swirling mean flow representative of a typical Rolls-Royce civil aeroengine. We plot the shear and swirl profiles in [Figure 3.8](#). The inner duct wall is at $h = 0.4$ and we consider both hard and lined walls with impedance $Z_j = 1 - 2i$. We consider two different frequency and azimuthal number regimes. In Examples 7 and 8, we consider $\omega = 22$ and $n = 7$, giving $\eta = n/\omega = 0.318$. The other regime is $\omega = 20$ and $n = 19$, giving $\eta = 0.95$, which we consider in Examples 9 and 10. These frequencies are close to the BPF, and we

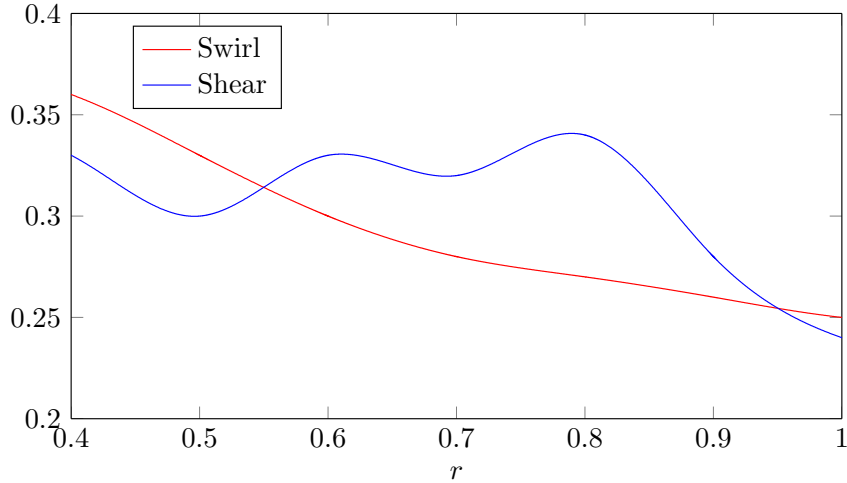


Figure 3.8: Semi-realistic mean flow profiles from a typical Rolls-Royce civil aeroengine.

choose the azimuthal number so that the region \mathcal{K} is of the first type in Examples 9 and 10. The boundary of the \mathcal{K} region is not smooth in [Figures 3.9](#) and [3.10](#), because the shear and swirl profiles are constructed using splines, so $U_x(r)$ and $U_\theta(r)$ are only twice continuously differentiable.

Example 7

In Example 7, we consider semi-realistic shear and swirl at $\omega = 22$. We plot the eigenmodes in [Figure 3.9](#), and we see that we do not find all the asymptotic cut-on modes. This is

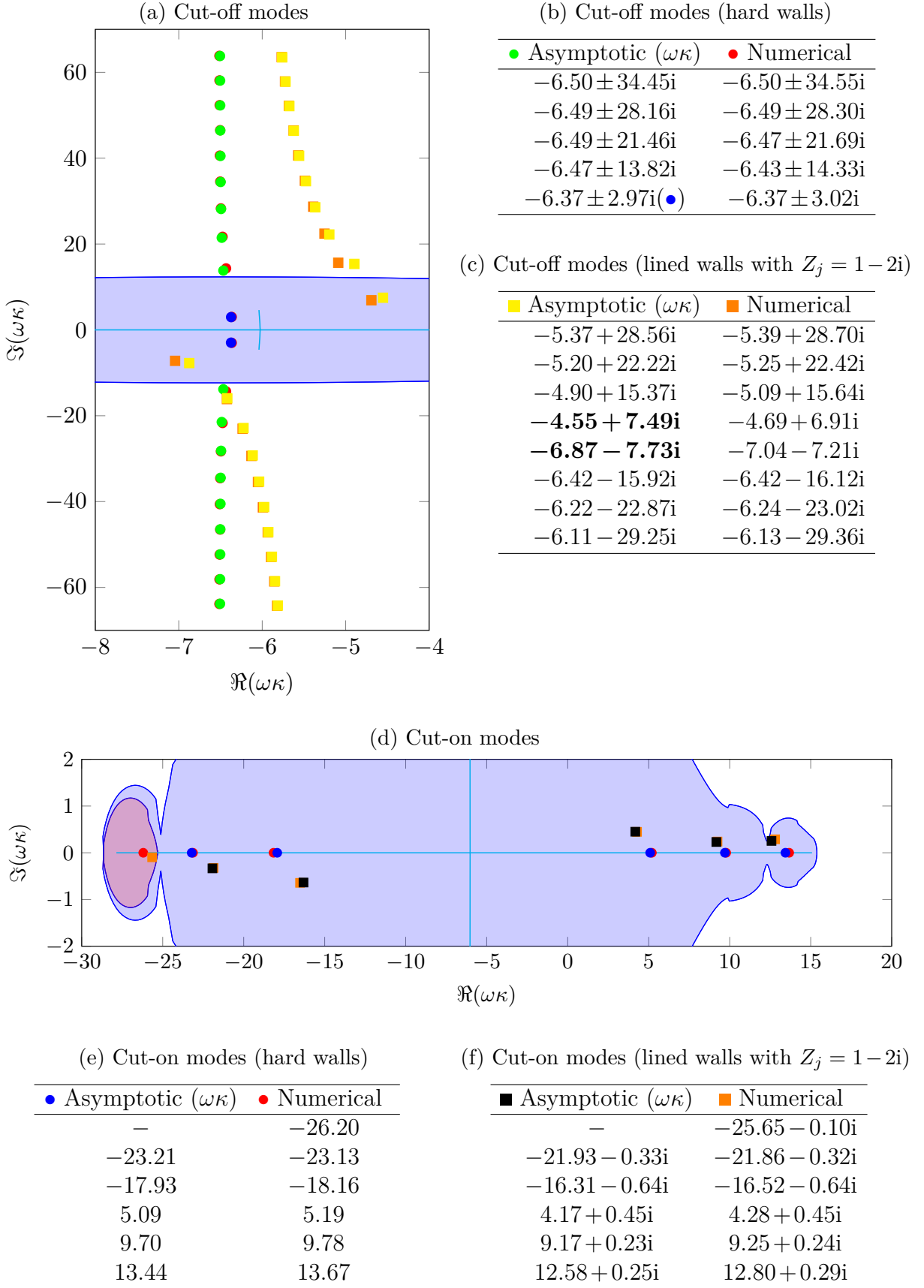


Figure 3.9: **Examples 7 & 8: semi-realistic shear and swirl at low azimuthal number.** Plot of the asymptotic and numerical eigenmodes. The parameters are $\omega = 22$, $n = 7$, $h = 0.4$ with both hard walls (green, blue; red) and lined walls of impedance $Z_j = 1 - 2i$ (yellow, black; orange).

because the furthest upstream cut-on mode lies in a region where $q_n(r, \kappa)$ has two zeros in the duct. This region is shaded in red in [Figure 3.9d](#). We discuss how to extend the asymptotic method to the case when $q_n(r, \kappa)$ has multiple zeros in the duct in [Section 3.7.2](#).

We clearly see that despite the more complicated mean flow, we asymptotically approximate all the other numerical modes accurately in [Figure 3.9](#). The accuracy is very comparable to the previous examples, for example the fifth asymptotic cut-off mode has a relative error of 0.28% compared to the numerical eigenmode.

Example 8

In [Figure 3.9](#), we see the effect of semi-realistic shear and swirl in a lined duct on the eigenmodes. We again fail to find the furthest upstream asymptotic cut-on mode, since the mode still lies in the two turning point region. We find the rest of the asymptotic modes, and see that they are very accurate compared to the numerical modes. We are able to find the furthest downstream cut-on mode accurately, despite it being very close to the edge of the $\omega\mathcal{K}$ region.

We solve the zero turning point dispersion relation for the first cut-off asymptotic mode, and find the rest by solving the one turning point dispersion relation. As in the previous examples, the introduction of lining breaks the symmetry of the cut-off modes about the real line and shifts most of them to the right, and further from the real line. If we instead consider negative values of the azimuthal number, then we find the cut-off modes still shift right when we introduce lining, but they move closer to the real line. Thus, counter-rotating modes are less effectively damped by the lining, in agreement with [Cooper and Peake \(2005\)](#). The lining also shifts the cut-on modes off the real line. It is interesting to note that the furthest downstream cut-on mode has a larger imaginary part than the next downstream cut-on mode, which is something we were not expecting based on the previous examples.

Example 9 & 10

In Examples 9 and 10, the region \mathcal{K} is of the first type, so there are no cut-on modes which solve the one turning point dispersion relation. Since most of the cut-on modes occur in the region $\omega\mathcal{K}$ or close to it, we find in [Figure 3.10](#) no asymptotic or numerical cut-on modes anywhere. In [Figure 3.10](#) we see that we asymptotically approximate the numerical cut-off modes well by solving the asymptotic dispersion relation, and we would find further cut-off eigenmodes with large imaginary part outside of the $\omega\mathcal{K}$ region.

3.4.3 Effect of entropy on the eigenmodes

When we vary the base flow entropy $s_0(r)$, there are three main features. First, as we increase entropy the line of cut-off modes shifts right. Second, as we increase entropy we reduce the number of cut-on modes. Third, when the duct has lining we find both upstream and downstream “surface-entropy” modes, once the entropy is below a certain threshold.

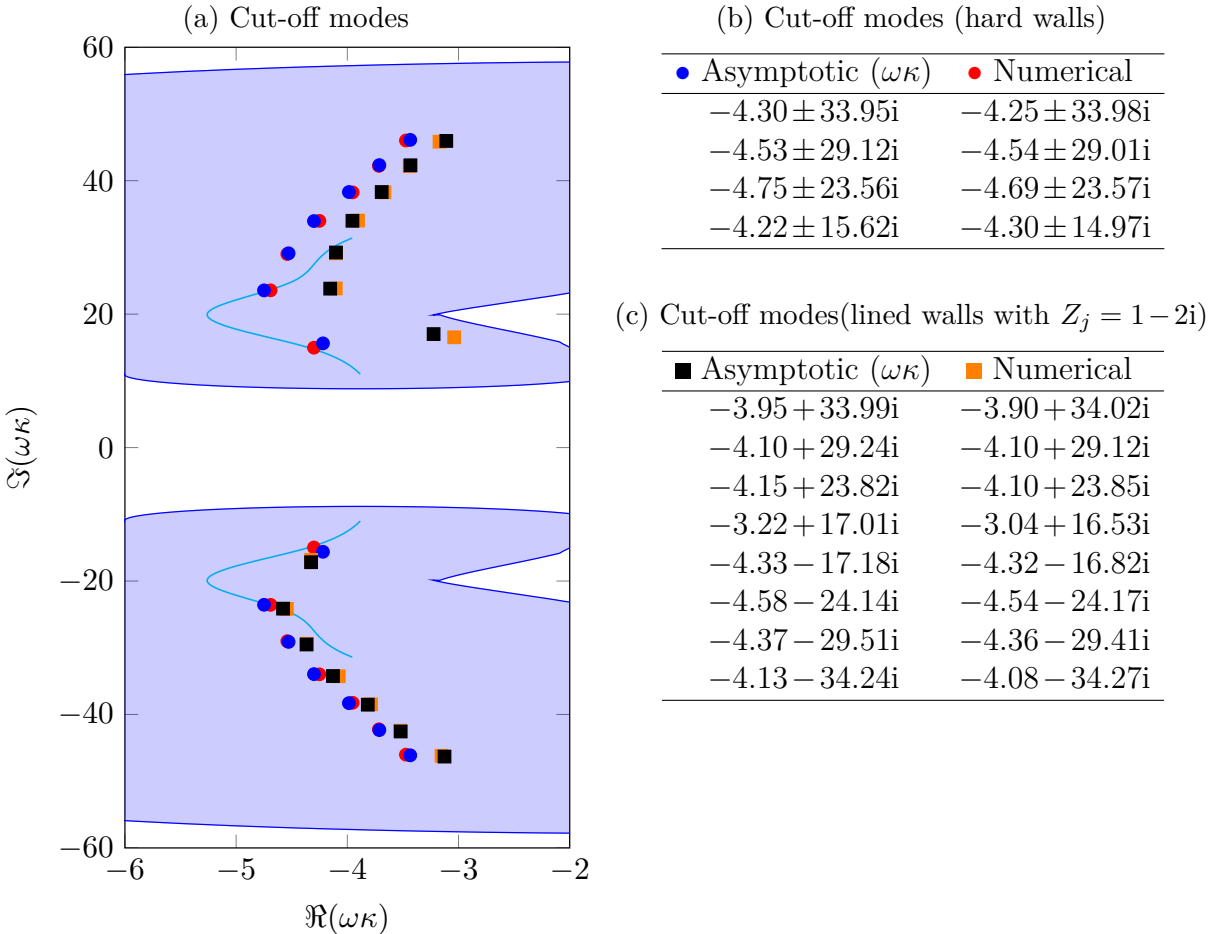


Figure 3.10: **Examples 9 & 10:** semi-realistic shear and swirl at high azimuthal number. Plot of the asymptotic and numerical eigenmodes. The parameters are $\omega = 20$, $n = 19$, $h = 0.4$ with both hard walls (green, blue; red) and lined walls of impedance $Z_j = 1 - 2i$ (yellow, black; orange).

We can easily explain the first two effects for uniform shear flow in a duct. As we increase the entropy $s_0(r)$, we increase the speed of sound $c_0(r)$. This therefore reduces the Mach number $M(r)$ of the flow. In uniform flow, the line of cut-off modes is given by $\Re(k) = -\omega M/(1 - M^2)$. Thus, increasing the entropy causes the line of cut-off modes to shift right. Furthermore, the condition for cut-on modes in a duct is $\alpha^2 < \omega/(1 - M^2)$, with α given in Vilenski and Rienstra (2007a) and involves finding zeros of Bessel functions. As we increase the entropy, we decrease M and hence decrease $1/(1 - M^2)$. Thus, we get less cut-on modes since previously accepted values of α no longer satisfy the cut-on condition.

We consider two different shear and swirl profiles in a lined duct. In Figure 3.11 we consider constant shear and zero swirl, while in Figure 3.12 we consider polynomial shear and swirl of the form $U_x(r) = 0.3 + 0.2r^2$ and $U_\theta(r) = 0.2r + 0.1/r$. We choose the base flow entropy to be $s_0(r) = -\log(r^\beta)$, so increasing β increases the entropy since $r < 1$. We plot the numerical and asymptotic eigenmodes in Figures 3.11 and 3.12 and observe the asymptotic and numeric eigenmodes display all three features.

In Figure 3.11 we see the development of the upstream and downstream “surface-entropy” modes. As we decrease entropy, the usually straight branch of cut-off modes pinches and then spits of an eigenmode. As we further decrease entropy, the branch of cut-off modes

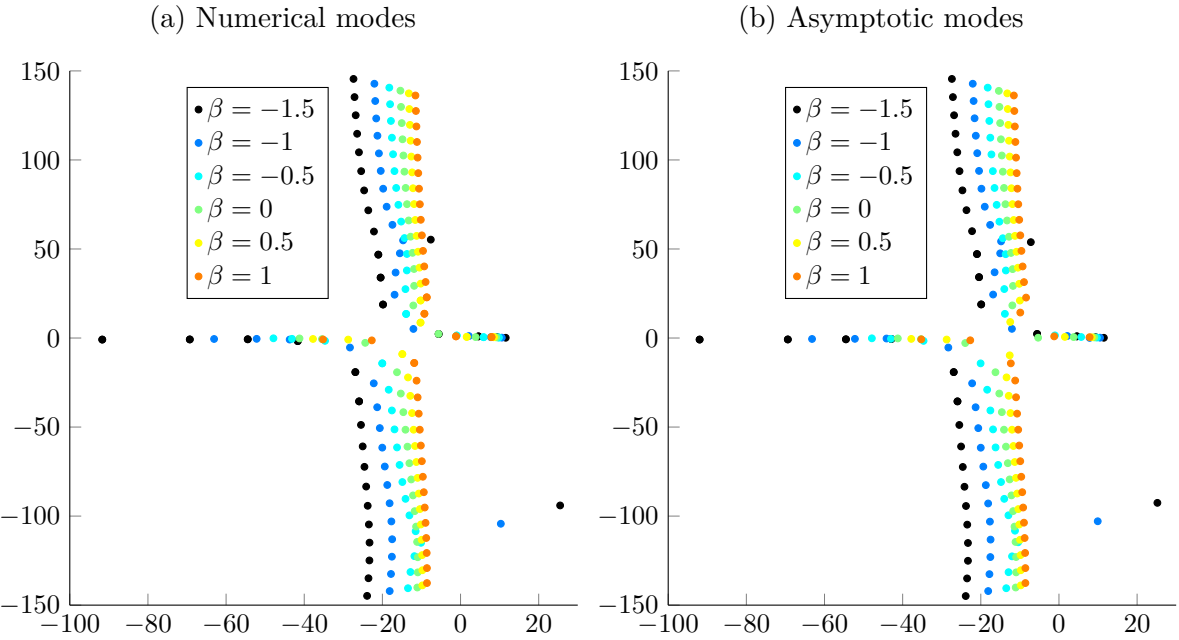


Figure 3.11: Comparison between numerical and asymptotic eigenmodes as the entropy $s_0(r) = -\log(r^\beta)$ varies. The parameters are $\omega = 25$, $\eta = 0.6$, $U_x = 0.5$, $U_\theta = 0$ and lined walls of impedance $Z_j = 1 - 2i$.

straightens again while the “surface-entropy” mode moves right. The downstream “surface-entropy” mode appears for $-1.5 < \beta < -1$, while the upstream “surface-entropy” mode appears for $-1 < \beta < -0.5$, so at certain values of entropy there is only one “surface-entropy” mode. The trajectory of the upstream “surface-entropy” mode means that for sufficiently negative entropy, this mode would eventually cross the real line, which would give problems with the integration contour. In [Figure 3.12](#) we do not see any “surface-entropy” modes, but

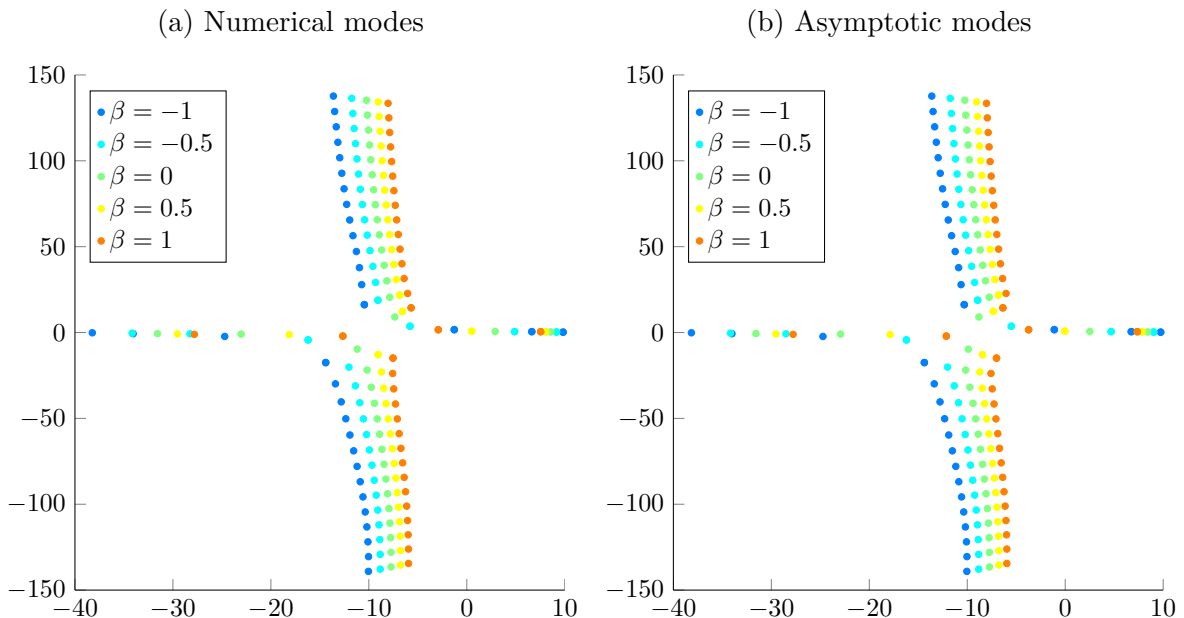


Figure 3.12: Comparison between numerical and asymptotic eigenmodes as the entropy $s_0(r) = -\log(r^\beta)$ varies. The parameters are $\omega = 25$, $\eta = 0.48$, $U_x(r) = 0.3 + 0.2r^2$, $U_\theta(r) = 0.2r + 0.1/r$ and lined walls of impedance $Z_j = 1 - 2i$.

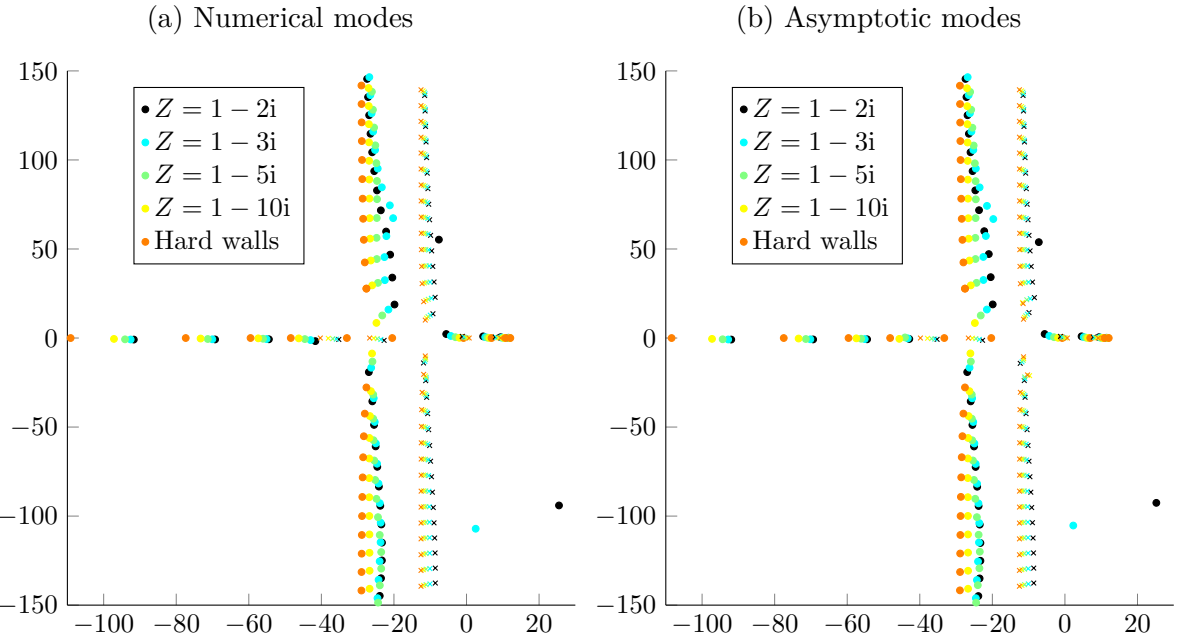


Figure 3.13: Comparison between numerical and asymptotic eigenmodes, for $\beta = -1.5$ (circles) and $\beta = 1$ (crosses). The parameters are $\omega = 25$, $\eta = 0.6$, $U_x = 0.5$, $U_\theta = 0$ and lined walls of different impedances.

this is because we have not considered sufficiently negative entropy. Choosing $-3 < \beta < -2$ would give us both the upstream and downstream ‘‘surface-entropy’’ modes.

In Figure 3.13 we see these ‘‘surface-entropy’’ modes disappear as we reduce the lining of the walls by increasing the imaginary part of the impedance. Surface modes can be present without entropy, with simple examples given in Brambley and Peake (2006a). In our case, we term them ‘‘surface-entropy’’ modes because we create them by varying entropy.

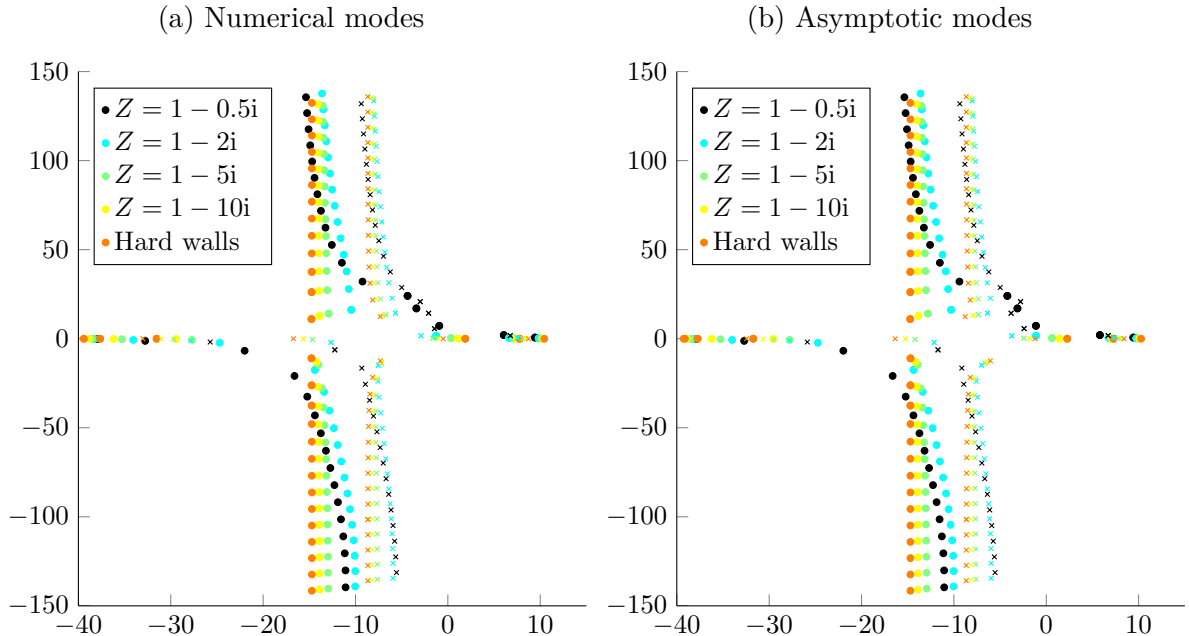


Figure 3.14: Comparison between numerical and asymptotic eigenmodes, for $\beta = -1$ (circles) and $\beta = 1$ (crosses). The parameters are $\omega = 25$, $\eta = 0.48$, $U_x(r) = 0.3 + 0.2r^2$, $U_\theta(r) = 0.2r + 0.1/r$ and lined walls of different impedances.

In Figure 3.11 we see that when $\beta = -1.5$ there are four cut-on downstream modes and four upstream cut-on modes. When $\beta = 0$ there are three cut-on downstream modes and three upstream cut-on modes, while when $\beta = 1$ there are only two of each. Additionally, the upstream cut-on modes move further and further downstream as we increase the entropy. When $\beta = -1.5$ the furthest upstream cut-on mode is given numerically by $k = -91.65$, while when $\beta = 1$ the furthest upstream cut-on mode is given numerically by $k = -35.19$. In contrast, the downstream cut-on modes only move a small amount upstream as we increase the entropy. In Figure 3.11 the furthest downstream mode is numerically given by $k = 11.56$ when $\beta = -1.5$ and given by $k = 7.93$ when $\beta = 1$.

In Figure 3.12 we see much the same story in terms of cut-on modes, with the number of cut-on modes decreasing as we increase entropy. When $\beta = -1$ we have three downstream and three upstream cut-on modes, while when $\beta = 1$ we have only two downstream and two upstream cut-on modes. In Figures 3.13 and 3.14 we see that no matter the lining of the duct walls, we reduce the number of cut-on modes as we increase entropy.

In Figures 3.11, 3.12, 3.13 and 3.14 we see that the branch of cut-off modes moves to the right as we increase entropy. The parameters of the flow determine exactly how much the line moves, and we see it moves more in Figure 3.11 than in Figure 3.12.

In Figures 3.13 and 3.14 we see the effect of entropy with and without lining. Even in a hard-walled duct, we still see less cut-on modes and the branch of cut-off modes shifting right as we increase entropy. However, in Figure 3.13 we see that the “surface-entropy” modes are drawn back into the branch of cut-off modes as we reduce the lining of the duct walls.

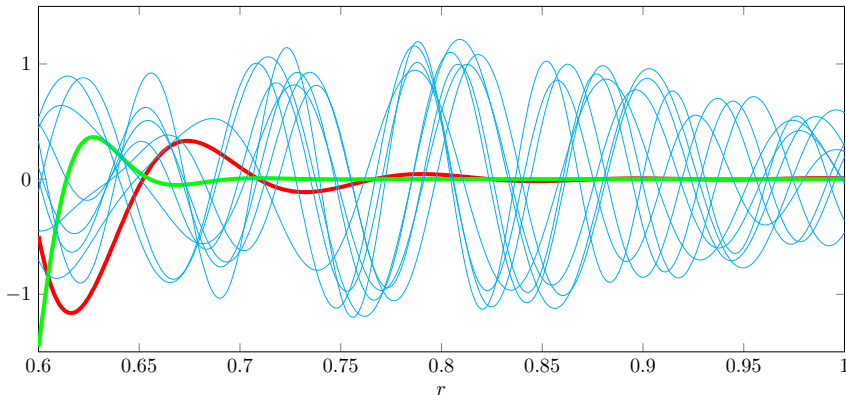


Figure 3.15: Real part of numerical pressure eigenfunction for different eigenmodes for the parameters in Figure 3.11 when $\beta = -1.5$. Red: “surface-entropy” mode $k = -7.62 + 55.25i$, green: “surface-entropy” mode $k = 25.49 - 94.02i$, blue: other cut-off modes.

Finally, we comment on the accuracy of the asymptotic eigenmodes compared with the numerical modes. We find every numerical eigenmode asymptotically, and generally approximate them very well. We are even able to approximate the “surface-entropy” modes quite well. In Figure 3.11, when $\beta = -1.5$, the downstream “surface-entropy” mode is numerically given by $k = -7.62 + 55.25i$ and asymptotically by $k = -7.20 + 53.84i$. The upstream “surface-entropy” mode is given numerically by $k = 25.49 - 94.02i$ and asymptotically by $k = 25.17 - 94.02i$. In Figure 3.15 we have plotted the numerical pressure

eigenfunctions for the cut-off eigenmodes in [Figure 3.11](#) when $\beta = -1.5$. The eigenfunctions associated to the “surface-entropy” modes have a considerably different shape to the rest of the cut-off acoustic modes, since they only oscillate at the inner wall.

When we start considering more complicated shear and swirl profiles for the mean flow, such as in [Figure 3.14](#), we are able to less accurately predict the “surface-entropy” modes asymptotically. The other acoustic modes are predicted asymptotically with the same level of accuracy as we would expect without entropy. We approximate some modes close to the edge of the $\omega\mathcal{K}$ poorly, but this comes down to the fact we should really be using a more accurate dispersion relation, such as the one in [Section 3.7.3](#).

3.5 Calculating the Green’s function G_ω

In [Sections 3.3](#) and [3.4](#) we showed how to compute the eigenmodes both numerically and asymptotically, and then presented comparisons between the two methods, showing the asymptotic eigenmodes generally predict the numerical eigenmodes very well. Having calculated G_n in [Section 3.2](#), we now find the Fourier transform of it, G_ω . Rather than numerically calculating the integral over the real line, we instead close the contour in the upper or lower half plane, and compute the residue at each acoustic eigenmode. This is why it was vital to calculate the asymptotic eigenmodes accurately to find the Green’s function.

Instead of finding G_ω we calculate \hat{p}_ω , which is defined by

$$\hat{p}_\omega(\mathbf{x}|\mathbf{x}_0) = \frac{1}{4\pi^2} \sum_{n=-\infty}^{\infty} e^{in(\theta-\theta_0)} \int_{\mathbb{R}} \hat{p}_n(r|r_0; \omega, k) e^{ik(x-x_0)} dk, \quad (3.5.1)$$

where

$$\hat{p}_n(r|r_0; \omega, k) = \frac{1}{r_0 \mathcal{W}(r_0, k)} \begin{cases} g_1(r_0; k)g_2(r; k) & r \leq r_0 \\ g_2(r_0; k)g_1(r; k) & r > r_0 \end{cases}, \quad (3.5.2)$$

so \hat{p}_n and G_n differ by a factor of $J(r_0, k)$. The pressure now solves

$$\frac{D_0^2}{Dt^2} \mathcal{R}(p) = \int \hat{p}_\omega(r, x, \theta|r_0, x_0, \theta_0) \mathbb{S}^M(r_0, x_0, \theta_0) d\mathbf{x}_0 e^{-i\omega t}, \quad (3.5.3)$$

since

$$\mathcal{F}^M(\hat{p}_\omega e^{-i\omega t}) = \frac{D_0^2}{Dt^2} \mathcal{R}(\delta(\mathbf{x} - \mathbf{x}_0) e^{-i\omega t}). \quad (3.5.4)$$

At first, calculating \hat{p}_ω and \hat{p}_n instead of G_ω and G_n looks to be less useful because of [\(3.5.3\)](#). However, when we actually use the definition of the source terms and follow [Posson and Peake \(2012, Section 3\)](#) then we find that \hat{p}_n is just as useful, if not more useful than G_n . This is because the integral with respect to k we evaluate to calculate the pressure is roughly given by ([Posson and Peake, 2012](#), Equations 35 and 37)

$$p_\omega \approx \sum_{n=-\infty}^{\infty} e^{in(\theta-\theta_0)} \int_{\mathbb{R}} \left[(a + bk) \left(1 - \frac{\mathcal{U}_\theta(r_0)}{\Omega^2(r_0, k)} \right) \hat{p}_n(r|r_0; \omega, k) + \frac{c}{\Omega^2(r_0, k)} \hat{p}_n(r|r_0; \omega, k) \right]$$

$$+ \frac{d}{\Omega(r_0, k)} \frac{d\hat{p}_n}{dr}(r|r_0; \omega, k) \Big] e^{ik(x-x_0)} dk. \quad (3.5.5)$$

This follows from applying the derivatives in the source terms to the Green's function, by using integration by parts. In (3.5.5) we would expect the dominant term to be the first, $(a+bk)\hat{p}_n$, which is why we focus on the Green's function \hat{p}_ω , which is obtained by Fourier transforming \hat{p}_n .

The Green's function \hat{p}_ω also allows easy comparison with the case of no swirl and uniform shear, which was considered in [Rienstra and Tester \(2008\)](#). In the case of no swirl and uniform shear, the right-hand side of (3.5.4) is the fourth power of the material derivative acting on the Dirac delta. The operator \mathcal{F}^M is given by the fourth power of the material derivative acting on the convected wave equation, so we just have to find the Green's function of the convected wave equation. In (3.5.3), the left-hand side becomes the fourth power of the material derivative acting on the pressure, and we can factor out a fourth power of the material derivative from the source terms. Thus, we get an explicit expression for pressure.

To calculate \hat{p}_ω we find the inverse Fourier transform of \hat{p}_n , which is given by

$$\begin{aligned} & \int_{\mathbb{R}} \hat{p}_n(r|r_0; \omega, k) e^{ik(x-x_0)} dk \\ &= \int_{\Gamma} \frac{1}{r_0 \mathcal{W}(r_0, k)} [g_1(r_0; k) g_2(r; k) \mathbb{1}_{r \leq r_0} + g_2(r_0; k) g_1(r; k) \mathbb{1}_{r > r_0}] e^{ik(x-x_0)} dk, \end{aligned} \quad (3.5.6)$$

where Γ is given in [Figure 1.11](#), and is determined by the Briggs-Bers procedure. The function $\mathbb{1}$ is the indicator function. To perform the integration we close the contour in the upper or lower half plane depending on whether $x > x_0$. When $x > x_0$ we close the contour in the upper half plane, and the Green's function is equal to the sum of the residues at the downstream eigenmodes, plus a critical layer contribution, which we describe in [Section 3.5.2](#). When $x < x_0$ we close the contour in the lower half plane, and get a sum of the residues at the upstream eigenmodes, with no contribution from the critical layer.

Contribution from acoustic eigenmodes

The total contribution from the acoustic eigenmodes is given by

$$\hat{p}_\omega^A(\mathbf{x}|\mathbf{x}_0) = \sum_{n=-\infty}^{\infty} e^{in(\theta-\theta_0)} \sum_{\mathcal{K}_n^\pm} \hat{p}_n^m(x, r|x_0, r_0), \quad (3.5.7)$$

where

$$\hat{p}_n^m(x, r|x_0, r_0) = \pm \frac{2\pi i}{4\pi^2} \text{Res}\{\hat{p}_n(r|r_0; \omega, k) e^{ik(x-x_0)}, k = k_n^m\}. \quad (3.5.8)$$

The \pm comes from whether $x > x_0$ or $x < x_0$, with \mathcal{K}_n^+ consisting of all downstream acoustic modes and \mathcal{K}_n^- consisting of all upstream acoustic modes. We calculate that

$$\hat{p}_n^m(x, r|x_0, r_0) = \pm \frac{2\pi i}{4\pi^2} \frac{1}{r_0 \frac{\partial \mathcal{W}}{\partial k}(r_0, k_n^m)} e^{ik_n^m(x-x_0)} \begin{cases} g_1(r_0; k_n^m) g_2(r; k_n^m) & r \leq r_0 \\ g_2(r_0; k_n^m) g_1(r; k_n^m) & r > r_0 \end{cases}. \quad (3.5.9)$$

Acoustic cut-off modes with large imaginary parts contribute very little to the Green's function, due to the exponential term $\exp(i k(x - x_0))$. We let

$$\hat{p}_n^A(x, r|x_0, r_0) = \sum_{\mathcal{K}_n^\pm} \hat{p}_n^m(x, r|x_0, r_0), \quad (3.5.10)$$

the total acoustic contribution at each azimuthal number.

Contribution from the critical layer and hydrodynamic modes

When $x > x_0$ we also need to consider the effect of the critical layer. We calculate the contribution from the critical layer by using a counter clockwise contour Γ_{CLH} enclosing the critical layer and hydrodynamic modes. We find

$$\hat{p}_\omega^{CL}(\mathbf{x}|\mathbf{x}_0) = \sum_{n=-\infty}^{\infty} e^{in(\theta-\theta_0)} \hat{p}_n^{CL}(x, r|x_0, r_0), \quad (3.5.11)$$

where

$$\hat{p}_n^{CL}(x, r|x_0, r_0) = \frac{1}{4\pi^2} \int_{\Gamma_{\text{CLH}}} \hat{p}_n(r|r_0; \omega, k) e^{ik(x-x_0)} dk. \quad (3.5.12)$$

We could evaluate the contribution from the first few hydrodynamics mode separately by using a similar method to the acoustic eigenmodes, but we would still be required to calculate the contribution from the critical layer and the rest of the hydrodynamic modes by calculating an integral.

3.5.1 Contribution from acoustic eigenmodes

Asymptotic method

The contribution from each acoustic mode is given by

$$\hat{p}_n^m(x, r|x_0, r_0) = \pm \frac{2\pi i \omega}{4\pi^2} \left(\frac{\rho_0(r)r_0}{\rho_0(r_0)r} \right)^{1/2} \frac{\Phi(r, \kappa_n^m) e^{i\omega\kappa_n^m(x-x_0)}}{r_0 \frac{\partial \mathcal{V}}{\partial \kappa}(\kappa_n^m) \Phi(r_0, \kappa_n^m)} \begin{cases} v_1(r_0; \kappa_n^m) v_2(r; \kappa_n^m) & r \leq r_0 \\ v_2(r_0; \kappa_n^m) v_1(r; \kappa_n^m) & r > r_0 \end{cases}, \quad (3.5.13)$$

where $v_1(r; \kappa)$ and $v_2(r; \kappa)$ were determined in [Section 3.2](#). The only difficulty in evaluating (3.5.13) is calculating the derivative of the Wroński with respect to κ . We consider this calculation only for the one turning point solution with $\Re(\mathcal{Q}) > 0$, with the other cases using a similar method.

The derivative of the Wroński is given by

$$\frac{\partial \mathcal{V}}{\partial \kappa}(\kappa_n^m) = \omega e^{i\pi/4} [\Sigma'_1(\kappa) [2\Sigma_h(\kappa) + i] + 2\Sigma_1(\kappa)\Sigma'_h(\kappa) - 2i\Sigma'_h(\kappa)]_{\kappa=\kappa_n^m}, \quad (3.5.14)$$

and we calculate that

$$\Sigma'_1(\kappa_n^m) = 2i\omega \frac{\partial \Psi_n}{\partial \kappa}(1, \kappa_n^m) e^{2i\omega \Psi_n(1, \kappa_n^m)} \frac{1 - \sigma_1(\kappa_n^m)}{1 + \sigma_1(\kappa_n^m)} + e^{2i\omega \Psi_n(1, \kappa_n^m)} \frac{\partial}{\partial \kappa} \left(\frac{1 - \sigma_1}{1 + \sigma_1} \right) (\kappa_n^m), \quad (3.5.15)$$

with a similar result for $\Sigma'_h(\kappa_n^m)$. We calculate the derivative of $\Psi_n(r, \kappa)$ with respect to κ numerically by using

$$\frac{\partial \Psi_n}{\partial \kappa}(r, \kappa_n^m) = \lim_{\varepsilon \rightarrow 0} \frac{1}{2} \int_{r_c + \varepsilon}^r \frac{\partial q_n}{\partial \kappa}(s, \kappa_n^m) \frac{1}{\sqrt{q_n(s, \kappa_n^m)}} ds, \quad (3.5.16)$$

where we calculate the derivative of $q_n(r, \kappa)$ with respect to κ analytically as

$$\frac{\partial q_n}{\partial \kappa}(r, \kappa) = -\frac{2U_x(r)\Phi(r, \kappa)}{c_0^2(r)} - 2\kappa. \quad (3.5.17)$$

We also calculate that

$$\sigma'_1(\kappa) = \frac{\rho_0(1)\Phi^2(1, \kappa)}{Z_1 \sqrt{q_n(1, \kappa)}} \left(-\frac{2U_x(1)}{\Phi(1, \kappa)} - \frac{\partial q_n}{\partial \kappa}(1, \kappa) \frac{1}{2q_n(1, \kappa)} \right), \quad (3.5.18)$$

and then use the quotient rule to calculate the derivative of $(1 - \sigma_1)/(1 + \sigma_1)$. We could calculate $\sigma'_h(\kappa)$ similarly, which we need to calculate $\Sigma'_h(\kappa_n^m)$. Thus, we are able to calculate the derivative of $\mathcal{V}(\kappa)$ with respect to κ analytically, aside from the numerical integration required to find Ψ_n and its derivative with respect to κ .

There is one further point to consider for the asymptotic solution, the branch cut of $q_n(r, \kappa)$. In [Section 3.2](#) we assumed that the branch cut was along the negative imaginary axis, so that [\(3.2.25\)](#) holds. However, as r varies in the duct $q_n(r, \kappa)$ goes through the branch cut for some eigenmodes κ . Clearly, this would not give correct results, and in

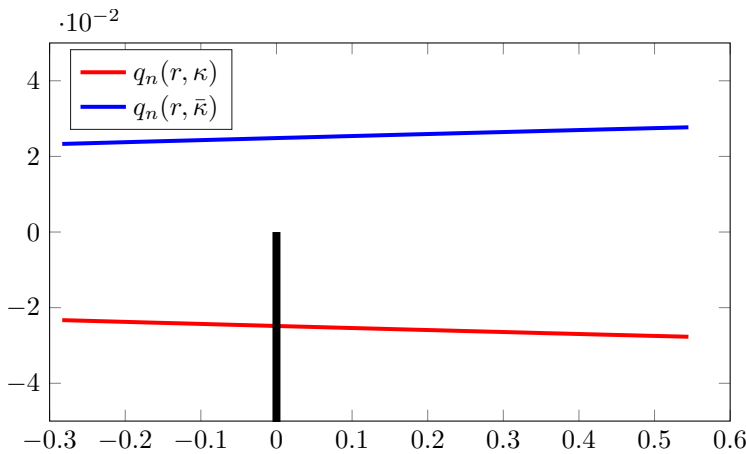


Figure 3.16: Plot of $q_n(r, \kappa)$ for $r \in [0.6, 1]$ for the parameters in Example 4 with $\omega\kappa = -4.29 + 1.11i$. Branch cut of square root in black.

[Figure 3.16](#) we see $q_n(r, \kappa)$ going through the branch cut for $\omega\kappa = -4.29 + 1.11i$, one of the downstream cut-on modes in Example 4. There are two possible solutions. The first is to move the branch cut of the square root to the positive imaginary axis. However, this

requires that $\sqrt{-1} = -i$ and $\sqrt{1} = -1$, in which case we would need to recalculate the constants $A^j(\kappa)$ and $B^j(\kappa)$ in the one turning point solution. The alternative solution, which we use, is to consider the conjugate of κ , and we see in Figure 3.16 that $q_n(r, \bar{\kappa})$ then passes above the branch cut. We can then calculate $\Psi(r, \bar{\kappa})$ and its 2/3 root to find $\tau(r, \bar{\kappa})$, while avoiding the square root branch cut. We then conjugate to find $\tau(r, \kappa)$, since $\tau(r, \kappa) = \overline{\tau(r, \bar{\kappa})}$.

Numerical method

The contribution from each acoustic eigenmode is given by

$$\hat{p}_n^m(x, r|x_0, r_0) = \pm \frac{2\pi i\omega}{4\pi^2} e^{i\omega\kappa_n^m(x-x_0)} \frac{1}{r_0 \frac{\partial \mathcal{W}}{\partial \kappa}(\kappa_n^m)} \begin{cases} g_1(r_0; \kappa_n^m)g_2(r; \kappa_n^m) & r \leq r_0 \\ g_2(r_0; \kappa_n^m)g_1(r; \kappa_n^m) & r > r_0 \end{cases}, \quad (3.5.19)$$

where we calculate $g_1(r; \kappa)$, $g_2(r; \kappa)$ and $\mathcal{W}(\kappa)$ numerically. Our Chebfun numerical solver for the eigenmodes from Section 3.3.2 already computes the eigenfunctions $g_j(r; \kappa_n^m)$, but we could instead find them by solving the differential equation

$$\mathcal{A}(r, \kappa_n^m) \frac{d^2 g_j}{dr^2}(r; \kappa_n^m) + \mathcal{B}(r, \kappa_n^m) \frac{dg_j}{dr}(r; \kappa_n^m) - \mathcal{C}(r, \kappa_n^m) g_j(r; \kappa_n^m) = 0, \quad (3.5.20)$$

where

$$\mathcal{A}(r, \kappa) = (\mathcal{U}_\theta(r) - \omega^2 \Phi^2(r, \kappa)) \omega^2 \Phi^2(r, \kappa), \quad (3.5.21)$$

$$\mathcal{B}(r, \kappa) = \omega^2 \Phi^2(r, \kappa) \left[(\mathcal{U}_\theta(r) - \omega^2 \Phi^2(r, \kappa)) \left(\frac{1}{r} - \frac{\rho'_0(r)}{\rho_0(r)} \right) + \frac{\partial}{\partial r} (\omega^2 \Phi^2(r, \kappa) - \mathcal{U}_\theta(r)) \right], \quad (3.5.22)$$

and $\mathcal{C}(r, \kappa)$ is given in (3.1.21). The boundary conditions are given by

$$g_1(1; \kappa_n^m) = 1 \text{ and } \frac{dg_1}{dr}(1; \kappa_n^m) = \hat{f}_1(1, \kappa_n^m) g_1(1; \kappa_n^m), \quad (3.5.23)$$

and

$$g_2(h; \kappa_n^m) = 1 \text{ and } \frac{dg_2}{dr}(h; \kappa_n^m) = \hat{f}_2(h, \kappa_n^m) g_2(h; \kappa_n^m). \quad (3.5.24)$$

We can easily determine the functions $\hat{f}_1(r, \kappa)$ and $\hat{f}_2(r, \kappa)$ from (3.1.22) and (3.1.23), and they are related to the functions $f_j(r, \kappa)$ in (3.2.6). The choice of $g_1(1; \kappa_n^m) = 1$ and $g_2(h; \kappa_n^m) = 1$ is arbitrary, and was chosen for simplicity.

The difficultly in evaluating (3.5.19) lies in calculating the derivative of the Wronskian with respect to κ . To calculate this we first find the derivatives of $g_1(r; \kappa)$ and $g_2(r; \kappa)$ with respect to κ , which we do by using the same method as Posson and Peake (2013b). We differentiate (3.5.20) with respect to κ , which then gives

$$\mathcal{A}(r, \kappa_n^m) \frac{d^2}{dr^2} \left(\frac{\partial g_j}{\partial \kappa} \right) + \mathcal{B}(r, \kappa_n^m) \frac{d}{dr} \left(\frac{\partial g_j}{\partial \kappa} \right) - \mathcal{C}(r, \kappa_n^m) \frac{\partial g_j}{\partial \kappa} \quad (3.5.25)$$

$$= \frac{\partial \mathcal{C}}{\partial \kappa}(r, \kappa_n^m) g_j - \frac{\partial \mathcal{B}}{\partial \kappa}(r, \kappa_n^m) \frac{dg_j}{dr} - \frac{\partial \mathcal{A}}{\partial \kappa}(r, \kappa_n^m) \frac{d^2 g_j}{dr^2}.$$

Since we have already calculated $g_1(r; \kappa)$ and $g_2(r; \kappa)$, the right-hand side is known. We calculate the new boundary conditions by differentiating (3.5.23) and (3.5.24) with respect to κ , which gives

$$\frac{\partial g_1}{\partial \kappa}(1; \kappa_n^m) = 0 \text{ and } \frac{\partial}{\partial r} \left(\frac{\partial g_1}{\partial \kappa} \right)(1; \kappa_n^m) = \frac{\partial \hat{f}_1}{\partial \kappa}(1, \kappa_n^m) g_1(1; \kappa_n^m) + \hat{f}_1(1, \kappa_n^m) \frac{\partial g_1}{\partial \kappa}(1; \kappa_n^m), \quad (3.5.26)$$

and

$$\frac{\partial g_2}{\partial \kappa}(h; \kappa_n^m) = 0 \text{ and } \frac{\partial}{\partial r} \left(\frac{\partial g_2}{\partial \kappa} \right)(h; \kappa_n^m) = \frac{\partial \hat{f}_2}{\partial \kappa}(h, \kappa_n^m) g_2(h; \kappa_n^m) + \hat{f}_2(h, \kappa_n^m) \frac{\partial g_2}{\partial \kappa}(h; \kappa_n^m). \quad (3.5.27)$$

We then solve (3.5.25) with the boundary conditions in (3.5.26) to calculate $\partial g_1 / \partial \kappa$, and (3.5.25) with the boundary conditions in (3.5.27) to calculate $\partial g_2 / \partial \kappa$. Finally, the derivative of the Wronskian is given by

$$\frac{\partial \mathcal{W}}{\partial \kappa} = \frac{\partial g_1}{\partial \kappa} \frac{\partial g_2}{\partial r} + g_1 \frac{\partial}{\partial r} \left(\frac{\partial g_2}{\partial \kappa} \right) - g_2 \frac{\partial}{\partial r} \left(\frac{\partial g_1}{\partial \kappa} \right) - \frac{\partial g_2}{\partial \kappa} \frac{\partial g_1}{\partial r}, \quad (3.5.28)$$

which is straightforward to calculate now, since derivatives with respect to r are easy to calculate numerically.

3.5.2 Contribution from critical layer integral

The contribution from the integral around the critical layer is very expensive to calculate numerically and very hard to calculate accurately asymptotically. We choose the contour of integration Γ_{CLH} such that it encloses the critical layer and all the hydrodynamic modes. A schematic of the contour is shown in Figure 3.17. The integrand of the critical layer integral has poles at every hydrodynamic mode, and two further poles κ_r and κ_{r_0} , corresponding to $\Phi(r, \kappa_r) = 0$ and $\Phi(r_0, \kappa_{r_0}) = 0$ (Heaton and Peake, 2006).

There might also be contributions from the ends of the critical layer, and possibly surface modes as shown in Brambley et al. (2012a) for the case of no swirl. Since the critical layer does not change in the presence of lining, and the hydrodynamic modes are insensitive to the lining due to not carrying any pressure (Posson and Peake, 2013a), then we expect the contribution from the integral to be very similar for a hard-walled or lined duct.

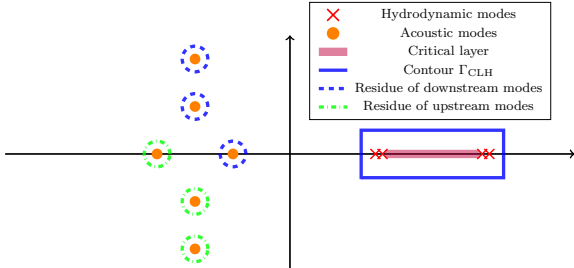


Figure 3.17: Schematic of contour Γ_{CLH} .

Numerical method

The contribution from the critical layer is numerically given by

$$\hat{p}_n^{CL}(x, r|x_0, r_0) = \frac{\omega}{4\pi^2} \int_{\Gamma_{CLH}} \hat{p}_n(r|r_0; \omega, \kappa) e^{i\omega\kappa(x-x_0)} d\kappa, \quad (3.5.29)$$

where

$$\hat{p}_n(r|r_0; \omega, \kappa) = \frac{1}{r_0 \mathcal{W}(\kappa)} \begin{cases} g_1(r_0; \kappa)g_2(r; \kappa) & r \leq r_0 \\ g_2(r_0; \kappa)g_1(r; \kappa) & r > r_0 \end{cases}. \quad (3.5.30)$$

We numerically calculate $g_1(r; \kappa)$ and $g_2(r; \kappa)$ at each κ on the integration contour by solving (3.5.20), with the boundary conditions in (3.5.23) for $g_1(r; \kappa)$ and the boundary conditions in (3.5.24) for $g_2(r; \kappa)$. We then use standard numerical integration schemes to calculate \hat{p}_n^{CL} . We are unable to successfully calculate \hat{p}_n^{CL} numerically using Chebfun, due to computation time, and instead we use the implementation by Hélène Posson in [Posson and Peake \(2012, 2013b\)](#), which is only valid for hard walls. This method is also expensive computationally, and in some cases Posson's code takes over half an hour to calculate \hat{p}_n^{CL} for a single azimuthal number.

Asymptotic method

We consider a new contour of integration $\bar{\Gamma}_{CLH}$, which is the largest circle that contains the critical layer and hydrodynamic modes but does not contain any acoustic modes. The integral of \hat{p}_n around $\bar{\Gamma}_{CLH}$ is the same as the integral around Γ_{CLH} by Cauchy's integral theorem. The advantage of choosing the new contour $\bar{\Gamma}_{CLH}$ is that our high-frequency limit applies on this contour, since we are sufficiently far away from the critical layer (see Sections 3.1.3 and 3.1.4).

We use the asymptotic form of $v_1(r; \kappa)$ and $v_2(r; \kappa)$ from [Section 3.2](#), and we find that $\mathcal{V}(\kappa)$ is non-zero inside the integration contour $\bar{\Gamma}_{CLH}$. We then use the residue theorem, since the denominator has a single zero at κ_{r_0} , corresponding to $\Phi(r_0, \kappa_{r_0}) = 0$. Thus, the asymptotic critical layer contribution \hat{p}_n^{CL} is given by

$$\hat{p}_n^{CL}(x, r|x_0, r_0) = -\frac{2\pi i\omega}{4\pi^2} \left(\frac{\rho_0(r)r_0}{\rho_0(r_0)r} \right)^{1/2} \frac{\Phi(r, \kappa_{r_0})e^{i\omega\kappa_{r_0}(x-x_0)}}{r_0 \mathcal{V}(\kappa_{r_0})U_x(r_0)} \begin{cases} v_1(r_0; \kappa_{r_0})v_2(r; \kappa_{r_0}) & r \leq r_0 \\ v_2(r_0; \kappa_{r_0})v_1(r; \kappa_{r_0}) & r > r_0 \end{cases}. \quad (3.5.31)$$

Our asymptotic critical layer contribution fails completely to capture any of the residues associated with the hydrodynamic modes, the pole at κ_r and any surface modes present. This is not surprising, as the high-frequency limit is not valid near the critical layer, even though it was a good approximation on the integration contour $\bar{\Gamma}_{CLH}$. This is because accurately approximating a function on a complex integration contour is no guarantee of the accuracy of the integral.

If we instead consider the critical layer contribution G_n^{CL} , with

$$G_n^{CL}(x, r|x_0, r_0) = \frac{\omega}{4\pi^2} \int_{\bar{\Gamma}_{CLH}} G_n(r|r_0; \omega, \kappa) e^{i\kappa(x-x_0)} d\kappa, \quad (3.5.32)$$

then we would pick up additional residues from $J(r_0, \kappa) = 0$. This could be calculated asymptotically but the expression will be much more complicated than (3.5.31) and will involve derivatives.

3.5.3 Significance of the critical layer

In general, we expect our asymptotic approximation for the critical layer contribution to be a poor approximation to the numerical result, since it fails to capture most of the behaviour. However, in the few cases we compared the numerical and asymptotic approximations (such as in Figure 3.21 for Example 3), the asymptotic approximation for the critical layer contribution is of a similar magnitude to the numerical critical layer contribution.

It has been suggested that the contribution from the critical layer can generally be ignored (Posson and Peake, 2012, 2013b). In Figure 3.18 we see the pressure field due to rotor self-noise, reproduced from Posson and Peake (2012, Figure 4). The pressure field was calculated using a numerical Green's function and a simple rotor model, which enabled the source terms to be calculated analytically. The top and bottom plots in each figure show the contribution from the acoustic modes and integral around the critical layer respectively. For the azimuthal numbers in Figure 3.18, we can safely ignore the critical layer contribution when calculating the pressure field.

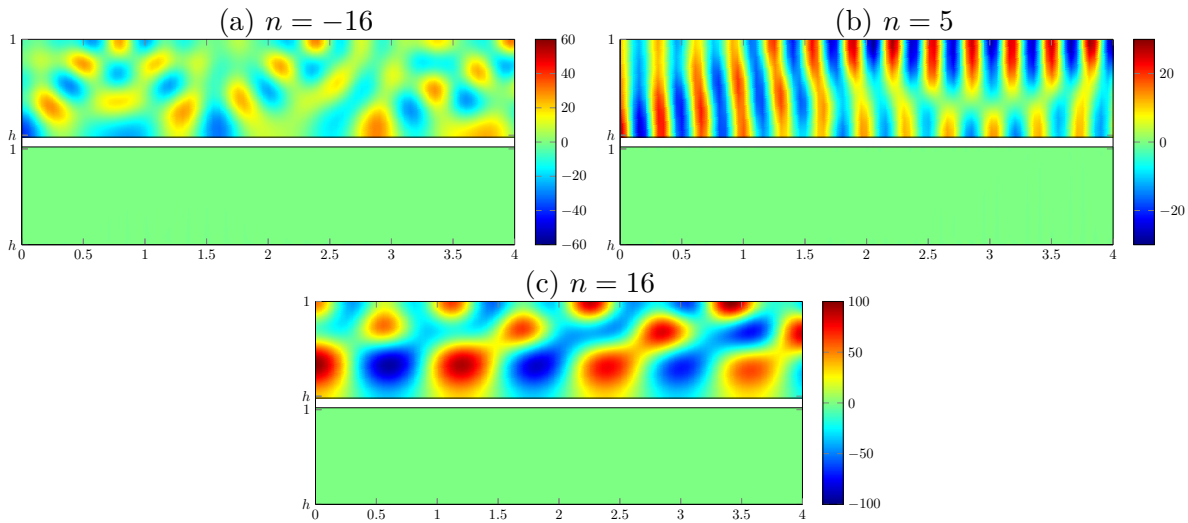


Figure 3.18: **Comparison of the effect of the acoustic modes and critical layer on the pressure.** We reproduce part of Figure 4 from Posson and Peake (2012) showing the pressure field. The pressure field was calculated using a numerical Green's function and a simple rotor model, which enabled the source terms to be calculated analytically. The top colour plot in each figure is the contribution from the acoustic modes and the bottom colour plot is the contribution from the critical layer. The parameters are $\omega = 30$, $h = 0.5$, $U_x = 0.4$, $U_\theta(r) = 0.28r$, hard walls and different azimuthal numbers.

There are some cases where we will have to calculate the critical layer contribution. For

some azimuthal numbers there are no cut-on acoustic modes and we have to consider the contribution from the critical layer to accurately calculate \hat{p}_n , since it would be larger than the contribution from the cut-off acoustic modes. However, the Green's function from these azimuthal numbers is dominated by the Green's function from azimuthal numbers where there are cut-on acoustic modes, so when calculating the total Green's function \hat{p}_ω we can still ignore the critical layer contribution.

When we get unstable hydrodynamic modes, with the condition given in [Heaton and Peake \(2006\)](#), we expect the contribution from the critical layer integral to be larger, but in general still considerably smaller than the contribution from the acoustic modes providing we are not too far downstream of the source. ([Posson and Peake, 2012](#), Figure 6).

3.6 Comparison of asymptotic and numerical Green's function

We now calculate the Green's function contribution $\hat{p}_n^m(x, r|x_0, r_0)$ for each cut-on acoustic mode κ_n^m and the nearest cut-off modes by using (3.5.9). We then sum these contributions to get the acoustic Green's function \hat{p}_n^A . We generally need to consider the Green's function contribution from at most the closest one or two cut-off modes, since the magnitude of the Green's function contribution for the cut-off modes far away from the real line is very small due to the exponentially small $\exp(ik(x - x_0))$ term. However, if $x - x_0$ is very small we might need to consider additional cut-off modes.

We compare the asymptotic and numerical Green's function for each mode, and show that the asymptotics provides a very good approximation to the numerical results. We validated our numerical Green's function by comparing with the program from [Posson and Peake \(2012, 2013a,b\)](#) and found excellent agreement for all parameters tested. Empirically, we find that the closer the asymptotic mode to the numerical mode then the more accurate the asymptotic Green's function is. The asymptotic Green's function is least accurate when we solve the “wrong” dispersion relation, such as modes $\kappa \in \mathcal{K}$ which we solve for by using the zero turning point dispersion relation. To improve the accuracy of the Green's function we could use a more accurate dispersion relation, which allows $v_1(r; \kappa)$ and $v_2(r; \kappa)$ to be neither exponential nor sinusoidal at the duct walls, and we describe this in [Section 3.7.3](#).

We only consider the Green's function for Examples 2, 3, 4, 7 and 8, although there are no difficulties in calculating the Green's function for the other five examples. We also present the comparison between the asymptotic and numerical contribution of the critical layer integral \hat{p}_n^{CL} for hard walls in Example 3. For each example we consider a single source (x_0, r_0) and vary r and x . We always consider $x - x_0 > 0$, so we only consider the downstream eigenmodes.

3.6.1 Test cases

Example 2

We first consider the parameters from Example 2, so we have constant shear, zero swirl and acoustic lining of impedance $Z_j = 1 - 2i$. In Figure 3.19 we see the Green's function contribution \hat{p}_n^m from the three cut-on modes and the first cut-off mode, and the sum of these four contributions \hat{p}_n^A . We see that the Green's function for the cut-off mode is $\mathcal{O}(10^{-7})$, while the contributions from the three cut-on modes are all $\mathcal{O}(10^{-3})$.

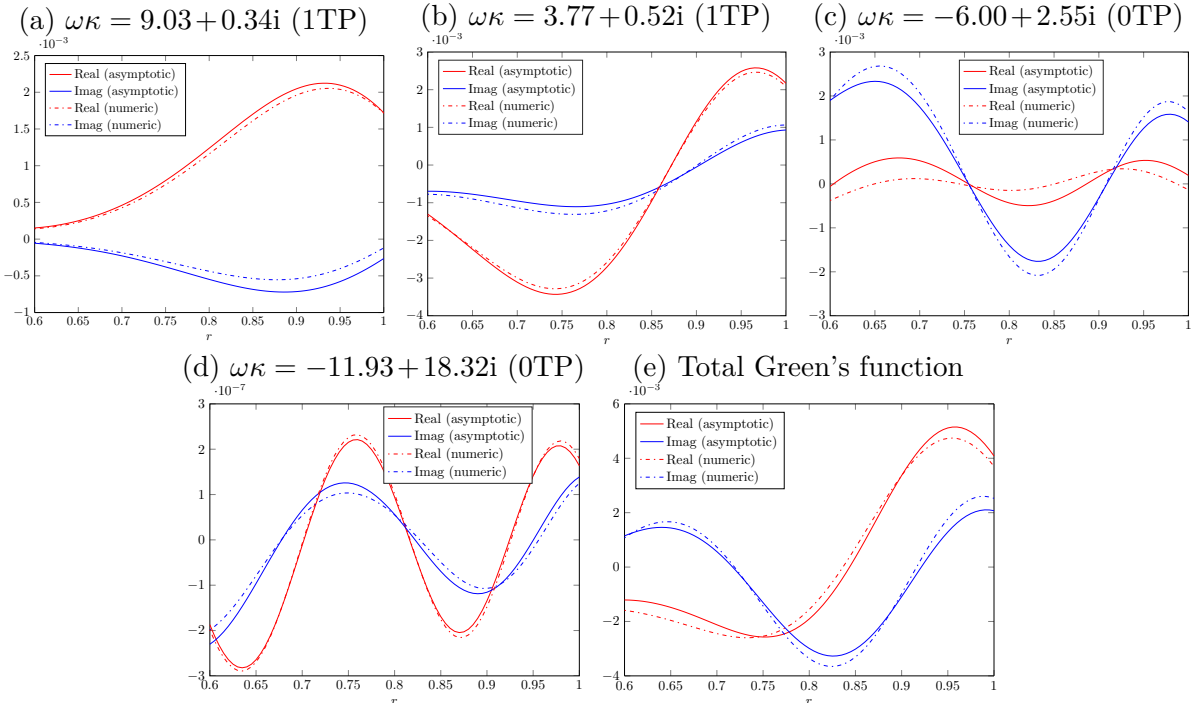


Figure 3.19: Comparison of the asymptotic and numerical Green's function \hat{p}_n^m for Example 2. The source is at $r_0 = 0.8$ and $x - x_0 = 0.5$.

In Figures 3.19a, 3.19b and 3.19d we see the asymptotic Green's function is a very good approximation to the numerical Green's function. However, in Figure 3.19c our asymptotic approximation is less accurate. This stems from the fact that we could use a more accurate dispersion relation to calculate the asymptotic eigenmode. Despite this inaccuracy, the total asymptotic Green's function is a very good approximation to the numerical Green's function in Figure 3.19e.

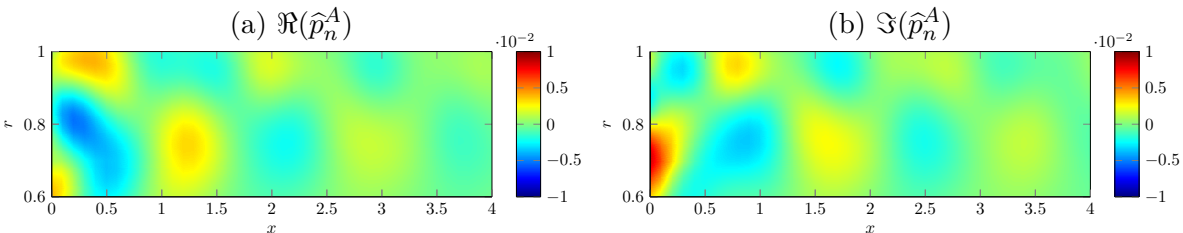


Figure 3.20: Colour plot of the asymptotic Green's function \hat{p}_n^A for Example 2, with a source at $(x_0, r_0) = (0, 0.8)$ as x and r vary.

We also consider the Green's function for a point source at $(x_0, r_0) = (0, 0.8)$ and let both x and r vary. In Figure 3.20 we plot the real and imaginary part of the asymptotic

Green's function, obtained by summing the contributions from the three cut-on modes and the first cut-off mode. The lining causes the Green's function to decay in the axial direction. We also see a distinct repeating pattern in the axial direction, with a period of about $x = 1/\eta$.

Example 3

In Example 3 the shear is constant, the swirl is of the form $U_\theta(r) = 0.1r + 0.1/r$ and the duct has hard walls. There are two cut-on modes and we see their Green's function contributions \hat{p}_n^m in Figures 3.21a and 3.21b. We see the asymptotic Green's function accurately approximates the numerical Green's function for these cut-on modes. In Example 2 the Green's function from the cut-on modes all had a similar magnitude, but in this example the eigenmode at $k = -2.15$ dominates.

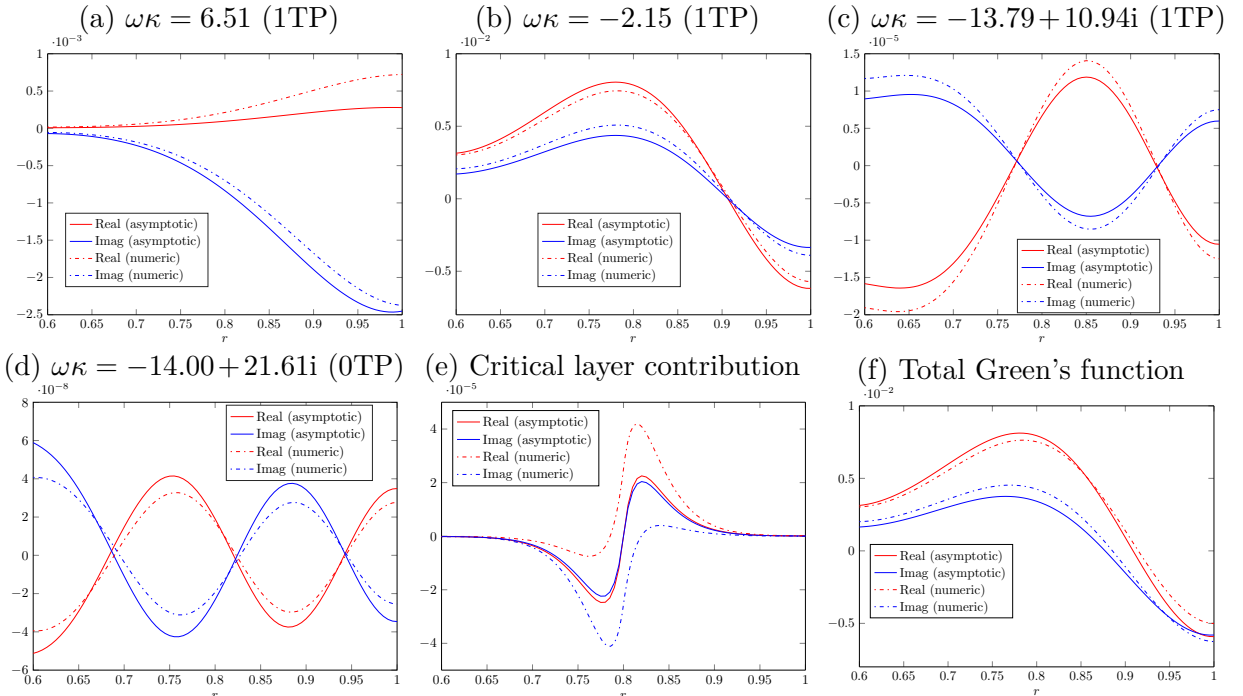


Figure 3.21: Comparison of the asymptotic and numerical Green's function \hat{p}_n^m for Example 3. The source is at $r_0 = 0.8$ and $x - x_0 = 0.5$.

The Green's function associated with the first cut-off mode in Figure 3.21c is several orders of magnitude smaller than the cut-on modes, but still well approximates the numerical Green's function. In Figure 3.21d we plot the Green's function contribution \hat{p}_n^m from the second cut-off mode and see that the asymptotic Green's function is quite accurate, but is even smaller in magnitude than the contribution from the first cut-off mode. In Figure 3.21e we see the contribution of the critical layer \hat{p}_n^{CL} asymptotically and numerically. We see that the asymptotic contribution is of a similar order of magnitude to the numerical contribution, but the asymptotics predicts the contribution of the critical layer to be exactly zero at $r = r_0 = 0.8$, while the numerical solution is clearly non-zero at $r = 0.8$. The reasons for the inaccurate asymptotic Green's function contribution are given in Section 3.5.2. As expected, the critical layer contribution is several orders of magnitude smaller than the

contribution from the cut-on modes, and of a similar magnitude to the contribution from the first cut-off mode.

Finally, in Figure 3.21f we see the sum of the contributions from Figures 3.21a to 3.21e, giving the Green's function. The Green's function can be attributed almost entirely to the single eigenmode $k = -2.15$.

Example 4

Example 4 has the same parameters as Example 3 but with lined walls of impedance $Z_j = 1 - 2i$. In Figures 3.22a and 3.22b we see the asymptotic Green's function contributions \hat{p}_n^m from

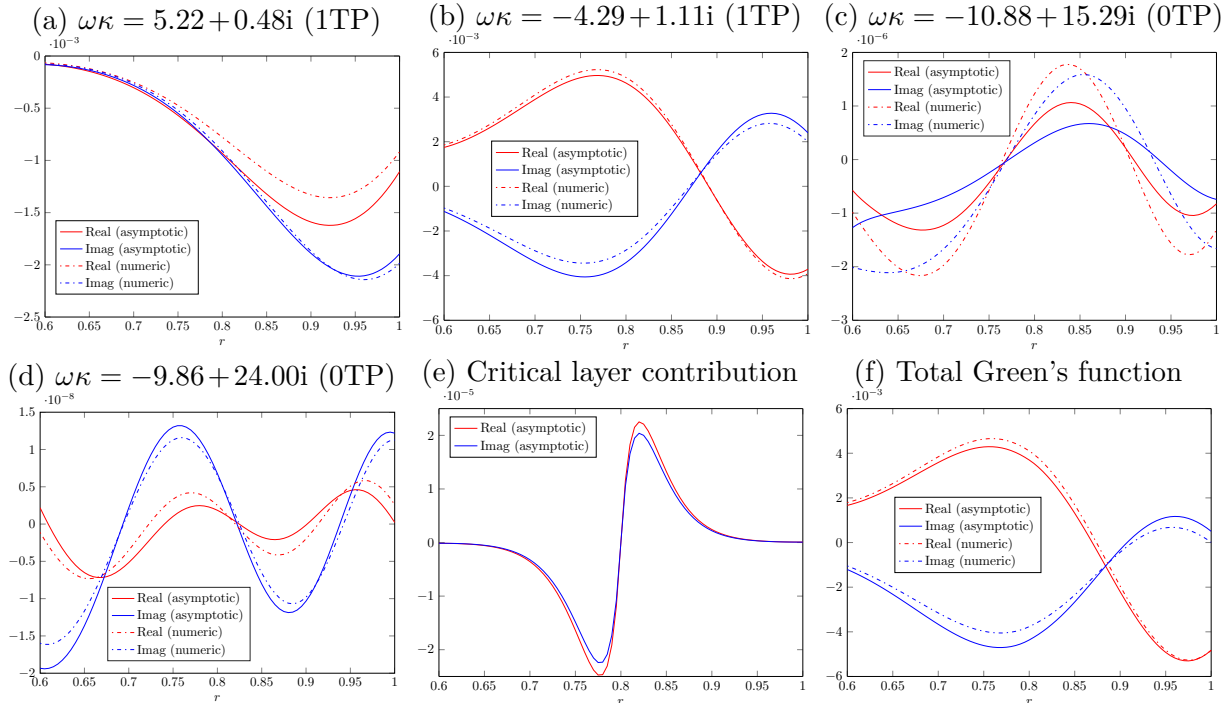


Figure 3.22: Comparison of the asymptotic and numerical Green's function \hat{p}_n^m for Example 4. The source is at $r_0 = 0.8$ and $x - x_0 = 0.5$.

the cut-on modes accurately approximates the numerical Green's function. Furthermore, the cut-on mode $k = -4.29 + 1.11i$ dominates the total acoustic Green's function \hat{p}_n^A in Figure 3.22f. This mode is the counterpart of the dominant mode $k = -2.15$ in Example 3.

In Figure 3.22c we plot the contribution to the Green's function from the first cut-off mode. We use the asymptotic eigenmode that solves the zero turning point dispersion relation despite $\kappa \in \mathcal{K}$, and this is what causes the inaccuracy in the asymptotic Green's function. Using a more accurate dispersion relation such as in Section 3.7.3 would give a much more accurate Green's function. In Figure 3.22d we plot the Green's function contribution \hat{p}_n^m from the second cut-off mode, which is $\mathcal{O}(10^{-8})$. Although we do not approximate the second cut-off eigenmode very accurately asymptotically (see Figure 3.6), the asymptotic Green's function contribution is still quite accurate. In Figure 3.22e we see the asymptotic Green's function contribution \hat{p}_n^{CL} from the critical layer is very similar to the contribution in Example 3 (the figures have different scales), and is still several orders of magnitude smaller than the contribution from the dominant cut-on modes.

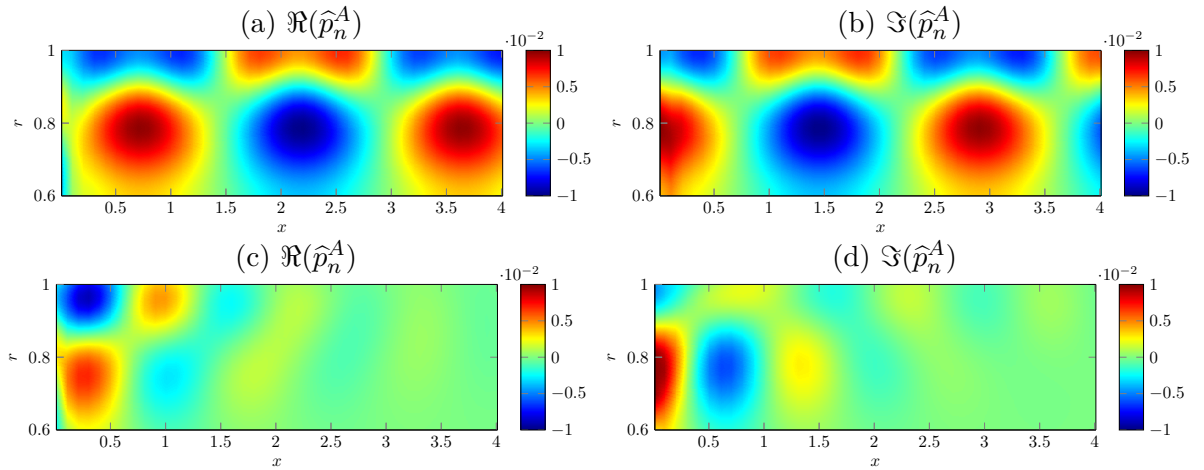


Figure 3.23: Colour plot of the asymptotic Green's function \hat{p}_n^A with a source at $(x_0, r_0) = (0, 0.8)$ as x and r vary. Top: Example 3 (hard-walled duct), bottom: Example 4 (lined walls).

In Figure 3.23 we plot the asymptotic acoustic Green's function \hat{p}_n^A for a fixed point source at $(x_0, r_0) = (0, 0.8)$ as we let both x and r vary. We plot the real and imaginary part of the asymptotic Green's function for both Examples 3 and 4. In a hard-walled duct, the Green's function infinitely repeats, while in a lined duct the Green's function decays in the axial direction. Additionally, the axial period changes significantly after the introduction of lining, while the magnitude of the Green's function is smaller in a lined duct.

We also note the difference between the bottom row of Figure 3.23 and Figure 3.20, with the difference due to the swirl in Example 4. This shows the effect of the swirl is very significant, especially close to the source.

3.6.2 Semi-realistic shear and swirl

Example 7

In Figure 3.24 we consider the Green's function for the semi-realistic swirling flow given in Figure 3.8. We consider the contributions \hat{p}_n^m from the three cut-on modes and the first two cut-off modes. The first of these cut-off modes, at $k = -6.37 + 2.97i$, only has a small imaginary part and the Green's function contribution from this mode, in Figure 3.24d, is of a similar magnitude, $\mathcal{O}(10^{-3})$, to the Green's function contribution from the cut-on modes in Figures 3.24a, 3.24b and 3.24c. Unlike some of the other examples, there is no single dominant eigenmode. The contribution to the Green's function from the second cut-off mode, at $k = -6.47 + 13.82i$, is $\mathcal{O}(10^{-7})$ so it is insignificant compared to the other modes.

The accuracy of the asymptotic Green's function for each mode is very good and compares extremely favourably to the numerical results. For the second cut-off mode, in Figure 3.24e, the amplitude of the asymptotic Green's function is not perfect, but otherwise the asymptotic results are very impressive. The error in the asymptotic Green's function in Figure 3.24e is due to a large error in the imaginary part of the asymptotic eigenmode (see Figure 3.9), which is because the eigenmode is very close to the edge of the region \mathcal{K} . In Figure 3.24f we see the total acoustic Green's function \hat{p}_n^A with the difference between the

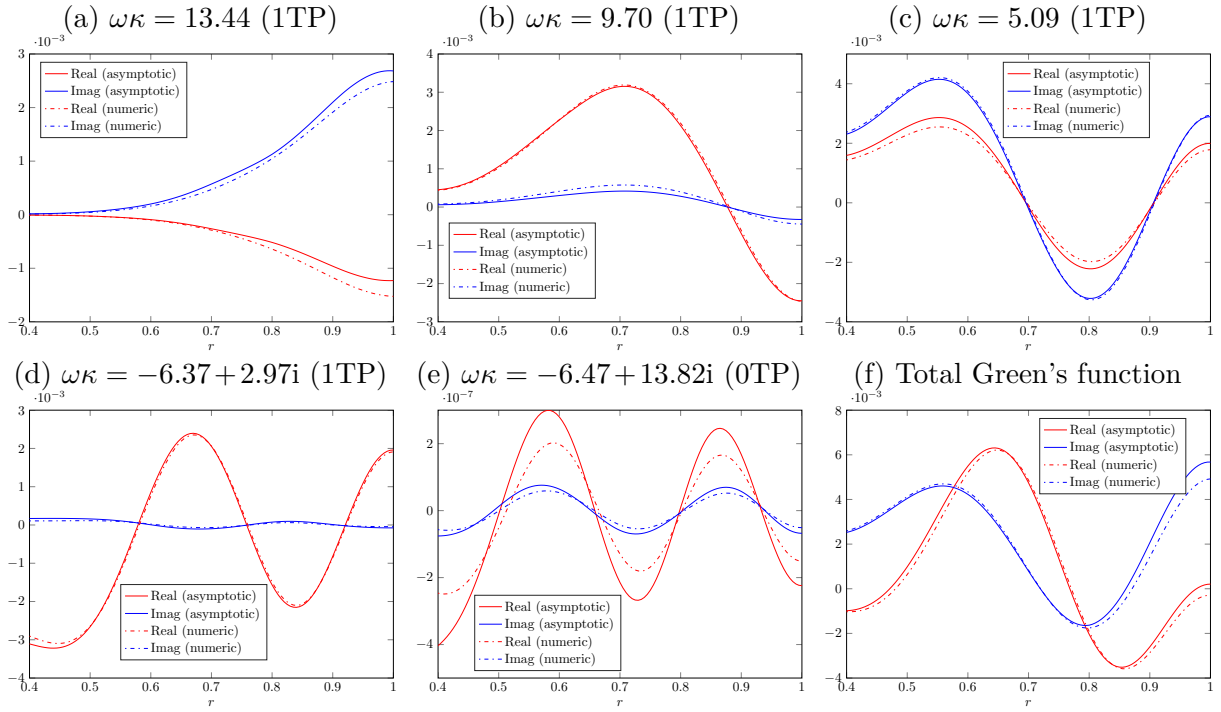


Figure 3.24: Comparison of the asymptotic and numerical Green's function \hat{p}_n^m for Example 7. The source is at $r_0 = 0.8$ and $x - x_0 = 0.5$.

asymptotic and numerical Green's function is between $\mathcal{O}(10^{-5})$ and $\mathcal{O}(10^{-4})$.

Example 8

In Figure 3.25 we calculate the Green's function contributions \hat{p}_n^m for Example 8, with the parameters the same as Example 7 except lined walls of impedance of $Z_j = 1 - 2i$. The first

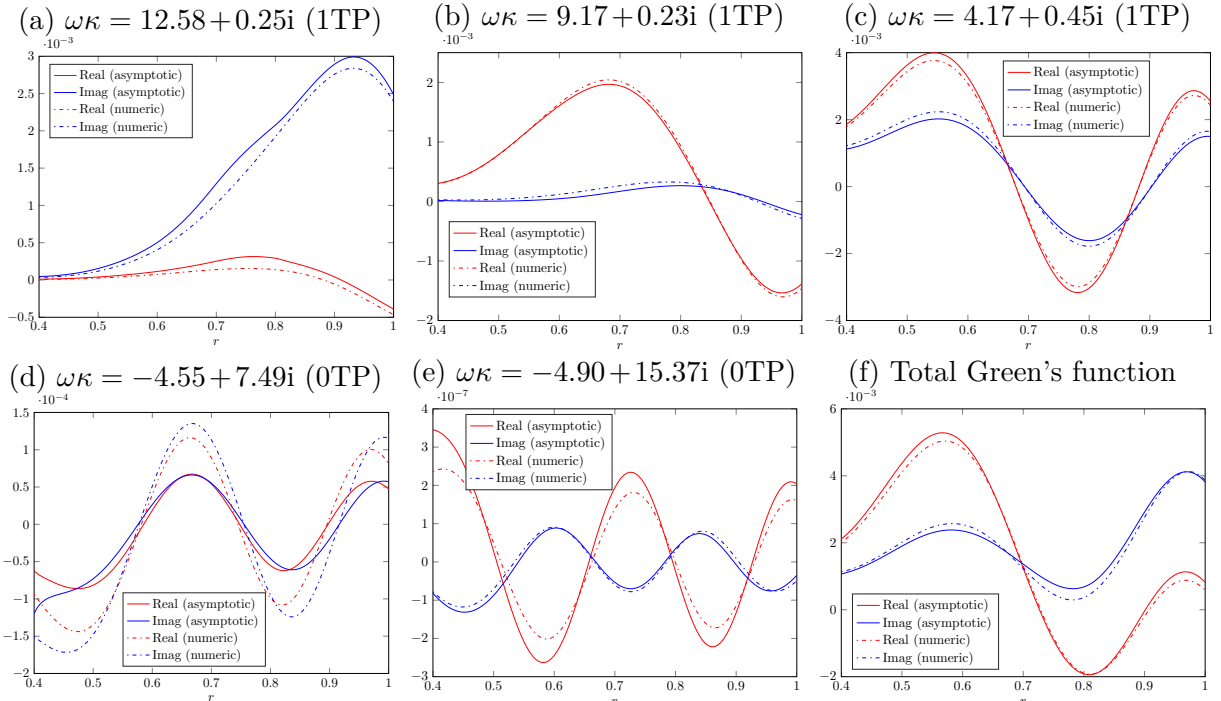
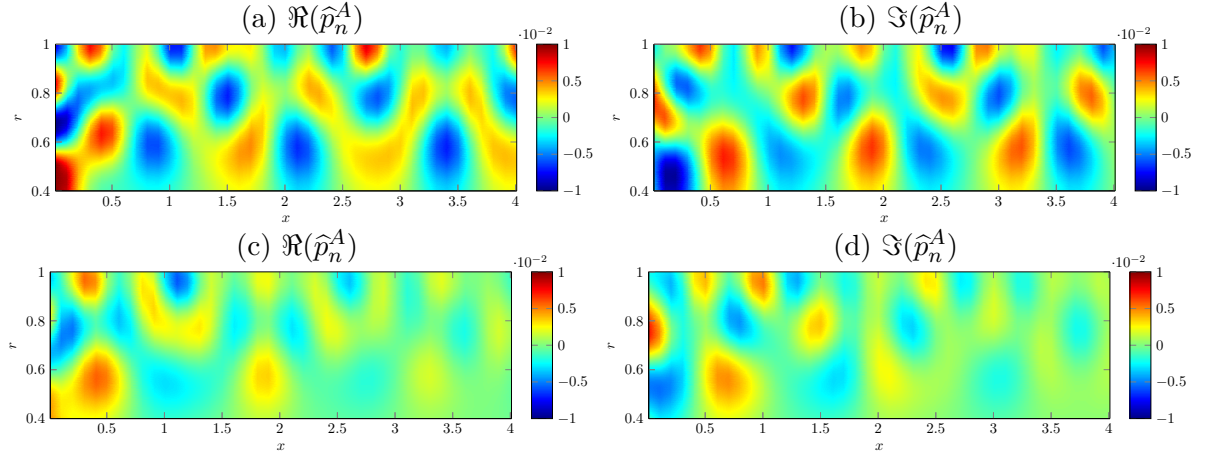


Figure 3.25: Comparison of the asymptotic and numerical Green's function \hat{p}_n^m for Example 8. The source is at $r_0 = 0.8$ and $x - x_0 = 0.5$.

thing we see is that asymptotic Green's function is very accurate when we compare it to the numerical Green's function. Only in [Figure 3.25d](#) is the asymptotic Green's function a poor approximation to the numerical results. This poor approximation stems from the fact that the asymptotic eigenmode $k = -4.55 + 7.49i$ is in the region $\omega \mathcal{K}$ but we solved the zero turning point dispersion relation to find it in [Figure 3.9](#), since it was more accurate than solving the one turning point dispersion relation.

Unlike Example 7, the contribution from the first cut-off mode in [Figure 3.25d](#) is one order of magnitude smaller than the contributions from the cut-on modes. The contribution from the second cut-off mode in [Figure 3.25e](#) is again $\mathcal{O}(10^{-7})$, and all subsequent cut-off modes have even smaller contributions. Thus, the total acoustic Green's function \hat{p}_n^A in [Figure 3.25f](#) is dominated by the three cut-on modes.

In [Figure 3.26](#) we plot the real and imaginary part of the asymptotic acoustic Green's function \hat{p}_n^A for the semi-realistic swirling flow. We consider a point source at $(x_0, r_0) = (0, 0.8)$ and vary x and r . We clearly see the effect of the lining in [Figures 3.26c](#) and [3.26d](#). The presence of lining changes the magnitude of the Green's function and makes it decay in the axial direction.



[Figure 3.26](#): Colour plot of the asymptotic Green's function \hat{p}_n^A with a source at $(x_0, r_0) = (0, 0.8)$ as x and r vary. Top: Example 7 (hard-walled duct), bottom: Example 8 (lined walls).

3.6.3 Effect of entropy on the Green's function

In [Section 3.4.3](#) we saw that entropy had three main effects on the eigenmodes; the appearance of “surface-entropy” modes, a shifting of the branch of cut-off modes to the right and a reduction in the number of cut-on modes. Since the main contribution to the acoustic Green's function comes from the cut-on modes, it is the last feature that causes the Green's function to change significantly as we vary entropy.

In [Figure 3.27](#) we plot the Green's function contributions \hat{p}_n^m from the three furthest downstream cut-on eigenmodes as the entropy varies. We also plot the total acoustic Green's function \hat{p}_n^A . The base flow entropy is given by $s_0(r) = -\log(r^\beta)$, with $\beta = -0.3$ (left), $\beta = 0$ (middle) and $\beta = 0.3$ (right). As we vary the value of β , the density, speed

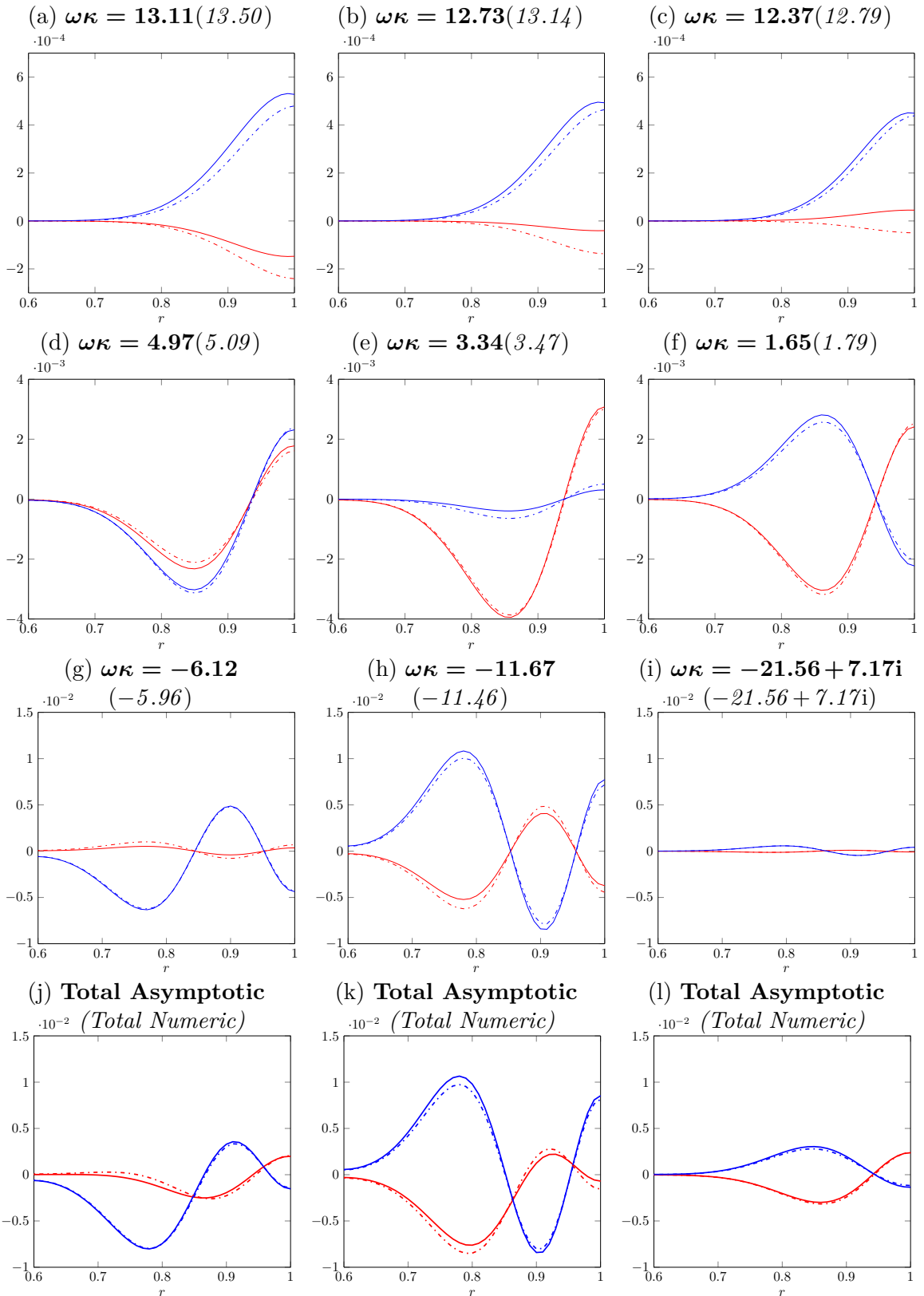


Figure 3.27: **Real and imaginary parts of asymptotic and numerical Green's function as entropy varies for a source at $x - x_0 = 0.5$ and $r_0 = 0.8$.**

The parameters of the flow are $U_x(r) = 0.3 + 0.2r^2$, $U_\theta(r) = 0.1r + 0.1/r$, $n = 32$, $\omega = 50$, $h = 0.6$ and hard walls. The entropy is given by $s_0(r) = -\log(r^\beta)$ with $\beta = -0.3$ (left), $\beta = 0$ (middle) and $\beta = 0.3$ (right).

From top to bottom, we plot the Green's function contributions \hat{p}_n^m from the three most cut-on downstream acoustic modes and at the bottom, the sum of these contributions \hat{p}_n^A . *Numerical eigenmodes are in italics, asymptotic eigenmodes are in bold.* Solid lines are the asymptotic Green's function; dashed lines are the numerical Green's function. Red is for the real part, blue is for the imaginary part.

of sound and pressure of the base flow all vary since the base flow must satisfy the Euler equations. This then causes functions such as $q_n(r, \kappa)$ and $\Phi(r, \kappa)$ to vary with entropy. As mentioned in [Section 3.4.3](#) it is the speed of sound increasing that causes there to be less cut-on modes.

In [Figure 3.27](#) we give the asymptotic eigenmodes in bold and the numerical eigenmodes in italic. We plot the asymptotic Green's function with solid lines and plot the numerical Green's function with dashed lines, with red and blue corresponding to the real and imaginary parts. We only need to consider the three most cut-on modes in [Figure 3.27](#) since subsequent downstream modes for all three values of β are cut-off, with the Green's function contributions \hat{p}_n^m from these cut-off modes orders of magnitude smaller than the contributions from the dominant cut-on modes. In [Figure 3.27](#) we see that for all values of entropy our asymptotic Green's function is very accurate compared to the numerical Green's function.

In [Figure 3.27](#) we see the Green's function contribution \hat{p}_n^m from the furthest downstream eigenmode (top row) is very similar for all values of β . When we consider the next eigenmode (second row) we see that the shape of the Green's function contribution changes significantly as we vary the entropy. This is because the second downstream eigenmode moves by a significant amount as we vary entropy.

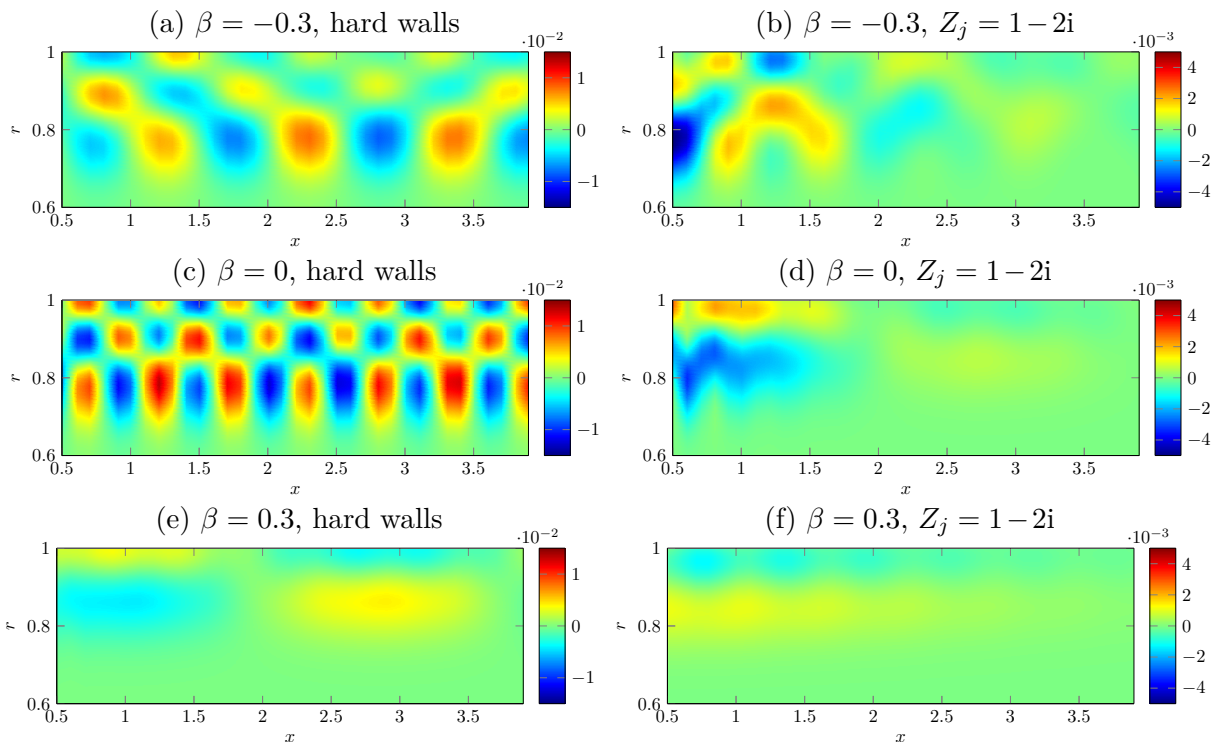


[Figure 3.28](#): Colour plot of real part of asymptotic Green's function \hat{p}_n^A with a source at $(x_0, r_0) = (0, 0.8)$ as x and r vary. From top to bottom, we consider $\beta = -0.3$, $\beta = 0$ and $\beta = 0.3$. On the left-hand side is \hat{p}_n^A for a hard-walled duct and on the right-hand side is \hat{p}_n^A for a lined duct with impedance $Z_j = 1 - 2i$. The other parameters are the same as [Figure 3.27](#).

When we consider the Green's function contribution \hat{p}_n^m from the third furthest downstream cut-on eigenmode (third row), we see significantly different shapes and amplitudes

for the Green's function. When $\beta = 0.3$ this eigenmode is cut-off with imaginary part 7.17, while when $\beta = 0$ or $\beta = -0.3$ it is completely cut-on. Finally, in the fourth row we see the total acoustic contribution \hat{p}_n^A obtained by summing the contribution from the three most cut-on modes, with vastly different Green's functions as the entropy varies. When $\beta = 0$ and $\beta = -0.3$ the third furthest downstream eigenmode contributes most to the Green's function, since it is $\mathcal{O}(10^{-2})$. However, when $\beta = 0.3$ the second furthest downstream mode is the dominant eigenmode. Thus, varying the entropy not only changes the Green's function at each mode, but changes the dominant eigenmode(s).

In [Figure 3.28](#) we plot the real part of the total asymptotic acoustic Green's function \hat{p}_n^A for a source at $(x_0, r_0) = (0, 0.8)$ as x and r vary. We see the effect of both entropy and lining on the Green's function. In both a lined duct and a hard-walled duct, we see that when $\beta = 0.3$ the Green's function is a lot smaller in magnitude than when $\beta = 0$ or $\beta = -0.3$.

As the entropy varies, we have three completely different colour plots, and the period in the axial direction varies significantly with entropy for both a hard-walled and a lined duct. It is clear from our results that a small difference in entropy can modify the Green's function substantially. Thus, we need to model the base flow entropy accurately so we calculate the correct Green's function.

The lining causes the Green's function to decay in the axial direction for all values of entropy. Additionally, in a lined duct the Green's function has a significantly smaller magnitude than in a hard-walled duct, with the right-hand scale in [Figure 3.28](#) three times smaller than the scale on the left-hand side.

3.7 Limitations of the method for calculating the asymptotic Green's function

We conclude the chapter with a brief overview of the limitations of the asymptotic method. We also suggest how we can overcome some of them.

3.7.1 Critical layer contribution

The first limitation is that the asymptotic calculation of the critical layer contribution is not very accurate in [Section 3.5.2](#), and is too expensive to calculate numerically with current techniques. However, we saw that most of the time we can ignore the critical layer contribution and still get an accurate Green's function.

3.7.2 Multiple zeros of $q_n(r, \kappa)$

In [Figure 3.9](#) we saw a region of κ space where $q_n(r, \kappa)$ had two zeros in the duct, at $r_{c,1}(\kappa)$ and $r_{c,2}(\kappa)$. We can easily construct a WKB solution to account for the two zeros by joining

together two one turning point solutions, as described in [Appendix A.1](#). We assume that $q_n(r, \kappa) > 0$ for $r_{c,1} < r < r_{c,2}$ and $q_n(r, \kappa) < 0$ when $r < r_{c,1}$ or $r > r_{c,2}$, and additionally that the zeros are simple. Let us define

$$\mathcal{Q}_1(\kappa) = \left(\frac{\partial q_n}{\partial r}(r_{c,1}(\kappa), \kappa) \right)^{1/3}, \quad \mathcal{Q}_2(\kappa) = \left(\frac{\partial q_n}{\partial r}(r_{c,2}(\kappa), \kappa) \right)^{1/3} \text{ and } \mu = \omega^{-2/3}, \quad (3.7.1)$$

then $v_j(r; \kappa)$ is given by

$$v_j(r; \kappa) = \begin{cases} (-q_n(r, \kappa))^{-1/4} (a_1^j e^{-i\omega\Psi_n^2(r, \kappa)} + b_1^j e^{i\omega\Psi_n^2(r, \kappa)}) & r - r_{c,2} \gg \mu \\ a_2^j \text{Ai}(\mathcal{Q}_2(\kappa)\mu(r_{c,2}-r)) + b_2^j \text{Bi}(\mathcal{Q}_2(\kappa)\mu(r_{c,2}-r)) & |r - r_{c,2}| \ll \mu \\ (q_n(r, \kappa))^{-1/4} (a_3^j e^{i\omega\Psi_n^1(r, \kappa)} + b_3^j e^{-i\omega\Psi_n^1(r, \kappa)}) & r_{c,1} + \mu \ll r \ll r_{c,2} - \mu, \\ a_4^j \text{Ai}(\mathcal{Q}_1(\kappa)\mu(r_{c,1}-r)) + b_4^j \text{Bi}(\mathcal{Q}_1(\kappa)\mu(r_{c,1}-r)) & |r - r_{c,1}| \ll \mu \\ (-q_n(r, \kappa))^{-1/4} (a_5^j e^{-i\omega\Psi_n^1(r, \kappa)} + b_5^j e^{i\omega\Psi_n^1(r, \kappa)}) & r_{c,1} - r \gg \mu \end{cases} \quad (3.7.2)$$

where

$$\Psi_n^1(r, \kappa) = \int_{r_{c,1}(\kappa)}^r \sqrt{q_n(s, \kappa)} ds \text{ and } \Psi_n^2(r, \kappa) = \int_{r_{c,2}(\kappa)}^r \sqrt{q_n(s, \kappa)} ds. \quad (3.7.3)$$

We match the constants a_l^j and b_l^j by using the asymptotic behaviour of the Airy functions, which is given in [\(A.1.13\)](#) and [\(A.1.14\)](#). We could then calculate the Wroński, and find asymptotic eigenmodes by finding zeros of the Wroński. The difficultly lies in the fact that a uniformly-valid solution when $q_n(r, \kappa)$ has two zeros is only known when the zeros are close together ([Nielsen and Peake, 2016](#)), so constructing the Green's function would be difficult.

3.7.3 A more accurate dispersion relation

Most of the inaccurate asymptotic eigenmodes in [Section 3.4](#) are because the Airy function was not exponential or sinusoidal at the duct walls, since r_c was close to one of the duct walls. This also causes some of the asymptotic Green's function contributions in [Section 3.6](#) to be inaccurate.

In this section we recalculate the constants $A^j(\kappa)$ and $B^j(\kappa)$, which gives us a new dispersion relation. We will also now use the full boundary conditions rather than just the leading order behaviour. Let $v_j(r; \kappa)$ be the WKB solutions to the equation

$$v_j''(r; \kappa) + \omega^2 q_n(r, \kappa) v_j(r; \kappa) = 0, \quad (3.7.4)$$

and let us define $r_2 = h$ and $r_1 = 1$. At the duct walls, we find that

$$v_j(r_j; \kappa) = A^j(\kappa) \mathcal{A}^j(\kappa) + B^j(\kappa) \mathcal{B}^j(\kappa), \quad (3.7.5)$$

where

$$\tau_j(\kappa) = \left(\frac{3\omega\Psi_n(r_j, \kappa)}{2} \right)^{2/3}, \quad (3.7.6)$$

$$\mathcal{A}^j(\kappa) = |q_n(r_j, \kappa)|^{-1/4} e^{i\omega\psi_n(r_j, \kappa)} \mathbb{1}_{\mathcal{K}^C} + \sqrt{\pi} \left[\left(\frac{\tau_j(\kappa)}{q_n(r_j, \kappa)} \right)^{1/4} \text{Ai}(-\tau_j(\kappa)) \right] \mathbb{1}_{\mathcal{K}}, \quad (3.7.7)$$

and

$$\mathcal{B}^j(\kappa) = |q_n(r_j, \kappa)|^{-1/4} e^{-i\omega\psi_n(r_j, \kappa)} \mathbb{1}_{\mathcal{K}^C} + \sqrt{\pi} \left[\left(\frac{\tau_j(\kappa)}{q_n(r_j, \kappa)} \right)^{1/4} \text{Bi}(-\tau_j(\kappa)) \right] \mathbb{1}_{\mathcal{K}}. \quad (3.7.8)$$

We now choose the region \mathcal{R} to contain critical points within a distance of $\omega^{-2/3}$ of the duct, so \mathcal{K} becomes larger than it was before. We also calculate that

$$\frac{dv_j}{dr}(r_j; \kappa) = A^j(\kappa)\mathbb{A}^j(\kappa) + B^j(\kappa)\mathbb{B}^j(\kappa), \quad (3.7.9)$$

where

$$\begin{aligned} \mathbb{A}^j(\kappa) &= \left(-\frac{\frac{\partial}{\partial r}q_n(r_j, \kappa)}{4q_n(r_j, \kappa)} + i\omega\sqrt{q_n(r_j, \kappa)} \right) |q_n(r_j, \kappa)|^{-1/4} e^{i\omega\psi_n(r_j, \kappa)} \mathbb{1}_{\mathcal{K}^C} + \sqrt{\pi} \left(\frac{\tau_j(\kappa)}{q_n(r_j, \kappa)} \right)^{1/4} \\ &\times \left[\left(\frac{1}{6} \frac{\frac{\partial}{\partial r}\Psi_n(r_j, \kappa)}{\Psi_n(r_j, \kappa)} - \frac{1}{4} \frac{\frac{\partial}{\partial r}q_n(r_j, \kappa)}{q_n(r_j, \kappa)} \right) \text{Ai}(-\tau_j(\kappa)) - \frac{2}{3} \frac{\frac{\partial}{\partial r}\Psi_n(r_j, \kappa)}{\Psi_n(r_j, \kappa)} \tau_j(\kappa) \text{Ai}'(-\tau_j(\kappa)) \right] \mathbb{1}_{\mathcal{K}}, \end{aligned} \quad (3.7.10)$$

and

$$\begin{aligned} \mathbb{B}^j(\kappa) &= \left(-\frac{\frac{\partial}{\partial r}q_n(r_j, \kappa)}{4q_n(r_j, \kappa)} - i\omega\sqrt{q_n(r_j, \kappa)} \right) |q_n(r_j, \kappa)|^{-1/4} e^{-i\omega\psi_n(r_j, \kappa)} \mathbb{1}_{\mathcal{K}^C} + \sqrt{\pi} \left(\frac{\tau_j(\kappa)}{q_n(r_j, \kappa)} \right)^{1/4} \\ &\times \left[\left(\frac{1}{6} \frac{\frac{\partial}{\partial r}\Psi_n(r_j, \kappa)}{\Psi_n(r_j, \kappa)} - \frac{1}{4} \frac{\frac{\partial}{\partial r}q_n(r_j, \kappa)}{q_n(r_j, \kappa)} \right) \text{Bi}(-\tau_j(\kappa)) - \frac{2}{3} \frac{\frac{\partial}{\partial r}\Psi_n(r_j, \kappa)}{\Psi_n(r_j, \kappa)} \tau_j(\kappa) \text{Bi}'(-\tau_j(\kappa)) \right] \mathbb{1}_{\mathcal{K}}. \end{aligned} \quad (3.7.11)$$

Setting $A^j(\kappa) = 1$ and applying the boundary conditions in (3.2.6) gives

$$B^2(\kappa) (\mathbb{B}^2(\kappa) + f_2(h, \kappa) \mathcal{B}^2(\kappa)) = -\mathbb{A}^2(\kappa) - f_2(h, \kappa) \mathcal{A}^2(\kappa), \quad (3.7.12)$$

and

$$B^1(\kappa) (\mathbb{B}^1(\kappa) + f_1(1, \kappa) \mathcal{B}^1(\kappa)) = -\mathbb{A}^1(\kappa) - f_1(1, \kappa) \mathcal{A}^1(\kappa), \quad (3.7.13)$$

which we solve to find $B^1(\kappa)$ and $B^2(\kappa)$. We then calculate that the Wrońskiian $\mathcal{V}(\kappa)$ is proportional to $B^1(\kappa) - B^2(\kappa)$, with the details given in Chapter 5. Thus, the dispersion relation is given by

$$B^1(\kappa) - B^2(\kappa) = 0, \quad (3.7.14)$$

which we solve to find the asymptotic eigenmodes. Our new dispersion relation is more accurate since we have including the whole boundary condition, rather than only the leading

order behaviour. It is also more accurate when the critical point is close to the edge of the duct, since we no longer assume that the Airy function behaves exponentially or sinusoidally at the duct walls.

Calculating the Green's function

The only difference in calculating the Green's function is calculating the derivative of the Wroński with respect to κ . In principle we could find the derivatives of $B^1(\kappa)$ and $B^2(\kappa)$ with respect to κ analytically by using (3.7.12) and (3.7.13). However, this result is so messy that we may as well calculate the derivatives with respect to κ numerically. We already have to solve for the eigenmodes numerically, so calculating the derivatives analytically or numerically doesn't matter too much, providing the numerical method is stable.

Results of the new dispersion relation

We return to Example 4, and in Table 3.3 we show the numerical eigenmodes, the old asymptotic eigenmodes calculated using the dispersion relations (3.3.1), (3.3.2) or (3.3.3) and the new asymptotic eigenmodes from solving the dispersion relation in (3.7.14). Using the

Table 3.3: Improved accuracy of asymptotic (cut-on) eigenmodes by using the new asymptotic dispersion relation.

	Asymptotic (old)	Numerical	Asymptotic	Relative error
Cut-on	$-32.470 - 0.481i$	$-32.449 - 0.523i$	$-32.450 - 0.523i$	0.0019%
	$-22.094 - 1.430i$	$-22.208 - 1.452i$	$-22.209 - 1.452i$	0.0037%
	$-4.287 + 1.112i$	$-4.091 + 1.128i$	$-4.090 + 1.127i$	0.0218%
	$5.223 + 0.476i$	$5.418 + 0.553i$	$5.419 + 0.553i$	0.0170%
Cut-off	$-12.761 - 25.589i$	$-12.844 - 25.629i$	$-12.843 - 25.629i$	0.0036%
	$-13.494 - 15.845i$	$-13.738 - 15.230i$	$-13.738 - 15.230i$	0.0039%
	$-10.878 + 15.286i$	$-10.880 + 14.499i$	$-10.880 + 14.498i$	0.0038%
	$-9.858 + 24.005i$	$-10.183 + 24.095i$	$-10.182 + 24.094i$	0.0042%

new dispersion relation gives asymptotic modes which are extremely good approximations to the numerical modes, with the most noticeable improvement for the asymptotic eigenmode corresponding to the numerical eigenmode at $k = -10.880 + 14.499i$. The largest relative error for the asymptotic cut-on modes or the first two asymptotic cut-off modes is 0.0218%.

In Figure 3.29 we consider the improvement in the asymptotic Green's function using the new dispersion relation. We only consider the Green's function contribution from the numerical eigenmode at $k = -10.880 + 14.499i$, and the total Green's function

In Figure 3.29a we see the asymptotic Green's function for the old dispersion relation is not at all accurate at this mode. In Figure 3.29b we see that if we use the new dispersion relation then we get an asymptotic Green's function which agrees perfectly with the numerical Green's function. Our total asymptotic Green's function is now indistinguishable from the numerical Green's function in Figure 3.29c, with the error between the Green's function now $\mathcal{O}(10^{-6})$. We also see remarkably accurate asymptotic Green's function for

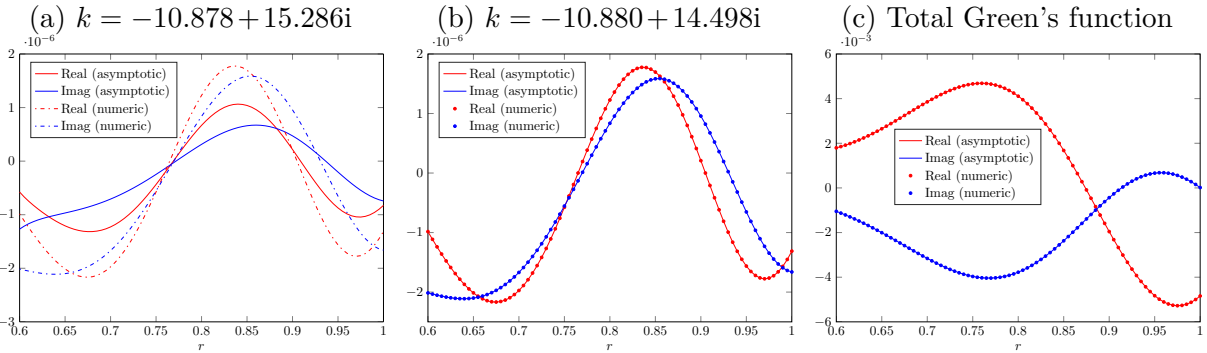


Figure 3.29: Effect of new dispersion relation on asymptotic Green's functions from the numerical eigenmode at $k = -10.880 + 14.499i$ in Example 4. (a) Green's function with old dispersion relations (3.3.1) to (3.3.3); (b) Green's function with new dispersion relation (3.7.14); (c) total Green's function with new dispersion relation.

the other examples with the new dispersion relation. Additionally, we no longer have any problems with the Green's function such as in Figures 3.22c and 3.25d. In the case of semi-realistic swirling flow, we still improve the results with this new dispersion relation but the results are no so dramatic.

Disadvantage of new dispersion relation

Despite the extremely good performance of the new dispersion relation for the asymptotic eigenmodes and asymptotic Green's function, there is one major disadvantage. We now need to make the branch cut of the $2/3$ root of τ in Figure 3.1 vary for some of the eigenmodes in order to find all of them. This is something that would be very hard to implement automatically.

3.7.4 A single azimuthal mode

So far, all of our results have considered just a single azimuthal mode. If we want the Green's function G_ω or \hat{p}_ω , then we have to sum over all azimuthal modes. For large values of n , we find that there are no cut-on eigenmodes and thus the Green's function contribution is very small. We find the dominant behaviour of G_ω is determined by azimuthal numbers $n = \mathcal{O}(\omega)$, as in Wundrow and Khavaran (2004), who considered the free-field Green's function for non-swirling flow.

In Figure 3.30 we plot the acoustic Green's function \hat{p}_ω^A as a function of θ and r and for a fixed value of x . We consider a single source with $r_0 = 0.8$, $\theta_0 = 0$ and $x - x_0 = 0.5$. The parameters are the same as Example 1 and Example 3, so $U_x = 0.5$, $\omega = 25$, $h = 0.6$, hard walls and we consider no swirl ($U_\theta = 0$) in Figures 3.30a and 3.30b, and swirl of the form $U_\theta(r) = 0.1r + 0.1/r$ in Figures 3.30c and 3.30d. We only consider the numerical Green's function here due to difficulties in implementing the correct branch cut automatically for the asymptotic method (with the new dispersion relation), and because it is possible $q_n(r, \kappa)$ has two zeros in the duct for certain azimuthal numbers, in which case our asymptotic method fails.

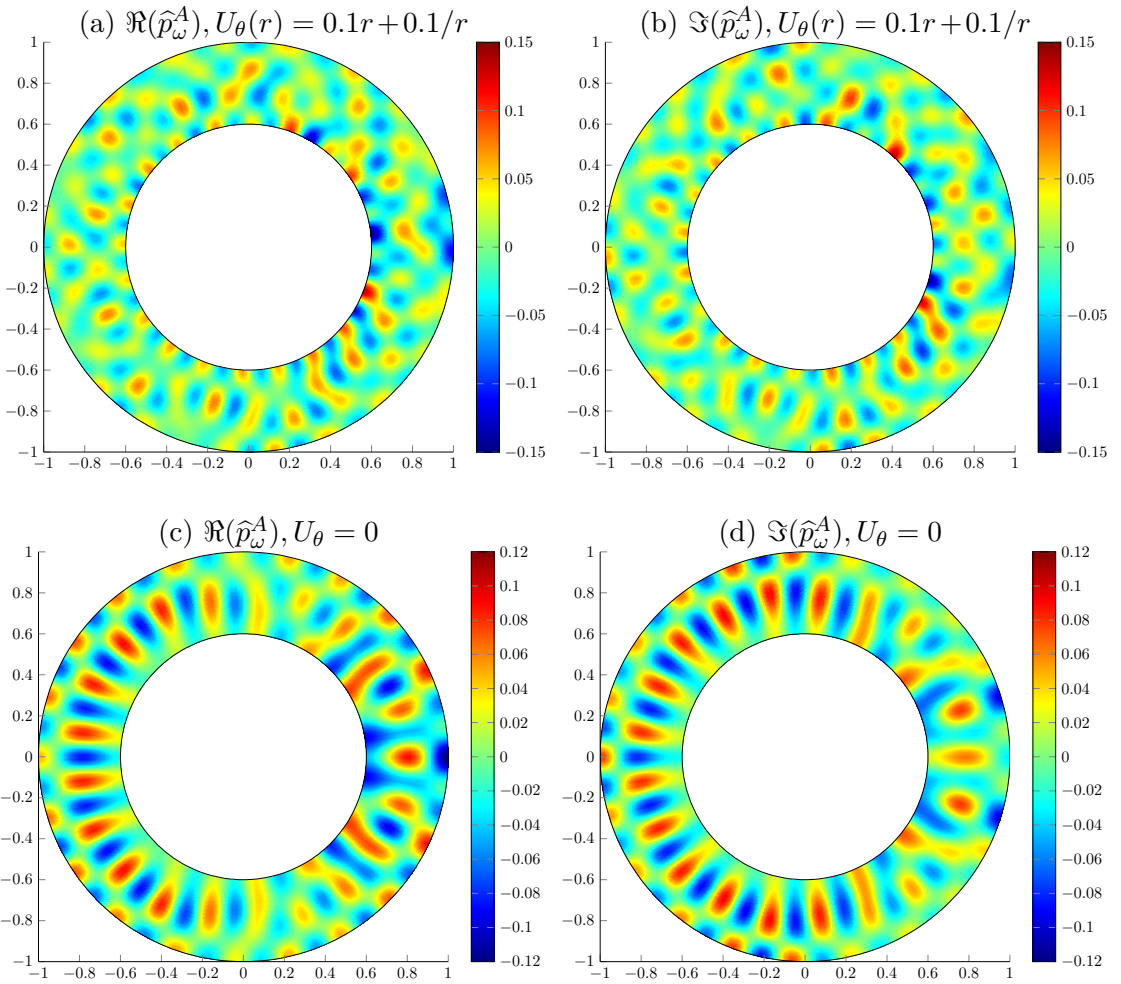


Figure 3.30: Colour plot of the numerical acoustic Green's function \hat{p}_ω^A with a source at $(r_0, \theta_0) = (0.8, 0)$ and $x - x_0 = 0.5$ as r and θ vary. The other flow parameters are $U_x = 0.5$, hard walls, $\omega = 25$ and $h = 0.6$.

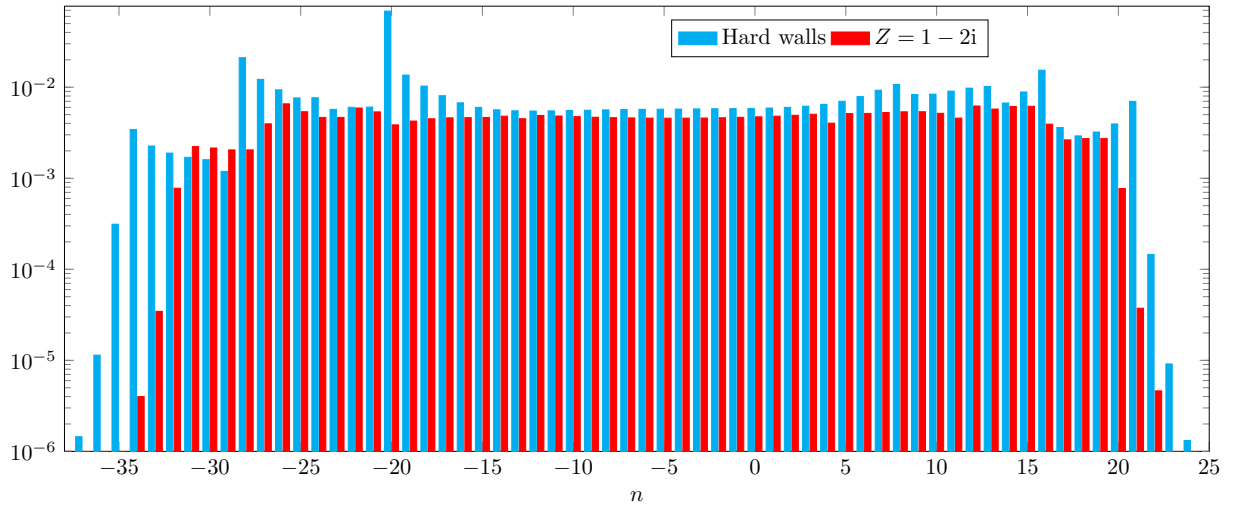


Figure 3.31: Plot of $\max_{r \in [h,1]} |\hat{p}_n^A(r|r_0)|$ for each azimuthal number n for both hard and lined walls (of impedance $Z_j = 1 - 2i$) with the other parameters $U_x = 0.5$, $U_\theta(r) = 0.1r + 0.1/r$, $\omega = 25$, $h = 0.6$, $x - x_0 = 0.5$ and $r_0 = 0.8$.

The effect of swirl is very clear in the figure, with significantly different colour maps. The swirl causes the Green's function to be significantly less uniform circumferentially. When

we have no swirl, the Green's function has two distinct regions. For $-\pi/2 \lesssim \theta \lesssim \pi/2$ the Green's function does not have rotational symmetry, but for $\pi/2 \lesssim \theta \lesssim \pi$ and $-\pi \lesssim \theta \lesssim -\pi/2$ the Green's function does have rotational symmetry. The Green's function is also symmetric along the horizontal axis. When we introduce swirl, the Green's function no longer has vertical symmetry, or any rotational symmetry.

In Figure 3.31 we plot $\max |\hat{p}_n^A(r|r_0)|$ for each azimuthal number n , when we have simple swirling flow in a hard-walled duct and a lined duct (with impedances $Z_j = 1 - 2i$). When we have no lining the dominant azimuthal number is $n = -20$. When we introduce lining, most of the azimuthal modes have a similar magnitude between $n = -27$ and $n = 18$. In Figure 3.31 we also see the decay in $|\hat{p}_n^A(r|r_0)|$ as $|n| \rightarrow \infty$ for both a hard-walled and a lined duct.

Chapter 4

Hydrodynamic modes

In this chapter, we discuss the hydrodynamic modes that accumulate at the end of the critical layer. In [Heaton and Peake \(2006\)](#) an asymptotic model for the accumulation of the hydrodynamic modes was developed, with three possible cases. First, we show that the method used in [Heaton and Peake \(2006, Section 3.1\)](#) is not totally correct, although it predicts the accumulation rate correctly. We show why the method fails and suggest an alternative method. We also show that, because of this failure, we are unable to determine the constant of proportionality for the accumulation of the modes in the simplest case, when they accumulate exponentially. This means that we will always need to calculate at least some of the hydrodynamic modes numerically, while using asymptotic results to predict the rest.

We also show that similar results to [Heaton and Peake \(2006\)](#) hold when we consider a base flow with non-constant entropy. For the parameters we consider, increasing entropy shifts the hydrodynamic modes away from the critical layer, stabilising the flow. Additionally, we show how the hydrodynamic modes bifurcate as we slowly vary the parameters of a specific base flow.

4.1 Results from [Heaton and Peake \(2006\)](#)

We begin by Fourier transforming the perturbations

$$\{u, v, w, p, \rho\}(r, x, \theta, t) = \int \sum_n \int \{U(r), V(r), W(r), P(r), R(r)\} e^{ikx} dk e^{in\theta} e^{-i\omega t} d\omega, \quad (4.1.1)$$

and then use (4.1.1) in the linearised Euler equations (1.4.44) to (1.4.48). We introduce the unsteady potential φ which satisfies

$$p = -\rho_0 \frac{D_0 \varphi}{Dt}, \quad (4.1.2)$$

while we use the swirling base flow given in [Section 2.1](#), but with constant entropy. Let us define the functions

$$D(r) = \Omega^2(r) - \mathcal{U}_\theta(r) \text{ and } \mathcal{U}_0(r) = U'_x(r)k + \frac{n(U_\theta(r)r)'}{r^2}, \quad (4.1.3)$$

then in the homentropic case ϕ (the Fourier transform of φ) satisfies ([Heaton and Peake, 2006](#))

$$-\frac{1}{r\rho_0}\frac{d}{dr}\left(\frac{r\rho_0\Omega(\mathcal{U}_0\phi - \Omega\phi')}{D}\right) + \frac{\mathcal{U}_0}{D}(\mathcal{U}_0\phi - \Omega\phi') + \phi\left(\frac{\Omega^2}{c_0^2} - \frac{n^2}{r^2} - k^2\right) = 0. \quad (4.1.4)$$

In [Heaton and Peake \(2006\)](#) Ω is denoted by $-\Lambda$ and $\mathcal{U}_0(r)$ is denoted by G . Since the hydrodynamic modes are largely unaffected by the acoustic lining, we consider hard walls, and the boundary conditions become

$$\frac{\Omega}{D}(\mathcal{U}_0\phi - \Omega\phi') = 0 \text{ for } r = h, 1, \quad (4.1.5)$$

for an annular duct. We solve the eigenvalue problem (4.1.4) and (4.1.5) to find the eigenmodes k close to the critical layer.

Once we find ϕ , we easily calculate P by

$$P(r) = i\rho_0(r)\Omega(r)\phi(r), \quad (4.1.6)$$

which follows from (4.1.2). Alternatively, we could calculate P from (3.1.8) with zero right-hand side, which in the homentropic case is given by ([Posson and Peake, 2013b](#))

$$\frac{1}{r}\frac{d}{dr}\left(\frac{r}{D}\left(BP + \frac{dP}{dr}\right)\right) + \frac{2nU_\theta}{\Omega Dr^2}\left(BP + \frac{dP}{dr}\right) + \frac{1}{\Omega^2}\left(\frac{\Omega^2}{c_0^2} - \frac{n^2}{r^2} - k^2\right)P = 0, \quad (4.1.7)$$

where

$$B(r) = -\frac{2nU_\theta(r)}{\Omega(r)r^2} - \frac{U_\theta^2(r)}{rc_0^2(r)}. \quad (4.1.8)$$

The boundary conditions then become

$$BP + \frac{dP}{dr} = 0 \text{ for } r = h, 1. \quad (4.1.9)$$

Let us define

$$k_c(r) = \frac{1}{U_x(r)}\left[\omega - \frac{nU_\theta(r)}{r}\right], \quad (4.1.10)$$

which are the values of k for which Ω , the coefficient of the highest derivative in (4.1.4), vanishes. The critical layer is defined by

$$\mathcal{K}^{CL} = \left[\min_{r \in [h, 1]} k_c(r), \max_{r \in [h, 1]} k_c(r)\right], \quad (4.1.11)$$

so if $k \in \mathcal{K}^{CL}$ then there is a physical radius $r \in [h, 1]$ for which $\Omega(r, k) = 0$. Also, given a critical radius r_{cl} , we can compute k_c such that $\Omega(k_c, r_{cl}) = 0$ by (4.1.10).

4.1.1 Deriving Heaton and Peake's result in the simplest case

We begin with the simplest case considered in [Heaton and Peake \(2006\)](#), where $k_c(r)$ is monotonic for $r \in [h, 1]$. Thus, if an eigenmode k is close to one end of the critical layer, the critical radius $r_{\text{cl}}(k)$ is close to one of the duct walls. Without loss of generality, suppose that $k_c(r)$ is an increasing function of r , so

$$\mathcal{K}^{CL} = [k_c(h), k_c(1)]. \quad (4.1.12)$$

Left end of critical layer

We first consider an eigenmode k close to the left end of the critical layer, which is given by

$$k = k_c(h) - \varepsilon, \quad (4.1.13)$$

and we determine ε . We use the approximation

$$h - r_{\text{cl}}(k) \approx \frac{\varepsilon}{k'_c(h)}, \quad (4.1.14)$$

where $\Omega(k, r_{\text{cl}}) = 0$, which comes from considering the Taylor expansion of Ω in both k and r .

We look for an inner, Frobenius solution and an outer solution. Let $\chi = \mathcal{U}_0\phi - \Omega\phi'$, then the boundary conditions simplify to $\chi(h) = \chi(1) = 0$. We look for a Frobenius solution of (4.1.4) in the vicinity of $r_{\text{cl}}(k)$, where Ω vanishes. This is given in [Heaton and Peake \(2006\)](#) as

$$\chi_I(r) \sim (r - r_{\text{cl}})^{-1/2} \sin(\lambda(r_{\text{cl}}) \log(r - r_{\text{cl}}) + \mu), \quad (4.1.15)$$

where

$$\lambda(r) = \sqrt{\frac{2U_\theta k_c[k_c(U_\theta r)' - nU'_x]}{r^2[n(U_\theta/r)' + k_c U'_x]^2} - \frac{1}{4}}, \quad (4.1.16)$$

and μ is a constant. We consider the full derivation of the Frobenius solution when the base flow entropy varies in [Section 4.2](#). In (4.1.15) we approximate $\lambda(r_{\text{cl}})$ by $\lambda(h)$ and hence the inner solution is given by

$$\chi_I(r) \sim (r - r_{\text{cl}})^{-1/2} \sin(\lambda(h) \log(r - r_{\text{cl}}) + \mu). \quad (4.1.17)$$

We could then numerically (or asymptotically in the high-frequency limit) solve for the outer solution. [Heaton and Peake \(2006\)](#) then conclude that the full form of the composite solution is given by

$$\chi(r) \sim f(r)(r - r_{\text{cl}})^{-1/2} \sin(\lambda(h) \log(r - r_{\text{cl}}) + \mu), \quad (4.1.18)$$

for some function $f(r)$ arising from the outer solution.

From the boundary conditions $\chi(h) = \chi(1) = 0$ we conclude

$$\lambda(h) \log(1 - r_{\text{cl}}) + \mu = m_1 \pi \text{ and } \lambda(h) \log(h - r_{\text{cl}}) + \mu = m_2 \pi, \quad (4.1.19)$$

where m_1 and m_2 are integers. Subtracting the two equations then gives

$$\lambda(h) \log(1 - r_{\text{cl}}) - \lambda(h) \log \frac{\varepsilon}{k'_c(h)} = m\pi, \quad (4.1.20)$$

where $m = m_1 - m_2$. Rearranging (4.1.20) and approximating $1 - r_{\text{cl}}$ by $1 - h$ we conclude that

$$\log \varepsilon \sim -\frac{m\pi}{\lambda(h)} + \log(k'_c(h)(1 - h)), \quad (4.1.21)$$

and hence

$$\varepsilon \sim k'_c(h)(1 - h) \exp\left(-\frac{m\pi}{\lambda(h)}\right), \quad (4.1.22)$$

so we find the constant of proportionality is equal to $k'_c(h)(1 - h)$ and the modes accumulate at an exponential rate of $m\pi/\lambda(h)$, where m labels the modes.

Right end of critical layer

We consider an eigenmode k close to the right end of the critical layer, so $k = k_c(1) + \varepsilon$, and then use a similar method to find

$$\varepsilon \sim k'_c(1)(1 - h) \exp\left(-\frac{m\pi}{\lambda(1)}\right). \quad (4.1.23)$$

4.1.2 Summary of Heaton and Peake's results

There are three distinct accumulation regimes identified by [Heaton and Peake \(2006\)](#) for the hydrodynamic modes. Before stating these regimes, we first define

$$\nu(r) = \frac{2U_\theta k_c[k_c(U_\theta r)' - nU'_x]}{r^2[n(U_\theta/r)' + k_c U'_x]^2}. \quad (4.1.24)$$

Case 1: k_c is monotonic and $\nu(r) > 1/4$ at the duct walls.

If k_c is monotonic in the duct, then the hydrodynamic modes accumulate at an exponential rate of

$$\exp\left(-\frac{m\pi}{\lambda(1)}\right) \text{ or } \exp\left(-\frac{m\pi}{\lambda(h)}\right), \quad (4.1.25)$$

depending on at which end of the critical layer they accumulate. Thus, the modes are asymptotically given by

$$k_m^\pm \sim k_c(1) \pm c_1 \exp\left(-\frac{m\pi}{\lambda(1)}\right) \text{ and } k_m^\mp \sim k_c(h) \mp c_h \exp\left(-\frac{m\pi}{\lambda(h)}\right), \quad m \in \mathbb{N}. \quad (4.1.26)$$

The \pm comes from whether k_c is increasing or decreasing, with k_m^+ to the right of the critical layer and k_m^- to the left of the critical layer. Unlike [Chapter 3](#), the \pm does not refer to the

half plane the modes lie in, since they all lie on the real line. For a homentropic flow λ is given by

$$\lambda(r) = \sqrt{\nu(r) - \frac{1}{4}}, \quad (4.1.27)$$

and is the same as (4.1.16). We only get accumulation at the duct walls when $\nu(r) > 1/4$ (λ is real), and it is possible that the modes accumulate at one end of the duct and not at the other.

Case 2: k_c has a single critical point r_{cl}^* , solving $k'_c(r_{\text{cl}}^*) = 0$. Additionally, $\nu(r_{\text{cl}}^*) > 0$.

In Case 2, k_c is not monotonic and has a single critical point. The modes accumulate at an algebraic rate in the real plane near $k_c(r_{\text{cl}}^*)$, with

$$|k_m - k_c(r_{\text{cl}}^*)| \sim \frac{1}{m^2} \left(\frac{2}{-k''_c(r_{\text{cl}}^*)} \right) \frac{2U_\theta k_c[k_c(U_\theta r)' - nU'_x]}{r^2 U_x^2} \Bigg|_{r=r_{\text{cl}}^*}. \quad (4.1.28)$$

At the other end of the critical layer, the modes accumulate exponentially if $\nu(r) > 1/4$ (and otherwise not at all), with accumulation rate given by (4.1.25).

Case 3: k_c has a single critical point r_{cl}^* , solving $k'_c(r_{\text{cl}}^*) = 0$. Additionally, $\nu(r_{\text{cl}}^*) < 0$.

In Case 3, k_c is not monotonic and has a single critical point. The modes accumulate at an algebraic rate in the complex plane near $k_c(r_{\text{cl}}^*)$, with

$$k_m - k_c(r_{\text{cl}}^*) \sim \frac{1}{m^2} \left(\frac{2}{k''_c(r_{\text{cl}}^*)} \right) \frac{2U_\theta k_c[k_c(U_\theta r)' - nU'_x]}{r^2 U_x^2} \Bigg|_{r=r_{\text{cl}}^*} + c_I \frac{i}{m^3}, \quad (4.1.29)$$

when the right end of the critical layer is given by $k_c(r_{\text{cl}}^*)$, and c_I is a constant of proportionality. A similar result holds when the left end of the critical layer is given by $k_c(r_{\text{cl}}^*)$. At the other end of the critical layer the modes accumulate exponentially if $\nu(r) > 1/4$ (and otherwise not at all), with accumulation rate given by (4.1.25).

4.1.3 Failure of Heaton and Peake's method for simplest case

We show that Heaton's method in Case 1 fails to correctly predict the constants c_1 and c_h in (4.1.26), which are needed to predict the modes asymptotically. However, the exponential accumulation rate is still correct.

The method in Section 4.1.1 gives values for c_h and c_1 , but sadly is not correct. The method fails at (4.1.18), where [Heaton and Peake \(2006\)](#) claim that the composite of the solution is given by

$$\chi(r) \sim f(r)(r - r_{\text{cl}})^{-1/2} \sin(\lambda(h) \log(r - r_{\text{cl}}) + \mu). \quad (4.1.30)$$

When we have an inner solution χ_I and an outer solution χ_O , we match them by using [Van Dyke \(1964\)](#). We calculate the inner limit of the outer solution or the outer limit of

the inner solution, and then the composite solution χ is given by

$$\chi = \frac{\chi_I \chi_O}{(\chi_I)_O} = \frac{\chi_I \chi_O}{(\chi_O)_I}. \quad (4.1.31)$$

In our case the outer limit of the inner Frobenius solution is zero, so Van Dyke's method does not apply. Using a composite solution of the form in (4.1.30) wrongly gives a periodic composite solution due to the periodic nature of the inner solution.

In Figure 4.1 we plot the pressure eigenfunction P for a particular hydrodynamic mode at $k = 44.0081$. The critical radius for this eigenmode is at $r_{\text{cl}} = 1.0013$, just outside the duct. The inner Frobenius solution is given by

$$P_I(r) \sim c(r - r_{\text{cl}})^{1/2} \sin(\lambda(1) \log(r - r_{\text{cl}}) + \mu), \quad (4.1.32)$$

which follows due to the relations between χ and ϕ , and ϕ and P in (4.1.6). We clearly see that the periodic nature of the inner solution does not transfer to the composite solution, since the numerical solution in Figure 4.1 is positive for all $0.6 < r < 0.9$.

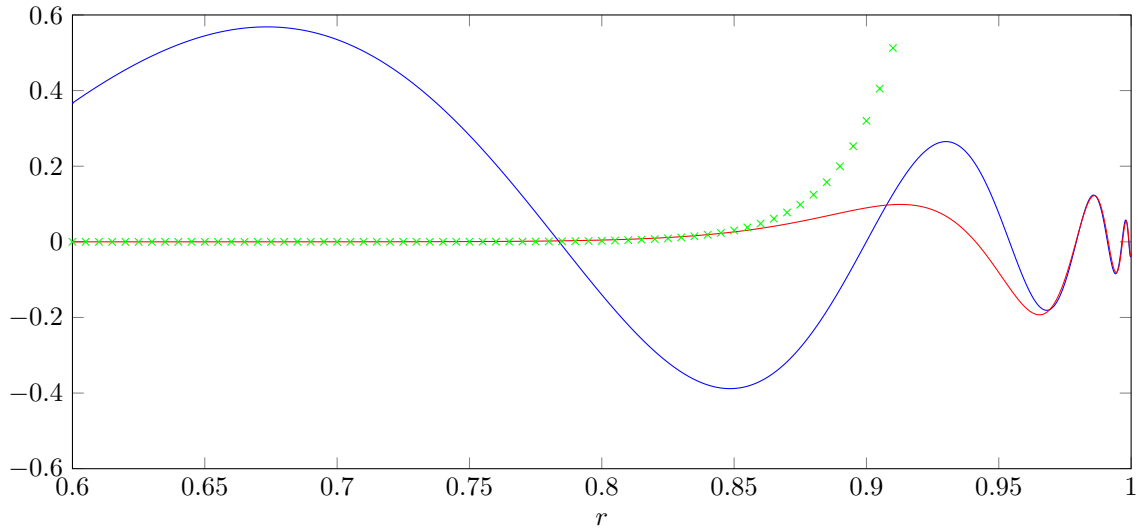


Figure 4.1: Plot of the pressure eigenfunction P for a hydrodynamic mode at $k = 44.0081$.

The parameters are $U_x(r) = 0.5 + 0.2(r - 1)^2$, $U_\theta = 0.2$, $n = 15$, $\omega = 25$, $h = 0.6$ and $\mathcal{K}^{CL} = [38.66, 44]$. In red is the numerical solution of (4.1.7) with boundary conditions (4.1.9). In blue is the inner, Frobenius solution from (4.1.32) and in green crosses the outer solution, calculated using a high-frequency limit using the asymptotic method of Chapter 3.

4.1.4 Showing that the exponential accumulation rate is correct

We switch to looking at the pressure eigenfunction P instead of the unsteady potential ϕ , so we wish to find eigenmodes of the system (4.1.7) and (4.1.9). We assume k_c is an increasing function, and look for hydrodynamic modes k near the right end of the critical layer, given by $k_c(1)$. The inner Frobenius solution is given by

$$P_I(r) \sim c(r - r_{\text{cl}}(k))^{1/2} \sin(\lambda(1) \log(r - r_{\text{cl}}(k)) + \mu). \quad (4.1.33)$$

We then calculate the outer solution. If we determine the outer solution numerically, we find that it is Airy-like and connects the exponential and sinusoidal behaviour seen in [Figure 4.1](#). The boundary condition at $r = h$ determines the constant μ in the inner solution when we match the inner and the outer solutions.

Alternatively, we could construct an outer solution using the WKB method from [Chapter 3](#). The high-frequency asymptotic limit is only applicable for r close to h , and furthermore, we would only use the simpler zero turning point solution. This gives us the correct exponential behaviour of the solution near $r = h$, but we are unable to match this outer solution to the inner solution because Van Dyke's method fails. We need an intermediate solution, which is valid near r_D , where $D(r_D) = 0$. In fact, there are two solutions to $D(r_D) = 0$, with the relevant one inside the duct. For the parameters in [Figure 4.1](#) we find $r_D = 0.9221$, at which point neither the inner nor outer solutions are valid.

Finding this intermediate solution accurately can only be done numerically; the Frobenius method fails to give an Airy-like function when we only calculate the first couple of terms. By Taylor expanding the coefficients of the differential equation in [\(4.1.7\)](#) about r_D , we justify that the intermediate solution looks like an approximate Airy function, although our solution is not valid in a large enough region to match to the inner and outer solutions. The boundary condition at $r = h$ would then determine the unknown constant in the intermediate solution (from matching to the outer solution), which would then determine the constant μ in the inner solution (from matching to the intermediate solution).

New accumulation rate

Having determined μ from the boundary condition at $r = h$, we now apply the boundary condition at $r = 1$. We calculate that

$$P'_I(1) = \frac{c}{2(r_{\text{cl}}-1)^{1/2}} [\sin(\lambda(1) \log(r_{\text{cl}}-1) + \mu) + 2\lambda(1) \cos(\lambda(1) \log(r_{\text{cl}}-1) + \mu)], \quad (4.1.34)$$

and hence to satisfy the boundary condition at $r = 1$ we require that

$$\frac{1}{2(r_{\text{cl}}-1)^{1/2}} [(1 - 2B(1)(r_{\text{cl}}-1)) \sin(\lambda(1) \log(r_{\text{cl}}-1) + \mu) + 2\lambda(1) \cos(\lambda(1) \log(r_{\text{cl}}-1) + \mu)] = 0, \quad (4.1.35)$$

or

$$\sin(\lambda(1) \log(r_{\text{cl}}-1) + \mu_1) = 0, \quad (4.1.36)$$

where

$$\mu_1 = \mu + \arctan \left(\frac{2\lambda(1)}{1 - 2B(1)(r_{\text{cl}}-1)} \right). \quad (4.1.37)$$

For hydrodynamic modes close to the duct wall $B(1)(r_{\text{cl}}-1) \rightarrow 0$ and hence $\mu_1 \rightarrow \mu + \arctan(2\lambda(1))$. The boundary condition in [\(4.1.36\)](#) is satisfied if

$$\lambda(1) \log \frac{\varepsilon}{k'_c(1)} + \mu_1 = -m\pi, \quad m \in \mathbb{N}, \quad (4.1.38)$$

using a similar result to (4.1.14) at $r = 1$. Hence, the eigenmodes to the right of the critical layer are asymptotically given by

$$k_m^+ = k_c(1) + c_1 \exp \left(-\frac{m\pi}{\lambda(1)} \right), \quad m \in \mathbb{N}, \quad (4.1.39)$$

where

$$c_1 = k'_c(1) \exp \left(-\frac{\mu_1}{\lambda(1)} \right), \quad (4.1.40)$$

is the constant of proportionality. In Section 4.3.2 we will see that the constant c_1 does depend on the intermediate solution, justifying the form in (4.1.40) since μ (and hence μ_1) depend on the matching of the outer solution to the intermediate or inner solution.

The relation in (4.1.39) is only accurate for hydrodynamic modes close to the duct wall for several reasons. First, μ_1 (and hence c_1) can be approximated by a constant only for these modes. Second, in our original inner solution (4.1.33) we approximated $\lambda(r_{\text{cl}})$ by $\lambda(1)$, which is valid only for modes close to the duct wall. Third, we approximated $r_{\text{cl}} - 1$ by $\varepsilon/k'_c(1)$ in (4.1.38), which is only accurate for hydrodynamic modes close to the ends of the critical layer. Finally, we only used the first term in the Frobenius expansion for the inner solution.

4.1.5 Heaton and Peake's method in the other cases

The other two accumulation regimes identified in Heaton and Peake (2006), where the hydrodynamic modes accumulate algebraically in the real line or complex plane, remain correct. This is because Heaton and Peake only state that the outer solution oscillates when we match it to the intermediate and inner solutions, and that when we apply boundary conditions at the duct walls we get Equation (3.18) of Heaton and Peake (2006). The constants q and Q in Heaton and Peake (2006) then only provide small corrections to the leading order solution. We thus come to the conclusion that we can calculate the asymptotic constant of proportionality for flows accumulating algebraically (it was checked in Heaton and Peake (2006, Section 3.4)), while we cannot determine the asymptotic constant of proportionality for flows accumulating exponentially.

However, knowing the constant of proportionality for algebraic flows is not very enlightening. It takes of the order of 100 modes (Heaton and Peake, 2006, Section 3.4) before the modes accumulate algebraically and the relation

$$k_m^+ = k_c(r_{\text{cl}}^*) + \frac{c_A}{m^2}, \quad m \in \mathbb{N}, \quad (4.1.41)$$

where c_A is given in (4.1.28) or (4.1.29), is accurate. In contrast, for modes accumulating

exponentially, relations of the form

$$k_m^+ = k_c(1) + c_1 \exp\left(-\frac{m\pi}{\lambda(1)}\right), \quad m \in \mathbb{N}, \quad (4.1.42)$$

where c_1 is to be determined, are accurate after only about ten modes (see [Section 4.3](#)). If we numerically calculate the first ten or so modes, then we can determine c_1 and hence the rest of the modes asymptotically. So to accurately calculate all of the hydrodynamic modes we would need to calculate significantly more of them numerically when they algebraically accumulate than when they exponentially accumulate.

4.2 Effect of entropy

When we consider a base flow with varying entropy we could derive a similar equation to [\(4.1.4\)](#) for unsteady potential ϕ . However, it is more convenient to use the equation for pressure we derived in [Section 3.1](#). Using [\(3.1.8\)](#) but with a right-hand side of zero, we find the Fourier transform of pressure satisfies the equation

$$\frac{d^2 P}{dr^2} + \hat{\mathcal{B}}(r) \frac{dP}{dr} + \hat{\mathcal{C}}(r) P = 0, \quad (4.2.1)$$

where $\hat{\mathcal{B}}$ is given by

$$\hat{\mathcal{B}} := \left[\left(\frac{1}{r} - \frac{\rho'_0}{\rho_0} \right) - \frac{D'}{D} \right] \quad (4.2.2)$$

and

$$\hat{\mathcal{C}} := \frac{1}{\Omega^2} \left(D \left(\frac{\Omega^2}{c_0^2} - k^2 - \frac{n^2}{r^2} \right) - \Upsilon \left[\Upsilon + \Omega \left(\frac{1}{r} - \frac{\rho'_0}{\rho_0} \right) \right] - \Upsilon \frac{[\Omega D]'}{D} - \Omega \Upsilon' \right). \quad (4.2.3)$$

We then use the Frobenius method ([Bender and Orszag, 1978](#)) to solve the differential equation near the critical point $r = r_{cl}$ of Ω . We first write $\hat{\mathcal{B}}(r)$ and $\hat{\mathcal{C}}(r)$ as Laurent series about r_{cl} , where $\Omega(k, r_{cl}) = 0$. We find that

$$\hat{\mathcal{B}}_{-1} = 0 \text{ and } \nu^* := \hat{\mathcal{C}}_{-2} = \frac{2U_\theta k_c [k_c(U_\theta r)' - nU'_x] + \mathcal{E}}{r^2[n(U_\theta/r)' + k_c U'_x]^2}, \quad (4.2.4)$$

where

$$\mathcal{E}(r) = r^2 \frac{U_\theta^2(r)}{r} \left(\frac{\rho'_0(r)}{\rho_0(r)} - \frac{U_\theta^2(r)}{rc_0^2(r)} \right) \left(k_c^2 + \frac{n^2}{r^2} \right). \quad (4.2.5)$$

Although [Lalas \(1975\)](#) considered a flow with entropy, he did not consider the Frobenius expansion so this is a new result. From [Lalas \(1975\); Heaton and Peake \(2006\)](#) we see that the entropy term $\mathcal{E}(r)$ is related to the Brunt-Väisälä frequency.

The indicial equation in the Frobenius method becomes (where ς is the indicial exponent)

$$\varsigma^2 - \varsigma + \nu^*(r_{cl}) = 0, \quad (4.2.6)$$

and it has solutions

$$\zeta_{\pm} = \frac{1}{2} \pm \sqrt{\frac{1}{4} - \nu^*(r_{\text{cl}})}. \quad (4.2.7)$$

When $\nu^*(r_{\text{cl}}) > 1/4$ we find the Frobenius solution is given, to leading order, by

$$P_I(r) = c_P(r - r_{\text{cl}})^{1/2} [\sin(\lambda^*(r_{\text{cl}}) \log(r - r_{\text{cl}}) + \mu)], \quad (4.2.8)$$

where

$$\lambda^*(r_{\text{cl}}) = \sqrt{\nu^*(r_{\text{cl}}) - \frac{1}{4}}. \quad (4.2.9)$$

Using (4.1.2) we find that

$$P_I(r) = i\rho_0(r)\Omega(r)\phi_I(r) \approx i\rho_0(r_{\text{cl}})\Omega'(r_{\text{cl}})(r - r_{\text{cl}})\phi_I(r), \quad (4.2.10)$$

and hence to leading order

$$\phi_I(r) = c_\phi(r - r_{\text{cl}})^{-1/2} [\sin(\lambda^*(r_{\text{cl}}) \log(r - r_{\text{cl}}) + \mu)]. \quad (4.2.11)$$

4.2.1 Summary of asymptotic results

We now apply exactly the same analysis as in Heaton and Peake (2006), but the function $\nu(r)$ changes and is now given by

$$\nu^*(r) = \frac{2U_\theta k_c [k_c(U_\theta r)' - nU'_x] + \mathcal{E}}{r^2 [n(U_\theta/r)' + k_c U'_x]^2}, \quad (4.2.12)$$

where $\mathcal{E}(r)$ is given by (4.2.5) and is the additional entropy factor. For the simple case of $s_0(r) = -\log(r^\beta)$ we calculate that

$$\mathcal{E}(r) = \frac{\beta}{c_p} U_\theta^2(r) \left(k^2 + \frac{n^2}{r^2} \right). \quad (4.2.13)$$

It is clear for a homentropic fluid that $\mathcal{E} = 0$ and hence $\nu^* = \nu$ and $\lambda^* = \lambda$.

Case 1: k_c is monotonic and $\nu^*(r) > 1/4$.

If k_c is monotonic in the duct, then the hydrodynamic modes accumulate at an exponential rate of

$$\exp\left(-\frac{m\pi}{\lambda^*(1)}\right) \text{ or } \exp\left(-\frac{m\pi}{\lambda^*(h)}\right), \quad (4.2.14)$$

depending on at which end of the critical layer they accumulate. The function λ^* is given in (4.2.9).

Case 2: k_c has a single critical point r_{cl}^* , solving $k'_c(r_{\text{cl}}^*) = 0$. Additionally, $\nu(r_{\text{cl}}^*) > 0$.

In Case 2 k_c is not monotonic and has a single critical point. The modes accumulate at an

algebraic rate in the real plane near $k_c(r_{\text{cl}}^*)$, with

$$|k_m - k_c(r_{\text{cl}}^*)| \sim \frac{1}{m^2} \left(\frac{2}{-k_c''(r_{\text{cl}}^*)} \right) \frac{2U_\theta k_c [k_c(U_\theta r)' - nU_x'] + \frac{\beta}{c_p} U_\theta^2 \left(k_c^2 + \frac{n^2}{r^2} \right)}{r^2 U_x^2} \Bigg|_{r=r_{\text{cl}}^*}. \quad (4.2.15)$$

At the other end of the critical layer, the modes accumulate exponentially if $\nu^*(r) > 1/4$ (and otherwise not at all), with accumulation rate given by (4.2.14).

Case 3: k_c has a single critical point r_{cl}^* , solving $k_c'(r_{\text{cl}}^*) = 0$. Additionally, $\nu(r_{\text{cl}}^*) < 0$.

In Case 3 k_c is not monotonic and has a single critical point. The modes accumulate at an algebraic rate in the complex plane near $k_c(r_{\text{cl}}^*)$, with

$$k_m - k_c(r_{\text{cl}}^*) \sim \frac{1}{m^2} \left(\frac{2}{k_c''(r_{\text{cl}}^*)} \right) \frac{2U_\theta k_c [k_c(U_\theta r)' - nU_x'] + \frac{\beta}{c_p} U_\theta^2 \left(k_c^2 + \frac{n^2}{r^2} \right)}{r^2 U_x^2} \Bigg|_{r=r_{\text{cl}}^*} + c_I \frac{i}{m^3}, \quad (4.2.16)$$

when the right end of the critical layer is given by $k_c(r_{\text{cl}}^*)$, and c_I is a constant of proportionality. A similar result holds when the left end of the critical layer is given by $k_c(r_{\text{cl}}^*)$. At the other end of the critical layer the modes accumulate exponentially if $\nu^*(r) > 1/4$ (and otherwise not at all), with accumulation rate given by (4.2.14).

4.2.2 Numerical results

We now consider the effect of entropy on the hydrodynamic modes. We calculate these modes numerically, using either Chebfun (in the same way as Section 3.3.2) or using the program from Heaton and Peake (2006). We get the same results from both programs. We consider a base flow entropy of the form $s_0(r) = -\log(r^\beta)$, and consider the three cases $\beta = -0.3$, $\beta = 0$ and $\beta = 0.3$. In Figure 4.2 we plot the hydrodynamic modes for a certain base flow, and we see that they move as we vary entropy.

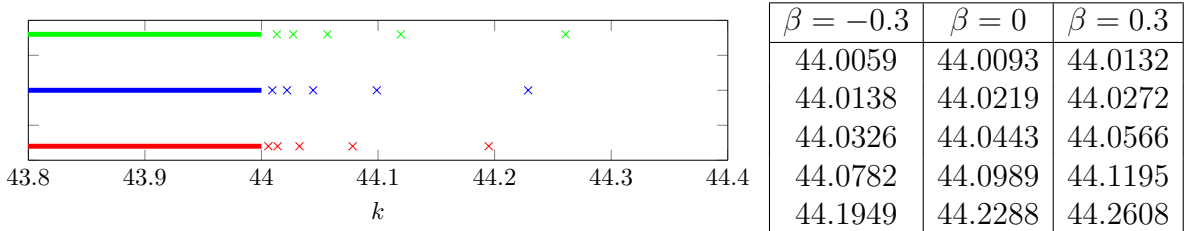


Figure 4.2: Right-hand side of critical layer (solid line) showing first five hydrodynamic modes (crosses). The parameters are $U_x = 0.5$, $U_\theta(r) = 0.1r + 0.1/r$, $\omega = 25$, $n = 15$ and $h = 0.6$. Green: $\beta = 0.3$, blue: $\beta = 0$ and red: $\beta = -0.3$. $\mathcal{K}^{CL} = [38.66, 44]$.

In Figure 4.2 we see that for this choice of parameters, larger values of β (and hence larger entropy) shift all the hydrodynamic modes right at the right end of the critical layer. We find at the other end of the critical layer that as we increase the entropy the modes shift left. Thus, at both ends the hydrodynamic modes shift away from the critical layer as we increase β . In Table 4.1 we calculate the values of $\lambda^*(1) = \sqrt{\nu^*(1) - 1/4}$, where ν^* is given in (4.2.12). Since we are in Case 1, the modes accumulate at an exponential rate,

and hence at the right end of the critical layer they are asymptotically given by

$$k_m^+ \sim k_c(1) + c_1 \exp\left(-\frac{m\pi}{\lambda^*(1)}\right), \quad m \in \mathbb{N}, \quad (4.2.17)$$

where c_1 is the constant in [Table 4.1](#). We calculate this constant numerically. Thus, in [Figure 4.2](#) the hydrodynamic modes shift right as we increase entropy because the constant of proportionality c_1 increases, while the exponential accumulation rate $\lambda^*(1)$ also increases as the entropy increases. From [\(4.2.9\)](#), [\(4.2.12\)](#) and [\(4.2.13\)](#) it is clear why the latter happens, but because we cannot determine the constant of proportionality asymptotically it is not clear of the exact effect β has on the the constant of proportionality.

[Table 4.1](#): Analytic accumulation rate $\lambda^*(1)$ and numerical constant of proportionality of the hydrodynamic modes for the flows given in [Figure 4.2](#).

	$\beta = -0.3$	$\beta = 0$	$\beta = 0.3$
$\lambda^*(1)$	3.7539	4.1181	4.4526
constant c_1	0.3873	0.4217	0.4503

In [Figure 4.3](#) we show the other two cases for accumulation at the ends of the critical layer. We take the examples given in [Heaton and Peake \(2006\)](#) and consider them with different base flow entropies by varying β . In [Figure 4.3a](#) we see the modes accumulating algebraically on the real line. As we increase the entropy the accumulation rate in [\(4.2.15\)](#) varies and the hydrodynamic modes all shift to the right.

- (a) $U_x(r) = 0.5 + 0.1r^4$, $U_\theta(r) = 0.5r^4$, $n = -3$, (b) $U_x(r) = 0.7 - 0.5r^2$, $U_\theta(r) = 0.1r + 0.25/r$, $n = -5$, $\omega = 3$, $h = 0.5$.

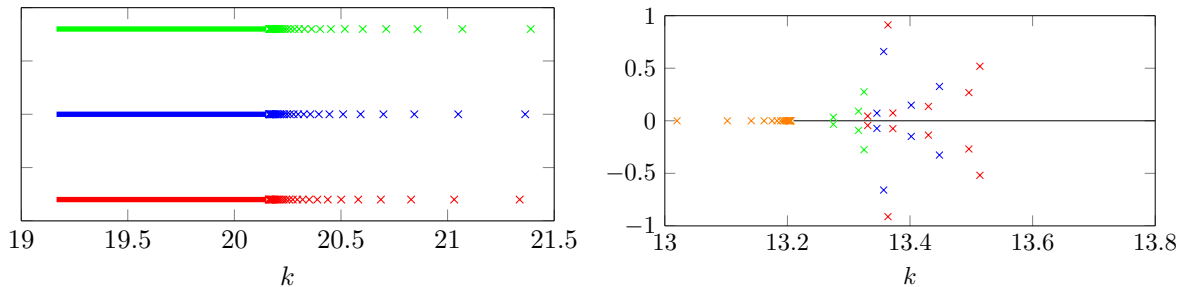


[Figure 4.3](#): Plot of the hydrodynamic modes for the given parameters. We only consider the first few modes in [Figure 4.3b](#). Orange: $\beta = 0.6$ (only in [Figure 4.3b](#)), green : $\beta = 0.3$, blue: $\beta = 0$ and red: $\beta = -0.3$.

In [Figure 4.3b](#) we see the first few hydrodynamic modes accumulating in the complex plane. As we increase entropy, the modes move to the left at the left end of the critical layer, as in the previous two cases. We also see that as we increase the entropy from $\beta = 0.3$ (green) to $\beta = 0.6$ (orange) we change accumulation regime and go from clustering in the complex plane to clustering on the real line. From [\(4.2.12\)](#) and [\(4.2.13\)](#) and the definition of the accumulation regimes it is clear why this happens. Thus, increasing the entropy (by increasing β) is stabilising the flow since we have changed accumulation regime ([Heaton and Peake, 2006](#)).

4.3 Failure to calculate the exponential constant of proportionality asymptotically

We now consider the constant of proportionality when the modes accumulate exponentially, but only in the homentropic case. In [Section 4.1](#) we saw that the exponential accumulation rate depends only on $\lambda(h)$ or $\lambda(1)$, and since $\lambda(r)$ only depends on $U_x(r)$ and $U_\theta(r)$ and their first derivatives (and ω and n), then we see that the accumulation rate is a local property. We could find new base flows U_x^\dagger and U_θ^\dagger which agree with U_x and U_θ and their first derivatives at $r = 1$ or $r = h$ and are different everywhere else. The hydrodynamic modes for these new flows would then accumulate at the same rate.

By contrast, we show that the constant of proportionality is a global property of the flow, and we need to know the flow everywhere (or at least a small closed interval rather than at a point) to calculate this constant. If we use the flawed method from [Section 4.1.1](#) then the constant of proportionality is a local property, and we show that this is not the case.

4.3.1 Showing the constant of proportionality is not a local property

We consider a range of different mean flows such that the shear, swirl and their first derivatives have the same values at $r = 1$ in each case. We calculate the hydrodynamic modes at the right end of the critical layer numerically, and show that the predicted accumulation rate from [\(4.1.25\)](#) is correct, but the constant of proportionality varies for each flow. The parameters we choose are $U_\theta = 0.2$, $n = 15$, $\omega = 25$ and $h = 0.6$. We initially consider six shear flows with $U_x(1) = 0.5$ and $U'_x(1) = 0$, which are given in [Table 4.2](#). For all of these shear flows, the right end of the critical layer is given by $k_c(1) = 44$, and the accumulation rate $\lambda(1)$ is the same.

In [Figure 4.4](#) we plot the shear flows and the function $k_c(r)$ for each flow \mathbf{X}_l in [Table 4.2](#). We also introduce four more flows, \mathbf{X}_1 to \mathbf{X}_4 , which are given in [Table 4.3](#). These flows

Table 4.2: Different shear flows with $U_x(1) = 0.5$ and $U'_x(1) = 0$.

Case	Shear flow
\mathbf{X}_a	$U_x(r) = 0.5 + 0.3(r - 1)^2$
\mathbf{X}_b	$U_x(r) = 0.5 + 0.2(r - 1)^2$
\mathbf{X}_c	$U_x(r) = 0.5 + 0.1(r - 1)^2$
\mathbf{X}_d	$U_x(r) = 0.5$
\mathbf{X}_e	$U_x(r) = 0.5 - 0.1(r - 1)^2$
\mathbf{X}_f	$U_x(r) = 0.5 - 0.2(r - 1)^2$

all have the same accumulation rate as flows \mathbf{X}_a to \mathbf{X}_f , and all have the right end of the critical layer at $k = 44$. For the two flows \mathbf{X}_3 and \mathbf{X}_4 the function k_c comes very close to not being monotonic, since for example if $U_x(r) = 0.5 - 0.3(r - 1)^2$ then k_c is not monotonic. Furthermore, if $U_x(r) = 0.5 - 0.3(r - 1)^2$ then the right end of the critical layer is no longer

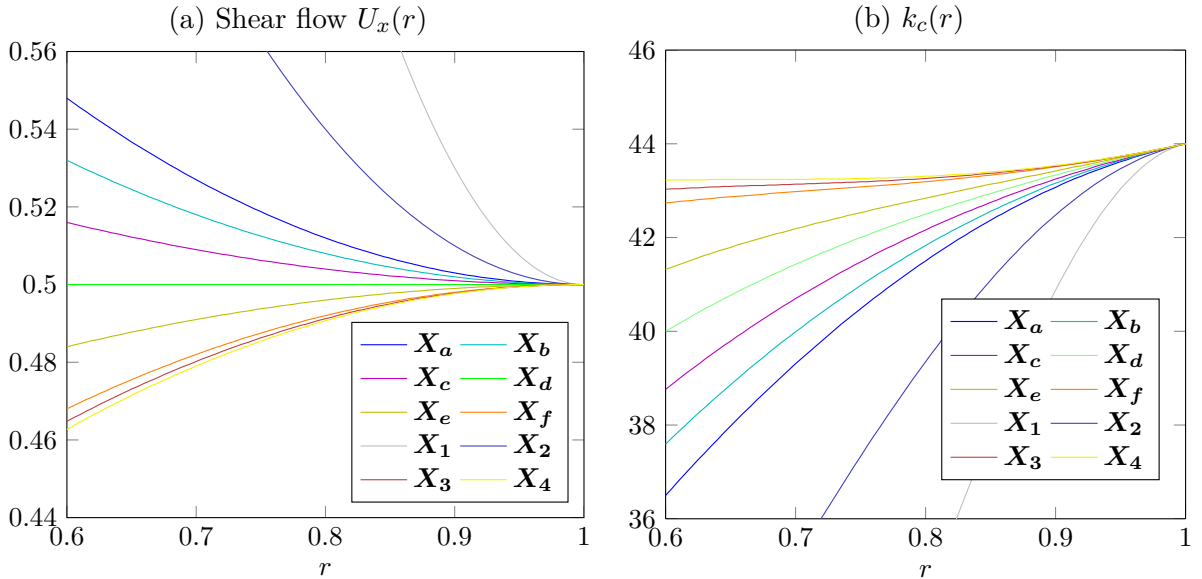


Figure 4.4: Graph of shear flow $U_x(r)$ (left) and $k_c(r)$ (right) for the flows \mathbf{X}_l .

Table 4.3: More shear flows with $U_x(1) = 0.5$ and $U'_x(1) = 0$.

Case	Shear flow
\mathbf{X}_1	$U_x(r) = 0.5 + 3(r-1)^2$
\mathbf{X}_2	$U_x(r) = 0.5 + (r-1)^2$
\mathbf{X}_3	$U_x(r) = 0.5 - 0.22(r-1)^2$
\mathbf{X}_4	$U_x(r) = 0.5 - 0.233(r-1)^2$

given by $k = 44$. In flows \mathbf{X}_1 and \mathbf{X}_2 the left end of the critical layer $k_c(h)$ becomes smaller and smaller and in a sense k_c becomes “more monotonic”.

The first nine hydrodynamic modes for each flow at the right end of the critical layer are given in [Table 4.4](#). We clearly see from the table that it is not sufficient to just know

Table 4.4: First nine hydrodynamic modes for the flows \mathbf{X}_l .

\mathbf{X}_1	44.0001	44.0002	44.0004	44.0010	44.0022	44.0052	44.0129	44.0361	44.1278
\mathbf{X}_2	44.0002	44.0004	44.0009	44.0020	44.0045	44.0102	44.0242	44.0624	44.1821
\mathbf{X}_a	44.0003	44.0007	44.0015	44.0033	44.0073	44.0161	44.0367	44.0867	44.2167
\mathbf{X}_b	44.0004	44.0008	44.0017	44.0037	44.0081	44.0178	44.0399	44.0923	44.2231
\mathbf{X}_c	44.0004	44.0009	44.0019	44.0042	44.0091	44.0198	44.0439	44.0988	44.2302
\mathbf{X}_d	44.0005	44.0011	44.0023	44.0049	44.0105	44.0227	44.0490	44.1068	44.2381
\mathbf{X}_e	44.0006	44.0013	44.0028	44.0060	44.0127	44.0268	44.0562	44.1170	44.2469
\mathbf{X}_f	44.0009	44.0018	44.0039	44.0081	44.0169	44.0342	44.0677	44.1310	44.2571
\mathbf{X}_3	44.0009	44.0020	44.0043	44.0089	44.0184	44.0367	44.0711	44.1345	44.2594
\mathbf{X}_4	44.0010	44.0022	44.0046	44.0097	44.0196	44.0387	44.0736	44.1371	44.2609

properties of the flow at $r = 1$ to accurately calculate the hydrodynamic modes, since they vary for the flows \mathbf{X}_l . The exponential rate of accumulation is the same for all the flows and we calculate that the rate is given by

$$\exp\left(-\frac{m\pi}{\lambda(1)}\right) = \exp(-0.7629m). \quad (4.3.1)$$

We calculate the constant of proportionality by calculating the limit of

$$(k - k_c(1)) \exp\left(\frac{m\pi}{\lambda(1)}\right) = (k - 44) \exp(0.7629m), \quad (4.3.2)$$

and we plot this in [Figure 4.5](#). The constants of proportionality are then given in [Table 4.5](#). We see that the constant of proportionality slowly varies as we vary the flow and is not a local property of the flow.

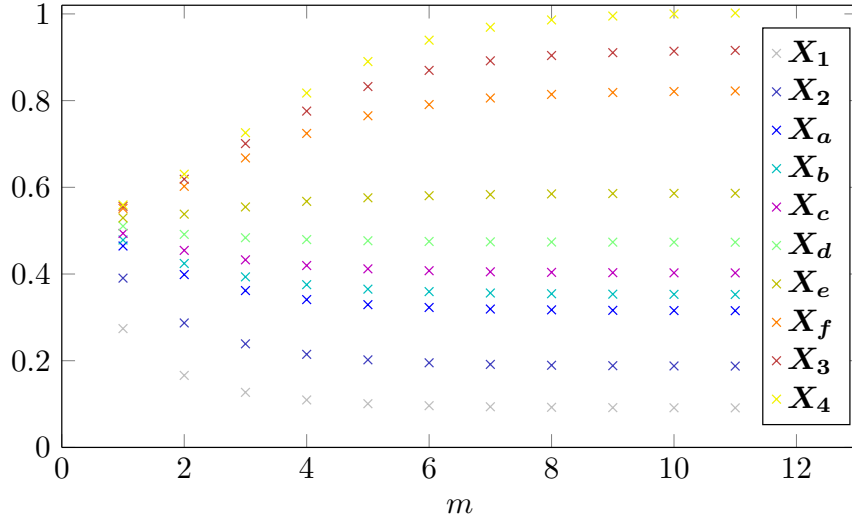


[Figure 4.5](#): Plot of $(k - 44) \exp(0.7629m)$ against m for each of the ten flows \mathbf{X}_l to determine constant of proportionality numerically.

[Table 4.5](#): Constant of proportionality for each of the ten flows \mathbf{X}_l .

\mathbf{X}_1	\mathbf{X}_2	\mathbf{X}_a	\mathbf{X}_b	\mathbf{X}_c	\mathbf{X}_d	\mathbf{X}_e	\mathbf{X}_f	\mathbf{X}_3	\mathbf{X}_4
0.0912	0.1874	0.3151	0.3525	0.4023	0.4731	0.5862	0.8230	0.9170	1.0041

We see in [Figure 4.5](#) that for some flows, such as flow \mathbf{X}_d , $(k - 44) \exp(0.7629m)$ is relatively unchanged as we vary m . For this flow the asymptotic relation

$$k_m^+ = 44 + 0.4731 \exp(-0.7629m), \quad m \in \mathbb{N}, \quad (4.3.3)$$

is then accurate after only a couple of modes. For other flows, such as flow \mathbf{X}_4 , $(k - 44) \exp(0.7629m)$ varies dramatically for the first few hydrodynamic modes. Thus, for these flows we can only accurately use an asymptotic relation of the form in [\(4.3.3\)](#) from the eighth or ninth mode onwards.

4.3.2 Showing that the constant of proportionality is a global property

We now show that the hydrodynamic modes only depend on a small region of the flow, near the ends of the critical layer. We begin with the flow ζ , with parameters $U_x(r) = 0.5 + (r - 1)^2$, $U_\theta = 0.2$, $n = 15$, $\omega = 25$ and $h = 0.6$. This flow was denoted by \mathbf{X}_2 in [Section 4.3.1](#). We consider flows which agree exactly with ζ in some region near $r = 1$ and

differ elsewhere. To do this we introduce a smooth, non-analytical transition function such as

$$\hat{H}(r) = \left[1 + \exp\left(-\frac{r}{\varepsilon}\right) \right]^{-1}, \quad (4.3.4)$$

for some small value of ε . The function \hat{H} is a smooth approximation to the Heaviside function. We then define new shear flows by

$$U_x^a(r) = \hat{H}(r-a)U_x^\dagger(r) + (1 - \hat{H}(r-a)) [0.5 + (r-1)^2], \quad (4.3.5)$$

which agree with the shear flow from ζ in the region $(a, 1)$. We consider different values of a , and we choose $U_x^\dagger(r)$ to be a simple exponential function with $U_x^\dagger(1) = 0.55$ and $U_x^\dagger(a) = U_x(a)$. We denote these flows ζ_a and show the shear flows and $k_c(r)$ for these flows in Figure 4.6. The results from Heaton and Peake (2006) still apply for non-analytic flows, so we expect the hydrodynamic modes to accumulate exponentially for the flows ζ_a .

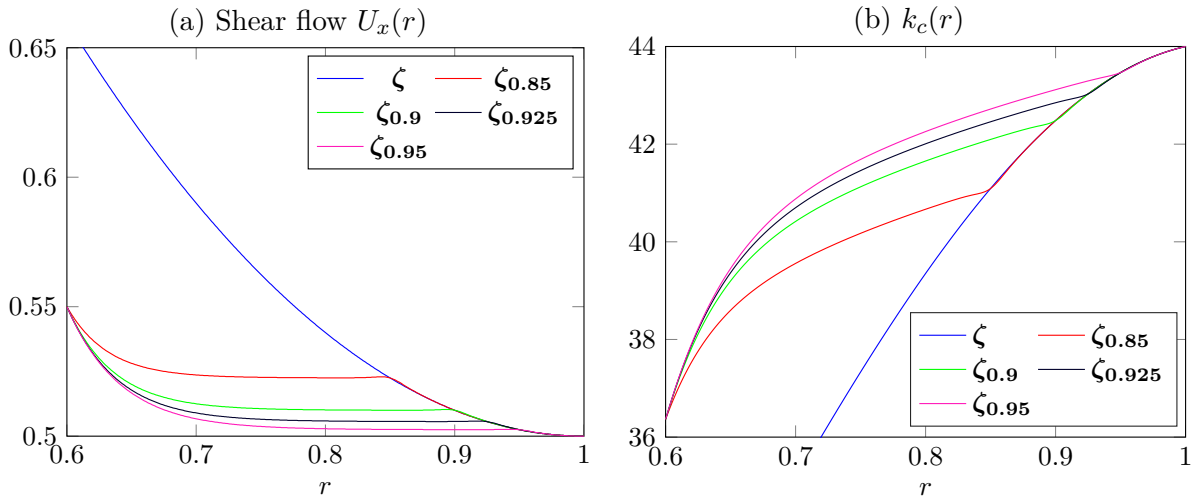


Figure 4.6: Graph of shear flow $U_x(r)$ (left) and $k_c(r)$ (right) for the flows ζ_a .

In Table 4.6 we show the first five hydrodynamic modes to the right of the critical layer for each flow. It is clear from the table that only the behaviour of the flow in a small region near $r = 1$ is important for the hydrodynamic modes accumulating at the right end of the critical layer. It is only when we start varying the flow in the region $[0.9, 0.95]$ that the hydrodynamic modes start to move. The hydrodynamic modes all accumulate exponentially, with the rate of accumulation given by $\exp(-0.7629m)$, while the constants of proportionality for the flows ζ_a only differ by about 0.05% as we vary the flow from $\zeta_{0.85}$ to $\zeta_{0.95}$. The significance of $r = 0.95$ is that it is close to the critical point r_D , which solves

Table 4.6: First five hydrodynamics modes for the flows ζ_a .

ζ	44.0044548	44.0101538	44.0242254	44.0624379	44.1820755
$\zeta_{0.85}$	44.0044548	44.0101538	44.0242254	44.0624379	44.1820756
$\zeta_{0.9}$	44.0044554	44.0101550	44.0242281	44.0624438	44.1820836
$\zeta_{0.925}$	44.0044687	44.0101855	44.0242981	44.0625918	44.1822699
$\zeta_{0.95}$	44.0047038	44.0107368	44.0255810	44.0653128	44.1855919

$D(r_D) = 0$. For the flows ζ , $\zeta_{0.85}$ and $\zeta_{0.9}$ the critical point r_D is given by 0.946. For these

flows, the intermediate solution is the same near r_D , so when we match the intermediate solution to the inner solution to determine the constant of proportionality, it is unchanged. For the flow $\zeta_{0.95}$, we are modifying the intermediate solution near $r_D = 0.942$, and thus the constant of proportionality is modified and hence the hydrodynamic modes shift right.

In conclusion, if two flows are the same at the end of the critical layer and near r_D , then we expect the hydrodynamic modes for each flow to be the same. We have shown that the constant of proportionality for exponential accumulation must be a global property of the flow, since it depends on the flow properties in a small region (comprising of an inner and intermediate region), and not a single point. It is not completely a global property, since it does not depend on the flow parameters in the outer region.

4.4 Bifurcating hydrodynamic modes

So far, we have seen that as we slowly vary the flow parameters the hydrodynamic modes move slowly. We also saw this was the case for the acoustic modes in [Chapter 3](#). We now show that the hydrodynamic modes can bifurcate as we vary the flow, for some choices of parameters. We fix the right end of the critical layer and vary the shear flow, and look for hydrodynamic modes to the right of the critical layer. Our starting flow is the flow \mathbf{X}_4 (which we now denote as \mathbf{Y}_1), where k_c is monotonic and the right end of the critical layer is given by $k_c(1) = 44$. We slowly vary the shear flow so that k_c becomes non-monotonic, and continue to vary the shear flow right up to the point where $k_c(h) = k_c(1)$. If we vary the shear flow any further then the right end of the critical layer would be given by $k_c(h) > 44$.

We calculate the hydrodynamic modes numerically for each flow. We show that it is possible for the hydrodynamic modes to accumulate at a rate somewhere between algebraically and exponentially. It is possible that this occurs because the critical layer becomes so small that the analysis from [Heaton and Peake \(2006\)](#) fails.

Table 4.7: Shear flows as $k_c(r)$ goes from being monotonic to non-monotonic.

Case	Shear flow	Properties	$k_c(h)$
\mathbf{Y}_1	$U_x(r) = 0.5 - 0.233(r-1)^2$	k_c monotonic	43.2227
\mathbf{Y}_2	$U_x(r) = 0.5 - 0.241(r-1)^2$	$k'_c(r) = 0$ at $r = 0.7311$	43.3426
\mathbf{Y}_3	$U_x(r) = 0.5 - 0.284(r-1)^2$	$k'_c(r) = 0$ at $r = 0.8188$	43.9986

In [Table 4.7](#) we consider several different shear flows as $k_c(r)$ goes from a monotonic function to not being monotonic and $k_c(h) \rightarrow k_c(1)$. The other parameters are $U_\theta = 0.2$, $n = 15$, $\omega = 25$ and $h = 0.6$. In [Figure 4.7](#) we plot $k_c(r)$ for each of these flows.

Table 4.8: Hydrodynamic modes for flows \mathbf{Y}_1 and \mathbf{Y}_2 . Numerical constant of proportionality for exponential accumulation given in brackets.

\mathbf{Y}_1	44.0010	44.0022	44.0046	44.0097	44.0196	44.0387	44.0736	44.1371	44.2609	(1.0041)
\mathbf{Y}_2	44.0011	44.0024	44.0050	44.0102	44.0206	44.0401	44.0754	44.1387	44.2618	(1.0795)

In [Table 4.8](#) we give the first nine hydrodynamic modes at the right end of the critical layer for the flows \mathbf{Y}_1 and \mathbf{Y}_2 . We see that the modes accumulate exponentially, with the

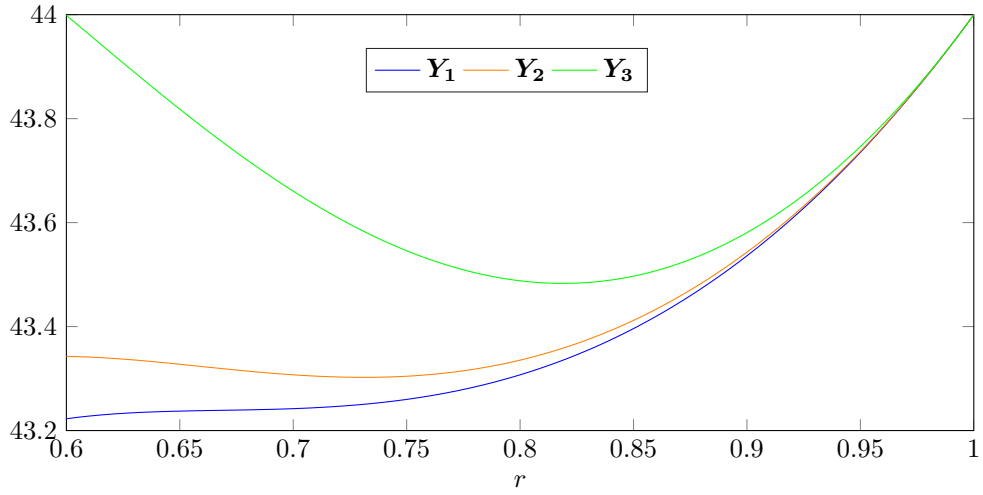


Figure 4.7: Graph of $k_c(r)$ for the flows in Table 4.7.

constant of proportionality given in brackets. The accumulation rate for each flow is still given by $\exp(-0.7629m)$. As we vary the shear flow, the hydrodynamic modes move by a very small amount, since the constant of proportionality increases from 1.0041 to 1.0795.

We now plot the hydrodynamic modes as we vary the flow between \mathbf{Y}_2 and \mathbf{Y}_3 in Figure 4.8. We consider flows where the shear flow is given by $U_x(r) = 0.5 - y(r-1)^2$, with $0.241 \leq y \leq 0.284$. We increase y by increments of 0.005, and we consider $y \leq 0.284$ to

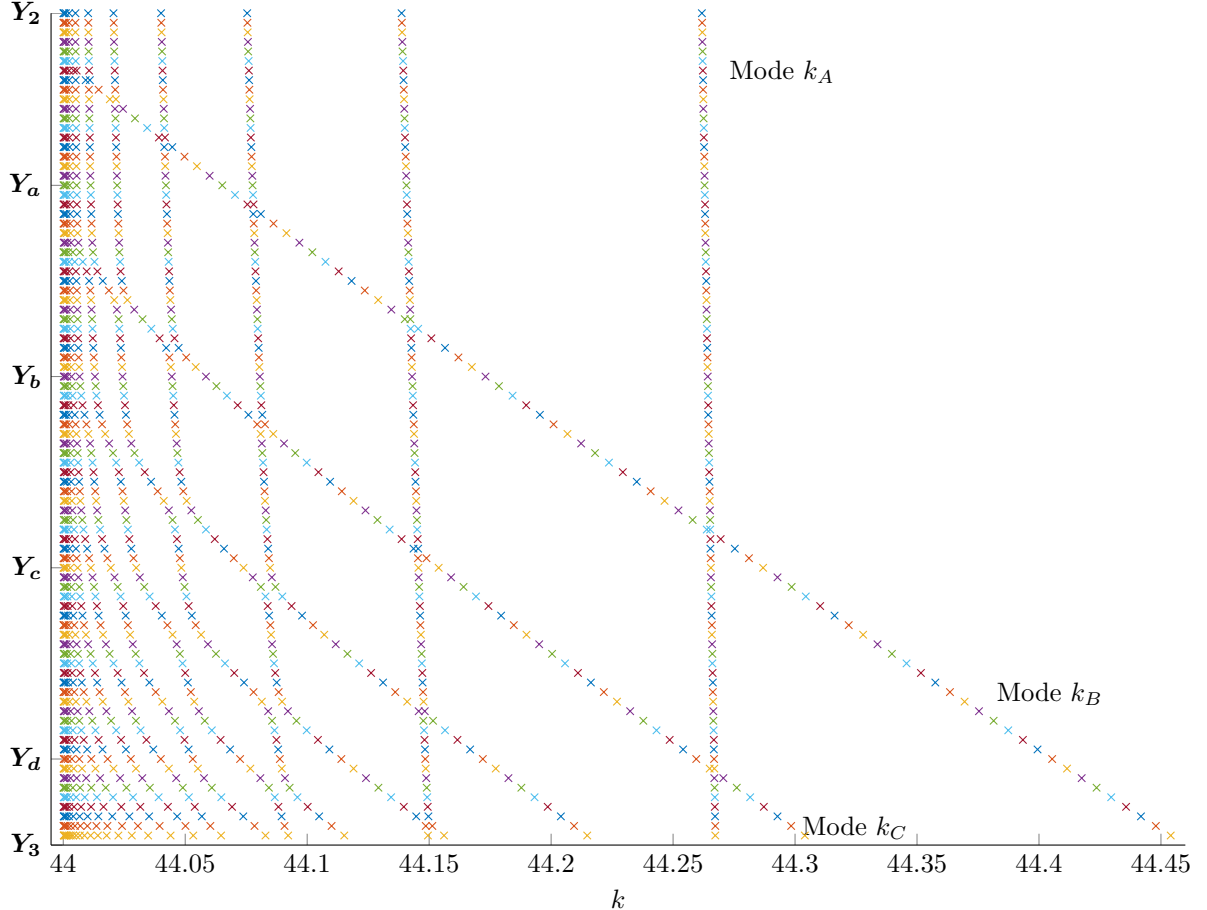


Figure 4.8: Plot of hydrodynamic modes as we consider shear flows of the form $U_x(r) = 0.5 - y(r-1)^2$, with $0.241 \leq y \leq 0.284$. The vertical scale is different values of y in increments of 0.005. The other parameters are $n = 15$, $\omega = 25$, $U_\theta = 0.2$ and $h = 0.6$.

ensure the right end of the critical layer is still given by $k = 44$. We introduce the flows \mathbf{Y}_a to \mathbf{Y}_d which correspond to $y = 0.25, 0.26, 0.27$ and 0.28 .

We only calculate and plot the hydrodynamic modes further than 10^{-4} from the critical layer for each flow. We see that as we vary the flow from \mathbf{Y}_2 to \mathbf{Y}_3 some modes bifurcate and all the eigenmodes also shift right. Some modes, such as mode k_A , do not move much as we vary the flow. Other modes, such as modes k_B and k_C , move significantly downstream. For example, we create the mode k_B through a bifurcation at $k = 44.0043$, for the shear flow with $y = 0.244$, and then it moves to $k = 44.45$ by flow \mathbf{Y}_3 .

The number of modes further than 10^{-4} from the critical layer has increased from 12 for the flow \mathbf{Y}_2 to 30 for the flow \mathbf{Y}_3 , as a result of the bifurcating modes. If we calculate the constant of proportionality (for exponential accumulation) of the flows we find that the constant is given by 2.63 (\mathbf{Y}_a), 7.53 (\mathbf{Y}_b), 31.7 (\mathbf{Y}_c) and 383 (\mathbf{Y}_d). These constants of proportionality for the flows \mathbf{Y}_a to \mathbf{Y}_d are only accurate for the hydrodynamic modes very near to the critical layer. For the first few hydrodynamic modes for each flow, the constant of proportionality (from calculating $(k_m^+ - 44) \exp(0.7629)$) is orders of magnitude out from the true value, calculated from the tail of the hydrodynamic modes.

As this constant of proportionality eventually tends to infinity (and as the asymptotic approximation become more and more inaccurate for the first few hydrodynamic modes), the flows stop accumulating exponentially. Instead, if we plot $\log(m)$ against $\log(k_m^+ - 44)$ for some of the flows close to \mathbf{Y}_3 we find it tends to a straight line, signifying algebraic accumulation.

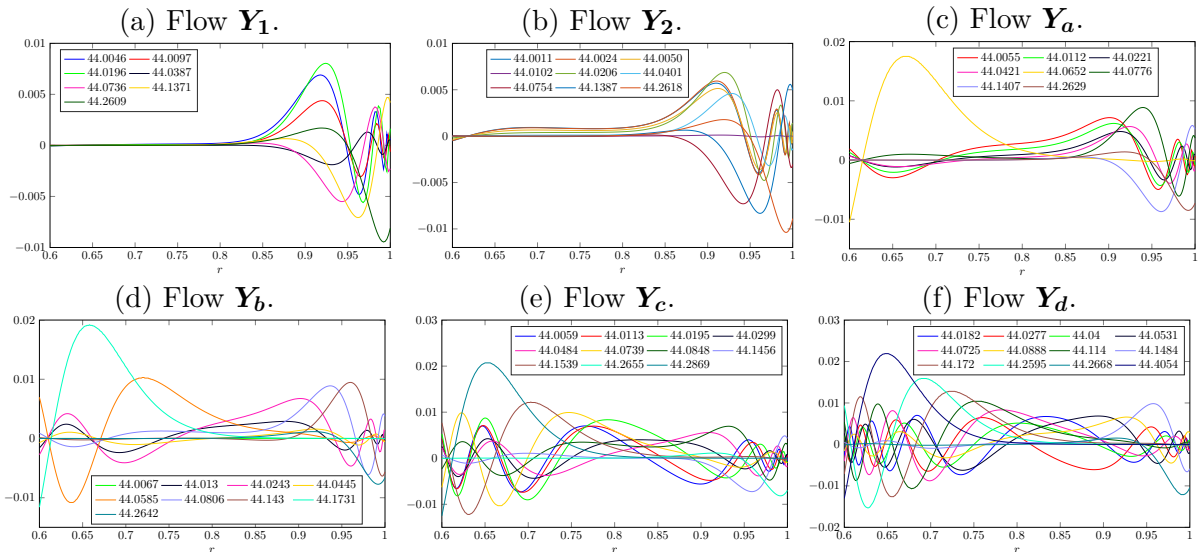


Figure 4.9: Plot of the pressure eigenfunctions P for the hydrodynamic modes from flows \mathbf{Y}_1 , \mathbf{Y}_2 and \mathbf{Y}_a to \mathbf{Y}_d .

Finally, we plot the pressure eigenfunctions P for the first few hydrodynamic modes for the flows \mathbf{Y}_1 , \mathbf{Y}_2 and \mathbf{Y}_a to \mathbf{Y}_d in Figure 4.9. For the flow \mathbf{Y}_1 the pressure eigenfunctions only oscillate near the duct wall at $r = 1$ and decay near $r = h$. When we look at flow \mathbf{Y}_2 , we begin to see some eigenfunctions which are non-zero near the duct wall at $r = h$, which signifies the start of the transition to algebraic accumulation through bifurcating modes.

For the flow \mathbf{Y}_a there is single eigenfunctions oscillating near $r = h$. The eigenmode for the eigenfunction plotted in yellow in [Figure 4.9c](#) is given by $k = 44.0652$, which corresponds to mode k_B in [Figure 4.8](#).

We also find eigenfunctions oscillating near $r = h$ in [Figures 4.9d](#) to [4.9f](#), and these correspond to the bifurcated modes, such as modes k_B and k_C in [Figure 4.8](#). In [Figure 4.9d](#), we see two eigenfunctions oscillating significantly near $r = h$, which are plotted in orange and cyan. The eigenmode for the orange eigenfunction is given by $k = 44.0585$ and corresponds to mode k_C , while the eigenmode for the cyan eigenfunction is given by $k = 44.1731$ and corresponds to mode k_B . In [Figures 4.9e](#) and [4.9f](#) we see eigenfunctions oscillating near $r = h$, corresponding to bifurcated modes, while we also find some eigenfunctions that oscillate over the whole duct. These are generally associated with eigenmodes that move significantly as the flow varies.

Chapter 5

Green's function with acoustic lining varying circumferentially

In this chapter we consider the effect that an acoustic lining varying circumferentially has on the eigenmodes and the Green's function of the Euler equations in swirling flow. To do this, we first write the impedance of the lining as a Fourier series, and calculate the Ingard-Myers boundary conditions as the lining varies in θ . We then consider the high-frequency limit and use a similar method to [Chapter 3](#) to calculate the Green's function. To calculate the eigenmodes asymptotically we find a new dispersion relation, which comes from solving a system of linear equations. We also show two different methods for calculating the eigenmodes numerically as the lining varies circumferentially, but both are too expensive computationally to generate any results on a desktop computer. We only consider results for a lining that varies smoothly, and we do not consider any results for splices, although our method is applicable.

This is the first time (to the author's knowledge) that the Green's function and eigenmodes have been studied asymptotically for a smoothly varying acoustic lining. It is also the first time that the eigenmodes and Green's function have been considered in swirling flow for any sort of acoustic lining varying circumferentially, with [Brambley et al. \(2012b\)](#) studying the eigenmodes asymptotically for splices in constant shear flow.

5.1 Examples of lining varying circumferentially

We allow the impedances of the acoustic lining at the duct walls to depend on the circumferential coordinate, so we consider $Z_h(\theta)$ and $Z_1(\theta)$. We further assume $Z_h(\theta) = Z_1(\theta) = Z(\theta)$, although this is not necessary. We can choose the impedance function $Z(\theta)$ such that the impedance smoothly varies with θ or is discontinuous to model splices in the duct. Three important examples of impedance functions are given by

$$Z^a(\theta) = Z, \tag{5.1.1}$$

$$Z^b(\theta) = 1 - 2i(\sin(2\theta) + 2), \tag{5.1.2}$$

$$\frac{1}{Z^c(\theta)} = \frac{1}{Z} \left[1 - \mathbb{1}_{-\frac{1}{2} < \theta < \frac{1}{2}} \right], \quad (5.1.3)$$

for Z of the form $Z = 1 - Z_{\text{imag}}i$, where Z_{imag} is positive. The first example is where the impedance is constant and we use [Chapter 3](#) to calculate the eigenmodes and Green's function. The second example is where the lining varies smoothly between $Z = 1 - 2i$ and $Z = 1 - 6i$. The third example is an example of when we consider a single splice in the duct for $-\frac{1}{2} < \theta < \frac{1}{2}$. The splice is used to join together pieces of acoustic lining, and the splice has hard walls with $Z^c(\theta) = \infty$. Away from the splice $Z^c(\theta) = Z$.

Often, there is more than one splice and the splices would be relatively thin. Although recent developments (see [Section 1.3](#)) have seen the introduction of zero-splice liners for the inlet, splices are still needed in the interstage between the rotor and stator. We could exploit the thinness of the splicing as a small parameter and perform asymptotics similar to [Brambley et al. \(2012b\)](#). Instead, we use the high-frequency asymptotic method from [Chapter 3](#), but with different boundary conditions.

It is necessary to represent the impedance function as a Fourier series, in the form

$$\frac{1}{Z(\theta)} = \sum_{m=-\infty}^{\infty} d_m e^{im\theta}. \quad (5.1.4)$$

For some sufficiently large M , we can truncate the series, with

$$\frac{1}{Z(\theta)} \approx \sum_{m=-M}^M d_m e^{im\theta}. \quad (5.1.5)$$

The Fourier series of $Z^a(\theta)$ only has one non-zero term. In [Figure 5.1](#) we plot the truncated Fourier series for $1/Z^b(\theta)$ in red when $M = 8$. We plot the function $1/Z^b(\theta)$ in blue and we see the approximation is very good, with an error of $\mathcal{O}(10^{-4})$. The reason we could take

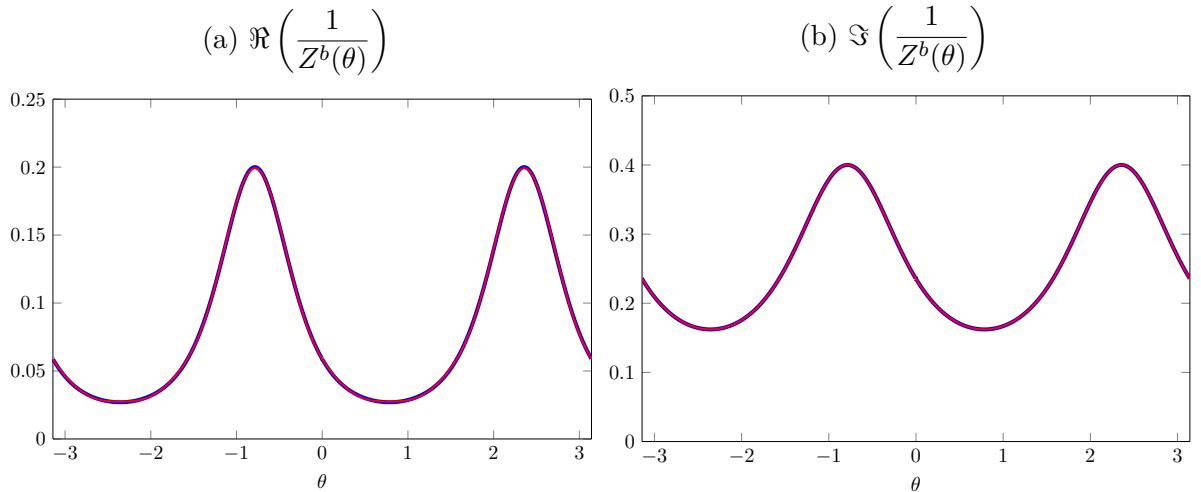


Figure 5.1: Real and imaginary part of the truncated Fourier series of $1/Z^b(\theta)$ when $M = 8$ (red) and $1/Z^b(\theta)$ (blue).

so few terms in the truncated Fourier series is the smoothness of $Z^b(\theta)$. By contrast, we need to take a significant number of terms in the truncated Fourier series for $Z^c(\theta)$. In

Figure 5.2 we plot the truncated Fourier series for $M = 10$, $M = 30$ and $M = 100$. We see that we need a significant amount of terms in the truncation to accurately approximate the original impedance function, and furthermore Gibbs phenomena occurs near $\theta = \pm 1/2$.

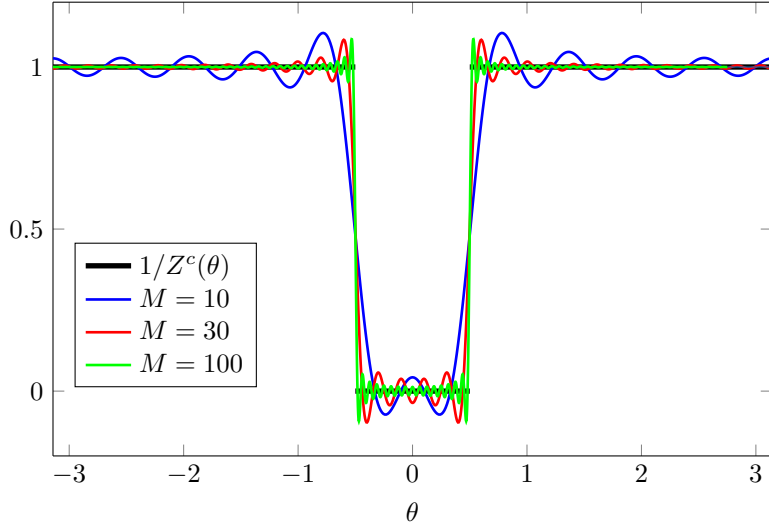


Figure 5.2: Plot of truncated Fourier series of $1/Z^c(\theta)$ (black) for $M = 10$ (blue), $M = 30$ (red), $M = 100$ (green).

5.2 Green's function with new boundary conditions

In this section we find the Green's function $G_\omega(\mathbf{x}|\mathbf{x}_0)$ of \mathcal{F}^M in (2.2.39), but now with the impedance of the acoustic lining varying circumferentially. The differential equation for the Green's function remains unchanged, while the boundary conditions become significantly more complicated and coupled. We consider a base flow of the form given in Section 2.1, although we restrict to the case of constant entropy.

5.2.1 Green's function

The Green's function $G_\omega(\mathbf{x}|\mathbf{x}_0)$ satisfies

$$\mathcal{F}^M(G_\omega(\mathbf{x}|\mathbf{x}_0)e^{-i\omega t}) = \delta(\mathbf{x}-\mathbf{x}_0)e^{-i\omega t} = \delta(x-x_0)\frac{\delta(r-r_0)}{r}\delta(\theta-\theta_0)e^{-i\omega t}, \quad (5.2.1)$$

and we look for a Green's function of the form

$$G_\omega(\mathbf{x}|\mathbf{x}_0) = \frac{1}{4\pi^2} \sum_{n=-\infty}^{\infty} e^{in(\theta-\theta_0)} \int_{\mathbb{R}} G_n(r|r_0; \omega, k) e^{ik(x-x_0)} dk. \quad (5.2.2)$$

We find it is given by

$$G_n(r|r_0; \omega, k, n) = \frac{1}{r_0 \mathcal{W}_n(r_0) J_n(r_0, k)} \begin{cases} g_n^1(r_0; \omega, k) g_n^2(r; \omega, k) & r \leq r_0 \\ g_n^2(r_0; \omega, k) g_n^1(r; \omega, k) & r > r_0 \end{cases}, \quad (5.2.3)$$

where J_n is given by (3.1.11) and the Wrońskián is given by

$$\mathcal{W}_n(r_0; \omega, k, n) = g_n^1(r_0; \omega, k) \frac{dg_n^2}{dr}(r_0; \omega, k) - \frac{dg_n^1}{dr}(r_0; \omega, k) g_n^2(r_0; \omega, k). \quad (5.2.4)$$

The functions g_n^j satisfy

$$\begin{aligned} & \frac{p_0}{c_0^2 r} (\mathcal{U}_\theta - \Omega^2)^2 \Omega^2 \frac{d}{dr} \left(\frac{rc_0^2}{p_0(\Omega^2 - \mathcal{U}_\theta)} \frac{dg_n^j}{dr} \right) + \left[(\mathcal{U}_\theta - \Omega^2)^2 \left(\frac{\Omega^2}{c_0^2} - k^2 - \frac{n^2}{r^2} \right) \right. \\ & \left. + \Upsilon(\mathcal{U}_\theta - \Omega^2) \left[\Upsilon + \Omega \left(\frac{1}{r} - \frac{\rho'_0}{\rho_0} \right) \right] - \Upsilon' \Omega (\Omega^2 - \mathcal{U}_\theta) + \Upsilon [\Omega(\Omega^2 - \mathcal{U}_\theta)]' \right] g_n^j = 0. \end{aligned} \quad (5.2.5)$$

where the functions Ω , Υ and \mathcal{U}_θ are defined in [Chapters 2](#) and [3](#).

5.2.2 Boundary conditions

We write the Ingard-Myers boundary conditions from (1.2.4) as

$$i\omega v = \frac{D_0}{Dt} \left(\frac{p}{Z(\theta)} \right) \text{ on } r = h \text{ and } -i\omega v = \frac{D_0}{Dt} \left(\frac{p}{Z(\theta)} \right) \text{ on } r = 1, \quad (5.2.6)$$

where we assume the time dependence of $p \propto e^{-i\omega t}$. We then apply the operator \mathcal{R} from [Chapter 2](#) to both sides and use $\rho_0 \mathcal{R}(v) = \mathcal{T}(p)$ (which holds when there are no source terms) and hence the boundary conditions become

$$\frac{i\omega \mathcal{T}(p)}{\rho_0} = \mathcal{R} \left[\frac{1}{Z(\theta)} \frac{D_0 p}{Dt} + p \frac{U_\theta}{r} \frac{d}{d\theta} \left(\frac{1}{Z(\theta)} \right) \right] \text{ on } r = h, \quad (5.2.7)$$

$$-\frac{i\omega \mathcal{T}(p)}{\rho_0} = \mathcal{R} \left[\frac{1}{Z(\theta)} \frac{D_0 p}{Dt} + p \frac{U_\theta}{r} \frac{d}{d\theta} \left(\frac{1}{Z(\theta)} \right) \right] \text{ on } r = 1. \quad (5.2.8)$$

Using the definition of \mathcal{R} in (2.2.23), we see that

$$\mathcal{R} = \frac{\partial^2}{\partial t^2} + U_x^2 \frac{\partial^2}{\partial x^2} + \frac{U_\theta^2}{r^2} \frac{\partial^2}{\partial \theta^2} + 2U_x \frac{\partial^2}{\partial x \partial t} + 2 \frac{U_\theta}{r} \frac{\partial^2}{\partial t \partial \theta} + \frac{2U_x U_\theta}{r} \frac{\partial^2}{\partial x \partial \theta} + \mathcal{U}_\theta, \quad (5.2.9)$$

and hence the boundary conditions become

$$\begin{aligned} \epsilon_r \frac{i\omega \mathcal{T}(p)}{\rho_0} &= \frac{1}{Z(\theta)} \mathcal{R} \left(\frac{D_0 p}{Dt} \right) + \left(\frac{1}{Z(\theta)} \right)' \left[\frac{2U_\theta}{r} \frac{D_0^2 p}{Dt^2} + \frac{U_\theta}{r} \mathcal{R}(p) \right] \\ &\quad + \left(\frac{1}{Z(\theta)} \right)'' \frac{3U_\theta^2}{r^2} \frac{D_0 p}{Dt} + \left(\frac{1}{Z(\theta)} \right)''' \frac{U_\theta^3}{r^3} p, \end{aligned} \quad (5.2.10)$$

for $r = h, 1$ where $\epsilon_h = 1$ and $\epsilon_1 = -1$. Setting $Z(\theta) = Z$, a constant, reduces the boundary conditions to

$$\epsilon_r \frac{i\omega \mathcal{T}(p)}{\rho_0} = \frac{1}{Z} \frac{D_0}{Dt} \mathcal{R}(p), \quad (5.2.11)$$

since \mathcal{R} and the material derivative always commute. Thus, we recover the boundary conditions from (3.1.14) for a constant impedance. We would also get a boundary condition of the form in (5.2.11) when there is no swirl but the lining varies circumferentially.

We now substitute in $G_\omega(\mathbf{x}|\mathbf{x}_0)e^{-i\omega t}$ to (5.2.10), using the form of G_ω in (5.2.2). This gives (using (??) to (??))

$$\begin{aligned} \epsilon_r \frac{i\omega}{\rho_0} \sum_{n=-\infty}^{\infty} e^{in(\theta-\theta_0)} & \int_{\mathbb{R}} i \left[\Omega_n \frac{dG_n}{dr} - \Upsilon_n G_n \right] e^{ik(x-x_0)} dk \\ &= \sum_{n=-\infty}^{\infty} e^{in(\theta-\theta_0)} \frac{1}{Z(\theta)} \int_{\mathbb{R}} -i\Omega_n (\mathcal{U}_\theta - \Omega_n^2) G_n e^{ik(x-x_0)} dk \\ &+ \sum_{n=-\infty}^{\infty} e^{in(\theta-\theta_0)} \left(\frac{1}{Z(\theta)} \right)' \int_{\mathbb{R}} \left[\frac{U_\theta}{r} (\mathcal{U}_\theta - \Omega_n^2) - \Omega_n^2 \frac{2U_\theta}{r} \right] G_n e^{ik(x-x_0)} dk \\ &+ \sum_{n=-\infty}^{\infty} e^{in(\theta-\theta_0)} \left(\frac{1}{Z(\theta)} \right)'' \int_{\mathbb{R}} -3i\Omega_n \frac{U_\theta^2}{r^2} G_n e^{ik(x-x_0)} dk \\ &+ \sum_{n=-\infty}^{\infty} e^{in(\theta-\theta_0)} \left(\frac{1}{Z(\theta)} \right)''' \int_{\mathbb{R}} \frac{U_\theta^3}{r^3} G_n e^{ik(x-x_0)} dk, \end{aligned} \quad (5.2.12)$$

for $r = h$ and $r = 1$. We write Ω_n and Υ_n to emphasise their dependence on the axial wavenumber n . Next, we write the impedance as a truncated Fourier series

$$\frac{1}{Z(\theta)} = \sum_{m=-M}^M c_m(\theta_0) e^{im(\theta-\theta_0)}, \quad (5.2.13)$$

where the coefficients $c_m(\theta_0)$ differ by a factor of $e^{im\theta_0}$ compared to the standard Fourier series coefficients d_m . We easily calculate the Fourier series of the l -th derivative of $1/Z$, with the Fourier coefficients given by $(im)^l c_m(\theta_0)$. We then use the convolution theorem, which states that

$$\left(\sum_{n=-\infty}^{\infty} e^{in(\theta-\theta_0)} a_n(r) \right) \left(\sum_{m=-M}^M c_m(\theta_0) e^{im(\theta-\theta_0)} \right) = \sum_{n=-\infty}^{\infty} e^{in(\theta-\theta_0)} \left[\sum_{m=n-M}^{n+M} a_m(r) c_{n-m}(\theta_0) \right], \quad (5.2.14)$$

for some arbitrary function $a_n(r)$. Writing the impedance as a truncated Fourier series in (5.2.12) and then using the convolution theorem gives

$$\begin{aligned} -\epsilon_r \frac{\omega}{\rho_0} \left[\Omega_n \frac{dG_n}{dr} - \Upsilon_n G_n \right] &= \sum_{m=n-M}^{n+M} c_{n-m}(\theta_0) (-i\Omega_m) (\mathcal{U}_\theta - \Omega_m^2) G_m \\ &+ \sum_{m=n-M}^{n+M} i(n-m) c_{n-m}(\theta_0) \left[\frac{U_\theta}{r} (\mathcal{U}_\theta - \Omega_m^2) - \Omega_m^2 \frac{2U_\theta}{r} \right] G_m \\ &+ \sum_{m=n-M}^{n+M} (n-m)^2 c_{n-m}(\theta_0) 3i\Omega_m \frac{U_\theta^2}{r^2} G_m \\ &- \sum_{m=n-M}^{n+M} i(n-m)^3 c_{n-m}(\theta_0) \frac{U_\theta^3}{r^3} G_m, \end{aligned} \quad (5.2.15)$$

for $r = h$ and $r = 1$. To find the Green's function we thus solve (5.2.5) for $g_n^1(r; \omega, k)$ and $g_n^2(r; \omega, k)$, where $g_n^1(r; \omega, k)$ solves the boundary condition (5.2.15) for $r = 1$ and $g_n^2(r; \omega, k)$ solves the boundary condition (5.2.15) for $r = h$. We then use (5.2.3) to calculate G_n . We will have to solve a coupled system of equations to determine $g_n^j(r; \omega, k)$, unless the impedance is constant.

When there is no swirl, the boundary conditions simplify significantly and we solve

$$-\epsilon_r \frac{\omega}{\rho_0} \Omega_n \frac{dG_n}{dr} = \sum_{m=n-M}^{n+M} c_{n-m}(\theta_0) i \Omega_m^3 G_m, \quad (5.2.16)$$

although we still have a coupled system.

5.3 High-frequency limit

We now consider the high-frequency limit, so we assume that the frequency $k = \mathcal{O}(\omega)$, where ω is large, so that $k = \kappa\omega$ with $\kappa = \mathcal{O}(1)$. We also assume that $n = \mathcal{O}(\omega)$.

5.3.1 Green's function differential equation

The differential equation that $g_n^j(r; \kappa)$ satisfies in the high-frequency limit is given by (see Section 3.1)

$$\frac{d^2 g_n^j}{dr^2}(r; \kappa) + \left(\frac{1}{r} - \frac{\rho'_0(r)}{\rho_0(r)} - 2 \frac{\partial}{\partial r} \Phi_n(r, \kappa) \right) \frac{dg_n^j}{dr}(r; \kappa) + \omega^2 q_n(r, \kappa) g_n^j(r; \kappa) = 0, \quad (5.3.1)$$

where

$$\Phi_n(r, \kappa) = 1 - \kappa U_x(r) - \frac{n U_\theta}{\omega r}, \quad (5.3.2)$$

and

$$q_n(r, \kappa) := \left(\frac{\Phi_n^2(r, \kappa)}{c_0^2(r)} - \kappa^2 - \frac{n^2}{\omega^2 r^2} \right). \quad (5.3.3)$$

We introduce the change of variables

$$g_n^j(r; \kappa) = \frac{\rho_0^{1/2}(r) \Phi_n(r, \kappa) v_n^j(r; \kappa)}{r^{1/2}}, \quad (5.3.4)$$

and then we look for solutions to the equation

$$\frac{d^2 v_n^j}{dr^2}(r; \kappa) + [\omega^2 q_n(r, \kappa) + q_n^*(r, \kappa)] v_n^j(r; \kappa) = 0, \quad (5.3.5)$$

where q_n^* is irrelevant for the leading order solution. The Green's function is then given by

$$G_n(r|r_0; \kappa) = \left(\frac{\rho_0(r)r_0}{\rho_0(r_0)r} \right)^{1/2} \frac{\Phi_n(r, \kappa)}{r_0 \mathcal{V}_n(r_0, \kappa) J_n(r_0, \kappa) \Phi_n(r_0, \kappa)} \begin{cases} v_n^1(r_0; \kappa) v_n^2(r; \kappa) & r \leq r_0 \\ v_n^2(r_0; \kappa) v_n^1(r; \kappa) & r > r_0 \end{cases}, \quad (5.3.6)$$

where the Wrońskiian

$$\mathcal{V}_n(r_0, \kappa) = v_n^1(r_0; \kappa) \frac{dv_n^2}{dr}(r_0; \kappa) - \frac{dv_n^1}{dr}(r_0; \kappa) v_n^2(r_0; \kappa), \quad (5.3.7)$$

is now independent of r_0 by Abel's theorem.

5.3.2 WKB solution

We solve the differential equation (5.3.5) using the WKB method, as in [Section 3.2](#). We find there are two different possible forms for the solutions, when $\kappa \in \mathcal{K}_n$ and when $\kappa \in \mathcal{K}_n^C$. For $\kappa \in \mathcal{K}_n$, $q_n(r, \kappa)$ has a single zero near the duct and the WKB solution is a linear combination of Airy functions. For $\kappa \in \mathcal{K}_n^C$, $q_n(r, \kappa)$ has no zeros near the duct and hence the solution is given by a linear combination of exponentials or sines and cosines.

The region \mathcal{K}_n

Using the work from [Section 3.2.3](#), let us define

$$\mathcal{R} = \left\{ r \in \mathbb{C} \mid |r - s| < \omega^{-2/3} \text{ for } s \in [h, 1] \right\}, \quad (5.3.8)$$

and then

$$s_n^\pm(r) = \frac{U_x(r) \left(1 - \frac{nU_\theta(r)}{\omega r} \right) \pm c_0(r) \sqrt{\left(1 - \frac{nU_\theta(r)}{\omega r} \right)^2 + \frac{n^2}{\omega^2 r^2} [U_x^2(r) - c_0^2(r)]}}{U_x^2(r) - c_0^2(r)}. \quad (5.3.9)$$

The region of κ space where we use the Airy solution is defined by

$$\mathcal{K}_n = s_n^+(\mathcal{R}) \cup s_n^-(\mathcal{R}). \quad (5.3.10)$$

In [Figure 5.3](#) we plot how $\omega \mathcal{K}_n$ changes as we vary n for the base flow we will consider in [Section 5.7](#).

The solution

Using the WKB method in a similar way to [Sections 3.2](#) and [3.7.3](#), we find the zero and one turning point solutions of (5.3.5). We find that

$$v_n^j(r; \kappa) = A_n^j(\kappa) \mathcal{A}_n(r; \kappa) + B_n^j(\kappa) \mathcal{B}_n(r; \kappa), \quad (5.3.11)$$

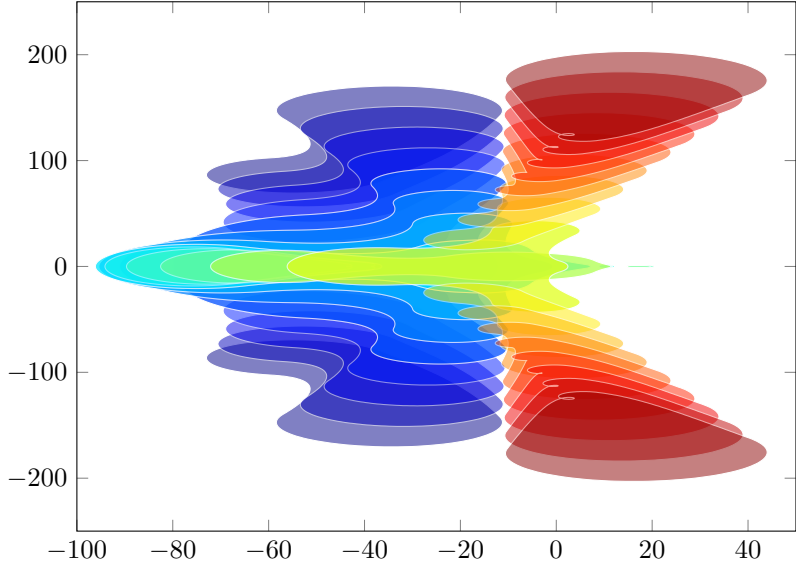


Figure 5.3: Plot of regions $\omega \mathcal{K}_n$ as n varies from $n = -100$ (blue) to $n = 100$ (red). We only plot intervals of $n = 10$. The other parameters of the flow are $\omega = 25$, $h = 0.6$, $U_x(r) = 0.2 + 0.4r^2$ and $U_\theta(r) = 0.1r + 0.2/r$.

where

$$\mathcal{A}_n(r; \kappa) = |q_n(r, \kappa)|^{-1/4} e^{i\omega\psi_n(r, \kappa)} \mathbb{1}_{\mathcal{K}_n^C} + \sqrt{\pi} \left[\left(\frac{\tau_n(r, \kappa)}{q_n(r, \kappa)} \right)^{1/4} \text{Ai}(-\tau_n(r, \kappa)) \right] \mathbb{1}_{\mathcal{K}_n}, \quad (5.3.12)$$

and

$$\mathcal{B}_n(r; \kappa) = |q_n(r, \kappa)|^{-1/4} e^{-i\omega\psi_n(r, \kappa)} \mathbb{1}_{\mathcal{K}_n^C} + \sqrt{\pi} \left[\left(\frac{\tau_n(r, \kappa)}{q_n(r, \kappa)} \right)^{1/4} \text{Bi}(-\tau_n(r, \kappa)) \right] \mathbb{1}_{\mathcal{K}_n}, \quad (5.3.13)$$

with

$$\tau_n(r, \kappa) = \left(\frac{3\omega\Psi_n(r, \kappa)}{2} \right)^{2/3}, \quad (5.3.14)$$

and $\mathbb{1}$ the indicator function. The functions $\psi_n(r, \kappa)$ and $\Psi_n(r, \kappa)$ are defined by

$$\psi_n(r, \kappa) = \int_h^1 \sqrt{q_n(s, \kappa)} ds \text{ and } \Psi_n(r, \kappa) = \int_{r_n^c(\kappa)}^1 \sqrt{q_n(s, \kappa)} ds, \quad (5.3.15)$$

where $r_n^c(\kappa)$ is such that $q_n(r_n^c(\kappa), \kappa) = 0$. To determine $A_n^j(\kappa)$ and $B_n^j(\kappa)$ we use the coupled boundary conditions.

5.3.3 Boundary conditions

We now calculate the boundary conditions in the high-frequency limit. Using (5.2.15) we find that

$$-\frac{\omega}{\rho_0(h)} \Phi_n(h, \kappa) \frac{dg_n^2}{dr}(h; \kappa) = \sum_{m=n-M}^{n+M} \left[c_{n-m}(\theta_0) \mathcal{Z}_{n,m}(h, \kappa) + \mathcal{Z}_{n,m}^*(h, \kappa) \right] g_m^2(h; \kappa), \quad (5.3.16)$$

and

$$\frac{\omega}{\rho_0(1)} \Phi_n(1; \kappa) \frac{dg_n^1}{dr}(1, \kappa) = \sum_{m=n-M}^{n+M} [c_{n-m}(\theta_0) \mathcal{Z}_{n,m}(1, \kappa) + \mathcal{Z}_{n,m}^*(1, \kappa)] g_m^1(1; \kappa), \quad (5.3.17)$$

where

$$\mathcal{Z}_{n,m}(r, \kappa) = i\omega^2 \left(\Phi_m(r, \kappa) - \frac{n-m}{\omega} \frac{U_\theta(r)}{r} \right)^3 - i \left[\frac{n-m}{\omega} \frac{U_\theta(r) \mathcal{U}_\theta(r)}{r} - \Phi_m(r, \kappa) \mathcal{U}_\theta(r) \right],$$

and

$$\mathcal{Z}_{n,m}^*(r, \kappa) = -\omega \delta_{mn} \epsilon_r \frac{\Upsilon_m^*(r, \kappa)}{\rho_0(r)}, \quad (5.3.18)$$

with $\Upsilon_n = \omega \Upsilon_n^*$. In the limit of large frequency we could simplify $\mathcal{Z}_{n,m}$ and ignore $\mathcal{Z}_{n,m}^*$, with

$$\mathcal{Z}_{n,m}(r, \kappa) \approx i\omega^2 \hat{\mathcal{Z}}_{n,m}(r, \kappa) \text{ where } \hat{\mathcal{Z}}_{n,m}(r, \kappa) := \left(\Phi_m(r, \kappa) - \frac{n-m}{\omega} \frac{U_\theta(r)}{r} \right)^3. \quad (5.3.19)$$

However, we will use the full form of $\mathcal{Z}_{n,m}$ and $\mathcal{Z}_{n,m}^*$. If the impedance is constant with $Z(\theta) = Z$, then $c_{n-m} = 0$ for $m \neq n$, so we recover the boundary conditions from [Chapter 3](#).

If we substitute (5.3.4) into (5.3.16) and (5.3.17) then we get the boundary conditions for $v_n^j(r; \kappa)$, which are given by

$$-\frac{\omega}{\rho_0(h)} \Phi_n^2(h, \kappa) \frac{dv_n^2}{dr}(h; \kappa) = \sum_{m=n-M}^{n+M} [c_{n-m}(\theta_0) \mathcal{X}_{n,m}(h, \kappa) + \mathcal{X}_{n,m}^*(h, \kappa)] v_m^2(h; \kappa), \quad (5.3.20)$$

and

$$\frac{\omega}{\rho_0(1)} \Phi_n^2(1, \kappa) \frac{dv_n^1}{dr}(1; \kappa) = \sum_{m=n-M}^{n+M} [c_{n-m}(\theta_0) \mathcal{X}_{n,m}(1, \kappa) + \mathcal{X}_{n,m}^*(1, \kappa)] v_m^1(1; \kappa), \quad (5.3.21)$$

where

$$\mathcal{X}_{n,m}(r, \kappa) = \Phi_m(r, \kappa) \mathcal{Z}_{n,m}(r, \kappa), \quad (5.3.22)$$

and

$$\mathcal{X}_{n,m}^*(r, \kappa) = \Phi_m(r, \kappa) \mathcal{Z}_{n,m}^*(r, \kappa) + \epsilon_r \delta_{mn} \frac{\omega \Phi_m^2(r, \kappa)}{2\rho_0(r)} \left(\frac{\rho'_0(r)}{\rho_0(r)} - \frac{1}{r} + 2 \frac{\partial}{\partial r} \frac{\Phi_m(r, \kappa)}{\Phi_m(r, \kappa)} \right). \quad (5.3.23)$$

In the high-frequency limit we could ignore the $\mathcal{X}_{n,m}^*$ term and use the approximation

$$\mathcal{X}_{n,m}(r, \kappa) \approx i\omega^2 \Phi_m(r, \kappa) \hat{\mathcal{Z}}_{n,m}(r, \kappa), \quad (5.3.24)$$

but we will use the full form of $\mathcal{X}_{n,m}$ and $\mathcal{X}_{n,m}^*$.

5.4 Calculating the eigenmodes asymptotically

We now discuss how to find the eigenmodes of the flow. To do this asymptotically, we find a dispersion relation from the Wrońskiian of $v_n^1(r; \kappa)$ and $v_n^2(r; \kappa)$, and then solve this dispersion relation for κ . We begin by calculating the values of $v_n^1(r; \kappa)$ and $v_n^2(r; \kappa)$ and their derivatives at the duct walls. We find

$$v_n^2(h; \kappa) = A_n^h(\kappa) \mathcal{A}_n^h(\kappa) + B_n^h(\kappa) \mathcal{B}_n^h(\kappa) \text{ and } v_n^1(1; \kappa) = A_n^1(\kappa) \mathcal{A}_n^1(\kappa) + B_n^1(\kappa) \mathcal{B}_n^1(\kappa), \quad (5.4.1)$$

where

$$\mathcal{A}_n^r(\kappa) = \mathcal{A}_n(r, \kappa) \text{ and } \mathcal{B}_n^r = \mathcal{B}_n(r, \kappa), \quad (5.4.2)$$

for $r = h, 1$, with \mathcal{A}_n defined in (5.3.12) and \mathcal{B}_n in (5.3.13). Next, we find that at the duct walls the radial derivatives of $v_n^1(r; \kappa)$ and $v_n^2(r; \kappa)$ are given by

$$\frac{dv_n^2}{dr}(h; \kappa) = A_n^h(\kappa) \mathbb{A}_n^h(\kappa) + B_n^h(\kappa) \mathbb{B}_n^h(\kappa) \text{ and } \frac{dv_n^1}{dr}(1; \kappa) = A_n^1(\kappa) \mathbb{A}_n^1(\kappa) + B_n^1(\kappa) \mathbb{B}_n^1(\kappa), \quad (5.4.3)$$

where

$$\begin{aligned} \mathbb{A}_n^r(\kappa) &= \left(-\frac{\frac{\partial}{\partial r} q_n(r, \kappa)}{4q_n(r, \kappa)} + i\omega \sqrt{q_n(r, \kappa)} \right) |q_n(r, \kappa)|^{-1/4} e^{i\omega\psi_n(r, \kappa)} \mathbb{1}_{\mathcal{K}_n^C} + \sqrt{\pi} \left(\frac{\tau_n(r, \kappa)}{q_n(r, \kappa)} \right)^{1/4} \times \\ &\left[\left(\frac{1}{6} \frac{\partial}{\partial r} \Psi_n(r, \kappa) - \frac{1}{4} \frac{\partial}{\partial r} q_n(r, \kappa) \right) \text{Ai}(-\tau_n(r, \kappa)) - \frac{2}{3} \frac{\partial}{\partial r} \Psi_n(r, \kappa) \tau_n(r, \kappa) \text{Ai}'(-(\tau_n(r, \kappa))) \right] \mathbb{1}_{\mathcal{K}_n}, \end{aligned} \quad (5.4.4)$$

and

$$\begin{aligned} \mathbb{B}_n^r(\kappa) &= \left(-\frac{\frac{\partial}{\partial r} q_n(r, \kappa)}{4q_n(r, \kappa)} - i\omega \sqrt{q_n(r, \kappa)} \right) |q_n(r, \kappa)|^{-1/4} e^{-i\omega\psi_n(r, \kappa)} \mathbb{1}_{\mathcal{K}_n^C} + \sqrt{\pi} \left(\frac{\tau_n(r, \kappa)}{q_n(r, \kappa)} \right)^{1/4} \times \\ &\left[\left(\frac{1}{6} \frac{\partial}{\partial r} \Psi_n(r, \kappa) - \frac{1}{4} \frac{\partial}{\partial r} q_n(r, \kappa) \right) \text{Bi}(-\tau_n(r, \kappa)) - \frac{2}{3} \frac{\partial}{\partial r} \Psi_n(r, \kappa) \tau_n(r, \kappa) \text{Bi}'(-(\tau_n(r, \kappa))) \right] \mathbb{1}_{\mathcal{K}_n}, \end{aligned} \quad (5.4.5)$$

for $r = h, 1$. We set $A_n^1 = A_n^h = 1$ and then determine B_n^j from the boundary conditions.

5.4.1 Wrońskiian and dispersion relation

We now calculate $\mathcal{V}_n(\kappa)$, the Wrońskiian of $v_n^1(r; \kappa)$ and $v_n^2(r; \kappa)$. The dispersion relation is then given by $\mathcal{V}_n = 0$. When $\kappa \in \mathcal{K}_n$, the Wrońskiian is given by

$$\begin{aligned} \mathcal{V}_n(\kappa) &= \frac{2\pi}{3} \frac{\frac{\partial}{\partial r} \Psi_n(r, \kappa)}{\Psi_n(r, \kappa)} \left(\frac{\tau_n^3(r, \kappa)}{q_n(r, \kappa)} \right)^{1/2} \left[(\text{Ai}' + B_n^1 \text{Bi}')(\text{Ai} + B_n^h \text{Bi}) - (\text{Ai}' + B_n^h \text{Bi}')(\text{Ai} + B_n^1 \text{Bi}) \right], \\ &= \pi\omega \left[(\text{Ai}' + B_n^1 \text{Bi}')(\text{Ai} + B_n^h \text{Bi}) - (\text{Ai}' + B_n^h \text{Bi}')(\text{Ai} + B_n^1 \text{Bi}) \right], \\ &= \pi\omega (B_n^1 - B_n^h) \left[\text{Ai} \text{Bi}' - \text{Ai}' \text{Bi} \right], \end{aligned} \quad (5.4.6)$$

where all the Airy functions are evaluated at $-\tau_n(r, \kappa)$. Since the Wroński is independent of r , we can evaluate it at any value of r . Using the definition of the Airy function, we calculate the derivative of $\text{Ai} \text{Bi}' - \text{Ai}' \text{Bi}$ is identically zero. We then evaluate this expression at zero to find $\text{Ai} \text{Bi}' - \text{Ai}' \text{Bi} = 1/\pi$. Hence, for $\kappa \in \mathcal{K}_n$ we conclude that

$$\mathcal{V}_n(\kappa) = \omega [B_n^1(\kappa) - B_n^h(\kappa)]. \quad (5.4.7)$$

When $\kappa \in \mathcal{K}_n^C$ we calculate the Wroński as in [Chapter 3](#), and find it is given by

$$\mathcal{V}_n(\kappa) = 2i\omega [B_n^1(\kappa) - B_n^h(\kappa)]. \quad (5.4.8)$$

Although the Wrońskians differ by a constant, the dispersion relation for finding the asymptotic eigenmodes is the same for all values of κ and is given by

$$B_n^1(\kappa) - B_n^h(\kappa) = 0. \quad (5.4.9)$$

It remains to find $B_n^1(\kappa)$ and $B_n^h(\kappa)$, which we do next by applying the boundary conditions. We could scale the solutions $v_n^j(r; \kappa)$ by $1/(1+i)$ when $\kappa \in \mathcal{K}_n^C$ so the Wroński for all values of κ is given by (5.4.7).

5.4.2 Reducing to a finite system

It is clear from the boundary conditions in (5.3.20) and (5.3.21) that we get an infinite, coupled system of the form

$$\Lambda_\infty^j \mathbf{B}_\infty^j = \boldsymbol{\mu}_\infty^j, \quad (5.4.10)$$

for $j = h, 1$ where

$$\mathbf{B}_\infty^j = [\dots, B_{-2}^j, B_{-1}^j, B_0^j, B_1^j, B_2^j, \dots]^T. \quad (5.4.11)$$

The matrix Λ_∞^j is square and banded, with entries on the diagonals $m = -M$ to $m = M$. Thus, the number of terms we take in the truncated Fourier series of the impedance function determines the sparsity of Λ_∞^j , with fewer terms giving a sparser matrix. For a splice, the matrix will be dense. In the case that $M = 0$ (constant impedance) then Λ_∞^j is a diagonal matrix and we decouple the system.

To solve the system we first need to reduce the dimension of it. To do this we assume that $G_n \rightarrow 0$ as $|n| \rightarrow \infty$, since G_n are the coefficients of a Fourier series, and this assumption can be validated numerically for the case of constant impedance (see [Figure 3.31](#)). We set $G_n = 0$ for $|n| > N$, where N is a constant such that $N > M$, and hence $B_n^j = 0$ for $|n| > N$. We thus consider the finite system

$$\Lambda^j \mathbf{B}^j = \boldsymbol{\mu}^j, \quad (5.4.12)$$

where

$$\mathbf{B}^j = [B_{-N}^j, \dots, B_{-1}^j, B_0^j, B_1^j, \dots, B_N^j]^T. \quad (5.4.13)$$

If we let $N_1 = 2N + 1$, then $\boldsymbol{\mu}^j$ is a column vector of size N_1 , while Λ^j is a square matrix of size $N_1 \times N_1$, and is of the form

$$\Lambda^j = \begin{bmatrix} \times & \times & \times & 0 \\ \times & \times & \times & \times & 0 \\ \times & \times & \times & \times & \times & 0 \\ 0 & \times & \times & \times & \times & \times & 0 \\ 0 & \times & \times & \times & \times & \times & \times & 0 \\ 0 & \ddots & \ddots & \ddots & \ddots & \ddots & 0 \\ 0 & \times & \times & \times & \times & \times & \times & 0 \\ 0 & \times \\ 0 & \times \\ 0 & \times \\ 0 & \times \\ 0 & \times \\ 0 & \times \\ 0 & \times \\ 0 & \times \end{bmatrix}, \quad (5.4.14)$$

when $M = 2$, with \times symbols representing non-zero entries.

There are two methods to solve the system (5.4.12). Either we find the inverse of Λ^j , or we perform row and column operators. We choose to do the latter as it is quicker and a more stable method, since we find Λ^j is badly conditioned for large N . This is because for large N the matrix contains exponentially large and exponentially small terms.

We should choose N sufficiently large such that when we solve the system for $N+1$, \mathbf{B}^j only differs by a very small amount. We find $N = 3M$ is generally sufficiently large.

5.4.3 Boundary condition at $r = h$ (calculating \mathbf{B}^h)

We now substitute in (5.4.1) and (5.4.3) into the boundary condition at $r = h$, given by (5.3.20). After setting $v_n^2(h; \kappa)$ and its radial derivative to be zero for $|n| > N$ we find that

$$\begin{aligned} & - \sum_{m=\max(n-M, -N)}^{\min(n+M, N)} \left[c_{n-m}(\theta_0) \mathcal{X}_{n,m}(h, \kappa) + \mathcal{X}_{n,m}^*(h, \kappa) \right] \mathcal{B}_m^h(\kappa) B_m^h(\kappa) - \frac{\omega}{\rho_0(h)} \Phi_n^2(h, \kappa) \mathbb{B}_n^h(\kappa) B_n^h(\kappa) \\ &= \sum_{m=\max(n-M, -N)}^{\min(n+M, N)} \left[c_{n-m}(\theta_0) \mathcal{X}_{n,m}(h, \kappa) + \mathcal{X}_{n,m}^*(h, \kappa) \right] \mathcal{A}_m^h(\kappa) + \frac{\omega}{\rho_0(h)} \Phi_n^2(h, \kappa) \mathbb{A}_n^h(\kappa). \end{aligned} \quad (5.4.15)$$

Hence, we have

$$\boldsymbol{\mu}^h = \left(\mu_n^h(\kappa) \right)_{n=-N}^{n=N}, \quad (5.4.16)$$

where

$$\mu_n^h(\kappa) = \sum_{m=\max(n-M, -N)}^{\min(n+M, N)} \left[c_{n-m}(\theta_0) \mathcal{X}_{n,m}(h, \kappa) + \mathcal{X}_{n,m}^*(h, \kappa) \right] \mathcal{A}_m^h(\kappa) + \frac{\omega}{\rho_0(h)} \Phi_n^2(h, \kappa) \mathbb{A}_n^h(\kappa). \quad (5.4.17)$$

If we define

$$\Lambda_{n,l}^h(\kappa) = - \left[c_{-l}(\theta_0) \mathcal{X}_{n,n+l}(h, \kappa) + \mathcal{X}_{n,n+l}^*(h, \kappa) \right] \mathcal{B}_{n+l}^h(\kappa) - \delta_{l0} \frac{\omega}{\rho_0(h)} \Phi_{n+l}^2(h, \kappa) \mathbb{B}_{n+l}^h(\kappa), \quad (5.4.18)$$

then

$$\Lambda^h = \begin{bmatrix} \Lambda_{-N,0}^h & \Lambda_{-N,1}^h & \Lambda_{-N,2}^h & 0 \\ \Lambda_{-N+1,-1}^h & \Lambda_{-N+1,0}^h & \Lambda_{-N+1,1}^h & \Lambda_{-N+1,2}^h & 0 \\ \Lambda_{-N+2,-2}^h & \Lambda_{-N+2,-1}^h & \Lambda_{-N+2,0}^h & \Lambda_{-N+2,1}^h & \Lambda_{-N+2,2}^h & 0 \\ 0 & \Lambda_{-N+3,-2}^h & \Lambda_{-N+3,-1}^h & \Lambda_{-N+3,0}^h & \Lambda_{-N+3,1}^h & \Lambda_{-N+3,2}^h & 0 \\ 0 & \ddots & \ddots & \ddots & \ddots & \ddots & 0 \\ 0 & \Lambda_{N-3,-2}^h & \Lambda_{N-3,-1}^h & \Lambda_{N-3,0}^h & \Lambda_{N-3,1}^h & \Lambda_{N-3,2}^h & 0 \\ 0 & \Lambda_{N-2,-2}^h & \Lambda_{N-2,-1}^h & \Lambda_{N-2,0}^h & \Lambda_{N-2,1}^h & \Lambda_{N-2,2}^h & 0 \\ 0 & \Lambda_{N-1,-2}^h & \Lambda_{N-1,-1}^h & \Lambda_{N-1,0}^h & \Lambda_{N-1,1}^h & 0 & \Lambda_{N,-2}^h & \Lambda_{N,-1}^h & \Lambda_{N,0}^h \end{bmatrix}, \quad (5.4.19)$$

where again we only consider the case when $M = 2$. For an alternative description of the matrix Λ^h , we could index the diagonals of Λ^h by l , with $l = 0$ corresponding to the main (or principle) diagonal. For $|l| \leq M$ we have

$$\text{diag}(\Lambda^h, l) = \boldsymbol{\Lambda}_l^h := \left(\Lambda_{n,l}^h(\kappa) \right)_{n=\max(-N, -N-l)}^{n=\min(N, N-l)}. \quad (5.4.20)$$

For $|l| > M$ the diagonal is zero. To calculate \boldsymbol{B}^h we solve

$$\Lambda^h \boldsymbol{B}^h = \boldsymbol{\mu}^h \quad (5.4.21)$$

using row and column operations, where $\boldsymbol{\mu}^h$ is given in (5.4.16) and Λ^h is given by (5.4.19) or (5.4.20).

5.4.4 Boundary condition at $r = 1$ (calculating \boldsymbol{B}^1)

We now consider the other boundary condition at $r = 1$, given by (5.3.21). After setting $v_n^1(1; \kappa)$ and its radial derivative to be zero for $|n| > N$ we find that

$$\begin{aligned} & - \sum_{m=\max(n-M, -N)}^{\min(n+M, N)} \left[c_{n-m}(\theta_0) \mathcal{X}_{n,m}(1, \kappa) + \mathcal{X}_{n,m}^*(1, \kappa) \right] \mathcal{B}_m^1(\kappa) B_m^1(\kappa) + \frac{\omega}{\rho_0(1)} \Phi_n^2(1, \kappa) \mathbb{B}_n^1(\kappa) B_n^1(\kappa) \\ &= \sum_{m=\max(n-M, -N)}^{\min(n+M, N)} \left[c_{n-m}(\theta_0) \mathcal{X}_{n,m}(1, \kappa) + \mathcal{X}_{n,m}^*(1, \kappa) \right] \mathcal{A}_m^1(\kappa) - \frac{\omega}{\rho_0(1)} \Phi_n^2(1, \kappa) \mathbb{A}_n^1(\kappa). \end{aligned} \quad (5.4.22)$$

Hence, we find that

$$\boldsymbol{\mu}^1 = \left(\mu_n^1(\kappa) \right)_{n=-N}^{n=N}, \quad (5.4.23)$$

where

$$\mu_n^1(\kappa) = \sum_{m=\max(n-M,-N)}^{\min(n+M,N)} [c_{n-m}(\theta_0)\mathcal{X}_{n,m}(1,\kappa) + \mathcal{X}_{n,m}^*(1,\kappa)] \mathcal{A}_m^1(\kappa) - \frac{\omega}{\rho_0(1)} \Phi_n^2(1,\kappa) \mathbb{A}_n^1(\kappa). \quad (5.4.24)$$

We also define

$$\Lambda_{n,l}^1(\kappa) = -[c_{-l}(\theta_0)\mathcal{X}_{n,n+l}(1,\kappa) + \mathcal{X}_{n,n+l}^*(1,\kappa)] \mathcal{B}_{n+l}^1(\kappa) + \delta_{l0} \frac{\omega}{\rho_0(1)} \Phi_{n+l}^2(1,\kappa) \mathbb{B}_{n+l}^1(\kappa), \quad (5.4.25)$$

so that

$$\text{diag}(\Lambda^1, l) = \Lambda_l^1 := (\Lambda_{n,l}^h(\kappa))_{n=\max(-N,-N-l)}^{n=\min(N,N-l)}, \quad (5.4.26)$$

for $|l| \leq M$ and zero for $|l| > M$. We then solve

$$\Lambda^1 \mathbf{B}^1 = \boldsymbol{\mu}^1, \quad (5.4.27)$$

to determine \mathbf{B}^1 .

5.4.5 Simplifications with no swirl

When there is no swirl there are a number of simplifications to our asymptotic method. First, the region \mathcal{K} is now independent of n , so we would only need to calculate it once. Second, the zeros of $q_n(r, \kappa)$ no longer depend on n , so we only need to calculate the critical point r_n^c once. Third, the terms \mathcal{X} and \mathcal{X}^* simplify significantly when $U_\theta = 0$.

5.4.6 Solving the dispersion relation

To find the eigenmodes for a particular azimuthal number n_1 we solve (5.4.21) and (5.4.27) for $N > |n_1|$ and a particular κ , to calculate $B_{n_1}^1(\kappa) - B_{n_1}^h(\kappa)$. We then use a numerical solver to find zeros of $B_{n_1}^1(\kappa) - B_{n_1}^h(\kappa)$ in κ space.

5.5 Calculating the eigenmodes numerically

We now discuss two possible ways to solve for the eigenmodes numerically. The first is in a similar spirit to the asymptotic method, and involves finding a numerical dispersion relation which we would then solve. The second is by finding the eigenmodes of the system, like in Section 3.3.2. However, we were unable to get either method to work successfully, mainly because both are very computationally expensive. This shows that our asymptotic method could be very useful, but it still requires validating.

5.5.1 Numerical dispersion relation

For each κ , we numerically find two, linearly independent solutions of (5.2.5) without any boundary conditions by using the “null” command in Chebfun, which finds the null space of a differential operator. Once we have these solutions, we then use the change of variables in (5.3.4) to find two, linearly independent solutions of the differential equation that $v_n^j(r; \kappa)$ satisfies. We then write

$$v_n^j(r; \kappa) = A_n^j(\kappa) \mathcal{A}_j^*(r, \kappa) + B_n^j(\kappa) \mathcal{B}_j^*(r, \kappa), \quad (5.5.1)$$

where \mathcal{A}_j^* and \mathcal{B}_j^* are the linearly independent solutions. We then follow the same method as in the asymptotic case to calculate B_n^j .

Implementation

This method would be very slow, since finding the null space of the differential equation in (5.2.5) numerically generally takes a few seconds for each wavenumber and azimuthal number. For some choices of wavenumber and large azimuthal number we were unable to find the null space numerically, since the null space consists of exponential functions which are hard to resolve accurately.

5.5.2 Eigenmode problem

Using the work from [Section 3.3.2](#) (but in the homentropic case), we Fourier transform the variables using

$$\{u, v, w, p\}(r, x, \theta, t) = \int \sum_n \int \{U_n(r), V_n(r), W_n(r), P_n(r)\} e^{ikx} dk e^{in\theta} e^{-i\omega t} d\omega, \quad (5.5.2)$$

and then our eigenvalue problem becomes

$$-\frac{U_x \hat{\Omega}_n}{c_0^2 \zeta} i U_n + \left[\frac{U_x}{c_0^2 \zeta} \frac{dU_x}{dr} - \frac{1}{r\zeta} - \frac{U_\theta^2}{\zeta r c_0^2} \right] V_n - \frac{1}{\zeta} \frac{dV_n}{dr} - \frac{n}{r\zeta} i W_n + \frac{i \hat{\Omega}_n}{c_0^2 \rho_0 \zeta} P_n = k i U_n, \quad (5.5.3)$$

$$\frac{\hat{\Omega}_n}{U_x} V_n - \frac{2U_\theta}{rU_x} i W_n + \frac{i}{\rho_0 U_x} \frac{dP_n}{dr} - \frac{i U_\theta^2}{\rho_0 U_x r c_0^2} P_n = k V_n, \quad (5.5.4)$$

$$-\frac{1}{U_x} \left[\frac{U_\theta}{r} + \frac{dU_\theta}{dr} \right] V_n + \frac{\hat{\Omega}_n}{U_x} i W_n - \frac{in}{r \rho_0 U_x} P_n = k i W_n, \quad (5.5.5)$$

$$\frac{\rho_0 \hat{\Omega}_n}{\zeta} U_n + i \frac{\rho_0}{\zeta} \left[\frac{dU_x}{dr} - \left(\frac{U_\theta^2}{c_0^2} + 1 \right) \frac{U_x}{r} \right] V_n - \frac{i \rho_0 U_x}{\zeta} \frac{dV_n}{dr} + \frac{n \rho_0 U_x}{r \zeta} W_n - \frac{U_x \hat{\Omega}_n}{c_0^2 \zeta} P_n = k P_n, \quad (5.5.6)$$

for each azimuthal wavenumber n , where

$$\hat{\Omega}_n = \omega - \frac{n U_\theta}{r} \text{ and } \zeta = 1 - \frac{U_x^2}{c_0^2}. \quad (5.5.7)$$

Boundary conditions

The boundary conditions are given by

$$i\omega v = \frac{1}{Z(\theta)} \frac{D_0 p}{Dt} + p \frac{U_\theta}{r} \frac{d}{d\theta} \left(\frac{1}{Z(\theta)} \right) \text{ on } r = h \quad (5.5.8)$$

and

$$-i\omega v = \frac{1}{Z(\theta)} \frac{D_0 p}{Dt} + p \frac{U_\theta}{r} \frac{d}{d\theta} \left(\frac{1}{Z(\theta)} \right) \text{ on } r = 1. \quad (5.5.9)$$

When we substitute in (5.5.2), the boundary condition at $r = h$ becomes

$$\begin{aligned} i\omega \sum_{n=-\infty}^{\infty} V_n(h) e^{in\theta} &= \frac{1}{Z(\theta)} \sum_{n=-\infty}^{\infty} \left(-i\omega + ikU_x(h) + i\frac{nU_\theta(h)}{h} \right) P_n(h) e^{in\theta} \\ &\quad + \frac{d}{d\theta} \left(\frac{1}{Z(\theta)} \right) \frac{U_\theta(h)}{h} \sum_{n=-\infty}^{\infty} P_n(h) e^{in\theta}. \end{aligned} \quad (5.5.10)$$

We then substitute in the truncated Fourier series from (5.1.5) and use the convolution theorem from (5.2.14). We get

$$\omega V_n(h) = \sum_{m=n-M}^{n+M} d_{n-m} \left[-\omega P_m(h) + U_x(h) \hat{P}_m(h) + m \frac{U_\theta(h)}{h} P_m(h) + \frac{U_\theta(h)}{h} P_m(h)(n-m) \right], \quad (5.5.11)$$

where $\hat{P} = kP$. The boundary condition at $r = h$ simplifies to

$$\omega V_n(h) = \sum_{m=n-M}^{n+M} d_{n-m} \left[-\omega P_m(h) + U_x(h) \hat{P}_m(h) + n \frac{U_\theta(h)}{h} P_m(h) \right]. \quad (5.5.12)$$

Similarly, we find the boundary condition at $r = 1$ is given by

$$-\omega V_n(1) = \sum_{m=n-M}^{n+M} d_{n-m} \left[-\omega P_m(1) + U_x(1) \hat{P}_m(1) + n U_\theta(1) P_m(1) \right]. \quad (5.5.13)$$

Reducing to a finite system

Finally, we reduce our infinite system of differential equations to a finite system. To do this we set

$$U_n = V_n = W_n = P_n = 0 \text{ for } |n| > N. \quad (5.5.14)$$

To find the eigenmodes at a particular azimuthal number l , we solve the system (5.5.3) to (5.5.6) for all $n \in [-N, N]$. The boundary conditions we use are

$$\omega V_l(h) = \sum_{m=l-M}^{l+M} d_{l-m} \left[-\omega P_m(h) + U_x(h) \hat{P}_m(h) + l \frac{U_\theta(h)}{h} P_m(h) \right], \quad (5.5.15)$$

$$-\omega V_l(1) = \sum_{m=l-M}^{l+M} d_{l-m} \left[-\omega P_m(1) + U_x(1) \hat{P}_m(1) + l U_\theta(1) P_m(1) \right], \quad (5.5.16)$$

and for $n \neq l$,

$$\omega V_n(h) = \sum_{m=\max(n-M, -N)}^{\min(n+M, N)} d_{n-m} \left[-\omega P_m(h) + U_x(h) \hat{P}_m(h) + n \frac{U_\theta(h)}{h} P_m(h) \right] \text{ and } P_n(h) = 1. \quad (5.5.17)$$

Implementation

We are unable to implement this successfully with Chebfun. This is because Chebfun needs to check the linearity of the system before solving the different equation, which becomes exponentially more expensive as we increase the number of variables. Since our system has $10N + 5$ variables, this method becomes too expensive to implement.

5.6 Calculating the Green's function

We now discuss how to find the Green's function when the lining varies circumferentially. We only consider the contribution from the acoustic modes, since we saw in [Chapter 3](#) the contribution from the critical layer is generally small but very expensive to calculate.

Instead of finding G_ω , we again find \hat{p}_ω , which is defined by

$$\hat{p}_\omega(\mathbf{x}|\mathbf{x}_0) = \frac{1}{4\pi^2} \sum_{n=-\infty}^{\infty} e^{in(\theta-\theta_0)} \int_{\mathbb{R}} \hat{p}_n(r|r_0; \omega, k) e^{ik(x-x_0)} dk, \quad (5.6.1)$$

where

$$\hat{p}_n(r|r_0; \omega, k) = \frac{1}{r_0 \mathcal{W}_n(r_0, k)} \begin{cases} g_n^1(r_0; k) g_n^2(r; k) & r \leq r_0 \\ g_n^2(r_0; k) g_n^1(r; k) & r > r_0 \end{cases}, \quad (5.6.2)$$

so \hat{p}_n and G_n differ by a factor of $J(r_0, k)$. The total contribution from the acoustic eigenmodes is given by

$$\hat{p}_\omega^A(\mathbf{x}|\mathbf{x}_0) = \sum_{n=-\infty}^{\infty} e^{in(\theta-\theta_0)} \sum_{\mathcal{K}_n^\pm} \hat{p}_n^m(x, r|x_0, r_0), \quad (5.6.3)$$

where

$$\hat{p}_n^m(x, r|x_0, r_0) = \pm \frac{2\pi i}{4\pi^2} \frac{1}{r_0 \frac{\partial \mathcal{W}_n}{\partial k}(r_0, k_n^m)} e^{ik_n^m(x-x_0)} \begin{cases} g_n^1(r_0; k_n^m) g_n^2(r; k_n^m) & r \leq r_0 \\ g_n^2(r_0; k_n^m) g_n^1(r; k_n^m) & r > r_0 \end{cases}, \quad (5.6.4)$$

with the \pm from $x - x_0 > 0$ or $x - x_0 < 0$. The set \mathcal{K}_n^+ consists of all downstream acoustic modes and \mathcal{K}_n^- consists of all the upstream acoustic modes.

5.6.1 Asymptotic method

The contribution from each acoustic mode is given by

$$\hat{p}_n^m(x, r|x_0, r_0) = \pm \frac{2\pi i\omega}{4\pi^2} \left(\frac{\rho_0(r)r_0}{\rho_0(r_0)r} \right)^{1/2} \frac{\Phi_n(r, \kappa_n^m) e^{i\omega\kappa_n^m(x-x_0)}}{r_0 \frac{\partial \mathcal{V}_n}{\partial \kappa}(\kappa_n^m) \Phi_n(r_0, \kappa_n^m)} \begin{cases} v_n^1(r_0; \kappa_n^m) v_n^2(r; \kappa_n^m) & r \leq r_0 \\ v_n^2(r_0; \kappa_n^m) v_n^1(r; \kappa_n^m) & r > r_0 \end{cases}, \quad (5.6.5)$$

where $v_n^1(r; \kappa_n^m)$ and $v_n^2(r; \kappa_n^m)$ are determined in (5.3.11). It remains to calculate the derivative of the Wrońskiian. This is given by

$$\frac{\partial \mathcal{V}_n}{\partial \kappa}(\kappa_n^m) = \omega \left[\frac{\partial B_n^1}{\partial \kappa}(\kappa_n^m) - \frac{\partial B_n^h}{\partial \kappa}(\kappa_n^m) \right], \quad (5.6.6)$$

provided we scale the solutions $v_n^j(r; \kappa)$ in (5.3.11) by $1/(1+i)$ when $\kappa \in \mathcal{K}_n^C$.

We could calculate these derivatives analytically, by differentiating the expressions (5.4.15) and (5.4.22) with respect to κ , which would give expressions of the form

$$\hat{\Lambda}^h \frac{\partial \mathbf{B}^h}{\partial \kappa} = \hat{\mu}^h \text{ and } \hat{\Lambda}^1 \frac{\partial \mathbf{B}^1}{\partial \kappa} = \hat{\mu}^1. \quad (5.6.7)$$

We would then solve these equations when $\kappa = \kappa_n^m$ to determine the derivatives to use in (5.6.6).

However, the analytical expressions for $\hat{\Lambda}^j$ and $\hat{\mu}^j$ would be so complicated that we may as well calculate the derivatives of \mathbf{B}^j numerically. For a particular eigenmode κ_n^m we solve the systems

$$\Lambda^h(\kappa_n^m + \varepsilon) \mathbf{B}^h = \boldsymbol{\mu}^h(\kappa_n^m + \varepsilon) \text{ and } \Lambda^1(\kappa_n^m + \varepsilon) \mathbf{B}^1 = \boldsymbol{\mu}^1(\kappa_n^m + \varepsilon) \quad (5.6.8)$$

to determine $B_n^h(\kappa_n^m + \varepsilon)$ and $B_n^1(\kappa_n^m + \varepsilon)$. The numerical derivatives are then given by

$$\frac{\partial B_n^1}{\partial \kappa}(\kappa_n^m) = \lim_{\varepsilon \rightarrow 0} \frac{B_n^1(\kappa_n^m + \varepsilon) - B_n^1(\kappa_n^m)}{\varepsilon} \text{ and } \frac{\partial B_n^h}{\partial \kappa}(\kappa_n^m) = \lim_{\varepsilon \rightarrow 0} \frac{B_n^h(\kappa_n^m + \varepsilon) - B_n^h(\kappa_n^m)}{\varepsilon}. \quad (5.6.9)$$

5.6.2 Numerical method

Since we are unable to find the eigenmodes numerically, we are not able to calculate the Green's function numerically. However, if we were able to calculate the eigenmodes and eigenfunctions numerically then we can use exactly the same method from Section 3.5.1 to calculate the Green's function.

5.7 Results

We only consider results when the impedance of the lining is smooth, and we choose an impedance function of the form

$$Z^\varsigma(\theta) = 1 - 2i(\varsigma \sin(2\theta) + 2), \quad (5.7.1)$$

for different values of ς . When $\varsigma = 0$ this corresponds to a constant impedance of $Z = 1 - 4i$. When $\varsigma = 1$ this corresponds to an impedance oscillating between $Z = 1 - 2i$ and $Z = 1 - 6i$. We see the different values of ς we choose in [Figure 5.5b](#).

The reason for not considering splices is that if we take sufficiently many terms in the Fourier series of the impedance to be accurate (large M), then we get large, badly conditioned matrices \mathbf{B}^j . When we then solve $\Lambda^1 \mathbf{B}^1 = \boldsymbol{\mu}^1$, we are unable to get a solution because of the badly conditioned matrix \mathbf{B}^1 .

We consider the flow $U_x(r) = 0.2 + 0.4r^2$ and $U_\theta(r) = 0.1r + 0.2/r$, which we plot in [Figure 5.4](#). We additionally set $h = 0.6$, $\omega = 25$ and $\theta_0 = 0$. We consider two different values of n , $n = 16$ and $n = -25$. The regions \mathcal{K}_n were plotted in [Figure 5.3](#).

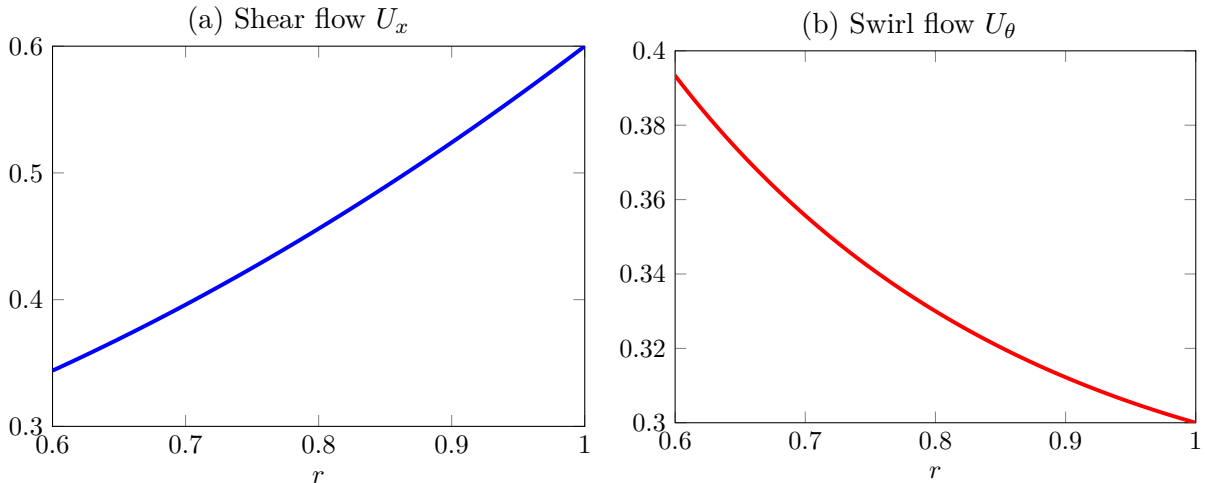


Figure 5.4: Plot of shear flow $U_x(r) = 0.2 + 0.4r^2$ and swirl $U_\theta(r) = 0.1r + 0.2/r$.

5.7.1 $n = 16$

In [Figure 5.5](#) we plot the eigenmodes when $n = 16$. We first note that we do not find all of the asymptotic eigenmodes. We are unable to find the asymptotic eigenmode associated with the numerical eigenmode $k = -9.21 - 28.14i$ for all values of ς . The reason for this is due to the implementation of the branch cut of the $2/3$ root of τ_n , which we chose in [Figure 3.1](#). If we vary this branch cut as we search for the eigenmodes then we would be able to find all of the eigenmodes, although this would be very difficult to implement automatically.

For the rest of the numerical eigenmodes we find the asymptotic eigenmodes for each value of ς . We find that the asymptotic eigenmodes when $Z = 1 - 4i$ (blue) are very accurate compared to the numerical eigenmodes, except at the second upstream cut-off mode where the asymptotic mode is a small distance away from the numerical mode. For most of the cut-off modes in [Figure 5.5a](#) we find as the impedance of the lining varies more (increasing ς), then the cut-off modes shift left. However, some cut-off modes with smaller imaginary part instead shift right. For the cut-on eigenmodes, the downstream cut-on asymptotic

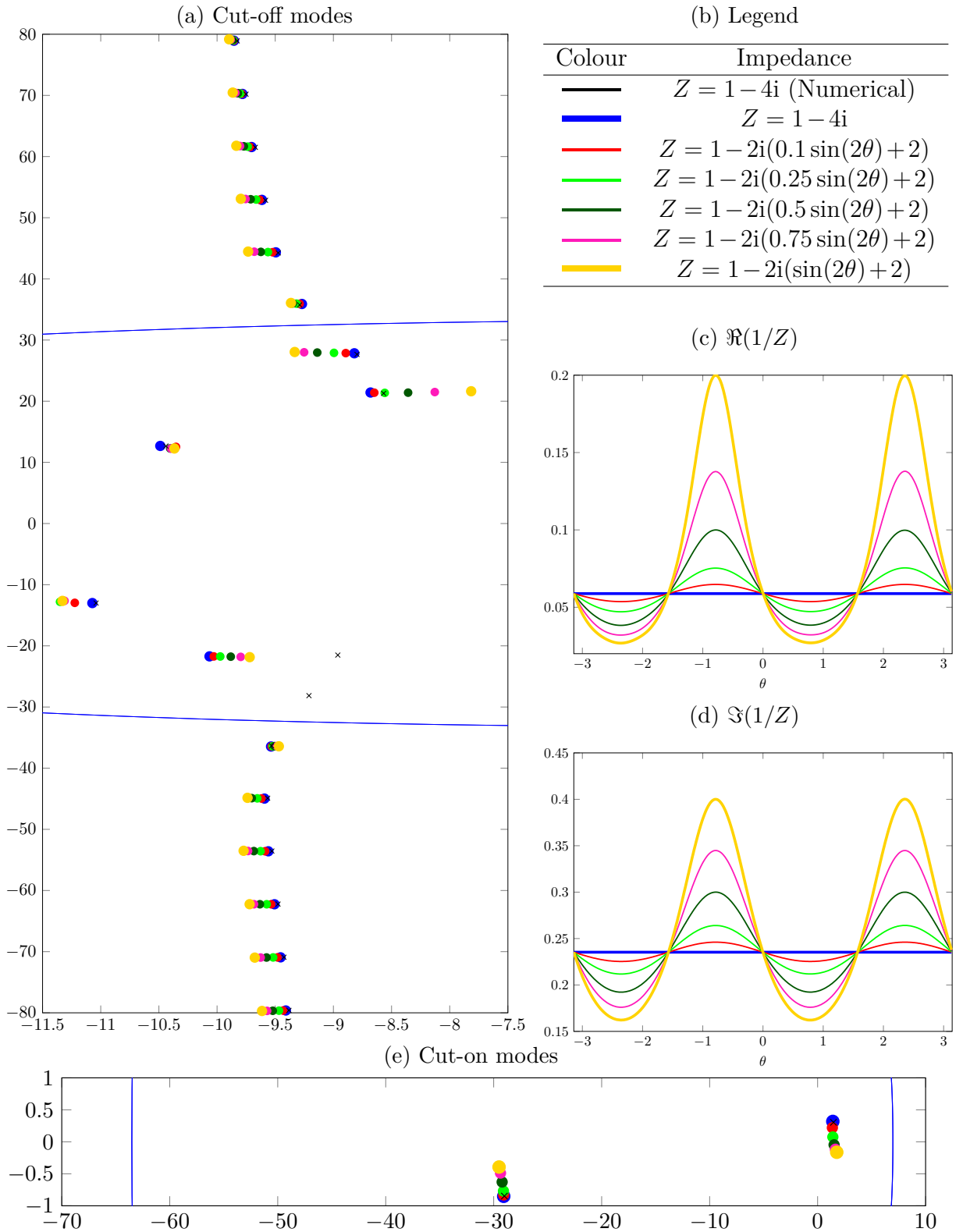


Figure 5.5: **Eigenmodes as lining varies circumferentially, $n = 16$.** We plot how the asymptotic eigenmodes vary as we consider different impedance functions, given in Figure 5.5b. We plot both the cut-on and cut-off modes. We plot the numerical eigenmodes when $Z = 1 - 4i$ with black crosses. The mean flow is given in Figure 5.4 and the other parameters are $\omega = 25$, $n = 16$, $h = 0.6$ and $\theta_0 = 0$.

mode moves down, crossing the real axis when $\varsigma \approx 0.6$. The upstream cut-on mode moves up, although it does not cross the real axis (yet). We see a close up of these trajectories in Figure 5.6, as is a close up on the first downstream cut-off mode. Unlike the rest of the cut-off modes (except the first upstream cut-off mode), this mode does not just move right or left as we vary the impedance, but moves in a complex way, in a backwards “s”. In Figure 5.6 we also plot in grey extra eigenmodes, which are for impedances Z^ς where ς takes the midpoint of the two values of ς of the coloured eigenmodes.

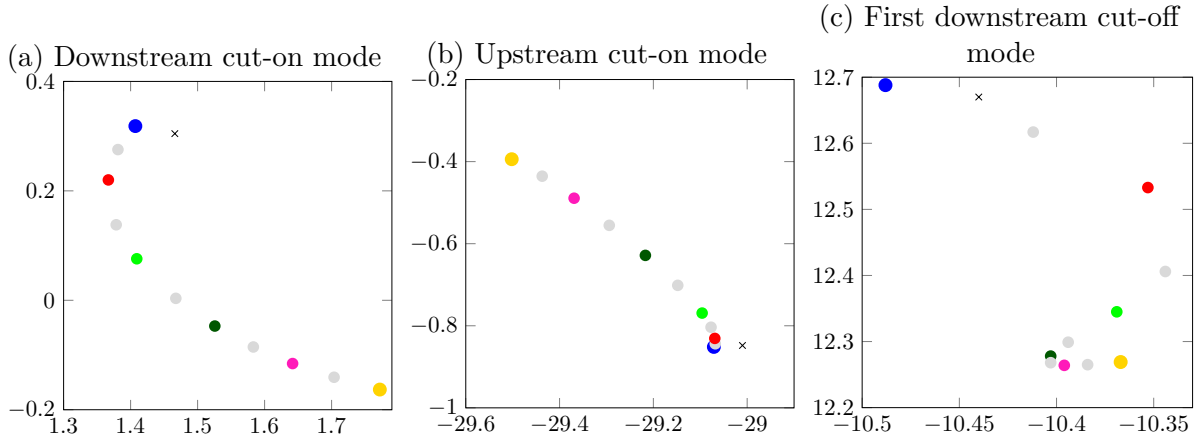


Figure 5.6: Close up of trajectories of eigenmodes from Figure 5.5 as we vary the impedance function Z^ς .

Next, we consider the Green’s function for each eigenmode as we vary the impedance function Z^ς . We consider a source at $x - x_0 = 0.5$ and $r_0 = 0.8$, so we only need to consider downstream eigenmodes, since we are unable to find all the upstream asymptotic eigenmodes. We assume the contribution of the critical layer is small enough to ignore.

In Figure 5.7 we plot the Green’s function contribution from each asymptotic eigenmode. The solid lines correspond to the real part of the Green’s function and the dotted lines to the imaginary part, while the colours of the lines correspond to the impedances in Figure 5.5b. In Figure 5.7a we see the dominant contribution to the Green’s function from the most cut-on eigenmode, given numerically when $Z = 1 - 4i$ by $k = 1.466 + 0.305i$. The contribution to the Green’s function from the other eigenmodes are several orders of magnitude smaller than this mode. In Figure 5.7 we see that the main effect of the impedance varying circumferentially is to change the amplitude of the Green’s function rather than change the shape.

In Figure 5.7a we see that varying the impedance changes the amplitude of the Green’s function for this mode significantly, and hence the total Green’s function. The imaginary part of the Green’s function slowly reduces in amplitude as we increase ς , and when $\varsigma = 1$ it is close to zero. As we increase ς , the amplitude of the real part of the Green’s function oscillates. At first it increases, and then starts to decrease once the imaginary part of the eigenmode turns negative. In Figure 5.7b we see the Green’s function contribution from the first cut-off downstream mode. As we increase ς , the amplitude of the imaginary part significantly reduces, in a similar way to the cut-on mode. When $\varsigma = 1$ the amplitude is around 1/100th of the amplitude compared to a constant impedance. Meanwhile,

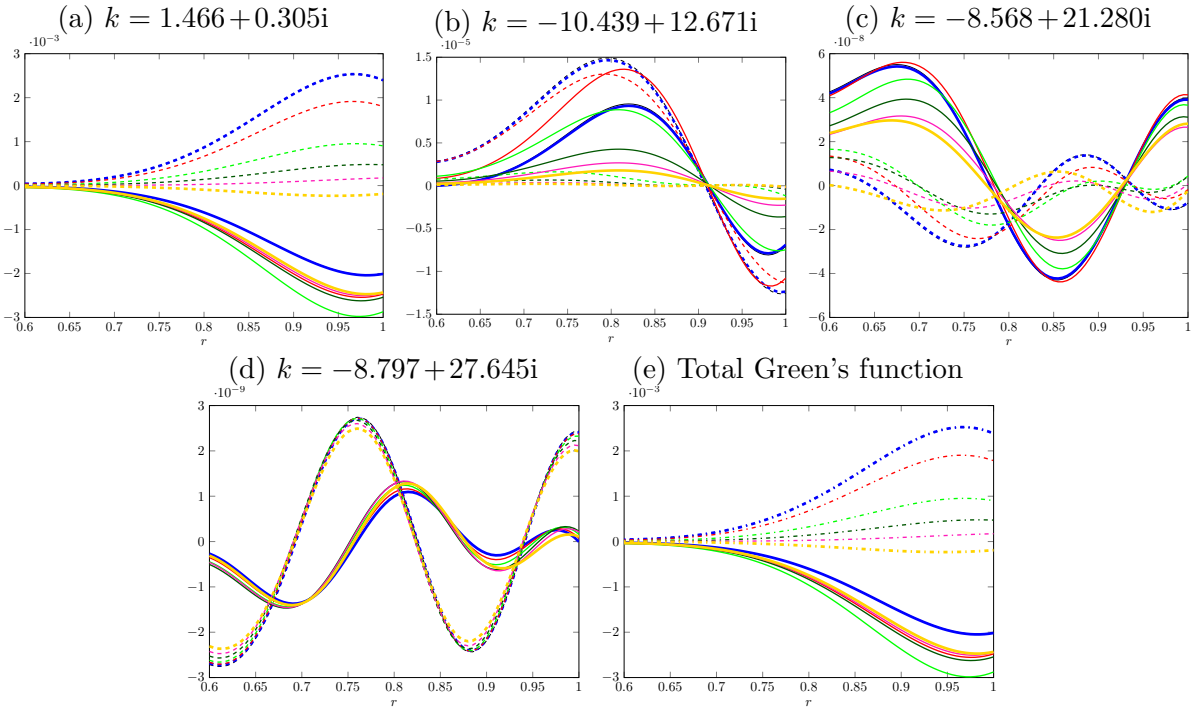


Figure 5.7: **Asymptotic Green's function for each mode as the impedance function varies when $n = 16$ with $x - x_0 = 0.5$ and $r_0 = 0.8$.** Solid lines correspond to the real part of the Green's function; dotted lines the imaginary part. The value of k in each figure refers to the numerical eigenmode when $Z = 1 - 4i$. The numerical Green's function when $Z = 1 - 4i$ is in black. The colours of the lines correspond to the impedances in Figure 5.5b. The other parameters are given in Figure 5.5.

amplitude of the real part of the Green's function first increases, and then decreases, as the real part of the mode increases and then decreases.

The impedance has significantly less effect on the contribution to the Green's function from the next two cut-off eigenmodes. In Figure 5.7c the amplitude of the Green's function varies a little as we vary the impedance, but not by as much as Figures 5.7a and 5.7b. In Figure 5.7d we see that the Green's function contribution is pretty much unchanged by varying the lining.

5.7.2 $n = -25$

We now consider the same parameters as before, but with $n = -25$. In Figure 5.8 we plot the eigenmodes. We fail to calculate all the asymptotic eigenmodes when we consider the constant impedance $Z = 1 - 4i$, as we are unable to asymptotically find the third cut-on upstream mode, numerically given by $k = -34.89 - 0.62i$. This is again because of the implementation of the 2/3 root branch cut of τ_n . For the cut-off modes, we see that letting the impedance oscillate more (by increasing ς) causes the downstream modes to move right and the upstream modes to mostly move left. The first upstream and downstream cut-off modes move by significantly more than all the other cut-off modes as we vary the impedance function. We see that the rest of the downstream modes all move a similar amount to each other as we vary the impedance function, while the upstream cut-off modes move by less.

We find that the upstream cut-on modes are not affected much by the impedance

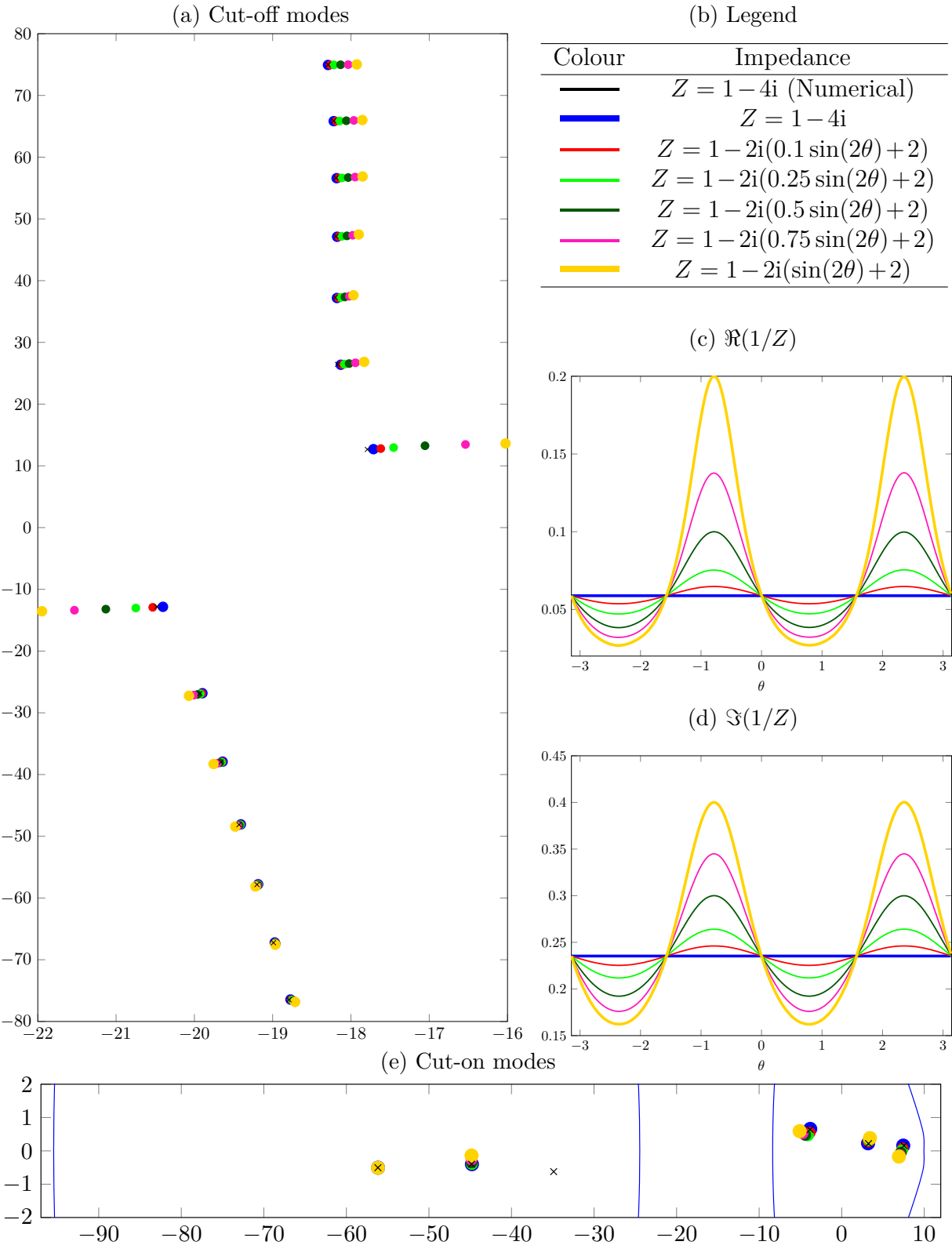
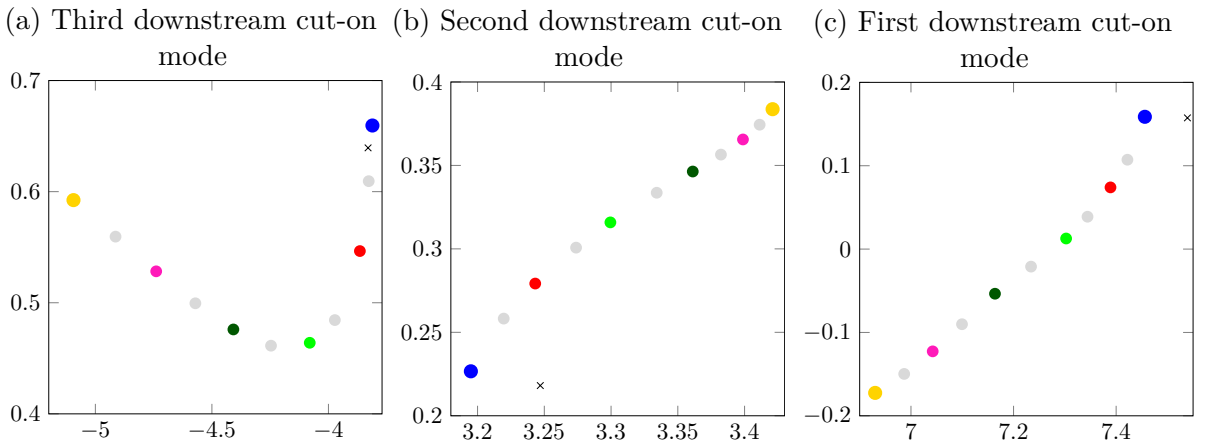


Figure 5.8: **Eigenmodes as lining varies circumferentially, $n = -25$.** We plot how the asymptotic eigenmodes vary as we consider different impedances functions, given in Figure 5.8b. We plot both the cut-on and cut-off modes. We plot the numerical eigenmodes when $Z = 1 - 4i$ with black crosses. The mean flow is given in Figure 5.4 and the other parameters are $\omega = 25$, $n = -25$, $h = 0.6$ and $\theta_0 = 0$.

varying circumferentially, with the first one (numerically given by $k = -56.18 - 0.51i$) barely moving. The second upstream mode moves up as we increase ς , like when $n = 16$, while we are unable to find the asymptotic eigenmode for the third upstream cut-on mode.

However, the downstream cut-on modes have more interesting behaviour, and we give a close up of the trajectories in [Figure 5.9](#). The first downstream mode ([Figure 5.9c](#)) moves down and crosses the real axis as we increase ς , like the previous example (although it moves left instead of right). The second downstream cut-on mode has completely the opposite behaviour, moving up and right as we increase ς . Instead of moving in a straight line, the third downstream cut-on mode moves in an arc, first moving down and left and then moving up and left. The real part of this mode also moves by significantly more than the other two downstream cut-on modes as we increase ς . In [Figure 5.9](#) we also plot in grey extra eigenmodes, which are for impedances Z^ς where ς takes the midpoint of the two values of ς of the coloured eigenmodes.



[Figure 5.9](#): Close up of trajectories of downstream eigenmodes from [Figure 5.8](#) as we vary the impedance function Z^ς .

We consider the Green's function in [Figure 5.10](#). The source is at $x - x_0 = 0.5$ and $r_0 = 0.8$ (and $\theta_0 = 0$), so we only consider downstream eigenmodes. We again ignore the contribution from the critical layer. From [Figure 5.10](#) it is clear that the main effect of an oscillating impedance is again to modify the amplitude of the Green's function rather than the shape.

In [Figure 5.10](#) we see that the Green's function contributions from the three cut-on modes all have a similar magnitude, with no dominant eigenmode. In [Figure 5.10a](#) we see the contribution from the first cut-on mode. The amplitude of both the real and imaginary part of the Green's function decrease a small amount as we increase ς . The imaginary part of the eigenmode passes through the real axis for $\varsigma \approx 0.32$, which causes the Green's functions to change shape. In [Figure 5.10b](#) we see the contribution from the second cut-on mode. As we increase ς , the amplitude of the real part slowly decreases. The amplitude of the imaginary part of the Green's function increases suddenly as the impedance starts oscillating, and then the imaginary part of the Green's function doesn't vary much more as we vary ς .

In [Figure 5.10c](#) we see that the amplitude of the Green's function smoothly varies as

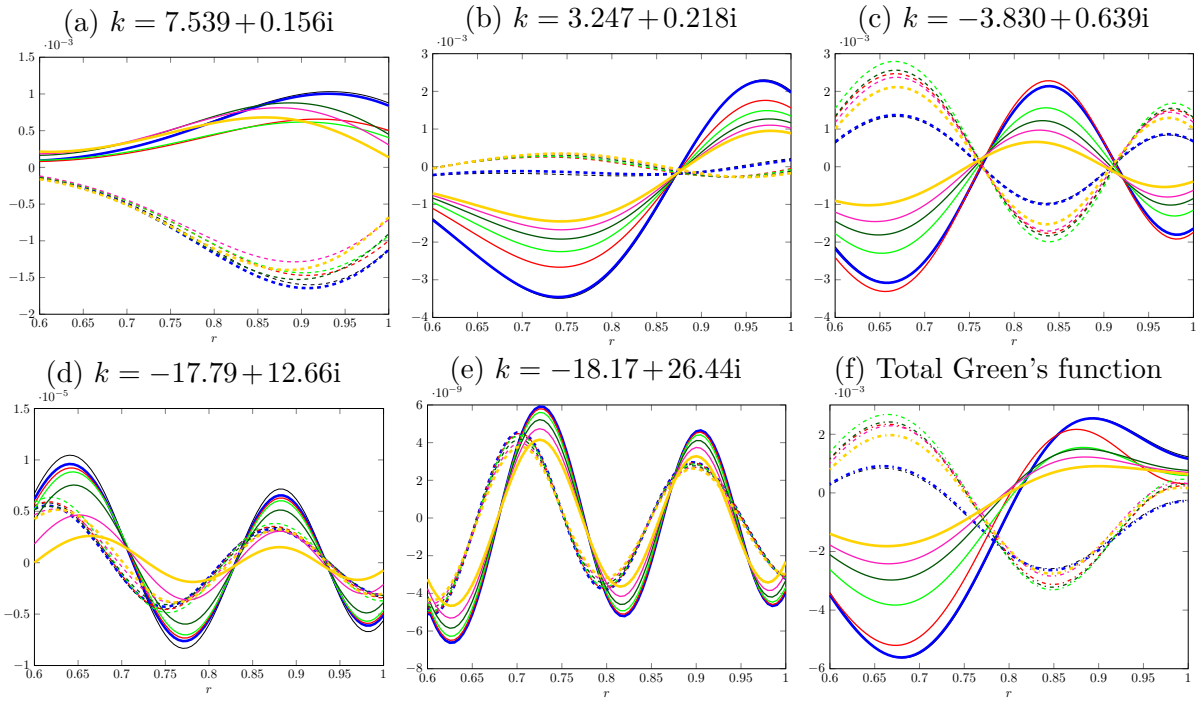


Figure 5.10: Asymptotic Green's function for each mode as the impedance function varies when $n = -25$ with $x - x_0 = 0.5$ and $r_0 = 0.8$.

Solid lines correspond to the real part of the Green's function; dotted lines the imaginary part. The value of k in each figure refers to the numerical eigenmode when $Z = 1 - 4i$. The numerical Green's function when $Z = 1 - 4i$ is in black. The colours of the lines correspond to the impedances in Figure 5.8b. The other parameters are given in Figure 5.8.

we vary the impedance function. For both the real and imaginary part of the Green's function, the amplitude initially increases before decreasing, corresponding roughly to when the imaginary part of the eigenmode is increasing and decreasing. In Figures 5.10d and 5.10e the Green's function contribution is several orders of magnitude smaller than the contribution from the cut-on modes. In Figure 5.10d the amplitude of the real part of the Green's function reduces quite significantly as we increase ζ , while the amplitude of the imaginary part is relatively unchanged. In Figure 5.10e we see that the effect of the impedance function is very limited, as we saw for the similarly cut-off mode in Figure 5.7d. In Figure 5.10f we plot the total Green's function, which varies significantly as ζ increases due to the cut-on eigenmodes moving significantly.

Chapter 6

Turbulence hitting an aerofoil with a serrated leading edge

In this chapter, we consider the effect of leading edge serrations on the noise from aerofoils. We model turbulence hitting a single aerofoil, with applications to the turbulent wake of the rotor hitting the stator. To do this, we use the Green's function and theory from Howe (1978), with synthetic turbulence given by Haeri et al. (2014). We derive results for the scattered pressure from the serrated aerofoil, for aerofoils at different angles of attack and when the turbulence consists of a number of eddies. We show that it is always possible to reduce the noise of an aerofoil by using a serrated leading edge compared to a straight leading edge, but the optimum choice very much depends on the turbulence. Additionally, the maximum amount of noise reduction varies. Our results are quite limited in scope due to the various approximations we make to calculate the Green's function, and are only valid in the far field, for turbulent sources close to the aerofoil, when the Mach number is small and the serrations are shallow.

In this study, we consider for the first time synthetic turbulence generated by eddies in Howe's model. We calculate the scattered pressure analytically, although we need to calculate one integral numerically. It is also the first time that multiple eddies interacting with each other in a non-linear way has been studied analytically. The majority of this chapter was presented at the 21st AIAA/CEAS Aeroacoustics Conference in Dallas (Mathews and Peake, 2015).

6.1 Howe's approach

We initially assume that the mean velocity flow is given by $(u_0, 0, 0)$. We consider an aerofoil of the form in Figure 1.9, and non-dimensionalise as in Section 1.2.2. The assumption that the aerofoil is infinite is valid providing the chord of the aerofoil is sufficiently large relative to the acoustic wavelength of the turbulence hitting it. We follow the derivation in Howe

([1991a](#)) to calculate the pressure. We write the pressure $p(\mathbf{x}, t)$ as

$$p(\mathbf{x}, t) = p_i(\mathbf{x}, t) + p_s(\mathbf{x}, t), \quad (6.1.1)$$

where $p_i(\mathbf{x}, t)$ is the incident pressure field that would be present without the aerofoil. The scattered pressure $p_s(\mathbf{x}, t)$ is the extra pressure due to reflections and diffractions of the pressure from the leading edge and the rest of the aerofoil.

Next, we introduce the Fourier transforms of pressure, $P_i(\mathbf{x}, \omega)$ and $P_s(\mathbf{x}, \omega)$, with

$$p_i(\mathbf{x}, t) = \int_{\mathbb{R}} P_i(\mathbf{x}, \omega) e^{-i\omega t} d\omega \text{ and } p_s(\mathbf{x}, t) = \int_{\mathbb{R}} P_s(\mathbf{x}, \omega) e^{-i\omega t} d\omega. \quad (6.1.2)$$

For flow with a low Mach number we find ([Howe, 1991a](#))

$$(\Delta + \omega^2)P_i = S_{\text{source}}(\mathbf{x}, \omega) \text{ and } (\Delta + \omega^2)P_s = 0, \quad (6.1.3)$$

since we ignore convection and scattering by the flow, and non-dimensionalise so that $c_0 = 1$. To derive the results in [\(6.1.3\)](#) we begin with the convected wave equation, and then use the Prandtl-Glauert transformation ([Chow and Kuethe, 1976](#)) and the assumption that the Mach number is small to get the wave equation. We then Fourier transform to get the Helmholtz equation. The source term S_{source} is given in [Howe \(1991a\)](#), but is not needed in our derivation.

We also have the boundary condition

$$\frac{\partial P_i}{\partial y} + \frac{\partial P_s}{\partial y} = 0 \quad (6.1.4)$$

on the aerofoil. This boundary condition follows from using the Euler equation and the no-slip and no-penetration velocity boundary conditions.

There are three ways described in [Howe \(1999\)](#) to solve the scattering problem and find P_s or the inverse Fourier transform of it, p_s . The first one involves the Weiner-Hopf procedure, the second involves Curle's representation of the pressure and the third involves using the Kirchhoff integral and a Green's function. We choose the latter.

The scattered pressure $P_s(\mathbf{x}, \omega)$ satisfies the Helmholtz equation everywhere. We introduce a Green's function $G(\mathbf{x}|\mathbf{x}_0; \omega)$ of the Helmholtz equation, satisfying

$$(\Delta + \omega^2)G(\mathbf{x}|\mathbf{x}_0; \omega) = \delta(\mathbf{x} - \mathbf{x}_0). \quad (6.1.5)$$

The Kirchhoff integral (essentially Green's second identity) then gives

$$P_s(\mathbf{x}, \omega) = \oint \left(G(\mathbf{x}|\mathbf{x}_0; \omega) \frac{\partial P_s}{\partial \mathbf{n}}(\mathbf{x}_0, \omega) - P_s(\mathbf{x}_0, \omega) \frac{\partial G}{\partial \mathbf{n}}(\mathbf{x}|\mathbf{x}_0; \omega) \right) dS(\mathbf{x}_0), \quad (6.1.6)$$

where \mathbf{n} is the normal to the aerofoil, pointing into the fluid. We choose a tailored Green's

function $G^{\mathcal{F}}$ of the Helmholtz equation, such that the normal derivative of the Green's function vanishes on the serrated aerofoil. We calculate this Green's function in [Section 6.2](#). The scattered pressure is then given by

$$\begin{aligned} P_s(\mathbf{x}, \omega) &= \oint G^{\mathcal{F}}(\mathbf{x}|\mathbf{x}_0; \omega) \frac{\partial P_s}{\partial \mathbf{n}}(\mathbf{x}_0, \omega) dS(\mathbf{x}_0), \\ &= - \oint G^{\mathcal{F}}(\mathbf{x}|\mathbf{x}_0; \omega) \frac{\partial P_i}{\partial \mathbf{n}}(\mathbf{x}_0, \omega) dS(\mathbf{x}_0), \\ &= - \int_{-\infty}^{\infty} \int_{\mathcal{F}(x)}^{\infty} \frac{\partial P_i}{\partial y}(x_0, 0, z_0, \omega) [G^{\mathcal{F}}(\mathbf{x}, \mathbf{x}_0; \omega)] dx_0 dz_0, \end{aligned} \quad (6.1.7)$$

where we used [\(6.1.4\)](#) and where

$$[G^{\mathcal{F}}(\mathbf{x}, \mathbf{x}_0; \omega)] = G^{\mathcal{F}}(\mathbf{x}, (x_0, +0, z_0); \omega) - G^{\mathcal{F}}(\mathbf{x}, (x_0, -0, z_0); \omega) \quad (6.1.8)$$

is the jump of the Green's function over the aerofoil. We introduce a change of variables, $x_1 = x_0 + \mathcal{F}(z_0)$, to make the integration region simpler. This then gives

$$P_s(\mathbf{x}, \omega) = - \int_{-\infty}^{\infty} \int_0^{\infty} \frac{\partial P_i}{\partial y}(x_1 + \mathcal{F}(z), 0, z_0, \omega) [G^{\mathcal{F}}(\mathbf{x}, (x_1 + \mathcal{F}(z_0), 0, z_0); \omega)] dx_1 dz_0. \quad (6.1.9)$$

6.2 Green's function for the Helmholtz equation tailored to an aerofoil with a serrated leading edge

In this section we find the Green's function of the Helmholtz equation in [\(6.1.5\)](#), but with boundary conditions tailored to our aerofoil, so that the normal derivative in [\(6.1.6\)](#) vanishes on the aerofoil. We begin by calculating the exact Green's function for an infinite half plane.

6.2.1 Infinite half plane

The Green's function $G(\mathbf{x}|\mathbf{x}_0)$ of the Helmholtz equation satisfies

$$\frac{\partial G^2}{\partial r^2} + \frac{1}{r} \frac{\partial G}{\partial r} + \frac{1}{r^2} \frac{\partial G^2}{\partial \theta^2} + \frac{\partial^2 G}{\partial z^2} + \omega^2 G = \frac{1}{r} \delta(r - r_0) \delta(\theta - \theta_0) \delta(z - z_0). \quad (6.2.1)$$

We look for a Green's function of the form

$$G(\mathbf{x}|\mathbf{x}_0) = \frac{1}{4\pi^2} \int_{\mathbb{R}} \sum_m a_m g_m(r|r_0) \cos \nu_m(\theta + \pi) \cos \nu_m(\theta_0 + \pi) e^{ik_z(z - z_0)} dk_z, \quad (6.2.2)$$

where a_m , g_m and ν_m are to be determined. We choose this form because a similar form to the integrand is given in [Duffy \(2001\)](#) as the Green's function for the Helmholtz equation on a wedge in two dimensions, where the normal derivative of the Green's function vanishes

at the boundary.

By substituting (6.2.2) into (6.2.1), we find that

$$g(r, \theta | r_0, \theta_0) = \frac{1}{2\pi} \sum_m a_m g_m(r | r_0) \cos \nu_m(\theta + \pi) \cos \nu_m(\theta_0 + \pi) \quad (6.2.3)$$

must satisfy

$$\frac{\partial g^2}{\partial r^2} + \frac{1}{r} \frac{\partial g}{\partial r} + \frac{1}{r^2} \frac{\partial g^2}{\partial \theta^2} + \gamma^2 g = \frac{1}{r} \delta(r - r_0) \delta(\theta - \theta_0), \quad (6.2.4)$$

where $\gamma(k_z) = \sqrt{\omega^2 - k_z^2}$. For the normal derivative to vanish, we require that

$$\frac{\partial g}{\partial \theta}(\theta = -\pi) = \frac{\partial g}{\partial \theta}(\theta = \pi) = 0, \quad (6.2.5)$$

since the top and bottom of the aerofoil are defined by $\theta = \pm\pi$. These boundary conditions are only satisfied if $\nu_m = m/2$. From [Duffy \(2001\)](#) we have

$$\delta(\theta - \theta_0) = \frac{1}{2\pi} + \frac{1}{\pi} \sum_{m=1}^{\infty} \cos\left(\frac{m}{2}(\theta + \pi)\right) \cos\left(\frac{m}{2}(\theta_0 + \pi)\right). \quad (6.2.6)$$

We use (6.2.6) and set $a_0 = 1$ and $a_m = 2$ for $m \geq 1$, which then gives an ordinary differential equation for $g_m(r | r_0)$. This is given by

$$\frac{d^2 g_m}{dr^2}(r | r_0) + \frac{1}{r} \frac{dg_m}{dr}(r | r_0) + \left(\gamma^2 - \frac{m^2}{4r^2} \right) g_m(r | r_0) = \frac{1}{r} \delta(r - r_0). \quad (6.2.7)$$

We can easily find the solution of this equation. We first find two solution $g_{m,1}(r)$ and $g_{m,2}(r)$ of the homogeneous equation and then use [Duffy \(2001\)](#) to calculate that

$$g_m(r | r_0) = \frac{1}{r_0 \mathcal{W}(r_0)} [g_{m,1}(r)g_{m,2}(r_0)H(r_0 - r) + g_{m,1}(r_0)g_{m,2}(r)H(r - r_0)], \quad (6.2.8)$$

where H is the Heaviside function and $\mathcal{W}(r)$ is the Wrońskián of $g_{m,1}(r)$ and $g_{m,2}(r)$. The solutions $g_{m,1}(r)$ and $g_{m,2}(r)$ to the homogeneous equation are a linear combination of Bessel and Hankel functions, with the exact choice depending on the boundary conditions. We apply the boundary conditions from [Howe \(1998\)](#), so we require $g_m(r)$ to be bounded as $r \rightarrow 0$ and behave like an outgoing wave as $r \rightarrow \infty$. This is achieved with $g_{m,1}(r) = J_{\nu_m}(\gamma r)$ and $g_{m,2}(r) = H_{\nu_m}^{(1)}(\gamma r)$.

To calculate the Wrońskián we use Abel's theorem ([Boyce et al., 1992](#)), and we find that $r\mathcal{W}(r)$ is constant. We then use the asymptotic behaviour of the Hankel and Bessel functions from [Bender and Orszag \(1978\)](#) to calculate the Wrońskián for a large argument r . We find that $\mathcal{W}(r_0) = 2i/(\pi r_0)$. Thus, we get a final result of

$$G(\mathbf{x} | \mathbf{x}_0) = -\frac{i}{8\pi} \int_{-\infty}^{\infty} \sum_{m=0}^{\infty} a_m \left[J_{\nu_m}(\gamma r) H_{\nu_m}^{(1)}(\gamma r_0) H(r_0 - r) + J_{\nu_m}(\gamma r_0) H_{\nu_m}^{(1)}(\gamma r) H(r - r_0) \right] \times \cos \nu_m(\theta + \pi) \cos \nu_m(\theta_0 + \pi) e^{ik_z(z - z_0)} dk_z, \quad (6.2.9)$$

where $\gamma = \gamma(k_z)$, which agrees with Howe (1998) once we correct a typo and account for the slightly different geometries of the aerofoil.

6.2.2 Far-field Green's function

We now consider the Green's function in the far field with $r \gg r_0$, which allows us to simplify the result in (6.2.9). For large r

$$H_\nu^{(1)}(\gamma r) \sim \sqrt{\frac{2}{\pi \gamma r}} e^{i\gamma r} e^{-i\pi/4} e^{-i\pi\nu/2}, \quad (6.2.10)$$

and so the Green's function becomes

$$G(\mathbf{x}|\mathbf{x}_0) \sim -\frac{i}{8\pi} \sum_{m=0}^{\infty} a_m \cos \nu_m(\theta + \pi) \cos \nu_m(\theta_0 + \pi) e^{-i\pi/4} e^{-i\pi m/4} \mathcal{G}_m(r|r_0), \quad (6.2.11)$$

where

$$\mathcal{G}_m(r|r_0) = \sqrt{\frac{2}{\pi r}} \int_{-\infty}^{\infty} J_{\nu_m}(\gamma(k_z)r_0)(\gamma(k_z))^{-1/2} e^{i\gamma(k_z)r} e^{ik_z(z-z_0)} dk_z. \quad (6.2.12)$$

We then approximate this integral by using the method of stationary phase (Bender and Orszag, 1978). We calculate that (Howe, 1998)

$$\mathcal{G}_m(r|r_0) \sim 2J_{\nu_m}(\omega r_0 \sin \iota) \frac{1}{|\mathbf{x} - \mathbf{e}_z z_0|} e^{i\omega|\mathbf{x} - \mathbf{e}_z z_0|} e^{-i\pi/4}, \quad (6.2.13)$$

where $\tan \iota = r/(z - z_0)$. Hence, the far-field Green's function is given by

$$G(r, \theta, z|r_0, \theta_0, z_0) \sim -\frac{1}{4\pi} \sum_{m=0}^{\infty} a_m \cos \nu_m(\theta + \pi) \cos \nu_m(\theta_0 + \pi) J_{\nu_m}(\omega r_0 \sin \iota) \frac{e^{i\omega|\mathbf{x} - \mathbf{e}_z z_0|}}{|\mathbf{x} - \mathbf{e}_z z_0|} e^{-i\pi m/4}. \quad (6.2.14)$$

Following Howe (1998), we assume that ωr_0 is small and then use the asymptotic behaviour of the Bessel function, with

$$J_{\nu_m}(\omega r_0 \sin \iota) \sim \frac{(\omega r_0 \sin \iota)^{\nu_m}}{2^{\nu_m} \Gamma(\nu_m + 1)}, \quad (6.2.15)$$

where Γ is the Gamma function. Hence, the terms in (6.2.14) get smaller as m increases so we only need to consider the first few terms, and we only consider the first two (as in Howe (1991a)), which we denote as ${}_0G$ and ${}_1G$. We calculate that

$${}_0G = -\frac{1}{4\pi|\mathbf{x} - \mathbf{e}_z z_0|} e^{i\omega|\mathbf{x} - \mathbf{e}_z z_0|} \text{ and } {}_1G = -\frac{1}{\pi\sqrt{2\pi}i} \frac{\sqrt{\omega}\sqrt{r} \sin(\theta/2)\sqrt{r_0} \sin(\theta_0/2)}{|\mathbf{x} - \mathbf{e}_z z_0|^{3/2}} e^{i\omega|\mathbf{x} - \mathbf{e}_z z_0|}, \quad (6.2.16)$$

which follows from using $|\mathbf{x} - \mathbf{e}_z z_0| \sin \iota = r$. We note that the jump of ${}_0G$, $[{}_0G]$, is zero

and hence we approximate the jump in the Green's function as

$$[G(\mathbf{x}, (x_1, 0, z_0); \omega)] \sim [{}_1 G] = -\frac{\sqrt{2}}{\pi \sqrt{\pi} i} \frac{\sqrt{\omega} \sqrt{r} \sin(\theta/2)}{|x - \mathbf{e}_z z_0|^{3/2}} e^{i\omega|x - \mathbf{e}_z z_0|} |x_1|^{1/2}. \quad (6.2.17)$$

The assumption that ωr_0 is small corresponds to assuming that the turbulent sources are close to the edge of the aerofoil.

6.2.3 Serrated aerofoil

For a serrated aerofoil, we consider the cylindrical coordinate system introduced in [Section 1.2.2](#), with the coordinates (r^*, θ^*, z^*) satisfying

$$(x, y, z) = (\mathcal{F}(z^*) - r^* \cos \theta^*, -r^* \sin \theta^*, z^*). \quad (6.2.18)$$

For the normal derivative of the Green's function $G^{\mathcal{F}}$ to vanish on the aerofoil, we now require

$$\frac{\partial G^{\mathcal{F}}}{\partial \theta^*}(\theta^* = -\pi) = \frac{\partial G^{\mathcal{F}}}{\partial \theta^*}(\theta^* = \pi) = 0. \quad (6.2.19)$$

In the new coordinate system the Helmholtz equation and Dirac delta become more complicated. We calculate that

$$\delta(\mathbf{x} - \mathbf{x}_0) = \frac{1}{r^* - \mathcal{F}'(z^*) \sin \theta^*} \delta(r^* - r_0^*) \delta(\theta^* - \theta_0^*) \delta(z^* - z_0^*), \quad (6.2.20)$$

and

$$\begin{aligned} \Delta G^{\mathcal{F}} &= \frac{\partial^2 G^{\mathcal{F}}}{\partial r^{*2}} \left[1 + (\mathcal{F}'(z^*) \sin \theta^*)^2 \right] + \frac{1}{r^*} \frac{\partial G^{\mathcal{F}}}{\partial r^*} \left[1 + \frac{1}{r^*} (\mathcal{F}'(z^*) \cos \theta^*)^2 \right] \\ &\quad + \frac{1}{r^{*2}} \frac{\partial^2 G^{\mathcal{F}}}{\partial \theta^{*2}} \left[1 + (\mathcal{F}'(z^*) \cos \theta^*)^2 \right] - \frac{\partial G^{\mathcal{F}}}{\partial \theta^*} \left[\frac{2}{r^{*2}} (\mathcal{F}'(z^*))^2 \sin \theta^* \cos \theta^* \right] \\ &\quad - \frac{\partial^2 G^{\mathcal{F}}}{\partial r^* \partial \theta^*} \left[\frac{1}{r^*} (\mathcal{F}'(z^*))^2 \sin \theta^* \cos \theta^* \right] + \frac{\partial^2 G^{\mathcal{F}}}{\partial z^{*2}}, \end{aligned} \quad (6.2.21)$$

which follows from using [\(6.2.18\)](#) and its inverse,

$$(r^*, \theta^*, z^*) = \left(\pm \left[r^2 + 2r\mathcal{F}(z) \cos \theta + \mathcal{F}^2(z) \right]^{1/2}, \arctan \left(\frac{r \sin \theta}{r \cos \theta + \mathcal{F}(z)} \right), z \right). \quad (6.2.22)$$

To make any progress finding the Green's function of the Helmholtz equation we assume that the serrations are shallow (called the slender body approximation in [Howe \(1991a\)](#)), so $|\mathcal{F}'(z)|$ is small. This allows us to make the approximation

$$\Delta G^{\mathcal{F}} \approx \frac{\partial^2 G^{\mathcal{F}}}{\partial r^{*2}} + \frac{1}{r^*} \frac{\partial G^{\mathcal{F}}}{\partial r^*} + \frac{1}{r^{*2}} \frac{\partial^2 G^{\mathcal{F}}}{\partial \theta^{*2}} + \frac{\partial^2 G^{\mathcal{F}}}{\partial z^{*2}}, \quad (6.2.23)$$

and hence the Green's function $G^{\mathcal{F}}$ for the Helmholtz equation is approximately the solution

to

$$\frac{\partial^2 G}{\partial r^{*2}} + \frac{1}{r^*} \frac{\partial G}{\partial r^*} + \frac{1}{r^{*2}} \frac{\partial^2 G}{\partial \theta^{*2}} + \frac{\partial^2 G}{\partial z^{*2}} + \omega^2 G = \frac{1}{r^*} \delta(r^* - r_0^*) \delta(\theta^* - \theta_0^*) \delta(z^* - z_0^*). \quad (6.2.24)$$

We solve this in a similar manner to [Section 6.2.1](#). We find that the exact solution to (6.2.24) is given by (6.2.9), but with the coordinates replaced by their starred versions. We then use the method of [Section 6.2.2](#) to calculate the far-field Green's function, which is given by

$$G^{\mathcal{F}}(\mathbf{x}|\mathbf{x}_0) \sim -\frac{1}{4\pi} \sum_{m=0}^{\infty} a_m \cos \nu_m(\theta^* + \pi) \cos \nu_m(\theta_0^* + \pi) J_{\nu_m}(\omega r_0^* \sin \iota^*) \frac{e^{i\omega|\mathbf{x}-\mathbf{z}_s|}}{|\mathbf{x}-\mathbf{z}_s|} e^{-i\pi m/4}, \quad (6.2.25)$$

where $\tan \iota^* = r^*/(z - z_0)$ and $\mathbf{z}_s = (\mathcal{F}(z_0), 0, z_0)$, so that $|\mathbf{x} - \mathbf{z}_s|^2 = r^{*2} + (z - z_0)$. We then again assume that ωr_0^* is small, so we only have to consider the first two terms in the series, and find that $[_0G^{\mathcal{F}}] = 0$. Thus, we find the jump in the Green's function is approximately given by

$$[G^{\mathcal{F}}(\mathbf{x}, (x_1 + \mathcal{F}(z_0), 0, z_0); \omega)] \sim -\frac{\sqrt{2}}{\pi \sqrt{\pi i}} \frac{\sqrt{\omega} \sqrt{r^*} \sin(\theta^*/2)}{|\mathbf{x} - \mathbf{z}_s|^{3/2}} e^{i\omega|\mathbf{x}-\mathbf{z}_s|} |x_1|^{1/2}. \quad (6.2.26)$$

In [Howe \(1991b\)](#) it is argued that we can extend the Green's function in (6.2.26) to aerofoils with non-shallow serrations, and that using the Green's function in (6.2.26) is expected to be an upper bound on the noise from the edge of the aerofoil. However, this relied on his form of the incident pressure, and was not shown rigorously.

6.2.4 Summary of approximations made

The approximations we used to derive the Green's function were a far-field approximation ($r \gg r_0$), turbulence sources are close to the aerofoil (ωr_0 is small), and that any serrations are shallow ($|\mathcal{F}'(z)|$ is small). Additionally, we assumed the Mach number was small, so that we only had to find the Green's function of the Helmholtz equation, and that the chord of the aerofoil was sufficiently large that we can approximate it by an infinite half plane. These approximations limit the usefulness and scope of the Green's function and subsequent results about scattered pressure, but our results are still useful in understanding the effect of serrated aerofoils analytically.

6.3 Synthetic turbulence

In [Sescu and Hixon \(2013\); Haeri et al. \(2014\)](#) the turbulence is modelled as a sum of synthetic eddies, where each eddy has different parameters and takes different “shapes”. The total velocity is given as the sum of a base flow \mathbf{u}_0 and a turbulent velocity \mathbf{u} . The

turbulent velocity is given as the curl of a vector Φ , so we have

$$\mathbf{u}_0(\mathbf{x}, t) = (u_0, 0, 0) \text{ and } \mathbf{u}(\mathbf{x}, t) = \nabla \times \Phi(\mathbf{x}, t). \quad (6.3.1)$$

In Haeri et al. (2014), Φ is given as a sum of eddies, with

$$\Phi(\mathbf{x}, t) = \sum_{l=1}^{N_e} (\Phi_{x,l}(\mathbf{x}, t) \mathbf{e}_x + \Phi_{y,l}(\mathbf{x}, t) \mathbf{e}_y + \Phi_{z,l}(\mathbf{x}, t) \mathbf{e}_z), \quad (6.3.2)$$

where $\Phi_{j,l}$ are shape functions with Gaussian or Mexican hat profiles acting on

$$R_{e,l}(\mathbf{x}, t) = (x - x_{e,l} - u_0 t)^2 + (y - y_{e,l})^2 + (z - z_{e,l})^2, \quad (6.3.3)$$

where $\mathbf{x}_{e,l} = (x_{e,l}, y_{e,l}, z_{e,l})$ denotes the source position of the l -th eddy. The number of eddies is given by N_e . We later choose the numerous parameters of the eddy stochastically. To calculate the pressure we use the momentum equation from the Euler equations;

$$\rho_0 \left(\frac{\partial \mathbf{u}}{\partial t} + \mathbf{u}_0 \cdot \nabla \mathbf{u} \right) + \nabla p = -\rho_0 \mathbf{u} \cdot \nabla \mathbf{u} - \rho \left(\frac{\partial \mathbf{u}}{\partial t} + \mathbf{u}_0 \cdot \nabla \mathbf{u} + \mathbf{u} \cdot \nabla \mathbf{u} \right), \quad (6.3.4)$$

where p and ρ are pressure and density perturbations to the constant pressure p_0 and constant density ρ_0 . Since Φ is a function of $R_{e,l}$ we necessarily have

$$\frac{\partial \mathbf{u}}{\partial t} + \mathbf{u}_0 \cdot \nabla \mathbf{u} = \mathbf{0}, \quad (6.3.5)$$

and hence to leading order $\nabla p = 0$, so the eddies do not create linear pressure perturbations. However, to second order we find

$$\frac{\partial p}{\partial y} = -\rho_0 \mathbf{u} \cdot \nabla v. \quad (6.3.6)$$

This non-linear form of the pressure perturbation leads to difficulties when we consider more than one eddy, since each eddy interacts with every other eddy.

6.4 Turbulence from a single eddy

We first consider a single eddy with a Gaussian profile, so we assume Φ is of the form

$$\Phi(\mathbf{x}, t) = A_1 e^{-B_1 R_e} \mathbf{e}_x + A_2 e^{-B_2 R_e} \mathbf{e}_y + A_3 e^{-B_3 R_e} \mathbf{e}_z, \quad (6.4.1)$$

with R_e given by (6.3.3). Since the total incident pressure p_i is given by $p_i = p + p_0$, with p_0 constant, then $\partial p_i / \partial y = \partial p / \partial y$. Inserting the definition of $\mathbf{u} = \nabla \times \Phi$ into (6.3.6) gives

$$\frac{\partial p}{\partial y} = -\rho_0 \left[\left(\frac{\partial \Phi_3}{\partial y} - \frac{\partial \Phi_2}{\partial z} \right) \left(\frac{\partial^2 \Phi_1}{\partial x \partial z} - \frac{\partial^2 \Phi_3}{\partial x^2} \right) + \left(\frac{\partial \Phi_1}{\partial z} - \frac{\partial \Phi_3}{\partial x} \right) \left(\frac{\partial^2 \Phi_1}{\partial z \partial y} - \frac{\partial^2 \Phi_3}{\partial x \partial y} \right) \right]$$

$$+ \left(\frac{\partial \Phi_2}{\partial x} - \frac{\partial \Phi_1}{\partial y} \right) \left(\frac{\partial^2 \Phi_1}{\partial z^2} - \frac{\partial^2 \Phi_3}{\partial x \partial z} \right) \Bigg]. \quad (6.4.2)$$

After inserting (6.4.1) into (6.4.2) we get

$$\frac{\partial p_i}{\partial y}(x, 0, z, t) = -4\rho_0 \left[(x - x_e - u_0 t) \beta_{12} e^{-\gamma_{12} R_e} + \beta_{23} (z - z_e) e^{-\gamma_{23} R_e} + \beta_{11} y_e e^{-\gamma_{11} R_e} + \beta_{33} y_e e^{-\gamma_{33} R_e} \right], \quad (6.4.3)$$

where $\beta_{jl} = A_j A_l B_j B_l$ and $\gamma_{jl} = B_j + B_l$. Next, we write

$$\exp(-\gamma_{jl} R_e) = \exp \left(-\gamma_{jl} u_0^2 \left(t - \frac{x - x_e}{u_0^2} \right) \right) \exp(-\gamma_{jl} (z - z_e)^2) \exp(-\gamma_{jl} y_e^2). \quad (6.4.4)$$

We then make use of the relations

$$\int_{\mathbb{R}} e^{-\gamma(t-\varsigma)^2} e^{i\omega t} dt = e^{i\omega\varsigma} e^{-\omega^2/4\gamma} \sqrt{\frac{\pi}{\gamma}}, \quad (6.4.5)$$

and

$$\int_{\mathbb{R}} t e^{-\gamma(t-\varsigma)^2} e^{i\omega t} dt = e^{i\omega\varsigma} e^{-\omega^2/4\gamma} \sqrt{\frac{\pi}{\gamma}} \left[\varsigma + \frac{i\omega}{2\gamma} \right], \quad (6.4.6)$$

where ς is arbitrary, to calculate the inverse Fourier transform of (6.4.3). We find that

$$\begin{aligned} \frac{\partial P_i}{\partial y}(x, 0, z, \omega) = & -\frac{2\rho_0}{u_0 \sqrt{\pi}} \left[\beta_{23} (z - z_e) \mathbb{E}_{\gamma_{23}}(\mathbf{x}, \omega) + \beta_{11} y_e \mathbb{E}_{\gamma_{11}}(\mathbf{x}, \omega) \right. \\ & \left. + \beta_{33} y_e \mathbb{E}_{\gamma_{33}}(\mathbf{x}, \omega) - \frac{i\omega}{2\gamma_{12} u_0} \beta_{12} \mathbb{E}_{\gamma_{12}}(\mathbf{x}, \omega) \right], \end{aligned} \quad (6.4.7)$$

where \mathbb{E}_{γ} is the product of exponential terms and is given by

$$\mathbb{E}_{\gamma}(\mathbf{x}, \omega) = \frac{1}{\sqrt{\gamma}} e^{-\gamma(z-z_e)^2} e^{-\gamma y_e^2} e^{i\omega(x-x_e)/u_0} e^{-\omega^2/(4\gamma u_0^2)}. \quad (6.4.8)$$

6.4.1 Calculation of scattered pressure

We now insert the incident pressure from a single eddy in (6.4.7) and the Green's function defined in (6.2.26) into the Kirchhoff integral in (6.1.9) to calculate the scattered pressure. This is given by

$$P_s^{\mathcal{F}}(\mathbf{x}, \omega) = A \sqrt{r^*} \sin \left(\frac{\theta^*}{2} \right) \int_{-\infty}^{\infty} \frac{e^{i\omega|\mathbf{x}-\mathbf{z}_s|}}{|\mathbf{x}-\mathbf{z}_s|^{3/2}} Q_1(z_0, \omega) dz_0, \quad (6.4.9)$$

where

$$A = -\frac{2\rho_0 \sqrt{2}}{\pi^2 \sqrt{\pi i}}, \quad (6.4.10)$$

and

$$Q_1(z_0, \omega) = -\frac{\pi \omega^{1/2}}{2\rho_0} \int_0^\infty x_1^{1/2} \frac{\partial P_i}{\partial y}(x_1 + \mathcal{F}(z_0), 0, z_0, \omega) dx_1. \quad (6.4.11)$$

Henceforth, we ignore the constant A since it is independent of the serration and the eddy. To calculate Q_1 analytically we use results from [Lighthill \(1958\)](#) to calculate integrals such as

$$\int_0^\infty x_1^{1/2} e^{i\omega x_1/u_0} dx_1 = \frac{\sqrt{\pi}}{2} \frac{u_0^{3/2}}{\omega^{3/2}}, \quad (6.4.12)$$

which we find by multiplying the integrand by $e^{-\varepsilon x_1}$ and then taking the limit as $\varepsilon \rightarrow 0$. If we define

$$Q_{\beta,\gamma}(z_0, \omega) = \frac{u_0^{1/2}}{2\omega} \frac{\beta\pi}{\sqrt{\gamma}} e^{3\pi i/4} e^{-\gamma y_e^2} e^{-\omega^2/(4\gamma u_0^2)} e^{-i\omega x_e/u_0} e^{-\gamma(z_0-z_e)^2} e^{i\omega \mathcal{F}(z_0)/u_0}, \quad (6.4.13)$$

we conclude that

$$\begin{aligned} Q_1(z_0, \omega) &= (z_0 - z_e) Q_{\beta_{23}, \gamma_{23}}(z_0, \omega) + y_e Q_{\beta_{11}, \gamma_{11}}(z_0, \omega) + y_e Q_{\beta_{33}, \gamma_{33}}(z_0, \omega) \\ &\quad - \frac{i\omega}{2\gamma_{12} u_0} Q_{\beta_{12}, \gamma_{12}}(z_0, \omega). \end{aligned} \quad (6.4.14)$$

We then calculate the integral with respect to z_0 in (6.4.9). This integral has terms of the form

$$\int_{-\infty}^\infty \exp\left(i\omega \left[r^*{}^2 + (z - z_0)^2\right]^{1/2}\right) \left[r^*{}^2 + (z - z_0)^2\right]^{-3/4} e^{-\gamma(z_0 - z_e)^2} e^{i\omega \mathcal{F}(z_0)/u_0} dz_0, \quad (6.4.15)$$

which we cannot analytically calculate. Instead, we perform the integration with respect to z_0 numerically, although we could make use of the techniques in [Bender and Orszag \(1978\)](#) to derive an analytical approximation to this integral.

In [Figures 6.1](#) and [6.2](#), we show some results of our calculations. We perform the

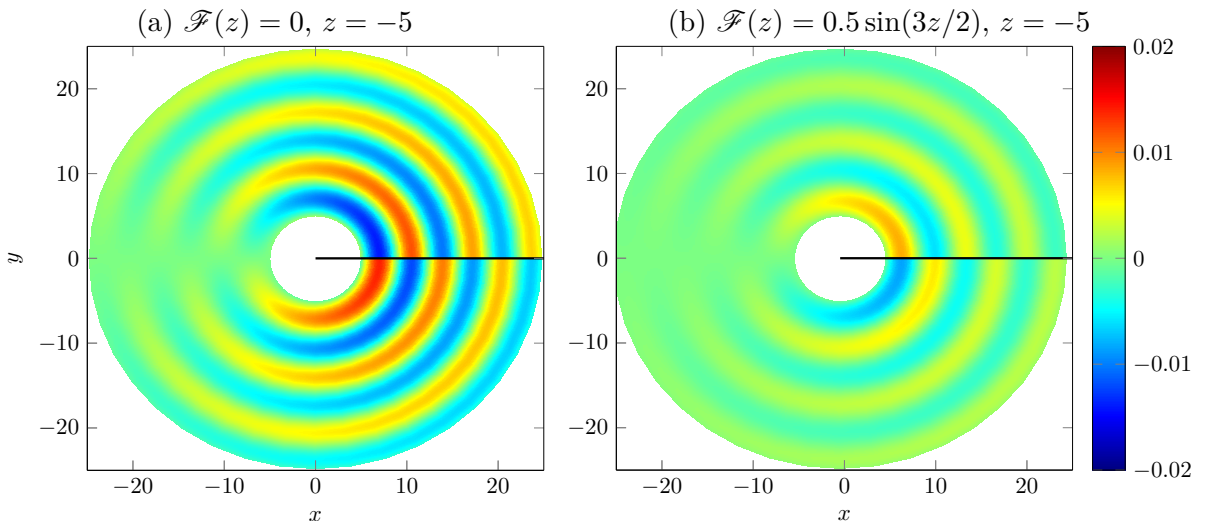


Figure 6.1: Plot of $\Re(P_s^{\mathcal{F}}(\mathbf{x}, \omega))$ for a straight and serrated edge at fixed $z = -5$. The parameters are $\omega = 1$, $u_0 = 0.25$ with eddy $\mathbf{A} = (1, 2, 1)$, $\mathbf{B} = (1, 1, 2)$ and $x_e = (0, 0, 0)$.

integration with respect to z_0 with a standard numerical solver and plot the real part of $P_s^{\mathcal{F}}$ for an eddy with source of $\mathbf{x}_e = (0, 0, 0)$. We set $u_0 = 0.25$, so that the Mach number is small, and additionally set $\omega = 1$. Since the eddy radius is close to the aerofoil, ωr_0 is still small. Our Green's function is only valid in the far field, so we choose to only plot the pressure for $5 < r < 25$. We plot different views in the figures; a slice in x - y space for Figure 6.1 and a projection onto the aerofoil in x - z space in Figure 6.2. From Figure 6.2 we could easily find the scattered pressure at other angles by multiplying the result by $\sin(\theta^*/2)$.

In both figures, the results are quite striking and look very hopeful. We see that moving from a straight edge to a leading edge serration of $\mathcal{F}(z) = 0.5 \sin(3z/2)$ reduces the scattered pressure considerably. The maximum serration we consider, $\mathcal{F}(z) = 0.5 \sin(3z/2)$, has $|\mathcal{F}'(z)| < 3/4$, so is still a shallow serration and our approximate Green's function is still valid. In Figure 6.2, we see that the optimum leading edge serration to minimise scattered pressure would be close to $\mathcal{F}(z) = 0.5 \sin(z)$, with larger serrations causing the scattered pressure to increase.

To get a global measure of the effect of a leading edge serration, we introduce the power of the scattered pressure, given by

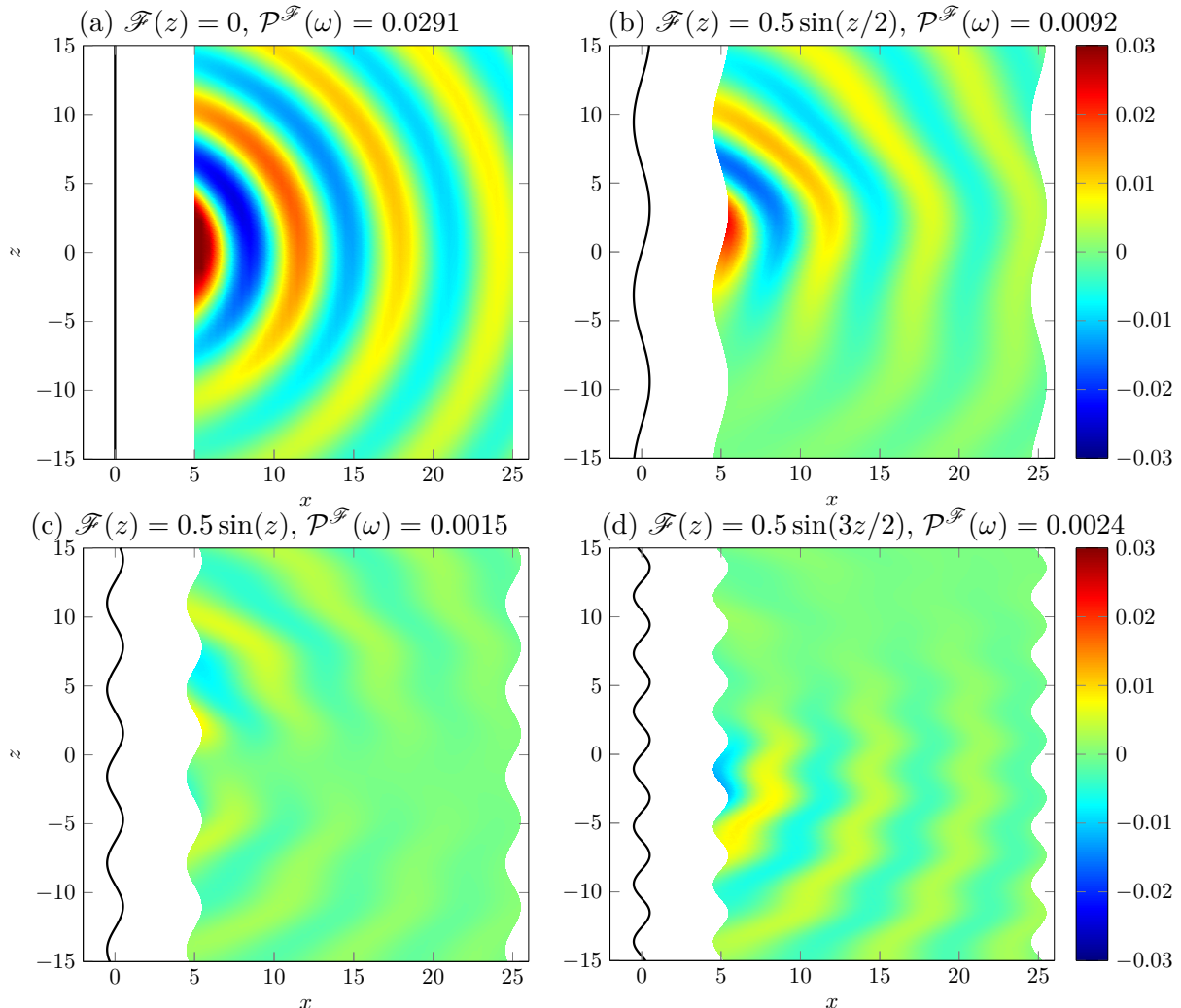


Figure 6.2: Plot of $\Re(P_s^{\mathcal{F}}(\mathbf{x}, \omega))$ for straight and serrated edges at fixed $\theta^* = \pi$. The parameters are $\omega = 1$, $u_0 = 0.25$ with eddy $\mathbf{A} = (1, 2, 1)$, $\mathbf{B} = (1, 1, 2)$ and $\mathbf{x}_e = (0, 0, 0)$.

$$\mathcal{P}^{\mathcal{F}}(\omega) = \iiint |P_s^{\mathcal{F}}(r^*, \theta^*, z^*, \omega)|^2 r^* d\theta^* dr^* dz. \quad (6.4.16)$$

We numerically calculate the r integration over the region shown in the figures, $5 < r < 25$, while the θ integration is easily calculated analytically between 0 and π and is independent of serration. We perform the z integration over a fixed region, given by $[-6\pi, 6\pi]$. We could instead integrate over a single wavelength, but this becomes ill-posed when the aerofoil has a straight leading edge (with infinite wavelength). Thus, we calculate

$$\mathcal{P}^{\mathcal{F}}(\omega) = \frac{1}{12\pi} \int_{-6\pi}^{6\pi} \int_5^{25} |P_s^{\mathcal{F}}(r^*, z, \omega)|^2 r^* dr^* dz. \quad (6.4.17)$$

We compute the power of the serrations in [Figure 6.2](#) and we see a noticeable reduction in the power of the scattered pressure as we reduce the wavelength of the serration, with the minimum power occurring for a leading edge serration close to $\mathcal{F}(z) = 0.5 \sin(z)$.

To measure the sound reduction of the serrated aerofoil at a particular frequency, we introduce

$$p_{\text{diff}}(\omega) = \log_{10} \left(\frac{\mathcal{P}^{\mathcal{F}}(\omega)}{\mathcal{P}^0(\omega)} \right) \text{ and } p_{\text{diff}}^\dagger(\omega) = 10 \log_{10} \left(\frac{\mathcal{P}^{\mathcal{F}}(\omega) + \mathcal{P}_i(\omega)}{\mathcal{P}^0(\omega) + \mathcal{P}_i(\omega)} \right), \quad (6.4.18)$$

where $\mathcal{P}_i(\omega)$ is the power from the incident pressure, calculated in an analogous way to [\(6.4.17\)](#). The actual sound reduction in Decibels is given by p_{diff}^\dagger , but we use p_{diff} as a proxy for the sound reduction. This is because calculating the incident pressure P_i is difficult, due to the source term S_{source} in [\(6.1.3\)](#).

6.4.2 Effect of the parameters

There are a lot of parameters to consider, with nine parameters for the eddy (amplitudes, Gaussian strengths and source position), two for the serration (wavelength, amplitude), the frequency and the velocity of the base flow.

Amplitude

First, we consider the effect of different amplitudes on the optimum serration. We choose a leading edge serration of $\mathcal{F}_\mu(z) = a \sin(\mu z)$, and vary a . In [Figure 6.3](#) we see the effect of the different amplitudes on p_{diff} as we reduce the wavelength (increase μ) of the serrations. We only plot the range of wavelengths such that $|\mathcal{F}'_\mu(z)| < 1$. The trend from the graph is that as we reduce the amplitude of the serration we reduce the effectiveness of the serrations. For serrations with amplitude $a = 4$, we reduce p_{diff} by around 2.5 with the optimum serration, while when $a = 1/5$ the maximum reduction in p_{diff} is about 0.1. Furthermore, as we reduce the amplitude, the wavelength of the optimum serration reduces monotonically to a limit of around 7.5 (corresponding to $\mu = 5/6$).

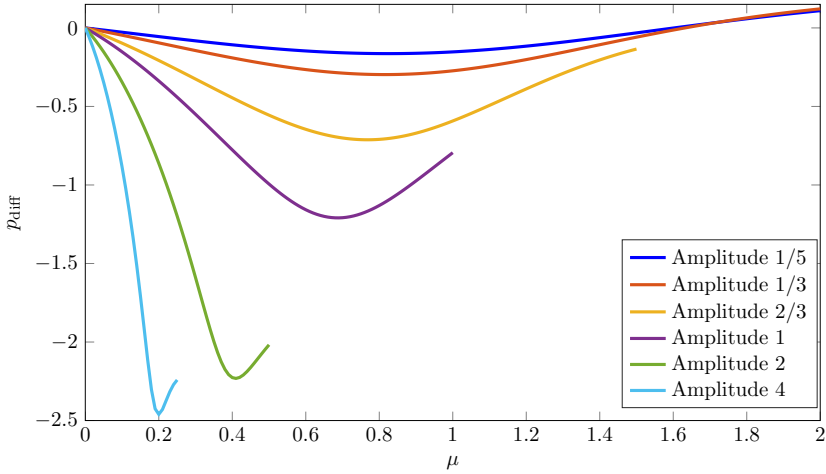


Figure 6.3: Plot of p_{diff} for serrations $\mathcal{F}_\mu(z) = a \sin(\mu z)$ as μ and a vary. The parameters are $\omega = 1$, $u_0 = 0.25$, $\mathbf{A} = (-1, 1, -2)$, $\mathbf{B} = (3, 1, 2)$ and $\mathbf{x}_e = (-3, 0, 1)$.

Frequency

We could also consider the effect of the frequency ω on the effectiveness of the serrations. To calculate the Green's function we assumed that ωr_0 was small, so we only had to take the first two terms in the sum for the Green's function. In Figures 6.1 and 6.2 we used $\omega = 1$, which is rather large. In Figure 6.4, we consider $\omega = 0.2$, and the rest of the parameters are the same as in Figures 6.1 and 6.2. We see that the serrations still reduce the noise by a significant amount.

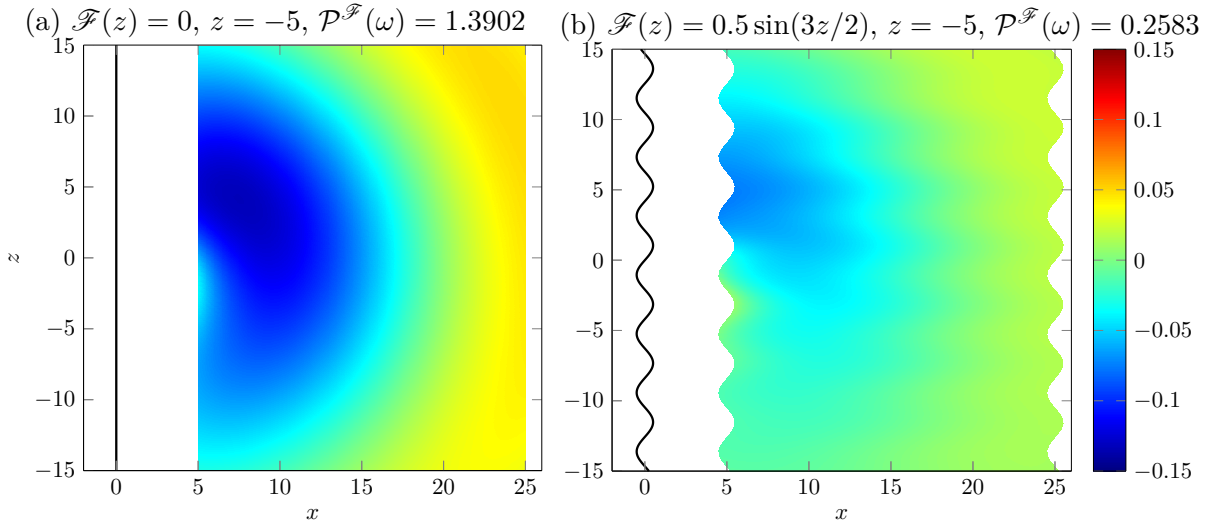


Figure 6.4: Plot of $\Re(P_s^{\mathcal{F}}(\mathbf{x}, \omega))$ for a straight and serrated edge at fixed $z = -5$. The parameters are $\omega = 0.2$, $u_0 = 0.25$ with eddy $\mathbf{A} = (1, 2, 1)$, $\mathbf{B} = (1, 1, 2)$ and $\mathbf{x}_e = (0, 0, 0)$.

Velocity

Some results with $u_0 = 0.5$ are given in Mathews and Peake (2015), but for this Mach number we really cannot ignore the convection of the flow as we did in Section 6.1.

Eddy and serration angles

We next investigate whether a leading edge serration always reduces the noise or whether it can actually increase the noise compared with a straight leading edge. What happens depends on the angle of the eddy in the x - z plane (which we calculate from the eddy amplitudes A_1 and A_3) and how this compares to the serration at z_0 . In Figure 6.5, we plot a straight edge and serrated edges of the form $\mathcal{F}(z) = \pm 0.5 \sin(z)$. We also plot the angle of the eddy in blue. In Figure 6.5c, we see that if the eddy and the serration are nearly parallel then we reduce the scattered pressure considerably compared to a straight edge. However, if the eddy and the serration are nearly perpendicular then we increase the noise compared with a straight leading edge, as we see in Figure 6.5a.

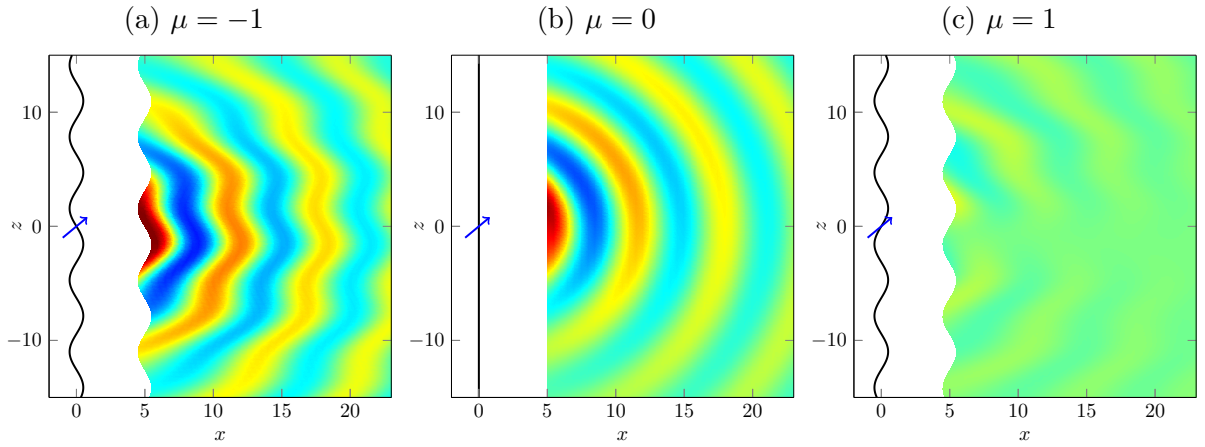


Figure 6.5: Effect of serrations of the form $\mathcal{F}_\mu(z) = 0.5 \sin(\mu z)$ on $\Re(P_s^{\mathcal{F}}(\mathbf{x}, \omega))$. The parameters are given by $\omega = 1$, $u_0 = 0.25$, $\mathbf{A} = (1, 2, 1)$, $\mathbf{B} = (1, 1, 2)$ and $\mathbf{x}_e = (0, 0, 0)$. The colour scale is the same on each plot.

In Figure 6.6 we plot p_{diff} against the angle of the serration (at $z = 0$) for a serration function $\mathcal{F}_\mu(z) = 0.5 \sin(\mu z)$. The angle of the serration (at $z = 0$) is given by $\angle \mathcal{F}_\mu = \arctan(0.5\mu)$. From the figure we clearly see that there are serration angles at which we reduce the noise compared to a straight edge but also angles where we increase the noise compared to a straight edge. From Figure 6.6 we see that the optimum angle (to reduce

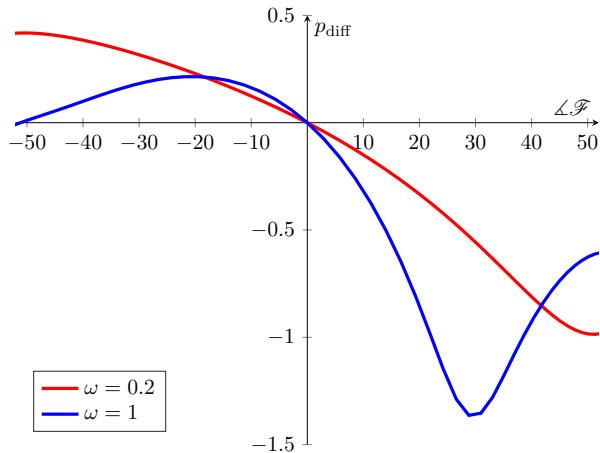


Figure 6.6: Plot of p_{diff} against serraton angle $\angle \mathcal{F}_\mu$ for $\mathcal{F}_\mu(z) = 0.5 \sin(\mu z)$. The eddy parameters are $\mathbf{A} = (1, 2, 1)$, $\mathbf{B} = (1, 1, 2)$ and $\mathbf{x}_e = (0, 0, 0)$. The other parameters are $u_0 = 0.25$ and $\omega = 1$ (blue), $\omega = 0.2$ (red).

noise) of the leading edge serration when $\omega = 1$ is around 29° , while the worst angle is at around -20° . When $\omega = 0.2$ the optimum angle of the serration is around 51° and the worst angle is at -50° . However, for $\omega = 0.2$ the optimum and worst serrations are not very shallow, so it is questionable whether these results are valid. When $\omega = 1$ we reduce p_{diff} by nearly 1.5 with the correct serration and increase it by 0.25 with the worst serration. For $\omega = 0.2$ the optimum serration is less effective at reducing noise compared to $\omega = 1$, while we increase the noise by more with the worst serration when $\omega = 0.2$ compared to $\omega = 1$. We also see that the optimum and worst serration are close to being symmetric, and they are also close to the eddy angle, 45° .

Other eddy parameters

We could also consider the effect of the other eddy parameters on the effectiveness of the leading edge serration, as in [Mathews and Peake \(2015\)](#). However, since we have no control over the eddy parameters to model realistic turbulence (since they are stochastic), we only consider different eddies when we study multiple, stochastic eddies in the next section.

6.5 Turbulence from multiple eddies

We now extend the results of [Section 6.4](#) to turbulence consisting of multiple eddies. We first consider the case of two eddies, and then extend the results to multiple eddies.

6.5.1 Two eddies

We seek to understand the effect of turbulence interacting with the leading edge when the turbulence consists of two eddies. Because of the form of the Euler equation in [\(6.3.6\)](#) we know that the two eddies interact with each other in a non-linear way. We assume both eddies have Gaussian profiles, since this is the case that has been mostly considered in literature. When the eddies have the same source position R_e , but different amplitudes and Gaussian strengths, we calculate the incident pressure relatively easily. When the eddies have different source positions, the interaction between the two eddies is more complicated, and calculating the incident pressure becomes harder.

Same source positions

We assume that the perturbation velocity is given by

$$\mathbf{u}(\mathbf{x}, t) = \nabla \times [\Phi(\mathbf{x}, t) + \Psi(\mathbf{x}, t)], \quad (6.5.1)$$

where

$$\Phi(\mathbf{x}, t) = A_1 e^{-B_1 R_e} \mathbf{e}_x + A_2 e^{-B_2 R_e} \mathbf{e}_y + A_3 e^{-B_3 R_e} \mathbf{e}_z, \quad (6.5.2)$$

and

$$\Psi(\mathbf{x}, t) = C_1 e^{-D_1 R_e} \mathbf{e}_x + C_2 e^{-D_2 R_e} \mathbf{e}_y + C_3 e^{-D_3 R_e} \mathbf{e}_z, \quad (6.5.3)$$

are the two eddies, with R_e defined in (6.3.3). We then perform a calculation similar to Section 6.4. We substitute (6.5.1) into (6.3.6) to calculate $\partial p_i / \partial y$ and Fourier transform to calculate the y derivative of P_i . Using the Kirchoff integral in (6.1.9) then gives

$$P_s^{\mathcal{F}}(\mathbf{x}, \omega) = A\sqrt{r^*} \sin\left(\frac{\theta^*}{2}\right) \int_{-\infty}^{\infty} \frac{e^{i\omega|\mathbf{x}-\mathbf{z}_s|}}{|\mathbf{x}-\mathbf{z}_s|^{3/2}} Q_2^S(z_0, \omega) dz_0, \quad (6.5.4)$$

where A is the constant given in (6.4.10) and Q_2^S is given by the lengthy formula

$$\begin{aligned} Q_2^S(z_0, \omega) = & (z_0 - z_e) Q_{\beta_{23}^{AB}, \gamma_{23}^B}(z_0, \omega) + y_e Q_{\beta_{11}^{AB}, \gamma_{11}^B}(z_0, \omega) + y_e Q_{\beta_{33}^{AB}, \gamma_{33}^B}(z_0, \omega) \\ & + (z_0 - z_e) Q_{\beta_{23}^{CD}, \gamma_{23}^D}(z_0, \omega) + y_e Q_{\beta_{11}^{CD}, \gamma_{11}^D}(z_0, \omega) + y_e Q_{\beta_{33}^{CD}, \gamma_{33}^D}(z_0, \omega) \\ & + (z_0 - z_e) Q_{\beta_{32}^{AD}, \gamma_{32}^{BD}}(z_0, \omega) + y_e Q_{\beta_{11}^{AD}, \gamma_{11}^{BD}}(z_0, \omega) + y_e Q_{\beta_{33}^{AD}, \gamma_{33}^{BD}}(z_0, \omega) \\ & + (z_0 - z_e) Q_{\beta_{23}^{AD}, \gamma_{23}^{BD}}(z_0, \omega) + y_e Q_{\beta_{11}^{AD}, \gamma_{11}^{BD}}(z_0, \omega) + y_e Q_{\beta_{33}^{AD}, \gamma_{33}^{BD}}(z_0, \omega) - \frac{i\omega}{2u_0} \times \\ & \left[\frac{1}{\gamma_{12}^B} Q_{\beta_{12}^{AB}, \gamma_{12}^B}(z_0, \omega) + \frac{1}{\gamma_{12}^D} Q_{\beta_{12}^{CD}, \gamma_{12}^D}(z_0, \omega) + \frac{1}{\gamma_{12}^{BD}} Q_{\beta_{12}^{AD}, \gamma_{12}^{BD}}(z_0, \omega) + \frac{1}{\gamma_{21}^{BD}} Q_{\beta_{21}^{AD}, \gamma_{21}^{BD}}(z_0, \omega) \right]. \end{aligned} \quad (6.5.5)$$

In (6.5.5), $Q_{\beta, \gamma}$ is still given by (6.4.13), but now the constants β_{jl} and γ_{jl} are given by

$$\beta_{jl}^{AB} = A_j B_j A_l B_l, \quad \beta_{jl}^{CD} = C_j D_j C_l D_l, \quad \beta_{jl}^{AD} = A_j B_j C_l D_l, \quad (6.5.6)$$

and

$$\gamma_{jl}^B = B_j + B_l, \quad \gamma_{jl}^D = D_j + D_l, \quad \gamma_{jl}^{BD} = B_j + D_l. \quad (6.5.7)$$

We have the relations $\beta_{jl}^{AB} = \beta_{lj}^{AB}$ and $\beta_{jl}^{AD} \neq \beta_{lj}^{AD}$, thus the third and fourth lines of Q_2^S are not the same. We next consider the more interesting (and realistic) case when the sources of the two eddies are different.

Different source positions

When the eddies have different source positions we have two different forms of R_e . Let us define them as

$$R_e^\Phi = (x - x_e^\Phi - u_0 t)^2 + (y - y_e^\Phi)^2 + (z - z_e^\Phi)^2 \text{ and } R_e^\Psi = (x - x_e^\Psi - u_0 t)^2 + (y - y_e^\Psi)^2 + (z - z_e^\Psi)^2, \quad (6.5.8)$$

where the eddy associated with Φ has source position $(x_e^\Phi, y_e^\Phi, z_e^\Phi)$ and similarly for Ψ . We define the displacement between the sources to be

$$\mathbf{d}^e = (d_x^e, d_y^e, d_z^e) = (x_e^\Phi - x_e^\Psi, y_e^\Phi - y_e^\Psi, z_e^\Phi - z_e^\Psi). \quad (6.5.9)$$

We calculate that the scattered pressure is of the form

$$P_s^{\mathcal{F}}(\mathbf{x}, \omega) = A\sqrt{r^*} \sin\left(\frac{\theta^*}{2}\right) \int_{-\infty}^{\infty} \frac{e^{i\omega|\mathbf{x}-\mathbf{z}_s|}}{|\mathbf{x}-\mathbf{z}_s|^{3/2}} Q_2^D(z_0, \omega) dz_0, \quad (6.5.10)$$

where the constant A is independent of the serration and given by (6.4.10).

To calculate the scattered pressure we use exactly the same method as in [Section 6.4](#). We define the terms

$$Q_{jl}^{\Phi}(z_0, \omega) = \frac{u_0^{1/2}}{2\omega} \frac{\beta_{jl}^{AB} \pi e^{3\pi i/4}}{\sqrt{\gamma_{jl}^B}} e^{-\gamma_{jl}^B y_e^{\Phi 2}} e^{-\omega^2/(4\gamma_{jl}^B u_0^2)} e^{-i\omega x_e^{\Phi}/u_0} e^{-\gamma_{jl}^B (z_0 - z_e^{\Phi})^2} e^{i\omega \mathcal{F}(z_0)/u_0}, \quad (6.5.11)$$

$$Q_{jl}^{\Psi}(z_0, \omega) = \frac{u_0^{1/2}}{2\omega} \frac{\beta_{jl}^{CD} \pi e^{3\pi i/4}}{\sqrt{\gamma_{jl}^D}} e^{-\gamma_{jl}^D y_e^{\Psi 2}} e^{-\omega^2/(4\gamma_{jl}^D u_0^2)} e^{-i\omega x_e^{\Psi}/u_0} e^{-\gamma_{jl}^D (z_0 - z_e^{\Psi})^2} e^{i\omega \mathcal{F}(z_0)/u_0}, \quad (6.5.12)$$

and

$$\begin{aligned} Q_{jl}^{\Phi, \Psi}(z_0, \omega) &= \frac{u_0^{1/2}}{2\omega} \frac{\beta_{jl}^{AD} \pi e^{3\pi i/4}}{\sqrt{\gamma_{jl}^{BD}}} e^{-B_j y_e^{\Phi 2} - D_l y_e^{\Psi 2}} e^{-\omega^2/(4\gamma_{jl}^{BD} u_0^2)} e^{-B_j (z_0 - z_e^{\Phi})^2 - D_l (z_0 - z_e^{\Psi})^2} e^{i\omega \mathcal{F}(z_0)/u_0} \\ &\times \exp\left(\frac{-i\omega}{u_0 \gamma_{jl}^{BD}} [B_j x_e^{\Phi} + D_l x_e^{\Psi}]\right) \exp\left(\frac{B_j D_l}{\gamma_{jl}^{BD}} [2x_e^{\Psi} x_e^{\Phi} - x_e^{\Psi 2} - x_e^{\Phi 2}]\right). \end{aligned} \quad (6.5.13)$$

We find that

$$Q_2^D(z_0, \omega) = Q_2^{D,1}(z_0, \omega) + 2Q_2^{D,2}(z_0, \omega), \quad (6.5.14)$$

where

$$\begin{aligned} Q_2^{D,1}(z_0, \omega) &= (z_0 - z_e^{\Phi}) Q_{23}^{\Phi}(z_0, \omega) + y_e^{\Phi} Q_{11}^{\Phi}(z_0, \omega) + y_e^{\Phi} Q_{33}^{\Phi}(z_0, \omega) - \frac{i\omega}{2\gamma_{12}^B u_0} Q_{12}^{\Phi}(z_0, \omega) \quad (6.5.15) \\ &+ (z_0 - z_e^{\Psi}) Q_{23}^{\Psi}(z_0, \omega) + y_e^{\Psi} Q_{11}^{\Psi}(z_0, \omega) + y_e^{\Psi} Q_{33}^{\Psi}(z_0, \omega) - \frac{i\omega}{2\gamma_{12}^D u_0} Q_{12}^{\Psi}(z_0, \omega) \\ &+ (z_0 - z_e^{\Psi}) Q_{32}^{\Phi, \Psi}(z_0, \omega) + (y_e^{\Phi} + y_e^{\Psi}) Q_{11}^{\Phi, \Psi}(z_0, \omega) + \left[-\frac{i\omega}{2\gamma_{12}^{BD} u_0} + \frac{d_x^e B_1}{\gamma_{12}^{BD}}\right] Q_{12}^{\Phi, \Psi}(z_0, \omega) \\ &+ (z_0 - z_e^{\Phi}) Q_{23}^{\Phi, \Psi}(z_0, \omega) + (y_e^{\Phi} + y_e^{\Psi}) Q_{33}^{\Phi, \Psi}(z_0, \omega) + \left[-\frac{i\omega}{2\gamma_{21}^{BD} u_0} - \frac{d_x^e D_1}{\gamma_{21}^{BD}}\right] Q_{21}^{\Phi, \Psi}(z_0, \omega), \end{aligned}$$

and the term $Q_2^{D,2}$ is given in (C.1.1) in [Appendix C.1](#). The integrals needed to calculate $Q_2^{D,j}$ are also given in [Appendix C.1](#). In the limit $\mathbf{d}^e \rightarrow 0$ we see that $Q_2^{D,2} \rightarrow 0$ and $Q_2^{D,1} \rightarrow Q_2^S$ and thus we recover the result in (6.5.4) for two eddies with the same source. The first two lines in (6.5.15) are the linear terms, which we get by adding the single eddy results for the eddies Φ and Ψ . The third and fourth lines are the quadratic terms, while the $Q_2^{D,2}$ term is a correction to the non-linear terms due to them having different sources.

6.5.2 Multiple eddies

It is clear that we can extend our approach for considering two eddies to N_e eddies, since we just need to deal with the cross terms between any two eddies, which consists of expressions similar to $Q_2^{D,2}$ in (C.1.1).

We find that

$$P_s^{\mathcal{F}}(\mathbf{x}, \omega) = A\sqrt{r^*} \sin\left(\frac{\theta^*}{2}\right) \int_{-\infty}^{\infty} \frac{e^{i\omega|\mathbf{x}-\mathbf{z}_s|}}{|\mathbf{x}-\mathbf{z}_s|^{3/2}} Q_{N_e}^D(z_0, \omega) dz_0, \quad (6.5.16)$$

where

$$Q_{N_e}^D(z_0, \omega) = Q_{N_e}^{D,1}(z_0, \omega) + 2Q_{N_e}^{D,2}(z_0, \omega). \quad (6.5.17)$$

For N_e eddies, the $Q_{N_e}^{D,1}$ term consists of N_e^2 lines of the form in (6.5.15), with one line for each eddy (N_e lines) and $N_e(N_e - 1)$ lines where the eddies interact with each other. The numbers of terms in the $Q_{N_e}^{D,2}$ term is $N_e(N_e - 1)/2$ times the number of terms in (C.1.1). For stochastic turbulence, we generate the amplitudes \mathbf{A} , Gaussian distributions \mathbf{B} and source positions \mathbf{x}_e of each eddy stochastically. We choose the simplest possible model, where we use a normal distribution (with zero mean and unit standard deviation) for the amplitudes and source positions, while we choose the Gaussian strengths of the eddies uniformly in [1, 5] to avoid them being zero.

In Figure 6.7 we randomly generate ten eddies, and each of the figures corresponds to a different random seed. The exact eddy parameters are detailed in Appendix C.2. For each different form of turbulence, we plot how p_{diff} varies with the serration $\mathcal{F}_\mu(z) = 0.5 \sin(\mu z)$. We see the effect of serrations very much depends on the form of the turbulence, and the key to understanding the effect of serrations is to model the turbulence accurately. For the turbulence in Figures 6.7b and 6.7e we see that a leading edge serration can only reduce p_{diff} by a tiny amount, around 0.1. In fact, nearly every serration we choose increases the noise compared to a straight leading edge, with p_{diff} as large as 0.9 in Figure 6.7b and as large as 1.7 in Figure 6.7e. In contrast, for the turbulence in Figure 6.7f, nearly every serration reduces the noise compared to a straight leading edge. We reduce p_{diff} by 0.8 with the optimum serration.

In the other figures, we can both increase and decrease the noise by using serrations. In Figure 6.7a the optimum serration (when $\mu \approx 1$) reduces p_{diff} by around 1, while the worst serration (when $\mu \approx -0.9$) increases p_{diff} by around 0.4. In Figure 6.7c we reduce p_{diff} by just over 0.1 with the optimum serration, but increase it by over 0.2 with the worst serration. In Figure 6.7d we see a reduction in p_{diff} of about 0.6 when we choose the optimum serration ($\mu \approx 1.7$), while we increase p_{diff} by about 0.25 when we choose the worst serration (when $\mu \approx -0.5$).

The synthetic turbulence we created was completely random, which would not be the case for real turbulence. For example, we should choose the parameters of the eddy so that the von Kármán energy spectrum (Wilson, 1998) is achieved. These parameters are given in Haeri et al. (2014); Gea-Aguilera et al. (2015), and we could use these to generate more realistic turbulence. With a more structured turbulence we would hope that the turbulence effects the optimum serration less.

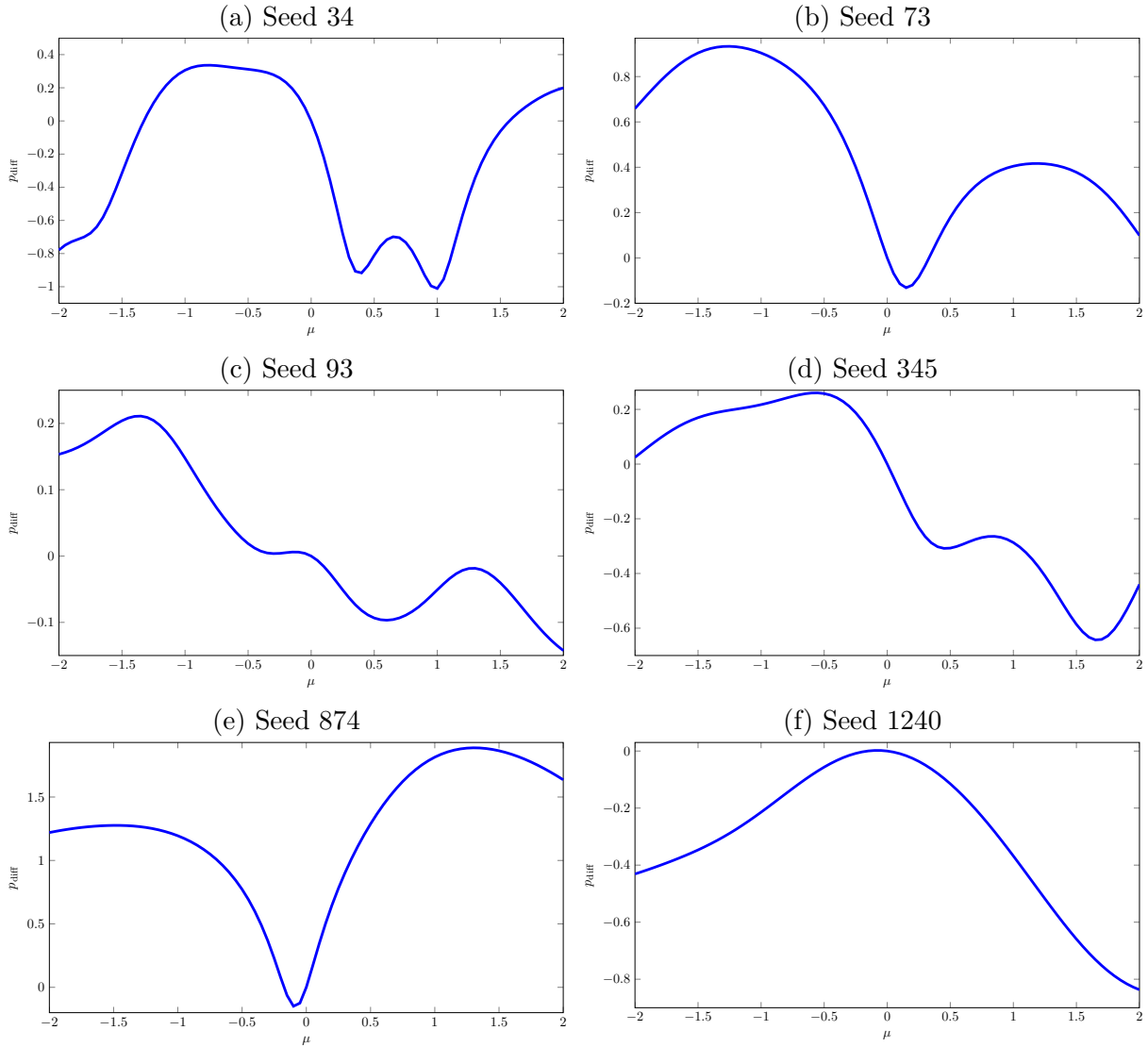


Figure 6.7: Plot of p_{diff} against serrations $\mathcal{F}_\mu(z) = 0.5 \sin(\mu z)$ as μ varies, for six randomly generated turbulence fields. The eddy parameters are given in [Appendix C.2](#). The other parameters are $\omega = 1$ and $u_0 = 0.25$.

6.6 Angle of attack

Our final consideration is a serrated aerofoil at a small angle of attack α . The geometry of the aerofoil is given in [Figure 1.9](#), and the coordinate system is given in [Section 1.2.2](#). The scattered pressure P_s still satisfies the Helmholtz equation in [\(6.1.3\)](#) since we are assuming a high Reynolds number and low Mach number. The normal to the aerofoil is now $\mathbf{n} = (\sin \alpha, \cos \alpha, 0)$ and hence

$$\frac{\partial P_i}{\partial \mathbf{n}}(\mathbf{x}_0, \omega) = \sin \alpha \frac{\partial P_i}{\partial x}(\mathbf{x}_0, \omega) + \cos \alpha \frac{\partial P_i}{\partial y}(\mathbf{x}_0, \omega). \quad (6.6.1)$$

Using the Kirchoff integral, we find that

$$P_s^{\mathcal{F},\alpha}(\mathbf{x}, \omega) = - \int_{-\infty}^{\infty} \int_0^{\infty} \left\{ \sin \alpha \frac{\partial P_i}{\partial x}(\mathbf{x}_1; \omega) + \cos \alpha \frac{\partial P_i}{\partial y}(\mathbf{x}_1; \omega) \right\} [G^{\mathcal{F},\alpha}(\mathbf{x}, \mathbf{x}_1; \omega)] dx_1 dz_0, \quad (6.6.2)$$

where

$$\mathbf{x}_1 = (x_1 + \mathcal{F}(z_0) \cos \alpha, -x_1 \tan \alpha - \mathcal{F}(z_0) \sin \alpha, z_0), \quad (6.6.3)$$

and $G^{\mathcal{F},\alpha}$ is the jump of the Green's function over the aerofoil at the angle of attack α .

6.6.1 Green's function at angle of attack

For a serrated leading edge, we calculate (using the same method as in [Section 6.2](#)) that the jump of the Green's function is approximately given by

$$[G^{\mathcal{F},\alpha}(\mathbf{x}, \mathbf{x}_1; \omega)] = - \frac{2\sqrt{\omega}}{\pi\sqrt{2\pi i}} \sqrt{r^*} \sin\left(\frac{\theta^*}{2} - \frac{\alpha}{2}\right) \frac{e^{i\omega|\mathbf{x}-\mathbf{z}_s|}}{|\mathbf{x}-\mathbf{z}_s|^{3/2}} (x_1 \sec \alpha)^{1/2}, \quad (6.6.4)$$

where $|\mathbf{x}-\mathbf{z}_s| = r^{*2} + (z - z_0)^2$. Compared to the Green's function at zero angle of attack, the coordinate system has changed, resulting in the $\sin(\theta^*/2)$ term now differing by a factor of $\alpha/2$ and an additional $\sec^{1/2} \alpha$ term.

6.6.2 Synthetic turbulence

We create the synthetic turbulence using one eddy with a Gaussian profile, in the same way as [Section 6.4](#). We define the eddy as

$$\Phi(\mathbf{x}, t) = A_1 e^{-B_1 R_e} \mathbf{e}_x + A_2 e^{-B_2 R_e} \mathbf{e}_y + A_3 e^{-B_3 R_e} \mathbf{e}_z, \quad (6.6.5)$$

and then the turbulent velocity is given by $\mathbf{u} = \nabla \times \Phi$. The mean flow for the incident pressure with no aerofoil present is still given by $(u_0, 0, 0)$. Using the Euler equation, we calculate

$$\frac{\partial p_i}{\partial x} = -\rho_0 \mathbf{u} \cdot \nabla u \text{ and } \frac{\partial p_i}{\partial y} = -\rho_0 \mathbf{u} \cdot \nabla v, \quad (6.6.6)$$

in a similar manner to [\(6.3.6\)](#). We then substitute in $\mathbf{u} = \nabla \times \Phi$, which gives [\(6.4.2\)](#) for $\partial p_i / \partial y$ and a similar result for $\partial p_i / \partial x$.

6.6.3 Calculating the scattered pressure

Using the same method as [Section 6.4](#) we calculate that

$$\begin{aligned} \frac{\partial P_i}{\partial y}(x, y, z; \omega) &= \frac{-2\rho_0}{u_0\sqrt{\pi}} \left[\beta_{23}(z - z_e) \mathbb{E}_{\gamma_{23}}^{AOA}(\mathbf{x}, \omega) + \beta_{11}(y_e - y) \mathbb{E}_{\gamma_{11}}^{AOA}(\mathbf{x}, \omega) \right. \\ &\quad \left. + \beta_{33}(y_e - y) \mathbb{E}_{\gamma_{33}}^{AOA}(\mathbf{x}, \omega) - \frac{i\omega}{2\gamma_{12}u_0} \beta_{12} \mathbb{E}_{\gamma_{12}}^{AOA}(\mathbf{x}, \omega) \right], \end{aligned} \quad (6.6.7)$$

and

$$\begin{aligned}\frac{\partial P_i}{\partial x}(x, y, z; \omega) = & \frac{-2\rho_0}{u_0\sqrt{\pi}} \left[\beta_{12}(y - y_e)\mathbb{E}_{\gamma_{12}}^{AOA}(\mathbf{x}, \omega) + \beta_{13}(z - z_e)\mathbb{E}_{\gamma_{13}}^{AOA}(\mathbf{x}, \omega) \right. \\ & \left. + \frac{i\omega}{2\gamma_{22}u_0}\beta_{22}\mathbb{E}_{\gamma_{22}}^{AOA}(\mathbf{x}, \omega) + \frac{i\omega}{2\gamma_{33}u_0}\beta_{33}\mathbb{E}_{\gamma_{33}}^{AOA}(\mathbf{x}, \omega) \right],\end{aligned}\quad (6.6.8)$$

where $\mathbb{E}_{\gamma}^{AOA}$ consists of various exponential terms and is given by

$$\mathbb{E}_{\gamma}^{AOA}(\mathbf{x}, \omega) = \frac{1}{\sqrt{\gamma}} e^{-\gamma(z-z_e)^2} e^{-\gamma(y-y_e)^2} e^{i\omega(x-x_e)/u_0} e^{-\omega^2/(4\gamma u_0^2)}. \quad (6.6.9)$$

Note that $\mathbb{E}_{\gamma}^{AOA}$ in (6.6.9) agrees with \mathbb{E}_{γ} in (6.4.8) when $y = 0$, i.e. at zero angle of attack.

The scattered pressure is then given by

$$P_s^{\mathcal{F}, \alpha}(\mathbf{x}, \omega) = A\sqrt{r^*} \sin\left(\frac{\theta^*}{2} - \frac{\alpha}{2}\right) \int_{-\infty}^{\infty} \frac{e^{i\omega|\mathbf{x}-\mathbf{z}_s|}}{|\mathbf{x}-\mathbf{z}_s|^{3/2}} Q_1^{\alpha}(z_0, \omega) dz_0, \quad (6.6.10)$$

where A is defined in (6.4.10). We find that

$$Q_1^{\alpha}(z_0, \omega) = \sin \alpha Q_1^{\alpha, x}(z_0, \omega) + \cos \alpha Q_1^{\alpha, y}(z_0, \omega), \quad (6.6.11)$$

where

$$Q_1^{\alpha, j}(z_0, \omega) = -\frac{\pi\omega^{1/2}}{2\rho_0} \int_0^{\infty} x_1^{1/2} \frac{\partial P_i}{\partial j}(x_1 + \mathcal{F}(z_0) \cos \alpha, -x_1 \tan \alpha - \mathcal{F}(z_0) \sin \alpha, z_0, \omega) dx_1, \quad (6.6.12)$$

so that $Q_1^0(z_0, \omega) = Q_1(z_0, \omega)$. Defining

$$Q_{\beta, \gamma}^{\alpha}(z_0, \omega) = \frac{\beta\sqrt{\pi}}{\sqrt{\gamma}u_0} e^{-\gamma y_e^2} e^{-\omega^2/(4\gamma u_0^2)} e^{-i\omega x_e/u_0} e^{-\gamma(z_0-z_e)^2} e^{i\omega \mathcal{F}(z_0) \cos \alpha/u_0}, \quad (6.6.13)$$

and

$$I_{\gamma}^{\alpha, l}(z_0, \omega) = \int_0^{\infty} x_1^l e^{i\omega x_1/u_0} \exp[-\gamma \tan^2 \alpha (x_1 + \mathcal{F}(z_0) \cos \alpha + y_e \cot \alpha)^2] dx_1, \quad (6.6.14)$$

then gives

$$\begin{aligned}Q_1^{\alpha, x}(z_0, \omega) = & (z_0 - z_e) Q_{\beta_{13}, \gamma_{13}}^{\alpha}(z_0, \omega) I_{\gamma_{13}}^{\alpha, 1/2}(z_0, \omega) + \frac{i\omega}{2\gamma_{22}u_0} Q_{\beta_{22}, \gamma_{22}}^{\alpha}(z_0, \omega) I_{\gamma_{22}}^{\alpha, 1/2}(z_0, \omega) \quad (6.6.15) \\ & + \frac{i\omega}{2\gamma_{33}u_0} Q_{\beta_{33}, \gamma_{33}}^{\alpha}(z_0, \omega) I_{\gamma_{33}}^{\alpha, 1/2}(z_0, \omega) - Q_{\beta_{12}, \gamma_{12}}^{\alpha}(z_0, \omega) J_{\gamma_{12}}^{\alpha}(z_0, \omega),\end{aligned}$$

and

$$\begin{aligned}Q_1^{\alpha, y}(z_0, \omega) = & (z_0 - z_e) Q_{\beta_{23}, \gamma_{23}}^{\alpha}(z_0, \omega) I_{\gamma_{23}}^{\alpha, 1/2}(z_0, \omega) - \frac{i\omega}{2\gamma_{12}u_0} Q_{\beta_{12}, \gamma_{12}}^{\alpha}(z_0, \omega) I_{\gamma_{12}}^{\alpha, 1/2}(z_0, \omega) \quad (6.6.16) \\ & + Q_{\beta_{11}, \gamma_{11}}^{\alpha}(z_0, \omega) J_{\gamma_{11}}^{\alpha}(z_0, \omega) + Q_{\beta_{33}, \gamma_{33}}^{\alpha}(z_0, \omega) J_{\gamma_{33}}^{\alpha}(z_0, \omega),\end{aligned}$$

where

$$J_\gamma^\alpha(z_0, \omega) = (y_e + \mathcal{F}(z_0) \sin \alpha) I_\gamma^{\alpha,1/2}(z_0, \omega) + I_\gamma^{\alpha,3/2}(z_0, \omega) \tan \alpha. \quad (6.6.17)$$

When we have no angle of attack

$$Q_{\beta,\gamma}^0 I_\gamma^{0,1/2} = Q_{\beta,\gamma} \text{ and } Q_{\beta,\gamma}^0 J_\gamma^0 = y_e Q_{\beta,\gamma}, \quad (6.6.18)$$

where $Q_{\beta,\gamma}$ is given in (6.4.13). We can calculate the integrals $I_\gamma^{\alpha,1/2}$ and $I_\gamma^{\alpha,3/2}$ analytically, and this is detailed in Appendix C.3. To calculate them analytically we no longer have to use the theory of generalised integrals (unless $\alpha = 0$), and we get results in term of modified Bessel functions.

6.6.4 Results

In Figure 6.8, we plot the scattered pressure for an aerofoil with a straight leading edge and a serrated leading edge $\mathcal{F}(z) = 0.5 \sin(z)$, at angle of attack $\alpha = 6^\circ$. The eddy parameters are given in Figure 6.8. We still see a noticeable reduction in the noise, and our serration still remains shallow (with $|\mathcal{F}'(z)| < 1/2$). By inserting (6.6.10) into (6.4.17) we calculate $\mathcal{P}^{\mathcal{F},\alpha}$, the power of the scattered pressure for a serration \mathcal{F} at angle of attack α .

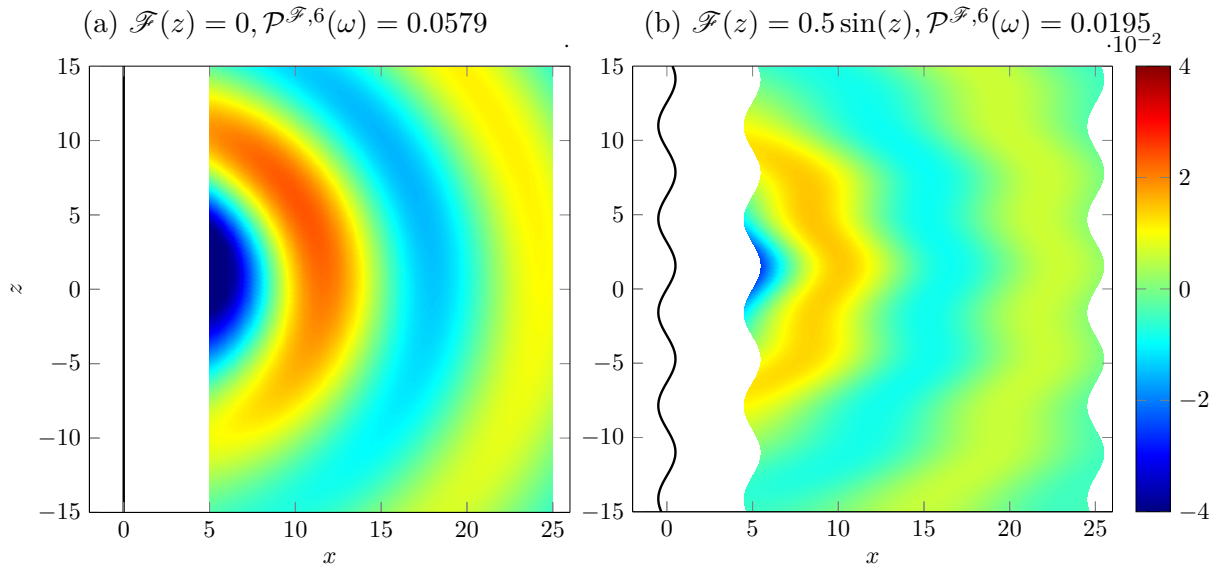


Figure 6.8: Plot of $\Re(P_s^{\mathcal{F},\alpha}(\mathbf{x}, \omega))$ for a straight edge and serrated edge at angle of attack $\alpha = 6^\circ$ and $\theta^* = \pi + \alpha$. The parameters are $\omega = 0.5$, $u_0 = 0.25$ with eddy $\mathbf{A} = (1, 1, 1)$, $\mathbf{B} = (1, 1, 1)$ and $\mathbf{x}_e = (-1, -0.1, 0)$.

Finally, in Figure 6.9 we see how the scattered pressure varies across different angle of attacks and different leading edge serrations. We consider angles of attack up to 9° , in 3° increments. To measure how effective the serration is at reducing noise we plot p_{diff} .

We see several features from Figure 6.9. First, as we increase the angle of attack, the maximum effectiveness of the serrations reduces. This is very much what we expect, since increasing the angle of attack effectively reduces the amplitude of the serrations, which reduces the effectiveness of the serrations as we saw in Figure 6.3. The maximum reduction

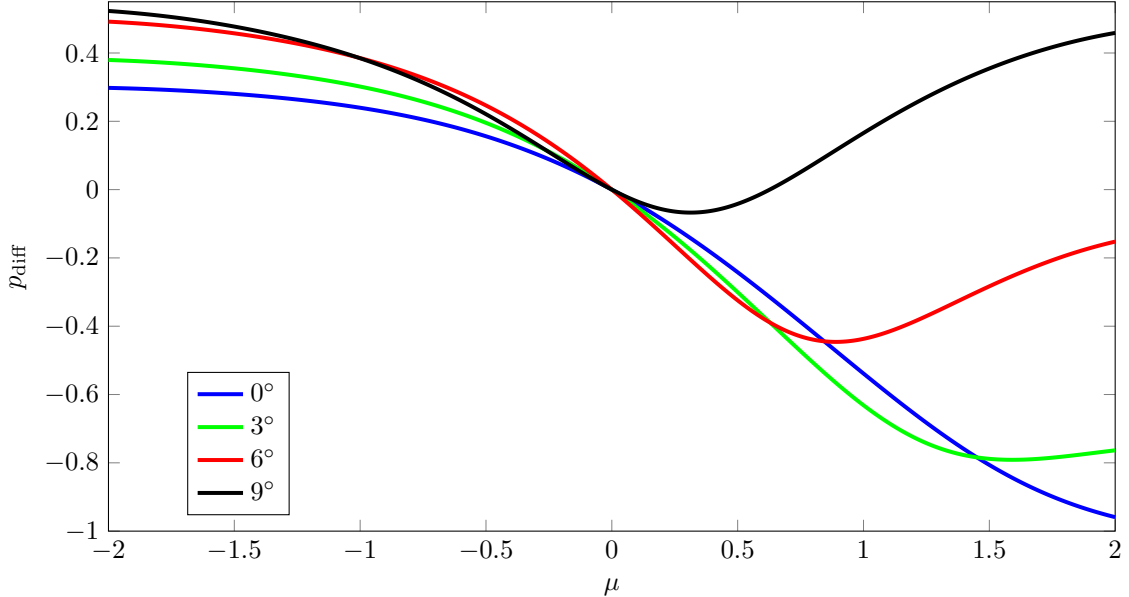


Figure 6.9: Plot of p_{diff} for serrations $\mathcal{F}_\mu(z) = 0.5 \sin(\mu z)$ as μ varies, for aerofoils at different angle of attacks. The parameters are $\omega = 0.5$, $u_0 = 0.25$ with eddy $\mathbf{A} = (1, 2, 1)$, $\mathbf{B} = (1, 1, 2)$ and $\mathbf{x}_e = (-1, 0.1, 0)$.

in p_{diff} is close to 1 when the angle of attack is 0° , while when the angle of attack is 9° the maximum reduction in p_{diff} is just 0.07. Second, we see that the optimum serration, where the maximum noise reduction occurs, varies. The wavelength of the optimum serration increases (μ decreases) as we increase the angle of attack. Third, we see that as the angle of attack increases the maximum possible value of p_{diff} increases, from 0.3 at zero angle of attack to 0.54 at an angle of attack of 9° .

Chapter 7

Conclusions

In this thesis we have presented a number of new ideas, methods and results to help mathematically model noise in turbofan aeroengines. Our work mainly has applications to modelling rotor-stator interaction noise, but some of the results we derived are relevant to other applications. We summarise the conclusions from each chapter before presenting future work.

In Chapter 2 we derived a new acoustic analogy, given in (2.2.38), by rearranging the Euler equations for a swirling base flow with varying entropy, extending the result from Posson and Peake (2013b). Our new acoustic analogy allowed us to see the effect of the base flow entropy on the Green's function and eigenmodes in Chapter 3. When we considered the acoustic analogy with constant base flow entropy, we got the same operator \mathcal{F} acting on the pressure perturbation as in Posson and Peake (2013b), although the source terms were slightly different due to using the energy equation in the derivation of the acoustic analogy. However, when we estimate the source terms to calculate the pressure we only use the loading noise source terms, which are the same for both analogies when the entropy is constant.

In Chapter 3 we considered a high-frequency asymptotic limit, which allowed us to calculate the acoustic eigenmodes and Green's function of swirling flow analytically, although we had to solve the analytic dispersion relations in (3.3.1)-(3.3.3) numerically. We compared our results to the exact numerical eigenmodes and Green's function, which we calculated using Chebfun in MATLAB and was validated against the program used in Posson and Peake (2013b). We found that the analytic eigenmodes approximated the numerical eigenmodes very well in Examples 1-10 (Figures 3.5 to 3.7, 3.9 and 3.10) for different flow parameters (including semi-realistic shear and swirl), and both hard and lined walls. To find the Green's function we calculated the residue at each upstream or downstream mode by using (3.5.9) and then summed these contributions. We also had a contribution from the critical layer towards the downstream Green's function, which we discuss further later.

In Figures 3.19 to 3.26, we showed some examples of the analytic and numerical Green's function, including when we had lined walls and semi-realistic mean flow, and we found in general that the analytic Green's function was a good approximation to the

numerical Green's function. In some cases, the analytic Green's function contribution from a particular eigenmode was less accurate, which was because the eigenmode was poorly approximated analytically, since it was on the edge of the two regions where we solve two different dispersion relations. This can be overcome by using a new dispersion relation, which was developed in [Section 3.7.3](#) and [Chapter 5](#), with the effect shown in [Figure 3.29](#). This new dispersion relation gives much more accurate analytic eigenmodes and Green's function, with the results shown in [Table 3.3](#) and [Figure 3.29c](#). When we have a more complicated mean flow profile (such as semi-realistic swirling flow) then we still improve the accuracy of the analytic results, but not so dramatically. We also saw that the effect of swirl is very significant, with [Figure 3.30](#) showing the effect of swirl numerically and the difference between [Figure 3.20](#) and the bottom row of [Figure 3.23](#) showing the effect of swirl asymptotically.

Our new acoustic analogy from [Chapter 2](#) allowed us to see the effect of entropy on the eigenmodes and Green's function, both numerically and analytically. We saw that in the high-frequency limit varying the base flow entropy only affects the base flow pressure, density and speed of sound; the dispersion relations for the eigenmodes and the Green's function do not otherwise change. We only considered the case of a logarithmic base flow entropy. If we made the base flow entropy sufficiently small we could find both an upstream and a downstream “surface-entropy” mode ([Figures 3.11](#) and [3.13](#)), which were created by a mode splitting off from the main line of cut-off modes. These “surface-entropy” modes were only present when there was lining in the duct. We were able to accurately approximate the eigenmodes analytically ([Figures 3.11](#) to [3.14](#)), including when “surface-entropy” modes were present. We found that the analytic Green's function was still very accurate compared to the numerical Green's function, as seen in [Figure 3.27](#). In [Figure 3.28](#) we saw that the base flow entropy affects the Green's function significantly, for both a hard-walled and a lined duct.

In the final part of [Chapter 3](#) we presented some difficulties with the asymptotic method, most of which are overcome with slightly more work, and the only real challenge remains calculating the contribution from the critical layer, including the effect of the hydrodynamic modes. The critical layer contribution comes from an integral around the critical layer and hydrodynamic modes, which is only present when considering the downstream Green's function. We mostly ignored this contribution since, in general, it is small compared to the contribution from the cut-on acoustic modes (see [Figure 3.18](#)). Calculating the critical layer contribution accurately and quickly remains a challenge. Our asymptotic method is not very applicable to calculating the critical layer contribution, and the results were inaccurate (although of a similar order of magnitude) compared to the very expensive numerical calculation in the cases we tested.

In [Chapter 4](#) we considered the calculation of the hydrodynamic modes accumulating at the end of the critical layer analytically, having already calculated the acoustic eigenmodes analytically in [Chapter 3](#). We extended the analytic results from [Heaton and Peake \(2006\)](#)

to a base flow with non constant entropy in (4.2.14) to (4.2.16) and then compared to numerical results. For the parameters we tested, increasing the entropy resulted in the hydrodynamic modes moving further away from the critical layer (Figures 4.2 and 4.3).

We also showed that it is not possible to analytically determine the constant of proportionality for the hydrodynamic modes accumulating exponentially at the ends of the critical layer, the first case in Heaton and Peake (2006). The accumulation rate can be calculated analytically, but the constant of proportionality has to be calculated numerically from the first ~ 10 modes. We showed that the constant of proportionality is a global property in Section 4.3, in the sense we need to know the flow in a region rather than at a single point. In Heaton and Peake (2006) it was shown that for the other two cases of accumulation it takes a significant number of modes before the analytical description of the modes is accurate. Thus, we will always need to calculate some of the hydrodynamic modes numerically, in the first case because we don't know the constant of proportionality and in the second and third cases because the first analytical modes are not accurate.

In Figure 4.8 we showed the hydrodynamic modes bifurcating as we slowly varied the shear flow, keeping all other flow parameters constant. This phenomenon had not been seen before, and the exact parameters where it occurs are yet to be determined. The bifurcations in Figure 4.8 might be caused by the very narrow critical layer. The effect of the bifurcating eigenmodes was seen in their eigenfunctions in Figure 4.9, with the eigenfunctions associated to the bifurcating eigenmodes significantly different in shape.

In Chapter 5 we developed a new analytical and numerical method for calculating the eigenmodes and Green's function for swirling flow when the impedance of the acoustic lining varies circumferentially. This work has particular applications to splices in the acoustic lining, although we were not able to compute any results with spliced liners due to the computation time, and instead only considered a lining smoothly varying circumferentially. The acoustic analogy remains unchanged from Chapter 2, but the boundary conditions couple together all of the azimuthal modes. The analytical method involved taking a high-frequency limit and using the WKB method, as in Chapter 3. The analytical dispersion relation for the eigenmodes is given by (5.4.7), and involves solving two infinite matrix problems numerically. These infinite matrix problems can be approximated by finite systems, given by (5.4.21) and (5.4.27). The size of the matrices depends on the number of Fourier coefficients needed to accurately approximate the impedance by a truncated Fourier series, which is very large for a spliced liner since the impedance is a discontinuous function. We also presented two methods for calculating the eigenmodes numerically, one in the spirit of the analytical method and one similar to the method in Chapter 3. However, both methods are currently too expensive to perform on a standard computer.

In Figures 5.5 to 5.6 and 5.8 to 5.9 we showed the effect of a smoothly varying lining on the acoustic eigenmodes. The effect of the lining varying circumferentially is significant for some of the modes which are cut-on or have a small imaginary part, while cut-off modes with a large imaginary part are largely unaffected by the lining varying circumferentially. To

calculate the Green's function we evaluated the residue at each acoustic mode in the same way as [Chapter 3](#). In [Figures 5.7](#) and [5.10](#) we plotted the Green's function for swirling mean flow at two different azimuthal modes, and we saw that the Green's function contribution from eigenmodes which are close to cut-on can vary significantly while the Green's function contribution from significantly cut-off eigenmodes is relatively unchanged as we vary the lining circumferentially.

Finally, in [Chapter 6](#) we considered the effect of turbulence hitting a single, isolated aerofoil. We analytically calculated the scattered pressure when turbulence given by synthetic eddies hits the leading edge of a serrated, infinite half plane. To derive this result we made a number of simplifying assumptions, such as assuming the serrations were shallow and that the Mach number was small, and additionally our results are only valid in the far field. This allowed us to calculate the Green's function for Helmholtz's equation on a serrated infinite half plane, given by [\(6.2.26\)](#). We then considered the cases where we had a single eddy, two eddies or multiples eddies driving the turbulence, with the Fourier transforms of the scattered pressure given by [\(6.4.9\)](#), [\(6.5.10\)](#) and [\(6.5.16\)](#) respectively.

One of the key results from this chapter is [Figure 6.7](#). This figure shows the level of noise reduction (or increase) as we compare an aerofoil with a serrated leading edge to an aerofoil with a straight leading edge, where we generated the turbulence with ten random synthetic eddies. The figure shows two clear trends. Firstly, there will always be some serrated aerofoil that will reduce the noise compared to a straight leading edge, although the maximum noise reduction depends on the form of the turbulence. Secondly, unless we know the exact form of turbulence, a particular serratation could just as easily lead to an increase in the noise as a decrease. We also saw in [Figure 6.9](#) the effect of the angle of attack, and for aerofoils at higher angles of attack the serratation is considerably less effective.

7.1 Future work

There are many possible directions for future work, and we list some of them below. We list future work for each chapter separately.

Chapter 2

- We could derive a new acoustic analogy for a base flow with axial and/or azimuthal dependence. This would give us a higher order, more complicated acoustic analogy.
- We could derive an acoustic analogy including temperature and viscosity effects. However, as soon as we include these effects, our base flow can no longer have only radial dependence. Thus, calculating the acoustic analogy will be difficult due to both the new base flow and the extra temperature and viscosity terms in the Euler equations.

Chapter 3

- If we can estimate the source terms (either numerically or analytically) then we could use our analytic Green's function and [Section 2.2.3](#) to calculate the pressure, as in [Posson and Peake \(2012, 2013b\); Masson et al. \(2016\)](#).
- As mentioned in [Section 1.3](#), we are hopeful that our analytic Green's function could be used in beamforming to improve results. We are currently investigating this issue further.
- We could calculate a lower bound on the frequency for which the high-frequency asymptotic Green's function is accurate. This lower bound will depend on the flow parameters. In this thesis the lowest frequency we presented results for was $\omega = 25$ (corresponding to 2050 Hz), although $\omega = 19.5$ (1600 Hz) was considered in [Mathews et al. \(2016\)](#) and was shown to produce excellent results for a semi-realistic mean flow.
- We could investigate the effect of the new proposed boundary conditions for acoustic liners ([Brambley, 2011; Khamis and Brambley, 2016](#)) on the Green's function, and see whether analytical and numerical results are still possible.
- We were unable to calculate the critical layer integral accurately analytically. It can be calculated numerically, but is very expensive. In the future, we hope to be able to either have a quick way of calculating the critical layer integral accurately, or at the very least, a method which allows us to accurately estimate the magnitude of this integral and decide when it can be safely ignored.
- Our analytic method currently fails to deal with the case when $q_n(r, \kappa)$ has multiple zeros in the duct, but we hope this can be overcome in the future using the work of [Section 3.7.2](#). We frequently found multiple zeros of $q_n(r, \kappa)$ when we considered semi-realistic mean flow.
- We could further investigate the “surface-entropy” modes, for example the parameters required to create them.

Chapter 4

- We could look at the stability of the hydrodynamic modes for a base flow with varying entropy, by using the Lalas inequality ([Lalas, 1975; Heaton and Peake, 2006](#)).
- We could investigate whether the Green's function contribution from each hydrodynamic mode can be calculated analytically by using the residue theorem.
- We could find the exact conditions which cause the hydrodynamic modes to bifurcate.

Chapter 5

- We need to further investigate a fast method to solve for the eigenmodes numerically when the lining varies circumferentially. This will then allow us to validate the asymptotic method. Once we have the eigenmodes, we would then be able to calculate the Green's function numerically.
- To consider the effect of splices, we would need to revisit the asymptotic method for finding the eigenmodes. This is because the matrices Λ^h and Λ^1 in (5.4.21) and (5.4.27) became badly conditioned as they became larger. One solution is to precondition the system (Wathen, 2015), so that it becomes possible to invert. One easy starting point is to multiply the matrix Λ^j and right-hand side μ^j by the inverse of the diagonal of Λ^j . Another completely different approach would be to look at different expansions for the Green's function and impedance function. Instead of using a Fourier series, which is bad at representing discontinuous functions, we could look at Chebyshev polynomials or wavelets.
- We could instead consider the Green's function and eigenmodes in a duct whose walls slowly vary axially. The eigenmode problem was first treated by Rienstra (1999), who found the eigenmodes of shear flow in an annular duct using the method of multiple scales. The method was extended in Cooper and Peake (2001) to include the effect of swirl, and in Rienstra (2003) to include ducts of arbitrary cross-section. However, deriving an acoustic analogy of the form in Posson and Peake (2013b) and Chapter 2 would be very difficult, and a much higher order equation would be found.
- We could also consider the case when the lining varies axially, such as axial splices. This problem would be much more suited to using the method of Weiner-Hopf. It was considered numerically by Liu et al. (2015). Our acoustic analogy would still be the same, but the boundary conditions would give us a coupled system like in Chapter 5. However, solving for the Green's function would be very challenging, since approximating Fourier transforms is a lot harder than approximating Fourier series.

Chapter 6

- We need to validate our work against numerical results, and consider realistic turbulence. We should choose the parameters of the eddy so that the von Kármán energy spectrum (Wilson, 1998) is achieved. These parameters are given in Haeri et al. (2014); Gea-Aguilera et al. (2015), and we could use these parameters to generate realistic turbulence.
- We could consider an aerofoil in swirling flow. The Green's function will be the same, but the synthetic turbulence in Section 6.3 would be different, and we would need to calculate both $\frac{\partial p}{\partial x}$ and $\frac{\partial p}{\partial y}$. The method would be similar to when the aerofoil is at non-zero angle of attack in Section 6.6.

- We could consider a more realistic Green's function, by solving a more complicated equation for the incident pressure which includes the effect of scattering and convection, rather than the Helmholtz equation.
- We could consider an aerofoil with finite chord, with the Green's function for a flat aerofoil given in [Howe \(2001\)](#). The difficulty in considering an aerofoil with a finite chord comes from applying the Kutta condition at the trailing edge of the aerofoil. The importance of the Kutta condition is discussed both analytically and numerically in [Ayton et al. \(2016\)](#).
- We could also consider the case of a finite wingspan, although it is not clear how to calculate the Green's function in this case.
- We could also consider aerofoils with shape and thickness. We can investigate these by considering a Joukowsky coordinate mapping from a flat, infinite aerofoil to a realistic aerofoil. An example of this transformation is given in [Ayton and Peake \(2013\)](#).

Appendix A

Further mathematical techniques

A.1 The WKB method

The WKB method is a technique for asymptotically solving linear, ordinary differential equations, exploiting the fact we have a small parameter. It was named after Wentzel, Kramers and Brillouin ([Bender and Orszag, 1978](#)), and is also commonly referred to as the WKBJ method (J for Jeffreys) or the Liouville-Green method. The method can be used to solve any linear, ordinary differential equation where the highest derivative is multiplied by a small parameter ε . It is related to the multiple scales technique ([Bender and Orszag, 1978](#)) and is essentially a simpler case of it. The WKB method involves substituting a series of the form

$$y(x) = \exp \left[\frac{1}{\varepsilon} \sum_{n=0}^{\infty} \delta^n S_n(x) \right], \quad (\text{A.1.1})$$

into the differential equation and then determining S_n and δ .

The classical example from [Bender and Orszag \(1978\)](#) is solving the Schrödinger equation

$$\varepsilon^2 y'' + Q(x)y = 0, \quad (\text{A.1.2})$$

where $Q(x) \neq 0$ in the domain we are solving the equation on. We determine that $\delta = \varepsilon$ from taking the distinguished limit of the differential equation ([Bender and Orszag, 1978](#)). We then substitute (A.1.1) into (A.1.2) and equate coefficients of ε :

$$\varepsilon^0 : S_0'^2 + Q(x) = 0, \quad (\text{A.1.3})$$

$$\varepsilon^1 : 2S_0'S_1' + S_0'' = 0, \quad (\text{A.1.4})$$

$$\varepsilon^m : 2S_0'S_m' + S_{m-1}'' + \sum_{j=1}^{m-1} S_j'S_{m-j}' = 0. \quad (\text{A.1.5})$$

The first equation is the eikonal equation and has solution

$$S_0(x) = \pm \int^x \sqrt{-Q(s)} ds. \quad (\text{A.1.6})$$

By solving (A.1.4) we find that S_1 is given by

$$S_1(x) = -\frac{1}{4} \log |Q(x)|. \quad (\text{A.1.7})$$

Analytical expressions for larger S_m become more and more complicated, with S_2 to S_5 given in Bender and Orszag (1978). Substituting in the expressions for S_0 and S_1 in (A.1.1) then gives the approximation

$$y(x) \sim c_1 |Q(x)|^{-1/4} \exp \left(\frac{1}{\varepsilon} \int_0^x \sqrt{-Q(s)} ds \right) + c_2 |Q(x)|^{-1/4} \exp \left(-\frac{1}{\varepsilon} \int_0^x \sqrt{-Q(s)} ds \right). \quad (\text{A.1.8})$$

This linear combination of solutions using just the S_0 and S_1 terms is sometimes referred to as the physical optics approximation (Bender and Orszag, 1978). It is easy to heuristically justify the form of the solution in (A.1.8), since if Q was a constant then we would have a linear combination of exponentials or sines and cosines, depending on the sign of Q .

The WKB solution in (A.1.8) is generally very accurate and extremely useful, but it does not apply if Q becomes zero at some point in the domain. This is because in the above analysis S_1 blows up, and using just the first term S_0 does not give a good approximation. To construct a solution when Q has a zero in the domain requires a modification to the method.

One turning point solution

To construct a solution when we have a single zero of Q (referred to as a one turning point solution) we use the solution (A.1.8) away from the zero and find a different form for the solution near the zero of Q . We then match together these solutions to get a smooth solution. We formalise this approach below.

We consider the equation (A.1.2) on the domain $[a, b]$, but now $Q(x_0) = 0$ for $x_0 \in [a, b]$. We assume further that it is a simple zero, so $Q(x) \sim \alpha(x - x_0)$ as $x \rightarrow x_0$. We also assume $\alpha > 0$. We split the domain into three regions. Region I is where $b > x > x_0$ and $x - x_0 \gg \varepsilon^{2/3}$. Region III is defined by $a < x < x_0$ and $x_0 - x \gg \varepsilon^{2/3}$, and region II is where $|x - x_0| \ll 1$. In regions I and III we use the WKB solution in (A.1.8), with

$$y_I(x) \sim [Q(x)]^{-1/4} \left[A_I \exp \left(\frac{i}{\varepsilon} \int_{x_0}^x \sqrt{Q(s)} ds \right) + B_I \exp \left(-\frac{i}{\varepsilon} \int_{x_0}^x \sqrt{Q(s)} ds \right) \right], \quad (\text{A.1.9})$$

and

$$y_{III}(x) \sim [-Q(x)]^{-1/4} \left[A_{III} \exp \left(\frac{1}{\varepsilon} \int_x^{x_0} \sqrt{-Q(s)} ds \right) + B_{III} \exp \left(-\frac{1}{\varepsilon} \int_x^{x_0} \sqrt{-Q(s)} ds \right) \right]. \quad (\text{A.1.10})$$

In region II we solve the approximate differential equation

$$\varepsilon^2 y'' + \alpha(x - x_0)y = 0. \quad (\text{A.1.11})$$

Making the substitution $t = \varepsilon^{-2/3}\alpha^{1/3}(x_0 - x)$ then gives the differential equation $y'' = ty$, the Airy equation. Hence we find that

$$y_{II}(x) \sim A_{II} \text{Ai}\left(\varepsilon^{-2/3}\alpha^{1/3}(x_0 - x)\right) + B_{II} \text{Bi}\left(\varepsilon^{-2/3}\alpha^{1/3}(x_0 - x)\right). \quad (\text{A.1.12})$$

It remains to match the solutions y_j by choosing the arbitrary constants A_j and B_j to give a smooth solution y .

We match the solutions on the overlap regions $\varepsilon^{2/3} \ll |x - x_0| \ll 1$. We let $|x - x_0| \rightarrow \infty$ in the y_{II} solution, and let $|x - x_0| \rightarrow 0$ in the y_I and y_{III} solutions. We make use of the asymptotic behaviour of the Airy function, which is given by

$$\text{Ai}(t) \sim \frac{(-t)^{-1/4}}{\sqrt{\pi}} \sin\left(\frac{2}{3}(-t)^{3/2} + \frac{\pi}{4}\right), \quad \text{Bi}(t) \sim \frac{(-t)^{-1/4}}{\sqrt{\pi}} \cos\left(\frac{2}{3}(-t)^{3/2} + \frac{\pi}{4}\right) \text{ as } t \rightarrow -\infty, \quad (\text{A.1.13})$$

and

$$\text{Ai}(t) \sim \frac{t^{-1/4}}{2\sqrt{\pi}} \exp\left(-\frac{2}{3}t^{3/2}\right), \quad \text{Bi}(t) \sim \frac{t^{-1/4}}{\sqrt{\pi}} \exp\left(\frac{2}{3}t^{3/2}\right) \text{ as } t \rightarrow \infty. \quad (\text{A.1.14})$$

These relations are stated in [Bender and Orszag \(1978\)](#). Since $Q(x) \sim \alpha(x - x_0)$ in region II then

$$[Q(x)]^{-1/4} \sim \alpha^{-1/4}(x - x_0)^{-1/4} \text{ and } \int_{x_0}^x \sqrt{Q(s)} ds \sim \frac{2}{3}\alpha^{1/2}(x - x_0)^{3/2} := \mu(x). \quad (\text{A.1.15})$$

We now determine the relationships between the arbitrary constants in the different regions. Using the asymptotic relations in (A.1.13) and (A.1.15) we find that

$$y_I(x) \sim [\alpha(x - x_0)]^{-1/4} \left[A_I \exp\left(\frac{i}{\varepsilon}\mu(x)\right) + B_I \exp\left(-\frac{i}{\varepsilon}\mu(x)\right) \right], \quad (\text{A.1.16})$$

$$y_{II}(x) \sim (x - x_0)^{-1/4}\alpha^{-1/12}\varepsilon^{1/6} \left[A_{II} \sin\left(\frac{1}{\varepsilon}\mu(x) + \frac{\pi}{4}\right) + B_{II} \cos\left(\frac{1}{\varepsilon}\mu(x) + \frac{\pi}{4}\right) \right], \quad (\text{A.1.17})$$

in the region $\varepsilon^{2/3} \ll x - x_0 \ll 1$, and thus we find the relationship between the constants A_I , B_I and A_{II} , B_{II} . We then match together the solutions y_{II} and y_{III} in the region $\varepsilon^{2/3} \ll x_0 - x \ll 1$ to determine the relationship between the constants A_{II} , B_{II} and A_{III} , B_{III} . If we let

$$\mathcal{Q}(x) = \int_{x_0}^x \sqrt{Q(s)} ds, \quad (\text{A.1.18})$$

then the full WKB one turning point solution is given by

$$y(x) \sim \begin{cases} [Q(x)]^{-1/4} (A_I e^{i\mathcal{Q}(x)/\varepsilon} + B_I e^{-i\mathcal{Q}(x)/\varepsilon}) & x - x_0 \gg \varepsilon^{2/3} \\ A_{II} \text{Ai}(\alpha^{1/3} \varepsilon^{-2/3} (x_0 - x)) + B_{II} \text{Bi}(\alpha^{1/3} \varepsilon^{-2/3} (x_0 - x)) & |x - x_0| \ll 1 \\ [-Q(x)]^{-1/4} (A_{III} e^{-i\mathcal{Q}(x)/\varepsilon} + B_{III} e^{i\mathcal{Q}(x)/\varepsilon}) & x_0 - x \gg \varepsilon^{2/3} \end{cases}, \quad (\text{A.1.19})$$

where

$$2A_{III} = \left(\frac{\alpha \varepsilon}{\pi^3} \right)^{1/6} A_{II} = A_I e^{i\pi/4} + B_I e^{-i\pi/4} \quad (\text{A.1.20})$$

and

$$B_{III} = \left(\frac{\alpha \varepsilon}{\pi^3} \right)^{1/6} B_{II} = A_I e^{-i\pi/4} + B_I e^{i\pi/4}, \quad (\text{A.1.21})$$

where the relationship between the constants was given in [Wundrow and Khavaran \(2004\)](#). A careful matching argument to derive these relations is shown in [Bender and Orszag \(1978\)](#), but only when the domain is \mathbb{R} , $x_0 = 0$ and we have the boundary condition $y(\infty) = 0$.

Amazingly, there is a uniformly valid solution which is equal to y_j in the three different regions, and it was found by Langer ([Langer, 1935](#); [Bender and Orszag, 1978](#)). The uniformly valid solution is given by

$$y(x) \sim \left(\frac{3\alpha \mathcal{Q}(x)}{2} \right)^{1/6} [Q(x)]^{-1/4} \left[A_{II} \text{Ai} \left(- \left(\frac{3\mathcal{Q}(x)}{2\varepsilon} \right)^{2/3} \right) + B_{II} \text{Bi} \left(- \left(\frac{3\mathcal{Q}(x)}{2\varepsilon} \right)^{2/3} \right) \right]. \quad (\text{A.1.22})$$

The proof of its validity is shown in [Bender and Orszag \(1978\)](#) for the simple case on the real line described above.

Multiple turning points and extensions

We can apply a similar method when we have a simple zero of Q where $\alpha < 0$. When we have a simple zero with $\alpha < 0$ the matching is done slightly differently, because to match the solutions between regions I and II we use the asymptotic formulae of the Airy function for $t \rightarrow \infty$ rather than $t \rightarrow -\infty$. The net result is that our solution is of a similar form to (A.1.19), but with different matching formulae to (A.1.20) and (A.1.21). Our uniformly valid solution is now given by

$$y(x) \sim \left(\frac{-3\alpha \mathcal{Q}(x)}{2} \right)^{1/6} [-Q(x)]^{-1/4} \left[A \text{Ai} \left(- \left(-\frac{3\mathcal{Q}(x)}{2\varepsilon} \right)^{2/3} \right) + B \text{Bi} \left(- \left(-\frac{3\mathcal{Q}(x)}{2\varepsilon} \right)^{2/3} \right) \right]. \quad (\text{A.1.23})$$

We could also consider the case when $\alpha \in \mathbb{C}$. We would then use the asymptotic behaviour of the Airy function in the complex plane to match between the different regions, and be especially careful about choosing branch cuts for the non-integer roots.

When $Q(x) \sim \alpha(x - x_0)^2$ a different uniformly valid solution is found, which in the case of $x_0 = 0$ and $y(\infty) = 0$ is given by

$$y(x) \sim \left(\frac{4\alpha \mathcal{Q}(x)}{\pi^2 Q(x)} \right)^{1/4} \Gamma \left(\frac{3}{4} \right) D_{-1/2} \left(\frac{2\mathcal{Q}(x)}{\varepsilon} \right)^{1/2}, \quad (\text{A.1.24})$$

where $D_{-1/2}$ is a parabolic cylinder function. This is left as an exercise in [Bender and Orszag \(1978\)](#). We could also consider the case when $Q(x) \sim \alpha(x - x_0)^m$, for $m \in \mathbb{N}$.

We can also solve the equation (A.1.2) where we have two or more zeros of $Q(x)$ in the domain. We match together two, one turning point solutions by using the asymptotic formulae given in (A.1.13) to (A.1.15). We can easily extend to m zeros of $Q(x)$ using this method. However, it is very difficult working with the solution unless it is uniformly valid, like the Langer solution. A uniformly valid solution for the case of two zeros which are close together was given in [Nielsen and Peake \(2016\)](#).

Finally, we can also solve the differential equation

$$\varepsilon^2 y'' + \varepsilon^2 P(x)y' + Q(x)y = 0, \quad (\text{A.1.25})$$

by using a similar method to the WKB method. When Q has no zeros in the domain we still get a solution of the form (A.1.8) since $P(x)$ only affects S_2 and larger terms. When we have a single zero of Q then we again make the substitution $t = \varepsilon^{-2/3}\alpha^{1/3}(x_0 - x)$ to solve the approximate differential equation near x_0 . However, this change of variables now only gives us an approximate Airy equation for $y(t)$. However, when matching to the two term zero turning point solution in (A.1.8) we can ignore the additional terms and just solve the Airy equation $y'' = ty$.

A.2 Chebfun

The creators of Chebfun describe it as follows; “Chebfun is an open-source software system for numerical computing with functions. The mathematical basis of Chebfun is piecewise polynomial interpolation implemented with what we call ‘Chebyshev technology’” ([Driscoll et al., 2014](#)). It is a tool which was created in MATLAB and allows computation with functions instead of points. It was conceived by Battles and Trefethen in 2002, and has been growing in both functionality and popularity ever since. The idea is to represent functions by Chebyshev polynomials or piecewise Chebyshev polynomials, which allows us to easily perform operations on the function. We briefly show some of the features of Chebfun, with most of the examples taken from [Driscoll et al. \(2014\)](#).

Creating a chebfun

We create a chebfun of the Airy function $\text{Ai}(x)$ on the interval $[-10, 10]$ and plot it by using the following commands.

```
f = chebfun(@(x) airy(x), [-10,10]);
plot(f)
```

The result is shown in [Figure A.1](#). We find the roots of the Airy function by using the roots command, which we show below.

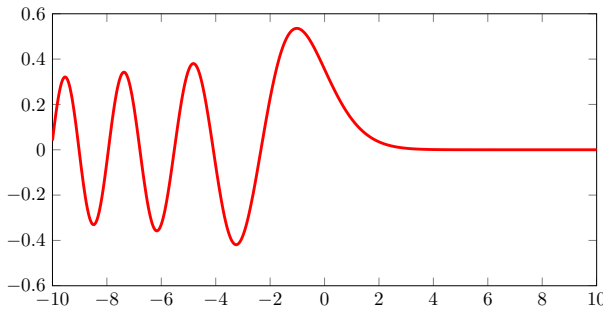


Figure A.1: Plot of a chebfun of the Airy function $\text{Ai}(x)$.

```
roots(f)
ans =
-9.022650853340977
-7.944133587120859
-6.786708090071763
-5.520559828095555
-4.087949444130972
-2.338107410459766
```

We find the maximum and the minimum of the function by using the max and min commands below.

```
max(f)
ans =
0.535656656015700
min(f)
ans =
-0.419015478032560
```

To integrate the function we use the sum command.

```
sum(f)
ans =
1.099031736433374
```

Finally, we differentiate the function using the diff command and then plot the result in [Figure A.2](#).

```
fprime=diff(f);
plot(fprime)
```

Solving a differential equation

We can use Chebfun to solve differential equations with ease, for example the Advection-Diffusion equation in one dimension. The equation we solve is given by

$$0.1g''(x) + g'(x) = -1, \quad g(-5) = 0, \quad g(5) = 0. \quad (\text{A.2.1})$$

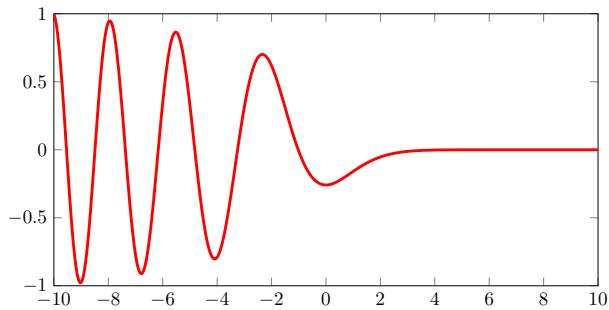


Figure A.2: Plot of a chebfun of the Airy function $\text{Ai}'(x)$.

Note that there is a boundary layer present near $x = -5$. To solve this problem in Chebfun we create a chebop for the equation we wish to solve, add boundary conditions and then solve it. This is shown below.

```
L = chebop(@(x,g) 0.1*diff(g,2) + diff(g), [-5, 5]);
L.lbc=0;
L.rbc=0;
g=L\(-1);
plot(g)
```

The solution $g(x)$ is plotted in [Figure A.3](#). We can also solve non-linear problems, initial value problems and systems of differential equations in Chebfun.

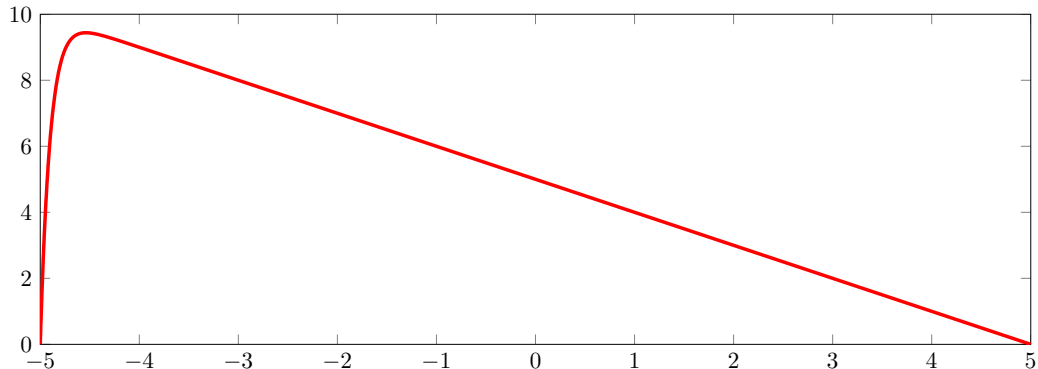


Figure A.3: Plot of Chebfun solution $g(x)$ of the differential equation $0.1g''(x) + g'(x) = -1$ with boundary conditions $g(-5) = 0$ and $g(5) = 0$.

An eigenvalue problem

A very famous eigenvalue problem from fluid dynamics is the Orr-Sommerfeld problem. This problem is a two dimensional problem concerning fluid flowing between two walls. If the base flow is plane Poiseuille flow then the stream function Ψ satisfies

$$\frac{1}{\text{Re}} \left[\Psi^{(4)} - 2\alpha^2 \Psi'' + \alpha^4 \Psi \right] - 2i\alpha \Psi - 1i\alpha(1-x^2)[\Psi'' - \alpha^2 \Psi] = \lambda [\Psi'' - \alpha^2 \Psi], \quad (\text{A.2.2})$$

with boundary conditions

$$\Psi(-1) = \Psi(1) = \Psi'(-1) = \Psi'(1) = 0. \quad (\text{A.2.3})$$

In (A.2.2) α is the axial wavenumber, λ the eigenvalue and Re the Reynolds number. The differential equation is derived from linearising the Navier–Stokes equation about a base flow, assuming all perturbations are proportional to $\exp(i\alpha(x - \lambda t))$ (Orszag, 1971). To solve the eigenvalue problem using Chebfun we define two operators, A and B such that $A = \lambda B$. We then add the boundary conditions to the chebop A . We solve the system using the `eigs` command with the number of eigenvalues we wish to find. We use the code from Driscoll et al. (2014).

```
Re = 5772;
alpha = 1;
A= chebop(@(x,psi) (diff(psi,4)-2*alpha^2*diff(psi,2)+alpha^4*psi)/Re - ...
    2i*alpha*psi - 1i*alpha*(1-x.^2).* (diff(psi,2)-alpha^2*psi) , [-1, 1]);
B= chebop(@(x,psi) diff(psi,2) - alpha^2*psi, [-1, 1]);
A.bc = @(x,psi) [psi(-1); feval(diff(psi),-1); psi(1); feval(diff(psi),1)];
EV = eigs(A, B, 50);
plot(EV, 'r.')
```

The eigenvalues are shown in Figure A.4. We can also find eigenvalues for systems of differential equations such as the Euler equations.

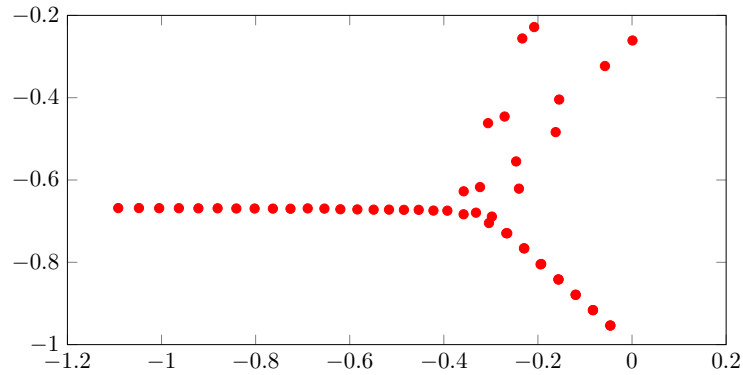


Figure A.4: Chebfun eigenvalues for the eigenvalue problem (A.2.2) with associated boundary conditions (A.2.3).

Appendix B

Hydrodynamic modes intermediate solution

B.1 Heuristic argument for intermediate solution for modes accumulating exponentially

We begin with equation (4.1.7) for the pressure P , which can be rewritten as

$$D(r) \frac{d^2P}{dr^2} + E(r) \frac{dP}{dr} + F(r)P = 0, \quad (\text{B.1.1})$$

where

$$E(r) := D(r) \left[\frac{1}{r} - \frac{\rho'_0(r)}{\rho_0(r)} \right] - D'(r), \quad (\text{B.1.2})$$

and

$$F(r) := \frac{D^2(r)}{\Lambda^2(r)} \left(\frac{\Lambda^2(r)}{c_0^2(r)} - \frac{n^2}{r^2} - k^2 \right) + D(r) \left[B'(r) - \frac{2nU_\theta(r)}{\Lambda(r)r^2} \right] - D'(r)B(r). \quad (\text{B.1.3})$$

We want to find solutions near $r = r_2$ where $D(r_2) = 0$. One possible way of proceeding would be to use the Frobenius method. We can write the equation as

$$\frac{d^2P}{dr^2} + \tilde{E}(r) \frac{dP}{dr} + \tilde{F}(r)P = 0, \quad (\text{B.1.4})$$

after dividing through by $D(r)$. We find the relevant Laurent series coefficients are $\tilde{E}_{-1} = -1$ and $\tilde{F}_{-2} = 0$ and hence the indicial equation becomes $\zeta^2 - 2\zeta = 0$. Thus, the two linearly independent solutions are given by (Bender and Orszag, 1978) as

$$y_1(r) = \sum_{n=0}^{\infty} a_n (r - r_2)^{n+2} \quad \text{and} \quad y_2(r) = \sum_{n=0}^{\infty} b_n (r - r_2)^n + \beta \log(r - r_2) y_1(r). \quad (\text{B.1.5})$$

While it is easy to calculate the form of y_1 and y_2 , calculating the coefficients is a laborious task. Additionally, it will not be clear how to use these solutions to match to the exponential

outer solution and the oscillatory inner solution. Instead we consider a different, heuristic argument. It is similar to the the method of dominant balance in (Bender and Orszag, 1978). We will consider the Taylor expansion of the coefficients of the differential equation in (B.1.1), and we will only keep the dominant terms.

Let us consider the parameters from Figure 4.1. Thus, we have $U_x(r) = 0.5 + 0.2(r-1)^2$, $U_\theta(r) = 0.2$, $n = 15$, $\omega = 25$, $h = 0.6$, and $k \approx 44$. We find that $r_2 = 0.9221$ and that to four significant figures, we have

$$D(r) = -2.801(r-r_2) + 31.41(r-r_2)^2 - 251.5(r-r_2)^3, \quad (\text{B.1.6})$$

$$E(r) = 2.801 - 65.75(r-r_2) + 413.2(r-r_2)^2 - 978.5(r-r_2)^3, \quad (\text{B.1.7})$$

$$F(r) = 64.32 - 1378(r-r_2) - 196441(r-r_2)^2 - 1936487(r-r_2)^3. \quad (\text{B.1.8})$$

Of course, the dominant terms in each Taylor series will depend on the value of $|r-r_2|$. We find that the dominant terms are given by

$$D(r) \approx -2.801(r-r_2) \quad \text{when } |r-r_2| < 0.089 \quad (\text{B.1.9})$$

$$E(r) \approx -65.75(r-r_2) \quad \text{when } 0.043 < |r-r_2| < 0.159 \quad (\text{B.1.10})$$

$$F(r) \approx -196441(r-r_2)^2 \quad \text{when } 0.018 < |r-r_2| < 0.101. \quad (\text{B.1.11})$$

Hence for $0.043 < |r-r_2| < 0.089$ our equation becomes approximately

$$(r-r_2) \frac{d^2P}{dr^2} + E_1(r-r_2) \frac{dP}{dr} + F_2(r-r_2)^2 P = 0, \quad (\text{B.1.12})$$

where $E_1 = 23.46$ and $F_2 = 70129$. The solution to the differential equation is then given by

$$P = \gamma_1 e^{-E_1(r-r_2)/2} \left[\text{Ai} \left(\frac{E_1^2 - 4F_2(r-r_2)}{4F_2^{2/3}} \right) + \gamma_2 \text{Bi} \left(\frac{E_1^2 - 4F_2(r-r_2)}{4F_2^{2/3}} \right) \right]. \quad (\text{B.1.13})$$

For $r > r_2$ the intermediate solution will oscillate and we would be able to match it to the oscillate inner solution. For $r < r_2$ the intermediate solution will be exponential and we will be able to match it to the outer solution. The fact that the solution is valid is such a small range of r means that the actual matching of constants will be difficult in practice. This is because the constants γ_1 and γ_2 could be different when $0.043 < r < 0.089$ and when $-0.089 < r < -0.043$, since the solution is not continuous.

Taking any more than the dominant terms in the Taylor expansion will generally lead to a an equation that needs to be solved numerically. However, we can find an exact solution to the equation

$$(r-r_2) \frac{d^2P}{dr^2} + [E_1(r-r_2) - 1] \frac{dP}{dr} + F_2(r-r_2)^2 P = 0, \quad (\text{B.1.14})$$

which corresponds to the approximation $E(r) \approx 2.801 - 65.75(r-r_2)$. The validity of

(B.1.14) will be for $0.018 < r < 0.089$, so significantly larger than the validity of (B.1.12). The solution of (B.1.14) is given in terms of a combination of Bessel functions of orders $-1/3$, $1/3$, $2/3$ and $4/3$, although the exact form is quite complicated. The Bessel functions of order $1/3$ and $-1/3$ correspond to the Airy functions in (B.1.12).

Appendix C

Calculations for an aerofoil with serrated leading edge

C.1 Analytic calculation of pressure for two eddies with different sources

The term $Q_2^{D,2}$ is given by the following expression:

$$\begin{aligned}
Q_2^{D,2}(z_0, \omega) = & B_1(z_0 - z_e^\Phi) Q_{13}^{\Phi,\Psi}(z_0, \omega) \left[d_y^e \frac{i\omega}{2\gamma_{13}^{BD}U} - d_x^e \frac{B_1 y_e^\Phi + D_3 y_e^\Psi}{\gamma_{13}^{BD}} \right] \\
& - D_1(z_0 - z_e^\Psi) Q_{31}^{\Phi,\Psi}(z_0, \omega) \left[d_y^e \frac{i\omega}{2\gamma_{31}^{BD}U} - d_x^e \frac{B_3 y_e^\Phi + D_1 y_e^\Psi}{\gamma_{31}^{BD}} \right] \\
& + D_1(z_0 - z_e^\Psi) Q_{21}^{\Phi,\Psi}(z_0, \omega) \left[d_z^e \frac{i\omega}{2\gamma_{21}^{BD}U} + d_x^e z_0 - d_x^e \frac{B_2 z_e^\Phi + D_1 z_e^\Psi}{\gamma_{21}^{BD}} \right] \\
& - B_1(z_0 - z_e^\Phi) Q_{12}^{\Phi,\Psi}(z_0, \omega) \left[d_z^e \frac{i\omega}{2\gamma_{12}^{BD}U} + d_x^e z_0 - d_x^e \frac{B_1 z_e^\Phi + D_2 z_e^\Psi}{\gamma_{12}^{BD}} \right] \\
& + (B_3 - D_3) Q_{33}^{\Phi,\Psi}(z_0, \omega) \left[\frac{d_y^e}{2\gamma_{33}^{BD}} + \frac{i\omega}{2\gamma_{33}^{BD}U} \left(d_y^e \frac{i\omega}{2\gamma_{33}^{BD}U} - d_x^e \frac{B_3 y_e^\Phi + D_3 y_e^\Psi}{\gamma_{33}^{BD}} \right) \right] \\
& + d_x^e \frac{2B_3 D_3}{\gamma_{33}^{BD}} Q_{33}^{\Phi,\Psi}(z_0, \omega) \left(d_y^e \frac{i\omega}{2\gamma_{33}^{BD}U} - d_x^e \frac{B_3 y_e^\Phi + D_3 y_e^\Psi}{\gamma_{33}^{BD}} \right) \\
& + D_3 Q_{23}^{\Phi,\Psi}(z_0, \omega) \left[\frac{d_z^e}{2\gamma_{23}^{BD}} + \left(\frac{i\omega}{2\gamma_{23}^{BD}U} - d_x^e \frac{B_2}{\gamma_{23}^{BD}} \right) \left(d_z^e \frac{i\omega}{2\gamma_{23}^{BD}U} + d_x^e z_0 - d_x^e \frac{D_3 z_e^\Phi + B_2 z_e^\Psi}{\gamma_{23}^{BD}} \right) \right] \\
& - B_3 Q_{32}^{\Phi,\Psi}(z_0, \omega) \left[\frac{d_z^e}{2\gamma_{32}^{BD}} + \left(\frac{i\omega}{2\gamma_{32}^{BD}U} + d_x^e \frac{D_2}{\gamma_{32}^{BD}} \right) \left(d_z^e \frac{i\omega}{2\gamma_{32}^{BD}U} + d_x^e z_0 - d_x^e \frac{D_2 z_e^\Phi + B_3 z_e^\Psi}{\gamma_{32}^{BD}} \right) \right] \\
& + (B_1(z_0 - z_e^\Phi) - D_1(z_0 - z_e^\Psi)) Q_{11}^{\Phi,\Psi}(z_0, \omega) \left[d_y^e z_0 + y_e^\Psi z_e^\Phi - y_e^\Phi z_e^\Psi \right] \\
& + B_3 Q_{31}^{\Phi,\Psi}(z_0, \omega) \left[\frac{i\omega}{2\gamma_{31}^{BD}U} + d_x^e \frac{D_1}{\gamma_{31}^{BD}} \right] \left[d_y^e z_0 + y_e^\Psi z_e^\Phi - y_e^\Phi z_e^\Psi \right] \\
& - D_3 Q_{13}^{\Phi,\Psi}(z_0, \omega) \left[\frac{i\omega}{2\gamma_{13}^{BD}U} - d_x^e \frac{B_1}{\gamma_{13}^{BD}} \right] \left[d_y^e z_0 + y_e^\Psi z_e^\Phi - y_e^\Phi z_e^\Psi \right]. \tag{C.1.1}
\end{aligned}$$

To derive the equation for $Q_2^{D,1}$ in (6.5.15) and for $Q_2^{D,2}$ in (C.1.1) we use the following integrals:

$$\int_{-\infty}^{\infty} e^{i\omega t} e^{-\gamma_1(t-\varsigma_1)^2} e^{-\gamma_2(t-\varsigma_2)^2} = f_{\omega}(\gamma_1, \gamma_2, \varsigma_1, \varsigma_2), \quad (\text{C.1.2})$$

$$\int_{-\infty}^{\infty} t e^{i\omega t} e^{-\gamma_1(t-\varsigma_1)^2} e^{-\gamma_2(t-\varsigma_2)^2} = \left[\frac{i\omega}{2\gamma_{12}} + \frac{\gamma_1 \varsigma_1}{\gamma_{12}} + \frac{\gamma_2 \varsigma_2}{\gamma_{12}} \right] f_{\omega}(\gamma_1, \gamma_2, \varsigma_1, \varsigma_2), \quad (\text{C.1.3})$$

and

$$\int_{-\infty}^{\infty} t^2 e^{i\omega t} e^{-\gamma_1(t-\varsigma_1)^2} e^{-\gamma_2(t-\varsigma_2)^2} = \left(\frac{1}{2\gamma_{12}} + \left[\frac{i\omega}{2\gamma_{12}} + \frac{\gamma_1 \varsigma_1}{\gamma_{12}} + \frac{\gamma_2 \varsigma_2}{\gamma_{12}} \right]^2 \right) f_{\omega}(\gamma_1, \gamma_2, \varsigma_1, \varsigma_2), \quad (\text{C.1.4})$$

where $\gamma_{12} = \gamma_1 + \gamma_2$ and

$$f_{\omega}(\gamma_1, \gamma_2, \varsigma_1, \varsigma_2) = \sqrt{\frac{\pi}{\gamma_1 + \gamma_2}} \exp\left(-\frac{\omega^2}{4(\gamma_1 + \gamma_2)}\right) \exp\left(i\omega \left[\frac{\gamma_1 \varsigma_1 + \gamma_2 \varsigma_2}{\gamma_1 + \gamma_2} \right]\right) \times \exp\left(\frac{\gamma_1 \gamma_2}{\gamma_1 + \gamma_2} [2\varsigma_1 \varsigma_2 - \varsigma_1^2 - \varsigma_2^2]\right). \quad (\text{C.1.5})$$

C.2 Parameters for stochastic eddies in Section 6.5

Table C.1: Parameters for stochastic eddies with seed 34.

A_1	A_2	A_3	B_1	B_2	B_3	x_e	y_e	z_e
-0.918	-1.971	0.526	1.699	2.411	1.315	-0.872	2.409	-0.101
0.789	0.686	-0.129	3.059	1.434	1.137	0.324	-1.523	1.496
-1.141	1.781	0.142	4.572	4.939	3.265	1.122	2.507	1.235
0.385	0.294	-0.319	4.695	1.604	1.599	-0.663	-3.034	-2.116
-0.739	0.830	1.248	4.344	2.114	1.965	-0.070	-0.950	0.320
1.792	1.767	-3.276	2.999	3.797	1.134	-1.241	0.483	-2.203
-0.185	-0.975	1.609	4.284	3.591	3.624	2.658	1.078	-1.237
-0.682	0.947	-0.230	4.738	1.894	4.418	-0.971	1.006	0.784
-1.357	-0.592	-0.180	4.179	4.207	1.799	0.956	0.106	1.612
-0.347	-0.999	-0.582	2.846	3.048	4.228	1.237	-0.964	1.553

Table C.2: Parameters for stochastic eddies with seed 73.

A_1	A_2	A_3	B_1	B_2	B_3	x_e	y_e	z_e
0.344	-0.327	0.767	4.280	1.326	2.063	0.322	-0.550	-0.174
0.134	0.295	-1.008	3.621	2.428	3.346	0.226	1.502	0.160
0.022	-1.231	-1.237	1.222	3.933	2.696	1.511	0.509	-0.400
0.346	1.000	0.108	3.757	3.925	3.539	-1.572	-0.631	-0.446
-0.017	-1.407	-1.814	3.547	1.472	1.205	-0.886	0.284	0.111
-0.407	0.139	-0.595	3.411	1.168	3.344	0.002	-0.135	-0.933
-1.212	-0.686	-1.676	1.486	2.275	4.856	2.149	2.044	0.457
0.217	0.791	-0.598	1.851	4.355	1.022	0.007	0.252	0.861
1.232	0.792	0.656	3.030	3.432	3.754	-0.746	0.990	-0.129
-1.096	-1.695	1.422	2.906	1.309	4.592	0.914	-0.298	-1.471

Table C.3: Parameters for stochastic eddies with seed 93.

A_1	A_2	A_3	B_1	B_2	B_3	x_e	y_e	z_e
0.358	1.653	0.169	2.910	2.863	3.882	-0.718	0.664	1.255
0.755	-0.291	-0.292	3.619	4.708	4.197	-1.453	-0.197	-2.409
-0.402	-0.094	0.354	1.804	1.510	3.571	-0.007	-1.340	1.352
0.713	0.341	0.539	2.501	1.706	1.370	0.496	-0.675	0.051
0.061	-0.425	1.003	2.114	2.871	2.821	-0.569	0.280	-0.351
0.503	-0.793	-1.928	2.299	4.786	1.821	0.918	-0.087	-0.591
0.140	0.191	3.049	3.236	3.315	3.811	-0.881	-0.888	0.122
0.472	0.128	0.701	4.442	1.006	1.848	2.128	-2.270	-1.036
-0.734	1.165	-0.367	4.792	1.165	1.122	-0.822	-0.789	1.477
-0.409	-2.033	-0.031	2.819	2.688	1.138	0.522	0.475	0.251

Table C.4: Parameters for stochastic eddies with seed 345.

A_1	A_2	A_3	B_1	B_2	B_3	x_e	y_e	z_e
-0.493	0.142	1.635	2.349	1.039	2.784	-0.933	0.447	-1.439
0.381	-1.997	-2.156	1.855	4.165	2.312	-0.251	0.430	-0.477
-0.020	-0.463	0.031	4.288	4.528	4.313	0.326	0.328	-1.656
0.480	1.805	-1.038	1.678	1.750	1.463	0.287	0.435	-1.500
-0.737	0.701	1.418	4.757	4.369	1.162	-2.886	-0.139	0.427
-0.021	-0.366	0.099	4.513	2.957	4.644	-1.708	0.450	0.679
0.343	-1.034	-0.524	1.730	2.224	2.670	0.496	-0.446	-0.709
-0.217	0.265	-0.116	1.878	1.576	2.069	0.379	1.497	-0.171
-1.973	-1.270	-0.720	3.638	1.527	3.786	-0.796	-0.007	1.431
0.128	0.672	-0.968	4.808	4.059	4.570	-0.263	-0.058	-0.615

Table C.5: Parameters for stochastic eddies with seed 874.

A_1	A_2	A_3	B_1	B_2	B_3	x_e	y_e	z_e
1.424	-1.175	-0.678	1.671	3.550	1.900	0.454	-0.333	1.035
-0.817	-0.961	0.083	2.048	2.467	4.878	-0.451	-0.159	-0.548
1.216	-0.146	1.495	4.922	1.110	3.206	-0.922	-1.026	0.268
-0.269	-0.298	-0.596	4.441	4.283	4.712	0.338	-0.262	1.491
1.895	0.020	-0.114	1.757	4.630	1.325	0.143	-0.578	0.431
0.355	0.376	-0.854	3.242	2.383	3.713	-0.249	-0.029	0.428
0.287	1.228	1.006	4.134	2.489	3.147	0.968	0.665	-0.902
1.033	0.804	-0.048	2.370	4.421	2.243	-0.874	-0.607	0.267
-1.014	0.543	0.533	4.659	2.420	2.451	-0.761	0.270	-0.607
1.099	-0.708	-1.681	2.293	1.341	4.357	0.081	0.747	0.085

Table C.6: Parameters for stochastic eddies with seed 1240.

A_1	A_2	A_3	B_1	B_2	B_3	x_e	y_e	z_e
1.352	-0.052	1.096	1.989	4.459	1.122	-1.097	0.817	0.403
-1.537	0.584	-1.654	4.992	2.529	3.574	-1.620	-0.478	-0.648
-0.589	0.039	-0.870	3.488	3.184	1.813	-0.414	0.985	0.194
1.785	1.199	0.634	3.640	2.287	3.044	-0.123	-0.736	0.391
0.501	0.500	-0.882	2.278	3.315	2.569	0.796	1.590	-0.936
-1.245	0.550	1.233	2.771	4.127	4.656	-0.562	0.325	-0.052
0.115	0.100	-0.553	4.450	2.757	3.238	-0.671	-1.507	2.038
0.592	0.310	0.047	1.143	2.070	1.782	-0.324	-0.384	0.416
0.551	-0.978	-0.639	3.420	4.445	4.198	0.743	1.285	0.750
0.385	-0.854	1.334	3.162	2.808	2.677	-1.344	-0.336	-0.827

C.3 Analytic calculation of integrals $I_\gamma^{\alpha,1/2}$ and $I_\gamma^{\alpha,3/2}$

In (6.6.14) we defined

$$I_\gamma^{\alpha,1/2}(z_0, \omega) = \int_0^\infty x_1^{1/2} e^{i\omega x_1/u_0} \exp[-\gamma \tan^2 \alpha (x_1 + \mathcal{F}(z_0) \cos \alpha + y_e \cot \alpha)^2] dx_1, \quad (\text{C.3.1})$$

and

$$I_\gamma^{\alpha,3/2}(z_0, \omega) = \int_0^\infty x_1^{3/2} e^{i\omega x_1/u_0} \exp[-\gamma \tan^2 \alpha (x_1 + \mathcal{F}(z_0) \cos \alpha + y_e \cot \alpha)^2] dx_1. \quad (\text{C.3.2})$$

If we further define the terms

$$\nu(z_0) = \mathcal{F}(z_0) \cos \alpha + y_e \cot \alpha, \quad \mu(z_0, \omega) = \left(2\gamma \nu(z_0) \tan^2 \alpha + \frac{i\omega}{u_0} \right)^2, \quad \lambda(z_0, \omega) = \frac{\mu(z_0, \omega)}{8\gamma \tan^2 \alpha}, \quad (\text{C.3.3})$$

then

$$I_\gamma^{\alpha,1/2}(z_0, \omega) = \frac{\exp(-\gamma \nu^2 \tan^2 \alpha) \exp(\lambda)}{2\gamma^{1/2} \mu^{1/4} \tan \alpha} [2\lambda K_{5/4}(\lambda) - (1+2\lambda) K_{1/4}(\lambda)] \operatorname{sgn}(\nu), \quad (\text{C.3.4})$$

where the functions K_l are modified Bessel functions of the second kind of order l and

$$\operatorname{sgn}(x) = \begin{cases} -1 & x \leq 0 \\ 1 & x > 0, \end{cases}. \quad (\text{C.3.5})$$

Our definition of sgn ensures that $\operatorname{sgn}(0) = -1$, so we have agreement when the serration is straight and $\mathcal{F} = 0$. We also calculate that

$$\begin{aligned} I_\gamma^{\alpha,3/2}(z_0, \omega) &= \frac{\exp(-\gamma \nu^2 \tan^2 \alpha) \exp(\lambda)}{2\gamma^{1/2} \mu^{3/4} \tan \alpha} \\ &\times \left[2\lambda(1+4\lambda) K_{7/4}(\lambda) - (3+12\lambda+8\lambda^2) K_{1/4}(\lambda) \right] \operatorname{sgn}(\nu). \end{aligned} \quad (\text{C.3.6})$$

Bibliography

- ACARE. Strategic Research Agenda: Volume 1. https://ec.europa.eu/research/transport/pdf/acare_strategic_research_en.pdf, 2002. [Online; accessed 15-January-2016]. [Cited on page 1.]
- RK Amiet. Noise due to turbulent flow past a trailing edge. *Journal of Sound and Vibration*, 47(3):387–393, 1976. [Cited on page 15.]
- Lorna J Ayton and Nigel Peake. On high-frequency noise scattering by aerofoils in flow. *Journal of Fluid Mechanics*, 734:144–182, 2013. [Cited on page 171.]
- Lorna J Ayton, James R Gill, and Nigel Peake. The importance of the unsteady Kutta condition when modelling gust-aerofoil interaction. *Journal of Sound and Vibration*, 378(9):28–37, 2016. [Cited on page 171.]
- Carl M Bender and Steven A Orszag. *Advanced mathematical methods for scientists and engineers I: Asymptotic methods and perturbation theory*. Springer, 1978. [Cited on pages xxvi, 45, 103, 144, 145, 150, 173, 174, 175, 176, 177, 181, and 182.]
- WenPing Bi. Calculations of modes in circumferentially nonuniform lined ducts. *The Journal of the Acoustical Society of America*, 123(5):2603–2612, 2008. [Cited on page 15.]
- WenPing Bi, Vincent Pagneux, Denis Lafarge, and Yves Aurégan. Modelling of sound propagation in a non-uniform lined duct using a multi-modal propagation method. *Journal of Sound and Vibration*, 289(4):1091–1111, 2006. [Cited on page 15.]
- William E Boyce, Richard C DiPrima, and Charles W Haines. *Elementary differential equations and boundary value problems*. Wiley New York, 1992. [Cited on pages 44 and 144.]
- Edward J Brambley. Fundamental problems with the model of uniform flow over acoustic linings. *Journal of Sound and Vibration*, 322(4):1026–1037, 2009. [Cited on page 24.]
- Edward J Brambley. Well-posed boundary condition for acoustic liners in straight ducts with flow. *AIAA journal*, 49(6):1272–1282, 2011. [Cited on pages 13 and 169.]
- Edward J Brambley and Nigel Peake. Classification of aeroacoustically relevant surface modes in cylindrical lined ducts. *Wave Motion*, 43(4):301–310, 2006a. [Cited on page 68.]

Edward J Brambley and Nigel Peake. Surface-waves, stability, and scattering for a lined duct with flow. In *12th AIAA/CEAS Aeroacoustics Conference, Cambridge (MA)*, volume 2688, 2006b. [Cited on page 24.]

Edward J Brambley, Mirela Darau, and Sjoerd W Rienstra. The critical layer in sheared flow. In *17th AIAA/CEAS Aeroacoustics Conference, Portland*, volume 2806, 2011. [Cited on page 23.]

Edward J Brambley, Mirela Darau, and Sjoerd W Rienstra. The critical layer in linear-shear boundary layers over acoustic linings. *Journal of Fluid Mechanics*, 710:545–568, 2012a. [Cited on page 75.]

Edward J Brambley, Anthony MJ Davis, and Nigel Peake. Eigenmodes of lined flow ducts with rigid splices. *Journal of Fluid Mechanics*, 690:399–425, 2012b. [Cited on pages 14, 115, and 116.]

Luís MBC Campos and João MGS Oliveira. On the acoustic modes in a cylindrical duct with an arbitrary wall impedance distribution. *The Journal of the Acoustical Society of America*, 116(6):3336–3347, 2004. [Cited on page 14.]

Christopher J Chapman. *High speed flow*. Cambridge University Press, 2000. [Cited on pages 18 and 19.]

Chuen-Yen Chow and Arnold M Kuethe. *Foundations of Aerodynamics: Bases of Aerodynamic Design*. Wiley New York, 1976. [Cited on page 142.]

Clean Sky. Work plan for 2014-2015. http://cleansky.eu/sites/default/files/documents/legal/cs-gb-2014-03-07_doc4a_work_plan_2014_-_2015.pdf, 2014. [Online; accessed 15-January-2016]. [Cited on page 2.]

Climate Change Act. Climate Change Act 2008 legislation. http://www.legislation.gov.uk/ukpga/2008/27/pdfs/ukpga_20080027_en.pdf, 2008. [Online; accessed 16-February-2016]. [Cited on page 1.]

Tim Colonius and Sanjiva K Lele. Computational aeroacoustics: progress on nonlinear problems of sound generation. *Progress in Aerospace sciences*, 40(6):345–416, 2004. [Cited on page 11.]

Tim Colonius, Sanjiva K Lele, and Parviz Moin. Sound generation in a mixing layer. *Journal of Fluid Mechanics*, 330:375–409, 1997. [Cited on page 11.]

Alison J Cooper. Effect of mean entropy on unsteady disturbance propagation in a slowly varying duct with mean swirling flow. *Journal of Sound and Vibration*, 291(3):779–801, 2006. [Cited on pages 13 and 27.]

Alison J Cooper and Nigel Peake. Propagation of unsteady disturbances in a slowly varying duct with mean swirling flow. *Journal of Fluid Mechanics*, 445:207–234, 2001. [Cited on page 170.]

Alison J Cooper and Nigel Peake. Upstream-radiated rotor–stator interaction noise in mean swirling flow. *Journal of Fluid Mechanics*, 523:219–250, 2005. [Cited on pages 5, 12, 13, and 65.]

David G Crighton, Ann P Dowling, John E Ffowcs Williams, M Heckl, and FG Leppington. *Modern methods in analytical acoustics lecture notes*. Springer-Verlag, 1992. [Cited on page 16.]

N Curle. The influence of solid boundaries upon aerodynamic sound. In *Proceedings of the Royal Society of London A: Mathematical, Physical and Engineering Sciences*, volume 231, pages 505–514. The Royal Society, 1955. [Cited on page 11.]

Toby A Driscoll, Nick Hale, and L Nick Trefethen. *Chebfun Guide*. Pafnuty Publications, Oxford, 2014. [Cited on pages 177 and 180.]

Dean G Duffy. *Green's functions with applications*. CRC Press, 2001. [Cited on pages 11, 22, 40, 143, and 144.]

F Farassat. Introduction to generalized functions with applications in aerodynamics and aeroacoustics. *NASA Technical Paper 3428*, 1996. [Cited on pages 16 and 17.]

John E Ffowcs Williams and David L Hawkings. Sound generation by turbulence and surfaces in arbitrary motion. *Philosophical Transactions of the Royal Society of London. Series A, Mathematical and Physical Sciences*, 264(1151):321–342, 1969. [Cited on page 11.]

Flightpath. Europe’s Vision for Aviation: Maintaining Global Leadership & Serving Society’s Needs. <http://ec.europa.eu/transport/modes/air/doc/flightpath2050.pdf>, 2011. [Online; accessed 15-January-2016]. [Cited on page 1.]

Chris R Fuller. Propagation and radiation of sound from flanged circular ducts with circumferentially varying wall admittances, I: Semi-infinite ducts. *Journal of Sound and Vibration*, 93(3):321–340, 1984. [Cited on page 14.]

Fernando Gea-Aguilera, Xin Zhang, Xiaoxian Chen, James R Gill, and Thomas Nodé-Langlois. Synthetic turbulence methods for leading edge noise predictions. In *21st AIAA/CEAS Aeroacoustics Conference, Dallas*, volume 2670, 2015. [Cited on pages 158 and 170.]

Stewart AL Glegg. The response of a swept blade row to a three-dimensional gust. *Journal of Sound and Vibration*, 227(1):29–64, 1999. [Cited on page 33.]

Marvin E Goldstein. Aeroacoustics of turbulent shear flows. *Annual Review of Fluid Mechanics*, 16:263–285, 1984. [Cited on page 12.]

Marvin E Goldstein. An exact form of Lilley’s equation with a velocity quadrupole/temperature dipole source term. *Journal of Fluid Mechanics*, 443:231–236, 2001. [Cited on pages 11, 12, and 19.]

Vladimir V Golubev and Hafiz M Atassi. Acoustic–vorticity waves in swirling flows. *Journal of Sound and Vibration*, 209:203–222, 1998. [Cited on pages 13 and 14.]

Gerd Grubb. *Distributions and operators*. Springer, 2009. [Cited on page 17.]

Mathieu Gruber. *Airfoil noise reduction by edge treatments*. PhD thesis, University of Southampton, 2012. [Cited on page 16.]

Mathieu Gruber, Phillip F Joseph, and Mahdi Azarpeyvand. An experimental investigation of novel trailing edge geometries on airfoil trailing edge noise reduction. In *19th AIAA/CEAS Aeroacoustic Conference, Berlin*, volume 2011, 2013. [Cited on page 16.]

Sina Haeri, Jae W Kim, Subramanian Narayanan, and Phillip F Joseph. 3D calculations of aerofoil-turbulence interaction noise and the effect of wavy leading edges. In *20th AIAA/CEAS Aeroacoustics Conference, Atlanta*, volume 2325, 2014. [Cited on pages 15, 16, 141, 147, 148, 158, and 170.]

Chris J Heaton and Nigel Peake. Acoustic scattering in a duct with mean swirling flow. *Journal of Fluid Mechanics*, 540:189–220, 2005. [Cited on pages 12, 13, and 53.]

Chris J Heaton and Nigel Peake. Algebraic and exponential instability of inviscid swirling flow. *Journal of Fluid Mechanics*, 565:279–318, 2006. [Cited on pages 14, 43, 75, 78, 95, 96, 97, 98, 99, 102, 103, 104, 105, 106, 110, 111, 166, 167, and 169.]

Michael S Howe. A review of the theory of trailing edge noise. *Journal of Sound and Vibration*, 61(3):437–465, 1978. [Cited on pages 15 and 141.]

Michael S Howe. Aerodynamic noise of a serrated trailing edge. *Journal of Fluids and Structures*, 5(1):33–45, 1991a. [Cited on pages 15, 141, 142, 145, and 146.]

Michael S Howe. Noise produced by a sawtooth trailing edge. *The Journal of the Acoustical Society of America*, 90(1):482–487, 1991b. [Cited on pages 15 and 147.]

Michael S Howe. *Acoustics of fluid-structure interactions*. Cambridge University Press, 1998. [Cited on pages 144 and 145.]

Michael S Howe. Trailing edge noise at low Mach numbers. *Journal of Sound and Vibration*, 225(2):211–238, 1999. [Cited on page 142.]

Michael S Howe. Edge-source acoustic Green's function for an airfoil of arbitrary chord, with application to trailing-edge noise. *The Quarterly Journal of Mechanics and Applied Mathematics*, 54(1):139–155, 2001. [Cited on pages 15 and 171.]

Uno Ingard. Influence of fluid motion past a plane boundary on sound reflection, absorption, and transmission. *The Journal of the Acoustical Society of America*, 31(7):1035–1036, 1959. [Cited on page 8.]

Jack L Kerrebrock. Small disturbances in turbomachine annuli with swirl. *AIAA Journal*, 15(6):794–803, 1977. [Cited on pages 13 and 24.]

Doran Khamis and Edward J Brambley. Acoustic boundary conditions at an impedance lining in inviscid shear flow. *Journal of Fluid Mechanics*, 796:386–416, 2016. [Cited on pages 13 and 169.]

Mehdi R Khorrami. A Chebyshev spectral collocation method using a staggered grid for the stability of cylindrical flows. *International journal for numerical methods in fluids*, 12:825–833, 1991. [Cited on page 56.]

Demetrios P Lalias. The “Richardson” criterion for compressible swirling flows. *Journal of Fluid Mechanics*, 69:65–72, 1975. [Cited on pages 103 and 169.]

Rudolph E Langer. On the asymptotic solutions of ordinary differential equations, with reference to the Stokes' phenomenon about a singular point. *Transactions of the American Mathematical Society*, 37(3):397–416, 1935. [Cited on page 176.]

Michael J Lighthill. On sound generated aerodynamically. I. General theory. In *Proceedings of the Royal Society of London A: Mathematical, Physical and Engineering Sciences*, volume 211, pages 564–587. The Royal Society, 1952. [Cited on page 11.]

Michael J Lighthill. *An introduction to Fourier analysis and generalised functions*. Cambridge University Press, 1958. [Cited on page 150.]

Geoffrey M Lilley. On the noise from jets. *AGARD Technical Report CP-131*, pages 13.1–13.12, 1974. [Cited on pages 11, 19, and 34.]

Xin Liu, Hanbo Jiang, Xun Huang, and Shiying Chen. Theoretical model of scattering from flow ducts with semi-infinite axial liner splices. *Journal of Fluid Mechanics*, 786:62–83, 2015. [Cited on page 170.]

Ana Luisa P Maldonado, R Jeremy Astley, John Coupland, Gwenael Gabard, and D Sutliff. Sound propagation in lined annular ducts with mean swirling flow. In *21st AIAA/CEAS Aeroacoustics Conference, Dallas*, volume 2522, 2015. [Cited on page 56.]

Vianney Masson, Hélène Posson, Marlène Sanjose, Stéphane Moreau, and Michel Roger. Fan-OGV interaction broadband noise prediction in a rigid annular duct with swirling

and sheared mean flow. In *22nd AIAA/CEAS Aeroacoustics Conference, Lyon*, volume 2944, 2016. [Cited on page 169.]

James Mathews and Nigel Peake. Noise generation by turbulence interacting with an aerofoil with a serrated leading edge. In *21st AIAA/CEAS Aeroacoustics Conference, Dallas*, volume 2204, 2015. [Cited on pages iii, 141, 153, and 155.]

James Mathews, Nigel Peake, and Stefano Bianchi. Asymptotic and numerical Green's function in a lined duct with realistic shear and swirl. In *22nd AIAA/CEAS Aeroacoustics Conference, Lyon*, volume 2922, 2016. [Cited on pages iii, v, 39, and 169.]

CL Morfey and MCM Wright. Extensions of Lighthill's acoustic analogy with application to computational aeroacoustics. In *Proceedings of the Royal Society of London A: Mathematical, Physical and Engineering Sciences*, volume 463, pages 2101–2127. The Royal Society, 2007. [Cited on page 12.]

Prateek Mustafi, R Jeremy Astley, Rie Sugimoto, and Andrew J Kempton. Acoustic effects of liner damage on zero-splice turbofan intake liners: Computational study. *AIAA Journal*, 53(3):703–712, 2014. [Cited on page 15.]

MK Myers. On the acoustic boundary condition in the presence of flow. *Journal of Sound and Vibration*, 71(3):429–434, 1980. [Cited on page 8.]

Subramanian Narayanan, Phillip F Joseph, Sina Haeri, Jae W Kim, Chaitanya Paruchuri, and Cyril Polacsek. Noise reduction studies from the leading edge of serrated flat plates. In *20th AIAA/CEAS Aeroacoustics Conference, Atlanta*, volume 2320, 2014. [Cited on page 16.]

Rasmus B Nielsen and Nigel Peake. Tunnelling effects for acoustic waves in slowly varying axisymmetric flow ducts. *Journal of Sound and Vibration*, 2016. [Cited on pages 88 and 177.]

Ronald Nijboer. Eigenvalues and eigenfunctions of ducted swirling flows. In *7th AIAA/CEAS Aeroacoustics Conference, Maastricht*, volume 2178, 2001. [Cited on page 14.]

Steven A Orszag. Accurate solution of the Orr–Sommerfeld stability equation. *Journal of Fluid Mechanics*, 50(4):689–703, 1971. [Cited on page 180.]

Vincent Pagneux, N Amir, and Jean Kergomard. A study of wave propagation in varying cross-section waveguides by modal decomposition. Part I. theory and validation. *The Journal of the Acoustical Society of America*, 100(4):2034–2048, 1996. [Cited on page 15.]

Nigel Peake and Anthony B Parry. Modern challenges facing turbomachinery aeroacoustics. *Annual Review of Fluid Mechanics*, 44:227–248, 2012. [Cited on pages 2, 4, 5, and 6.]

Hélène Posson and Nigel Peake. Acoustic analogy in swirling mean flow applied to predict rotor trailing-edge noise. In *18th AIAA/CEAS Aeroacoustics Conference, Colorado Springs*, volume 2267, 2012. [Cited on pages 13, 33, 56, 70, 76, 77, 78, and 169.]

Hélène Posson and Nigel Peake. Swirling mean flow effect on fan-trailing edge broadband noise in a lined annular duct. In *19th AIAA/CEAS Aeroacoustics Conference, Berlin*, volume 2150, 2013a. [Cited on pages 8, 13, 56, 75, and 78.]

Hélène Posson and Nigel Peake. The acoustic analogy in an annular duct with swirling mean flow. *Journal of Fluid Mechanics*, 726:439–475, 2013b. [Cited on pages xx, 10, 12, 13, 25, 27, 28, 29, 30, 33, 34, 35, 36, 37, 39, 41, 55, 56, 74, 76, 77, 78, 96, 165, 169, and 170.]

Hélène Posson, Stéphane Moreau, and Michel Roger. Fan-OGV broadband noise prediction using a cascade response. In *15th AIAA/CEAS Aeroacoustics Conference, Miami*, volume 3150, 2009. [Cited on pages 7 and 11.]

Hélène Posson, Michel Roger, and Stéphane Moreau. On a uniformly valid analytical rectilinear cascade response function. *Journal of Fluid Mechanics*, 663:22–52, 2010. [Cited on page 33.]

David C Pridmore-Brown. Sound propagation in a fluid flowing through an attenuating duct. *The Journal of the Acoustical Society of America*, 30(7):670–670, 1958. [Cited on pages 13 and 22.]

Sjoerd W Rienstra. Sound transmission in slowly varying circular and annular lined ducts with flow. *Journal of Fluid Mechanics*, 380:279–296, 1999. [Cited on page 170.]

Sjoerd W Rienstra. Sound propagation in slowly varying lined flow ducts of arbitrary cross-section. *Journal of Fluid Mechanics*, 495:157–173, 2003. [Cited on page 170.]

Sjoerd W Rienstra and Avraham Hirschberg. *An introduction to acoustics*. Eindhoven University of Technology, 2003. [Cited on page 5.]

Sjoerd W Rienstra and Brian J Tester. An analytic Green’s function for a lined circular duct containing uniform mean flow. *Journal of Sound and Vibration*, 317(3):994–1016, 2008. [Cited on page 71.]

Michel Roger and Stéphane Moreau. Back-scattering correction and further extensions of Amiet’s trailing-edge noise model. Part 1: theory. *Journal of Sound and Vibration*, 286 (3):477–506, 2005. [Cited on page 15.]

Adrian Sescu and Ray Hixon. Toward low-noise synthetic turbulent inflow conditions for aeroacoustic calculations. *International Journal for Numerical Methods in Fluids*, 73(12):1001–1010, 2013. [Cited on page 147.]

Pieter Sijsma. Using phased array beamforming to locate broadband noise sources inside a turbofan engine. In *AARC Engine Noise Phased Array Workshop, Cambridge (MA)*, 2006. [Cited on page 10.]

Pieter Sijtsma. Green's functions for in-duct beamforming applications. In *18th AIAA/CEAS Aeroacoustics Conference, Colorado Springs*, volume 2248, 2012. [Cited on page 10.]

Michael JT Smith. *Aircraft noise*. Cambridge University Press, 2004. [Cited on page 4.]

Christopher KW Tam and Laurent Auriault. The wave modes in ducted swirling flows. *Journal of Fluid Mechanics*, 371:1–20, 1998. [Cited on page 13.]

John M Tyler and Thomas G Sofrin. Axial flow compressor noise studies. *SAE Technical Paper*, 1962. [Cited on page 5.]

Milton Van Dyke. *Perturbation methods in fluid mechanics*. Academic Press New York, 1964. [Cited on page 99.]

Gregory G Vilenski and Sjoerd W Rienstra. On hydrodynamic and acoustic modes in a ducted shear flow with wall lining. *Journal of Fluid Mechanics*, 583:45–70, 2007a. [Cited on pages 13, 46, 49, 53, 57, 59, and 66.]

Gregory G Vilenski and Sjoerd W Rienstra. Numerical study of acoustic modes in ducted shear flow. *Journal of Sound and Vibration*, 307(3):610–626, 2007b. [Cited on page 13.]

Andy J Wathen. Preconditioning. *Acta Numerica*, 24:329–376, 2015. [Cited on page 170.]

Keith D Wilson. Turbulence models and the synthesis of random fields for acoustic wave propagation calculations. *Technical Report ARL-TR-1677*, 1998. [Cited on pages 158 and 170.]

MCM Wright. Hybrid analytical/numerical method for mode scattering in azimuthally non-uniform ducts. *Journal of Sound and Vibration*, 292(3):583–594, 2006. [Cited on page 14.]

David W Wundrow and Abbas Khavaran. On the applicability of high-frequency approximations to Lilley's equation. *Journal of Sound and Vibration*, 272(3):793–830, 2004. [Cited on pages 12, 91, and 176.]